Detonation and Two-Phase Flow

Progress in ASTRONAUTICS and ROCKETRY

A series of volumes sponsored by
American Rocket Society
500 Fifth Avenue, New York 36, New York

Progress Series Editor

Martin Summerfield
Princeton University, Princeton, New Jersey

Titles in the Series

Volume 1. SOLID PROPELLANT ROCKET RESEARCH. 1960
Editor: MARTIN SUMMERFIELD, *Princeton University, Princeton, New Jersey*

Volume 2. LIQUID ROCKETS AND PROPELLANTS. 1960
Editors: LOREN E. BOLLINGER, *The Ohio State University, Columbus, Ohio;* MARTIN GOLDSMITH, *The RAND Corporation, Santa Monica, California;* AND ALEXIS W. LEMMON, JR., *Battelle Memorial Institute, Columbus, Ohio*

Volume 3. ENERGY CONVERSION FOR SPACE POWER. 1961
Editor: NATHAN W. SNYDER, *Institute for Defense Analyses, Washington, D. C.*

Volume 4. SPACE POWER SYSTEMS. 1961
Editor: NATHAN W. SNYDER, *Institute for Defense Analyses, Washington, D. C.*

Volume 5. ELECTROSTATIC PROPULSION. 1961
Editors: DAVID B. LANGMUIR, *Space Technology Laboratories, Inc., Canoga Park, California;* ERNST STUHLINGER, *NASA George C. Marshall Space Flight Center, Huntsville, Alabama;* AND J. M. SELLEN, JR., *Space Technology Laboratories, Inc., Canoga Park, California*

Volume 6. DETONATION AND TWO-PHASE FLOW. 1962
Editors: S. S. PENNER, *California Institute of Technology, Pasadena, California;* AND F. A. WILLIAMS, *Harvard University, Cambridge, Massachusetts*

Volume 7. HYPERSONIC FLOW RESEARCH. 1962
Editor: FREDERICK R. RIDDELL, *Avco Corporation, Wilmington, Massachusetts*

Volume 8. GUIDANCE AND CONTROL. 1962 *(in preparation)*
Editors: ROBERT E. ROBERSON, *Consultant, Fullerton, California;* AND JAMES S. FARRIOR, *Lockheed Missiles and Space Company, Sunnyvale, California*

(Other volumes are planned.)

ACADEMIC PRESS • NEW YORK AND LONDON

Detonation and Two-Phase Flow

Edited by

S. S. Penner
California Institute of Technology, Pasadena, California

F. A. Williams
Harvard University, Cambridge, Massachusetts

A Selection of Technical Papers
based mainly on
A Symposium of the American Rocket Society
held at Palm Beach, Florida
April 26-28, 1961

ACADEMIC PRESS · NEW YORK · LONDON · 1962

IIA Lib.,

COPYRIGHT © 1962, BY ACADEMIC PRESS INC.

ALL RIGHTS RESERVED

NO PART OF THIS BOOK MAY BE REPRODUCED IN ANY FORM,
BY PHOTOSTAT, MICROFILM, OR ANY OTHER MEANS,
WITHOUT WRITTEN PERMISSION FROM THE PUBLISHERS.

ACADEMIC PRESS INC.
111 FIFTH AVENUE
NEW YORK 3, N. Y.

United Kingdom Edition
Published by
ACADEMIC PRESS INC. (London) LTD.

Library of Congress Catalog Card Number 62-13117

PRINTED IN THE UNITED STATES OF AMERICA

AMERICAN ROCKET SOCIETY

Propellants and Combustion Committee

April 1961

Peter L. Nichols, Jr., Chairman
Stanford Research Institute[1]

S. S. Penner, Vice Chairman
California Institute of Technology

Benson E. Gammon
National Aeronautics and Space Administration Headquarters

Leon Green, Jr.
Aeronutronic Division of Ford Motor Company

Jerry Grey
Princeton University

Robert A. Gross
Columbia University

K. Klager
Aerojet-General Corporation

Alexis W. Lemmon, Jr.
Battelle Memorial Institute

Charles J. Marsel
New York University

R. F. Muraca
Stanford Research Institute

Antoni K. Oppenheim
University of California, Berkeley

Thomas F. Reinhardt
Bell Aerosystems Company

Henry M. Shuey
Rohm & Haas Company

Robert J. Thompson, Jr.
Rocketdyne, A Division of North American Aviation, Inc.

Max Williams
California Institute of Technology

H. G. Wolfhard
Thiokol Chemical Corporation

C. M. Wong
United Technology Corporation[2]

---

[1] Presently at Aerojet-General Corporation
[2] Presently at Lockheed Missiles & Space Division

AMERICAN ROCKET SOCIETY

Liquid Rockets Committee

April 1961

Martin Goldsmith, Chairman
The Rand Corporation[1]

Charles H. King, Jr., Vice Chairman
Pratt & Whitney Aircraft Division, United Aircraft Corporation

Henry Burlage, Jr.
National Aeronautics and Space Administration

Paul D. Castenholz
Rocketdyne, A Division of North American Aviation, Inc.

Donald A. Dooley
Aerospace Corporation

Gerard W. Elverum, Jr.
Space Technology Laboratories, Inc.

Harry A. Koch
Reaction Motors Division, Thiokol Chemical Corporation

Harold J. McClellan
The Boeing Company

John C. Moise
Aerojet-General Corporation

William F. Radcliffe
General Dynamics/Astronautics

Rolf H. Sabersky
California Institute of Technology

Earl L. Wilson
Douglas Aircraft Company, Inc.

---

[1] Presently at Aerospace Corporation

PREFACE

The present volume contains a collection of technical papers, some of which were presented at the ARS Propellants, Combustion, and Liquid Rockets Conference, held in Palm Beach, Florida, April 26-28, 1961. These papers provide an excellent illustration of current research and development on a selected group of problems relating to detonations, two-phase nozzle flow, and combustion in liquid fuel rocket engines.

The papers on detonation, given in Part 1, cover the entire range of physical conditions under which detonation may be initiated or sustained — e. g., high explosives, solid propellants, liquid sprays, and gases. Experimental and theoretical studies are included. Significant progress is recorded in our understanding of basic phenomena involved in transition from deflagration to detonation, and in the nature of stable detonations in dilute sprays and other systems.

The perennial problems associated with high frequency instabilities in liquid fuel rocket engines are considered from various points of view in Part 2, Section A. The real challenge in this field, however, is not yet resolved: the origin of unstable burning in microscopic terms is not as yet understood. An account of combustion processes and vibrations in the spherical LR99 engine used in the X15 provides interesting contrasts with the stability behavior of more conventional rocket engines.

Considerable progress has been made in recent years in understanding the nature of two-phase flow phenomena in converging-diverging nozzles. The technical papers in Part 2, Section B, were supplemented, at the Palm Beach meeting, by a round-table discussion, moderated by S. S. Penner, in which S. I. Cheng, A. R. Hall, M. Farber, M. Gilbert, and R. Kushida participated. The salient conclusions reached by the panel include the following recommendations: The mathematical techniques used for solving the two-phase flow problem should be re-examined with particular emphasis on the nature of the singularity at the throat; a real understanding of chemical reaction rates offers the ultimate promise of controlling, as well as of describing, relaxation phenomena in nozzle flow; the quantitative nature of the relaxation processes in real rocket nozzles will depend on altitude; comparisons between theory and experiment in nozzle flow processes should be based on a realistic evaluation of the many phenomena that affect engine performance; there is a pressing need for more accurate rate equations in condensation processes and in chemical changes.

The present volume should be of value as a reference book to the investigator working in the field of propulsion research and development. It also should present challenging ideas to the serious student of combustion science who is interested in discovering important new areas of application in which further basic studies are required for proper understanding of observable data.

S. S. Penner and F. A. Williams

September 1961

CONTENTS

Propellants and Combustion Committee v

Liquid Rockets Committee vii

Preface ix

PART 1. DETONATIONS IN SOLIDS, LIQUIDS, AND GASES

Stability of Detonation Waves at Low Pressures 3
James A. Fay

Spectrophotometric Analysis of Detonation Wave Structure . . . 17
J. Kenneth Richmond

Parametric Studies of Strong Gaseous Detonations 47
K. M. Foreman, H. Pevney, and R. MacMillan

Estimating Caloric State Behavior in Condensed-Phase Detonations 65
Riley O. Miller

Theoretical Treatment of the Detonation Behavior of Composite Propellants 75
M. H. Boyer and Ray Grandey

Detonations in Dilute Sprays 99
F. A. Williams

PART 2. TWO-PHASE FLOW

A. Two-Phase Nozzle Flow

Perturbation Analysis of One-Dimensional Heterogeneous Flow in Rocket Nozzles 117
W. D. Rannie

Analysis of Two-Phase Flow in Supersonic Exhausts 145
John H. Morgenthaler

Flow of Gas-Particle Mixtures in Axially Symmetric Nozzles 173
James R. Kliegel and Gary R. Nickerson

Particle Velocity Lag in Metalized Propellants 195
B. Brown

Equilibrium Between Phases in Converging-Diverging Nozzles 209
Bruce A. Reese and Louis P. Richard

B. Stable and Unstable Combustion Processes in Liquid Fuel Rocket Engines

Spray Combustion Model With Droplet Breakup: Analytical and Experimental Results 243
Samuel Z. Burstein, Sanford S. Hammer, and Vito D. Agosta

Steady-State Combustion Measurements in a LOX/RP-1 Rocket Chamber and Related Spray Burning Analysis. 269
S. Lambiris and L. P. Combs

Application of Similarity Parameters for Correlating High Frequency Instability Behavior of Liquid Propellant Combustors. 305
Richard J. Priem and Gerald Morrell

Vibration and Combustion Investigation of the LR99 Engine 321
Mario J. Luperi and Sanford J. Tick

Tangential Mode of Combustion Instability 339
H. C. Krieg, Jr.

Contributors to Volume 6 367

PART 1

DETONATIONS IN SOLIDS, LIQUIDS, AND GASES

STABILITY OF DETONATION WAVES AT LOW PRESSURES

James A. Fay
Massachusetts Institute of Technology, Cambridge, Mass.

ABSTRACT

The question of detonation wave instability and its connection with spinning detonation is reviewed from the point of view of two-dimensional disturbances within the reaction zone of a detonation front. A method is proposed for determining the stability of detonation waves to two-dimensional disturbances by means of a linearized perturbation theory that is analogous to that used in laminar boundary layer stability studies. The general perturbation equations for this case are developed, but no solutions are given.

INTRODUCTION

One of the more interesting results of the experimental observations of the properties of gaseous detonation waves propagating in tubes is the accumulating evidence that the wave propagation is unsteady on a scale comparable with the wave front thickness (1, 2)[1] even though the average propagation velocity is constant. These more recent observations parallel much older ones (3) concerning the phenomenon of spinning detonation in which large scale (that is, comparable to tube diameter) periodic unsteadiness was also found to exist under certain conditions even though the average wave speed was equal to its value calculated according to the one-dimensional steady flow theory of Chapman and Jouguet. The recent observations stem entirely from Schlieren and interferometric photographs of detonation waves taken at sufficiently low initial pressure so that the reaction zone could be resolved with the usual optical arrangement (see Fig. 1).

J. A. FAY is Professor of Mechanical Engineering. Paper submitted for publication to the American Rocket Society, July 18, 1961. The preparation of this paper was sponsored by the Office of Naval Research through Project Squid.

[1] Numbers in parentheses indicate References at end of paper.

Although the evidence is far from complete, it is sufficient to suggest that under usual circumstances detonation waves proceeding at their characteristic Chapman-Jouguet velocities are apparently unstable. It is this proposition that will be discussed and for which a method of theoretical analysis is suggested.

There are several similarities between the phenomenon of spinning detonation and the more recently discovered unsteadiness, which may be termed structural instability. First of all, both phenomena appear at low pressures in any given mixture propagating through a tube of given diameter. Structural instability appears when the reaction zone thickness is discernable, e. g., a few millimeters thick in a 10-cm tube. Spin invariably occurs near the low pressure limit of detonation wave propagation (4). For the few mixtures for which the measurements have been made, it appears that spin (and hence extinction) occur when the reaction zone thickness becomes an appreciable fraction of the tube diameter. Secondly, both spin and structural instability appear only for Chapman-Jouguet waves, that is, those which are not overdriven. Even in mixtures that do not sustain a steady detonation wave, it has been observed that spin appears in an initially overdriven detonation as it decays through the Chapman-Jouguet velocity. Finally, in both cases, there is an extraordinary and apparently inexplicable peculiarity of the motion. In the case of spinning detonation, the remarkable agreement between the measured and calculated spin frequencies proves that the wave propagation in the wake of the detonation wave is almost entirely transverse to the tube axis, yet no suitable explanation of this effect has been suggested. In the case of the structural instability, both Schlieren and interferometric pictures show appreciable disturbances within the reaction zone which apparently decay within a very short distance behind the wave front (see Fig. 1).

It is tempting to consider both these phenomena as simply different manifestations of the same basic instability. In fact, on some occasions, both seem to exist side by side, as shown in Fig. 2, in which a periodic structure is superimposed on a smaller scale random nonuniformity. Although this may be the case, much more experimental evidence is needed before such a proposition can be considered proved.

In view of these experimental observations, it seems desirable to develop a stability theory for detonation waves. A first approach might follow that of Landau (5) and Markstein (6), who studied laminar flame stability by considering the flame as a discontinuity in an otherwise inviscid, adiabatic, two-dimensional unsteady flow field. Chu (7) has adopted this approach in studying the stability of overdriven detonation waves and has found that, like shock waves, they are stable. The perturbation considered in such an analysis is illustrated in Fig. 3, where an arbitrary plane wave in the subsonic flow downstream of the discontinuity is matched to the perturbed detonation front so that the Rankine-Hugoniot conditions are satisfied across the discontinuity. The purpose of the analysis is to determine whether the imaginary part of the complex frequency for a flow perturbation of this type has a negative or positive value, indicating instability or stability.

Chu did not discuss the case of the Chapman-Jouguet wave for which the flow downstream is just sonic. For this case, a perturbation of the wave front of the type shown in Fig. 3 cannot be permitted, at least to first order, because the Chapman-Jouguet velocity is the minimum velocity that will satisfy the Rankine-Hugoniot conditions, and any increase or decrease in pressure behind the wave would only cause an increase in velocity. Consequently, no distortion of the wave front is permitted, and the only possible wave pattern downstream which will meet this boundary condition is a standing wave with a wave front parallel to that of the detonation itself. The flow is neutrally stable to such a disturbance. The fact that such a neutral disturbance propagates in a direction normal to that observed in the spinning detonation merely serves to emphasize the drawback of the discontinuity approach to detonation wave stability.

Probably the chief reason for the failure of the discontinuity theory to predict instability is that the latter probably originates within the wave front itself--an effect which is necessarily absent when the detonation wave is considered as a discontinuity. By treating the detonation wave as a shock wave followed by a flame front, that is, as a double discontinuity, it is possible that a better model of the true process would result and a clearer insight into the problem in stability might be achieved. Instead, a method is proposed which is very similar to that used in laminar boundary layer stability studies, which has had great success in understanding the problem of transition to turbulence.

The theory of boundary layer stability will be summarized by considering the flow shown in Fig. 4. A viscous fluid flows parallel to a solid wall where there is a locally nongrowing boundary layer. This basic flow is thus parallel to the wall with a velocity and other properties depending only on y, the distance normal to the wall. If a perturbation is considered which is periodic in time and in the flow direction (real wave number α), then the y dependence of the disturbance is given by the Orr-Sommerfeld equation (8)

$$\left(\frac{d^2}{dy^2} - \alpha^2\right)^2 \phi = i\alpha R \left\{ (u-c)\left(\frac{d^2}{dy^2} - \alpha^2\right)\phi - \left(\frac{d^2u}{dy^2}\right)\phi \right\} \qquad [1]$$

where ϕ is any perturbation quantity, u is the unperturbed flow velocity, c is the wave phase velocity, and R is the Reynolds number based on boundary layer thickness and free stream velocity, all quantities having been made dimensionless by a suitable choice of reference values. The solution to this eigenvalue equation which satisfies the boundary conditions at the wall and disappears at infinity can only be found for the proper combinations of the parameters α, R, and c. In particular, if it is required that the imaginary part of the complex frequency (or of c) be zero, which is the condition for neutral stability, then for any given value of R there will be only discreet values of wave number α which will delimit the region of stability from that of instability. The general result of such a calculation is shown in Fig. 5, where the regions of stability and instability are indicated as a function of wave number α and Reynolds number R. The point of interest in fluid mechanics is that at sufficiently high Reynolds numbers there are always some waves that will grow in amplitude until nonlinear effects become dominant.

An analogous approach for the case of a detonation wave will be considered. The basic flow is the one-dimensional reacting flow behind a shock wave as given by the ordinary detonation theory (see Fig. 6). The unperturbed flow quantities depend only on the distance x normal to the shock front. The perturbed flow will be considered to be periodic in time and direction parallel to the shock front, and to have a dependence on x to be determined by the solution to the perturbation equations which, hopefully, will have a form similar to the Orr-Sommerfeld Eq. 1 above. The parameter or parameters equivalent to the Reynolds number of the boundary layer case can be expected to arise naturally out of the perturbation analysis. These important quantities would be expected to be related to the reaction rates.

The basic equations of conservation of mass, momentum, and energy, in which transport effects are considered unimportant, as well as a kinetic equation and equation of state are given below

$$\frac{\partial \rho}{\partial t} + \nabla \cdot (\rho \vec{q}) = 0 \qquad [2]$$

$$\left(\frac{\partial}{\partial t} + \vec{q} \cdot \nabla\right) \vec{q} + \frac{1}{\rho} \nabla p = 0 \qquad [3]$$

$$\left(\frac{\partial}{\partial t} + \vec{q} \cdot \nabla\right) e + p \left\{ \frac{\partial}{\partial t} + q \cdot \nabla \right\} \left(\frac{1}{\rho}\right) = 0 \qquad [4]$$

$$\left(\frac{\partial}{\partial t} + q \cdot \nabla\right) \epsilon = r\,(\epsilon, p, \rho) \qquad [5]$$

$$e = e(p, \rho, \epsilon) \qquad [6]$$

where ρ is the density, $\vec{q}$ the velocity, p the pressure, e the internal energy, and ϵ the single reaction coordinate of this simplified system having an irreversible reaction whose rate is specified by Eq. 5.

The steady one-dimensional solution to these equations will give the dependent variables as a function of position behind the shock front. Taking as reference quantities the values of these dependent variables immediately behind the shock front, a reference length that could be the thickness of the combustion zone for this solution, and a reference time that is this length divided by the velocity, this set of equations can be made dimensionless. By considering small perturbations to this basic flow, following the usual method of considering first-order effects only, the following set of equations for the dimensionless perturbation quantities is arrived at:

$$D\rho + \frac{1}{\bar{q}} \nabla \cdot \vec{q} = \beta \left\{ \frac{1}{(\bar{q})^2} \vec{q} \cdot \vec{i} - \rho \right\} \qquad [7]$$

$$D\vec{q} + \bar{q}\, \nabla p = -\beta \left\{ \vec{q} \cdot \vec{i} + (\bar{q})^2 \rho \right\} \vec{i} \qquad [8]$$

$$De + \bar{q}\,(P-\bar{q})\,\nabla\cdot\vec{q} = \beta\left\{(P-\bar{q})\vec{q}\cdot\vec{i} - \bar{q}p - \bar{q}^{2}(P-\bar{q})\,\rho\right\} \qquad [9]$$

$$D_{\epsilon} + \bar{r}_{\epsilon}\epsilon + \bar{r}_{p}p + \bar{r}_{\rho}\rho = -\,\delta\,\beta\,\vec{q}\cdot\vec{i} \qquad [10]$$

$$e = \bar{e}_{p}p + \bar{e}_{\rho}\rho + \bar{e}_{\epsilon}\epsilon \qquad [11]$$

where $$P \equiv 1 + \left(\frac{p}{\rho q^{2}}\right)_{\text{shock}} \qquad [12]$$

$$\beta \equiv \frac{d\bar{q}}{dx} \qquad [13]$$

$$\delta \equiv \frac{\bar{e}_{p} + \frac{1}{\bar{q}^{2}}\,(e\rho) - (P-\bar{q})}{e_{\epsilon}} \qquad [14]$$

$$D \equiv \frac{\partial}{\partial t} + \bar{q}\,\frac{\partial}{\partial x} \qquad [15]$$

The dimensionless perturbation quantities appear here without special notation. The bar over a symbol refers to the local value of the corresponding quantity as obtained from the steady-flow unperturbed solution, and subscripts refer to partial derivatives.

Next, each perturbation quantity is assumed to have the following form:

$$\phi = \phi\ (x)\ \exp\left\{ i\,\alpha\,(y - ct)\right\} \qquad [16]$$

On substituting this into the previous set of first-order equations, the result may be written in the following matrix form:

$$\{A\}\,\bar{q}\,\frac{d\bar{x}}{dx} = i\,\alpha\,\{B\}\bar{x} + \beta\,\{C\}\,\bar{x} \qquad [17]$$

where the vector x has the components

$$\bar{x} \equiv (q_x, q_y, \rho, p, e, \epsilon) \qquad [18]$$

and the matrices A, B, and C are given by

$$\{A\} \equiv \begin{matrix} 1 & 0 & q^2 & 0 & 0 & 0 \\ 1 & 0 & 0 & 1 & 0 & 0 \\ 0 & 1 & 0 & 0 & 0 & 0 \\ P-\bar{q} & 0 & 0 & 0 & 1 & 0 \\ 0 & 0 & 0 & 0 & 0 & 1 \\ 0 & 0 & (P-\bar{q})\bar{q} & -1 & \dfrac{\gamma-1}{\bar{q}} & \dfrac{(\gamma-1)Q}{\bar{q}} \end{matrix} \qquad [19]$$

$$\{B\} \equiv \begin{matrix} 0 & -\bar{q} & c\bar{q}^{\,2} & 0 & 0 & 0 \\ c & 0 & 0 & 0 & 0 & 0 \\ 0 & c & 0 & -\bar{q} & 0 & 0 \\ 0 & -c\bar{q}(P-\bar{q}) & 0 & 0 & c & 0 \\ 0 & 0 & -i\,\dfrac{r_\rho}{a} & -i\,\dfrac{r_p}{a} & 0 & c-i\,\dfrac{r_\epsilon}{a} \\ 0 & 0 & 0 & 0 & 0 & 0 \end{matrix} \qquad [20]$$

$$\{C\} \equiv \begin{matrix} 1 & 0 & -\bar{q}^{2} & 0 & 0 & 0 \\ -1 & 0 & -\bar{q}^{2} & 0 & 0 & 0 \\ 0 & 0 & 0 & 0 & 0 & 0 \\ P-\bar{q} & 0 & \bar{q}^{2}(P-\bar{q}) & \bar{q} & 0 & 0 \\ -\delta & 0 & 0 & 0 & 0 & 0 \\ 0 & 0 & -\bar{q}(2P-3\bar{q}) & 1 & 0 & 0 \end{matrix} \qquad [21]$$

It has also been assumed that the gas is perfect with a specific heat ratio γ and a dimensionless heat of reaction Q.

This system of linear equations could be reduced to a single equation comparable to the Orr-Sommerfeld equation above. However, the principal effects can be seen by a closer examination of Eq. 17 and the corresponding matrices in Eqs. 19-21. For example, if the flow behind the shock wave were uniform, then β would be zero, and the system given by the first two terms in Eq. 17 is identical to that for sound waves in a reacting medium. If no chemical reaction is permitted in the perturbation equations, then the fifth row in matrix B disappears except for the term containing c, and "frozen" sound waves are found.

If the basic flow is one for which $\bar{q}$ is a function of x, then in addition to the space dependent coefficients in the first two terms, the third term in Eq. 17 is also important. The general result is thus a system of dispersing sound waves in which one source of phase change (and hence possible instability) is that due to the reaction rate terms appearing in the fifth row of matrix B. Furthermore, it would appear that these terms would become of greater importance for small α, that is, for long wavelengths.

A word should be said about the boundary conditions at the shock wave, which will not be discussed in detail. The effect of perturbing the shock front is to introduce a phase difference between the x and y components of velocity at the shock front. In the absence of a chemical reaction, a shock front is stable to such a perturbation so that the solution to

Eq. 17 with the third term absent only exists if the phase velocity c has a positive imaginary part. Thus, in the absence of chemical reaction, there is an inherent tendency towards stability, so that if there is a basic instability in the detonation front, it must arise out of the effects of chemical reaction.

In principle, it appears possible to find solutions to the eigenvalue Eq. 17 and to determine the regions of stability and instability in a manner similar to that shown in Fig. 5. The parameter corresponding to Reynolds number would appear to be the quantities r_ρ , r_p, and r_ϵ. These quantities depict the sensitivity of the chemical reaction to changes in pressure, density, and concentration, and like the Reynolds number in the Orr-Sommerfeld equation, they are the terms that will introduce phase shifts.

It is possible that this scheme of analyzing the question of flow stability also contains the means of describing spinning detonations. The perturbation considered above is one for a wave of infinite extent in which only boundary conditions on the shock wave and the vanishing of the disturbance far downstream need be satisfied. If the wave is contained in a finite tube, then additional boundary conditions would have to be satisfied at the tube walls. This would generally require superposition of the waves considered above, but such can be accomplished within the linearized theory. Furthermore, the type of perturbation considered is identical with that observed in spinning detonation, that is, a wave with phase velocity parallel to the shock front. It would indeed be fortunate if the whole of the experimental phenomenon could be encompassed within this one simple point of view.

REFERENCES

1 J. A. Fay: The Structure of Gaseous Detonation Waves. Eighth International Symposium on Combustion, Butterworths, London (to be published).

2 D. R. White: The Turbulent Structure of Gaseous Detonation. Physics of Fluids, April 1961, vol. 4, pp. 465-480.

3 J. A. Fay: A Mechanical Theory of Spinning Detonation. J. Chem. Phys., June 1952, vol. 20, pp. 942-950 (see the references in this paper).

4 W. E. Gordon, A. J. Mooradian and S. A. Harper: Limit and Spin Effects in Hydrogen-Oxygen Detonations. Seventh Symposium (International) on Combustion, pp. 752-759, Butterworths, London, 1959.

5 L. Landau: Acta Physicochim (U. R. S. S.), 1944, vol. 19, p. 77.

6 G. H. Markstein: Experimental and Theoretical Studies of Flame-Front Stability. J. Aero. Sci., March 1951, vol. 18, pp. 199-209.

7 B.-T. Chu: Vibration of the Gaseous Column Behind a Strong Detonation Wave. Proceedings of the Gas-Dynamics Symposium on Aerothermochemistry, pp. 95-111, Northwestern Univ., Evanston, Ill., 1956.

8 C. C. Lin: The Theory of Hydrodynamic Stability, Cambridge University Press, Cambridge, 1955.

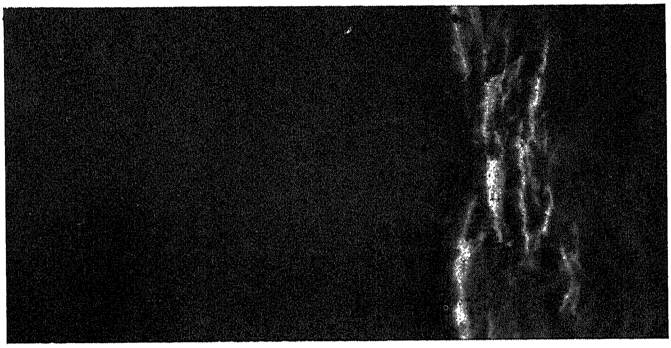

Fig. 1 a Schlieren photograph of a 20% C_2-H_2-45% O_2-35% A detonation at 30 mm initial pressure (wave moves toward left)

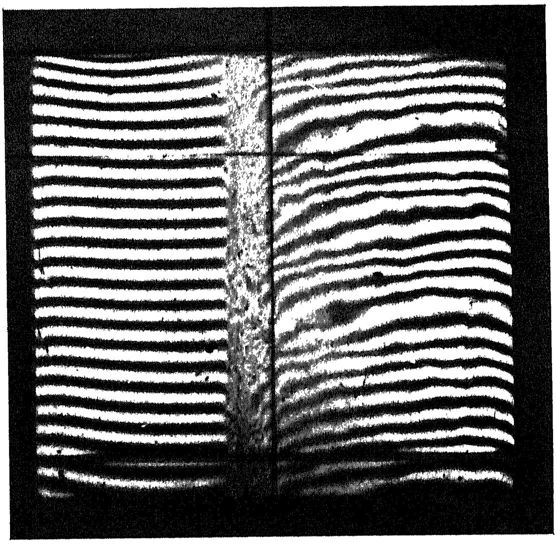

Fig. 1b Interferogram of a $2H_2$-O_2 detonation at 78 mm initial pressure in an 8 cm square tube (wave moves toward left). Note the random character of the interference pattern within the combustion zone (photograph by D. R. White)

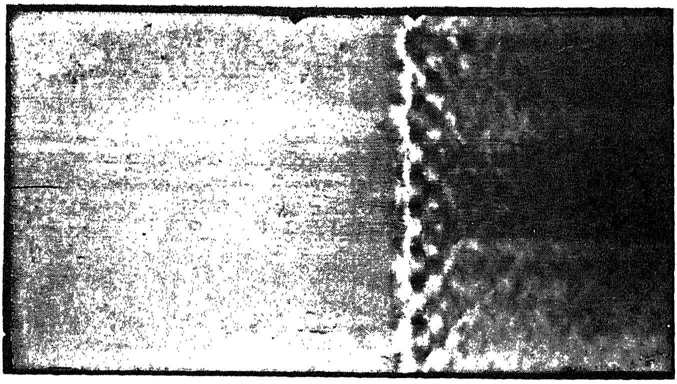

Fig. 2 Schlieren photograph of detonation in C_2H_2-O_2-A mixture at 20 mm initial pressure

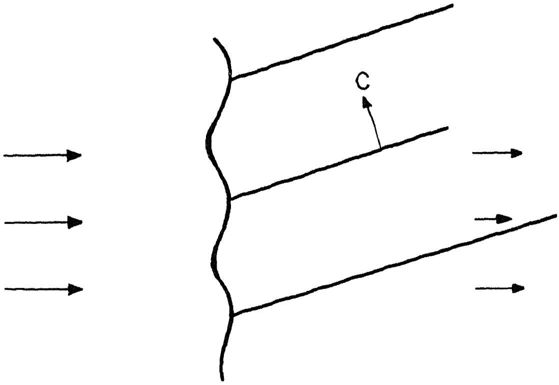

Fig. 3 Pattern of wave-like disturbance behind detonation (coordinates fixed in detonation front)

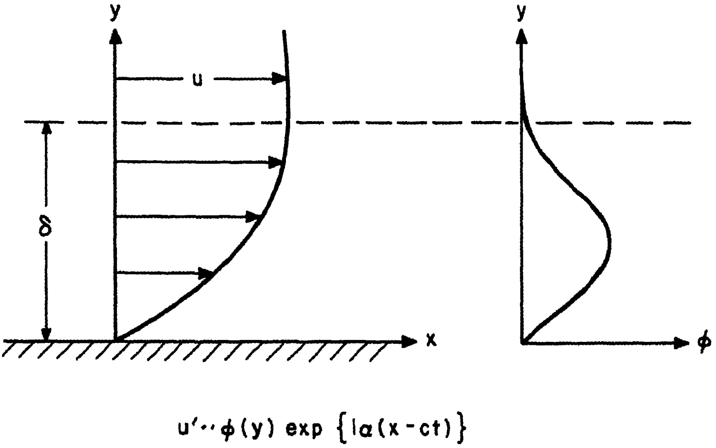

Fig. 4 Character of basic flow and perturbation used in laminar boundary layer stability analysis

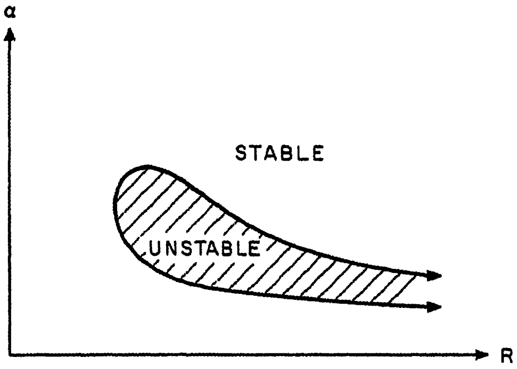

Fig. 5 Typical stability diagram for laminar boundary layer

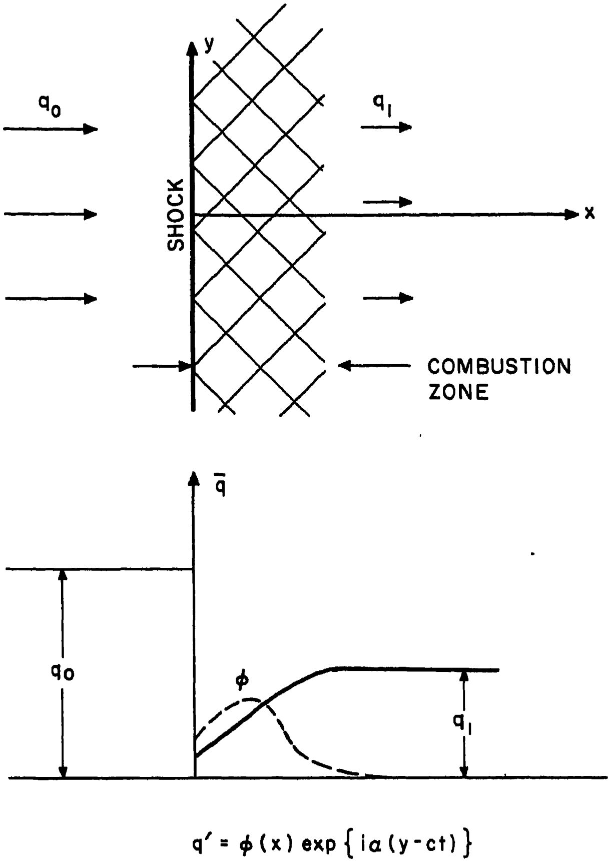

Fig. 6 Character of basic flow and its perturbation used in detonation wave stability analysis

SPECTROPHOTOMETRIC ANALYSIS OF DETONATION WAVE STRUCTURE

J. Kenneth Richmond

Boeing Scientific Research Laboratories
Seattle, Washington

ABSTRACT

In connection with the phenomena of standing detonation waves as a possible mode of propulsion, a controversy has arisen as to the nature of such waves and their thickness and internal structure. In order to provide criteria for critical analysis of such waves, ordinary moving detonation waves have been examined with the help of a spectrophotometer with high wave length and time resolution. The method used is an extension of ones previously applied to stationary laminar and turbulent flames. Both steady-state and unsteady detonations of propane or hydrogen, with air or oxygen, were examined. The thickness of the combustion wave, as defined by the rise time of the characteristic emission behind the shock front, varied from about 2 mm to 30 mm, depending on the mixture and the initial pressure. Even with the "strong" detonation waves, there was no indication of an "induction period" greater than one microsecond.

INTRODUCTION

The standing wave ramjet has been under critical examination in the past two years as a possible power plant for hypersonic flight within the atmosphere. In a review article, Dugger (1)[1] discusses the advantages of ramjets over turbojets and rockets for hypersonic propulsion and in particular, the advantages (as well as disadvantages)

J.K. RICHMOND, staff member in the Aerodynamics and Propulsion Group, Flight Sciences Laboratory. Paper presented at the ARS Propellants, Combustion, and Liquid Rockets Conference, Palm Beach, Fla., April 26-28, 1961.

[1] Numbers in parentheses indicate References at end of paper.

of supersonic combustion ramjets. Of the latter, the standing wave, or detonation wave, ramjet has at least the advantage of simplicity, with the possibility of a very short engine, since the heat addition is presumed to take place in a very short distance. This distance is one of the principal subjects of this paper.

STANDING DETONATION WAVES

The nature, thickness, and structure of standing detonation waves of hydrogen-air mixtures in the laboratory and proposed engines employing these waves have been discussed at length by Gross et al. (2, 3) and by Nicholls et al. (4, 5). A small controversy has arisen whether the phenomena observed in these cases were true detonations, and what the thickness and detailed structure of the reaction zone might be under various conditions. It is the general thesis of this paper that certain methods of analyzing the structure of ordinary traveling detonation waves will apply equally well to the standing wave by analogy of these methods as applied to moving and standing deflagration waves, respectively.

SURVEY OF WORK ON MOVING DETONATION WAVE STRUCTURE

Considerable work has been reported on transition from deflagration to detonation and on external effects such as velocity of propagation and pressure ratios, but not so much on the details of structure of the detonation wave. Experimental work is usually done at reduced pressures, so that the waves are thick enough to permit easy resolution.

The results of a number of such experiments were reported in the Second ONR Symposium on Detonations in 1955. Gilkerson and Davidson (6) detonated mixtures of hydrogen and oxygen at 0.035 atm by means of shock waves, using filtered phototubes and iodine vapor as indicators. Bennett and Wedaa (7) also ignited detonations in mixtures of acetylene-oxygen and hydrogen-oxygen down to 10 cm Hg pressure, reporting ionization and light profiles. In both of the forementioned papers, the light intensity rose to a maximum within 2 to 7 μsec but decayed very slowly. There were also indications that the detonations were overdriven or unsteady. Kistiakowsky (8), using x-ray absorption techniques, observed the thickness of reaction zones as zones of high initial density in $2H_2$-O_2 mixtures. The duration of the reaction zone varied from 2 to 20 μsec as the initial pressure varied from 85 mm to 20 mm, respectively.

Using an interferometer, White (9) observed detonations in mixtures of hydrogen and oxygen at initial pressures of 20 mm and upwards. All records showed nonplanar detonation fronts, with disturbances whose scale increased with decreasing pressure.

In a more recent work, Wagner (10) investigated the structure of the reaction zones of hydrogen and oxygen detonations. Temperature and density profiles were followed to a high degree of resolution by means of schlieren light and ultraviolet absorption. At about 1/10 atm initial pressure, he found an induction period of a few tenths of a μsec, followed by a reaction period of about 10 μsec.

Most of the work reported indicates reaction zone thicknesses inversely proportional to pressure, representing a value for a number of collisions somewhere between 10^3 and 10^4.

EXPERIMENTAL METHOD

One of the most helpful methods in examining the structure of the reaction zones of laminar and turbulent flames is the use of a spectrophotometer with sufficient spatial resolution to trace out the distribution of certain characteristic emitters in the flames. Hydrocarbon flames are commonly used, because of their high luminosity and the production of several convenient bands for comparison. Wohl and his co-workers (11) traversed laminar flames at reduced pressures, tracing out the radiation intensity from butane flames at 4312Å, due to CH radical radiation; at 4737Å due to C_2; at 4500Å, to follow the continuum radiation only, in between the bands; at 3065Å, due to OH radical radiation, and at 9600Å, which is one of the bands due to H_2O emission. The results of these measurements were amply verified by schlieren photographs and by chemical sampling.

This same technique has been extended by several workers (12-14) to turbulent flames, primarily to find out whether turbulent flames in any way resemble laminar flames.

Data obtained from spectrographic plates and from spectrophotometric traverses in this manner form the bases for the chemical kinetics of flame reactions and have become well established as indications of the combustion process itself. Hereafter in this paper, an attempt will be made to justify this method as applied to the study of detonation structure, and the results of applications to various fuel-oxygen systems will be presented.

There have been many reports of detonation spectra, one of the best of which was by Wagner (15) in the Sixth Combustion Symposium. Detonation spectra are somewhat different from the corresponding flame spectra, as discussed by Wagner, mainly because of the high temperatures existing. The band structure of detonations is much less complex, with a very strong continuum in most cases. But no new bands from the combustion process are ever found, and the brightest bands in the flame spectra may still be seen. Fig. 1 shows comparisons of detonation, flame, and calibration spectra taken under the conditions of the present work by a JACO f/6.3 grating spectrograph, viewing the detonations end-on. The dispersion is about 9Å/mm. It will be seen here, also, that the detonation band structure is almost washed out by the strong continuum, but that there is still available the CH band head at 4312Å for monitoring the propane detonations and the OH band head at 3065Å for monitoring the hydrogen detonations. Repeated shots with shock waves in air or oxygen produced neither measurable continuum nor band spectra, even in the reflected shock, but only line spectra due to metals vaporized from the walls of the shock tube. Most obvious of these, to be seen on the spectrograms of propane detonations, are lines at 4289Å, 4274Å, 4254Å, due to chromium, and of calcium at 4227Å.

The experimental method in this work consists of measuring the phase difference between the pressure and/or temperature step at the leading edge of the detonation wave, and the course of the chemical reaction following, as indicated by the distribution of characteristic emission. These data will be supplemented by pressure and velocity data and by a few calculated parameters.

DESCRIPTION OF APPARATUS

A schematic of the experimental apparatus is shown in Fig. 2. The detonations took place in the BSRL mechanical shock tube, built of stainless steel, with an overall length of 37 ft. The driver section has a 4-in. ID and a length of 5 ft; the driven section has a 3-in. ID. The driver section is equipped with a spark gap whose spacing is about 1.25 in.; the ignition source is one half of a luminous tube transformer, rated at 12,000 v and 1225 v-amp. With this ignition source, mixtures of propane and oxygen could be detonated at initial pressures as low as 1/150 atm. For spark ignition, the entire shock tube was filled with combustible mixture. With mixtures harder to ignite or to detonate, shock waves were used, in which case the driver section was closed off with a diaphragm and then filled with helium until the diaphragm ruptured, generating a shock wave in the combustible mixture.

The gases to be used were metered into a mixer and into the shock tube with standard rotameters that had been calibrated with a precision wet test meter, which was calibrated with a standard gas prover. The accuracy of the gas flow rates obtained in this manner is about ± 2%. After the shock tube had been pumped down to an absolute pressure less than 1/10 mm Hg, the gas mixture was flowed in and pumped out at a steady rate for several minutes; then the pump was closed off and the pressure adjusted to the final value.

All measurements were made in the test section, which was the last 3 ft of the shock tube, and which was equipped with suitable ports and windows. In order to be able to mark accurately the arrival of the pressure step at the leading edge of the detonation waves, thin film heat transfer probes were used. These probes consist of thin films of platinum on a glass backing (flush with the inside tube wall), which, with suitable circuitry, marked the arrival of shock waves. The overall rise time was about 1/2 µsec which is somewhat better than is possible with ionization probes or with pressure transducers. A pair of these thin film probes, with their outputs displayed on an oscilloscope, served as velocity measurements, with an accuracy of about ± 2%. Opposite one of these probes was a window with a slit and lens arrangement, through which the spectrograph could view the passing detonation wave. The resolution of this system will be discussed later.

In the focal plane of the spectrograph, a rack was located, containing exit slits and photomultiplier tubes that could be set on various lines in the spectrum. Photomultipliers used were type 1P21 for visible light and type 1P28 for ultraviolet. These exit slits were adjusted so that the spectral bandwidth of the signals produced was about 4.5Å. The rise time of the circuit including photomultipliers and amplifiers was checked with a steady light and a Kerr cell shutter and adjusted to be about 0.2 μsec. Typical oscillograms showing simultaneous records of heat flux and light emission are shown in Fig. 3. The coincidence of the two records was demonstrated by displaying them either on a dual-beam oscilloscope or on separate oscilloscopes with simultaneous display of the output of a time marker generator. With this equipment, the radiation from one or two radicals in the flame as well as the continuum radiation could be monitored simultaneously.

The peak pressure behind the detonation wave was measured with Kistler PZ-6 or PZ-14 piezo-electric transducers, used with the Kistler amplifier-calibrator. The transducers were calibrated statically on a dead-weight tester and dynamically with shock waves. In the latter case, the pressure ratios could only be verified to about ± 10% at high values of Mach number.

Synchronization of the instrumentation was accomplished by upstream triggering from an ionization gap or by a photomultiplier tube mounted on the shock tube wall.

The steadiness of the detonation waves was further verified by replacing the test section with a glass section with a horizontal slit and viewing the phenomenon with a rotating mirror streak camera.

RANGE OF EXPERIMENTS

Two mixtures of propane and oxygen were used - stoichiometric, at 16.7% propane, and the mixture with the highest detonation velocity, at 27.6% propane. With these mixtures, the initial pressure was varied from 1/150 to 1/3 atm. In all cases, the mixtures were ignited by the spark source described in the foregoing.

Stoichiometric mixtures of hydrogen and oxygen, with initial pressures ranging from 1/5 to 1 atm were detonated (all spark ignited). Both sparks and shock waves were used to detonate stoichiometric mixtures of hydrogen and air, at an initial pressure of 1/2 atm, only shock waves could detonate mixtures at 1/4 atm.

THEORETICAL CALCULATIONS

In order to estimate the extent to which the detonations attained their steady-state values, calculations were performed, in which the various detonation parameters were computed for some representative conditions, using the usual Chapman-Jouguet theory. The results are shown in Table 1. Some of the values needed are available in the literature and are also shown.

Manipulations were performed on the one-dimensional equations involving conservation of mass, energy, momentum, and atoms and on the equation of state for a perfect gas, the Chapman-Jouguet condition, and the various dissociation equations for all possible products. For the case for a "strong" detonation, a typical pressure ratio was first assumed. For ease of computation, the equations were reduced to the following forms:

Conservation of Momentum

$$\mu^2 \frac{\gamma_2 R}{M n_2 p_1} - \mu\left(\frac{\gamma_2 R}{M n_2 p_1} + \frac{1}{\rho_1 T_1 n_1}\right) + \frac{1}{\rho_1 T_2 n_2} = 0 \qquad [1]$$

Hugoniot Relation

$$(1/2) R T_1 n_1 (1 + y)\left(1 - \frac{1}{\mu}\right) = M(e_2 - e_1) \qquad [2]$$

Equation of State

$$y = \mu \frac{T_2 n_2}{T_1 n_1} \qquad [3]$$

Energy Balance

$M(e_2 - e_1)$ = (change of internal energy of products from 0°K to T_2)
- (change of internal energy of reactants from 0°K to T_1)
- (heat released by exothermic reactions)
+ (heat absorbed by endothermic reactions) [4]

General Expression for Velocity of Propagation of Detonation

$$D = \left(\frac{p_1}{\rho_1}\right)^{1/2} \left(\frac{1 - x}{y - 1}\right)^{1/2} \qquad [5]$$

Velocity of Propagation of Chapman-Jouguet Detonation

$$D = \mu\sqrt{\gamma_2 \frac{R}{M} T_2} \qquad [6]$$

For incompressible flame propagation (i.e., $y \approx 1$), all the heat released is used to heat the products, but in the case of supersonic combustion, some of the heat of reaction is used to compress the gas at the leading edge of the detonation wave. In the case of incompressible flow, Eqs. 2 and 4 reduce to

$$M(e_2 - e_1) = R(T_1 n_1 - T_2 n_2) \qquad [7]$$

In the case of compressible flow with no chemical reaction, the only energy available is that given the wave by its initial disturbance, and a higher pressure ratio results for a shock wave than for a detonation wave of the same Mach number.

The currently accepted theories of detonation structure postulate that a detonation consists of a shock wave propagating into an initially unreacting gas, followed by the combustion reaction. The first region of the wave is known as the von Neumann Spike, whose thickness, according to Hirschfelder (16) would be of the order of 10^{-5} cm, but few workers have ever reported measurements of this portion of the wave. In principle, there should be, behind the von Neumann spike, some finite induction period, in which no appreciable chemical change occurs. This region is then followed by the reaction zone, in which the chemical reaction goes to completion, attaining the final temperature, which corresponds to the sum of adiabatic compression plus heat addition. This zone should have a thickness of the order of 1 cm for detonations in gases, depending in some way on the initial density and the order of the reaction. In contrast with flames in incompressible flow, neither the velocity of propagation nor the thickness of a detonation wave depends on the thermal conductivity.

The complete solution of the problem of detonations or of shock waves in complex gases involves accounting for heat absorbed by dissociation. Since both temperature and dissociation depend on each other, the equations are nonlinear and require trial and error solutions. The general procedure is to assume a final temperature and a density ratio and to solve the problem by successive approximations, accounting for all possible dissociation equilibria. There is a possibility that all equilibria are not attained in the reaction zone within the time available, e.g., the formation of NO, but such possibilities are ignored in this treatment.

Following are some of the typical equilibrium equations for the solution of the detonation of propane and oxygen at initial conditions of 1/10 atm pressure and room temperature. In general, both high initial temperatures and low initial pressures favor dissociation. Both of these conditions would prevail in a hypersonic standing wave ramjet, flying at extremely high altitudes.

Combustion Equation

$$C_3H_8 + 5O_2 = \beta_1 CO_2 + \beta_2 H_2O + \beta_3 O_2 + \beta_4 CO$$

$$+ \beta_5 OH + \beta_6 O + \beta_7 H + \beta_8 H_2 \qquad [8]$$

Where β_1, β_2, . . . = number of moles of each product component.

Dissociation Equations

$$CO + (1/2)\ O_2 \rightleftarrows CO_2 + 66{,}767 \text{ cal/mol} \qquad [9]$$

$$H_2 + (1/2)\ O_2 \rightleftarrows H_2O + 57{,}107 \text{ cal/mol} \qquad [10]$$

$$2O \rightleftarrows O_2 + 117{,}172 \text{ cal/mol} \qquad [11]$$

$$OH + (1/2)\ H_2 \rightleftarrows H_2O + 67{,}107 \text{ cal/mol} \qquad [12]$$

$$2H \rightleftarrows H_2 + 103{,}240 \text{ cal/mol} \qquad [13]$$

Conservation of Atoms

$$2\beta_2 + \beta_5 + \beta_7 + 2\beta_8 = 8 \quad \text{(hydrogen)} \qquad [14]$$

$$2\beta_1 + \beta_2 + 2\beta_3 + \beta_4 + \beta_5 + \beta_6 = 10 \quad \text{(oxygen)} \qquad [15]$$

$$\beta_1 + \beta_4 = 3 \quad \text{(carbon)} \qquad [16]$$

Equilibrium Constants

$$K_1 = \left(\frac{T_2 p_1}{T_1 n_1}\right)^{1/2} \mu^{1/2} \frac{\beta_4 \sqrt{\beta_3}}{\sqrt{\beta_1}} \qquad [17]$$

$$K_2 = \left(\frac{T_2 p_1}{T_1 n_1}\right)^{1/2} \mu^{1/2} \frac{\beta_8 \sqrt{\beta_3}}{\beta_2} \qquad [18]$$

$$K_3 = \left(\frac{T_2 p_1}{T_1 n_1}\right) \mu \frac{\beta_6^2}{\beta_3} \qquad [19]$$

$$K_4 = \left(\frac{T_2 p_1}{T_1 n_1}\right)^{1/2} \mu^{1/2} \frac{\beta_5 \sqrt{\beta_8}}{\beta_2} \qquad [20]$$

$$K_5 = \left(\frac{T_2 p_1}{T_1 n_1}\right) \mu \frac{\beta_7^2}{\beta_8} \qquad [21]$$

The values for equilibrium constants, internal energy content as a function of temperature, and the heats of reaction were found in tables. The net change in internal energy for the combustion of a molecule as large as propane comes out as a small difference between very large numbers, so the result cannot be too accurate, even if done with an electronic computer. In some cases, it seemed better to use the values for the heats of formation of free atoms and radicals in the energy balance, rather than the heats of dissociation as previously given in the dissociation equations. This method was suggested by Gaydon and Wolfhard (17), who also criticized the tendency to quote the various equilibrium constants to four or five significant figures, whereas the data on which these constants are based may be accurate to only three significant figures.

EXPERIMENTAL RESULTS

Propane-Oxygen

With spark ignition only, reproducible detonations with stoichiometric mixtures were possible with initial pressures as low as 1/100 atm, although the pressure ratios and velocities were somewhat higher than those obtained at higher pressures. There was never a measurable change in velocity along the 3 ft length of test section, as measured either by probes or by the streak camera. With initial pressures between 1/3 and 1/4 atm, the velocity and pressure ratio trends began to level off and to approach the calculated values, as well as those reported in the literature for 1.0 atm, such as in Lewis and von Elbe (18).

The only radiation band with sufficient intensity to provide a good signal to noise ratio, with the slit resolution used, was at 4312Å (CH radical), although the rise times recorded with this band appeared to be about the same as those indicated by the band at 4737Å (C_2 radical) and by the continuum, measured at 4000Å (due to CO_2 association reaction). The resolution of the optical system was checked either by closing down the side wall slit until no further reduction in rise time occurred or by inserting an additional 0.5 mm slit between the lens and side wall slit, 1.5 in. away from the latter. When the insertion described in the foregoing was done, in the case of detonations at 3 in. initial pressure, for example, the rise time remained unchanged at 2 μsec, with only the signal height changed. It was apparent that the spectrograph itself has a sufficiently small acceptance angle to provide most of the resolution. The same procedure was applied to the experiments with hydrogen. The resulting resolution is about 2 mm in the shock tube, corresponding to a rise time of about 1.0 μsec. The effect of light scattered ahead of the detonation was reduced by blackening the inside of the tube and placing the side wall slit flush with the inside wall. Departure of the wave from a planar front also contributed to the scatter of the data. It is postulated that the distance corresponding to the rise time of radiation is the same as the thickness of the reaction zone, and the corresponding number of collisions N have been computed. No induction period could ever be measured. The experimental results, along with some comparisons with theory, are summarized in Table 2 and Figs. 4 and 5. Each item is an average of many trials. A significant result is found from the trend of the decay of radiation as recorded by the oscillograms. Further proof that the band radiation emitted by the short-lived radicals marks the combustion zone, is that the radiation decays rather rapidly down to the continuum level, whereas the continuum radiation itself, (measured between bands at 4000Å) decayed very slowly, as did the pressure and temperature. The decay time of the radical radiation appeared to be relatively independent of pressure for steady-state waves.

Hydrogen-Oxygen

Only spark ignition was used for these experiments, as it was thought desirable to have data free of complicating shocks or of the danger of overdriving. With sparks, consistent detonations at pressures below 1/4 atm could not be accomplished, although it was found that shocks could produce detonations at 1/10 atm or lower. An additional limitation was the fact that radiation levels became too low to measure at lower pressures. All the detonations reported propagated at nearly their Chapman-Jouguet rates. The pressure ratios also checked, within the experimental error. The results are shown in Table 3 and Fig. 6, along with radiation measurements and some theoretical values.

All radiation measurements with hydrogen were much less successful than with propane because of the scarcity of radiation from the former. No visible light comes from the reaction zone of a hydrogen-oxygen flame (see Fig. 1), but only radiation in the ultraviolet from bands due to OH (principal band head at 3065Å), plus some continuum due to the H_2O association reaction. There is the additional complication that the OH radiation also persists into the burned gas, due to the dissociation of water or to the slowness of recombination. Further evidence of the latter effect is the strong radiation in the ultraviolet that accompanied the reflected shock wave in the burned gas, with no visible light except from lines due to metallic impurities. In addition, the continuum was quite strong compared to the band radiation, so that the latter was practically swamped.

Due to lower radiation levels than those with propane and to the fact that more noisy photomultipliers had to be used, the signal to noise ratio was somewhat lower than with propane. As with propane, also, insertion of an additional slit did not improve the rise time, indicating a resolution of about 2 mm, or less than 1 μsec. Under these conditions, the rise time of the ultraviolet radiation varied between 5 and 10 μsec (15 to 30 mm in extent), with no systematic difference between signals at the different wavelengths. Postulating that this rise time indicates the thickness of the reaction zone, the required number of collisions N has also been tabulated. There was some indication that the decay time of the radiation at 3065Å (due to OH + continuum) was a little less than that at 3460Å (continuum only), but this distinction was much less marked than in the case of propane. Again, there was no measurable induction period between the shock wave and the beginning of the radiation.

Hydrogen-Air

Extremely large (for hydrogen) pressure ratios developed when mixtures of hydrogen and air were detonated with a spark at an initial pressure of 1/2 atm, below which sparks could not produce detonations in the tube. These detonations are called unsteady or strong detonations in this report; their velocities are correspondingly higher than the Chapman-Jouguet values, but they were quite reproducible. Sometimes orifices or turbulence generators placed in the tube at the end of the driver section were effective in bringing the final pressure and velocity down to more nearly their normal values. The role of turbulence in the transition period was discussed by Martin (9). The results are presented in Table 4. No significant pressure trend was investigated.

Shock ignition, in general, was more effective than spark ignition in producing normal detonation velocities. At low values of diaphragm pressure ratio, the result was similar to that with spark ignition, but as the diaphragm pressure ratio was increased, the pressure ratio across the detonations decreased, until velocities and pressure ratios very near the Chapman-Jouguet values were recorded. In all cases, the velocity of the initiating shock was somewhat less than that of the final detonation wave, so that the two could readily be distinguished. Further evidence of the ability to distinguish between shocks and detonations is the fact that shocks that did not produce ignition at all (until the reflected shock appeared) produced no ultraviolet light, whereas the shock-free (spark ignited) detonations always did. This evidence, plus that of the heat transfer probes, is cited to prove that all the waves reported here were free-running, i.e., quasi-steady, with only one shock wave followed by a continuous reaction zone.

As in the case of hydrogen-oxygen detonations, the intensity and rise time of the band radiation was hardly distinguishable from that of the continuum, and the decay times were likewise without much feature. The rise times of the normally propagating waves was markedly shorter than those for the waves running at high velocities and at high pressure ratios, being about 5 µsec (15 mm) for the former and about 15 µsec (45 mm) for the latter. The consequences of these and other experimental results will be discussed in the next section.

DISCUSSION OF RESULTS

The theoretical calculations verify the assumptions that the propane detonations at initial pressures below about 1.0 in Hg, and all the spark-ignited hydrogen-air detonations departed considerably from the Chapman-Jouguet conditions. The abnormally high pressure ratios and velocities which prevail under these circumstances are similar to those reported by White (19), who reported abnormally high pressures developed by hydrogen and other fuels in tubes too short for a normal detonation to develop. The early pressures noted were as high as four times normal, as also reported here, and were then followed by a normal development, if the distance was long enough. Such behavior was predicted by Oppenheim (20), who set up a model for the development of a detonation which was an unsteady double discontinuity system. In this model, a shock front is already running ahead of a combustion front; the pair will develop into a steady detonation wave only if the combustion front can overtake the shock wave. During this intermediate phase, Oppenheim predicts the attainment of extremely high peak pressures and velocities higher than those of the final Chapman-Jouguet state. Since this intermediate phase satisfies the same set of conservation equations as does the Chapman-Jouguet state, the former state must be the same as that commonly called strong detonations. It is postulated that the unsteady but reproducible detonations reported here are strong detonations in the classical sense, and the measured velocity and pressure ratio correlate approximately as the theory predicts, in the case of hydrogen and air with spark ignition. These are true detonations in the sense of Oppenheim's system, i.e., they consist of a single shock wave followed by a combustion wave, both propagating at a high velocity with an abnormally high pressure ratio. This distinction is important, in view of the fact that Gross (2) reported that the standing normal detonations he produced were of the strong variety; it is hoped that some of the criteria presented in this paper may serve to resolve the nature of such standing detonation waves.

The nature of these strong detonations is further demonstrated by the internal structure as indicated by the oscillograms. In the case of propane, the wave thicknesses are much less than those of the steady state waves. This may possibly be caused by the higher temperatures now existing behind the leading shock wave producing a great increase in the reaction rate, which may be more temperature dependent than is that for hydrogen. As a result of these factors, only the wave thickness in the pressure range of 1.5 to 3.0 in. Hg initial pressure could actually be resolved, since the limit of resolution was about 2 mm. Therefore, an upper limit of about 4 mm may confidently be placed on the thickness of propane-oxygen detonations at either 16.7% or 27.6% propane. An induction period, if any, would have to be somewhat less than 1 μsec.

It is also interesting to note that the decay rate of the radiation from the strong detonations was much greater than that from the normal detonations, which is further evidence of the higher temperatures existing in the former. This effect is further complicated by the fact that the rotational temperature of the CH radicals emitting this radiation is probably very much higher than the equilibrium value.

The apparent wave thickness of the hydrogen-oxygen detonations was always considerably larger than that of propane, with pressure taken into account, and also somewhat larger than that reported by other workers, such as in Refs. 6-8 and 10, using essentially densitometric methods. This discrepancy cannot be explained by lack of resolution, because the apparent wave thickness was always at least 10 times the resolution distance. The best explanation probably lies in the fact that the OH radical radiation, especially in the presence of strong continuum radiation, is a poor indication of the reaction zone of a flame, since the OH radical is formed in the dissociation of product gases, as well as being formed as an intermediate in the original reaction. This more diffuse distribution of OH radicals was found by Wohl (11) in hydrocarbon flames. The decay time for the OH radiation was of the same order as the rise time, indicating that most of the radiation observed was produced in the reaction zone itself, rather than from dissociation of the product gas.

Because spark ignition of hydrogen-air detonations below 1/2 atm was not possible, and because the peak pressures developed were considered unsafe with an initial pressure of 1.0 atm, tests were limited to a small pressure range. As mentioned previously, ignition by sparks or by weak shocks produced strong detonations, whereas ignition by strong shocks produced normal detonations. Oscillograms of the former always showed a much more open structure than those of the latter, tending to verify the model of Oppenheim, where the combustion wave has not yet caught up with the shock wave. Even though any induction period was still undetected, the rise time of the strong detonation was about 3 times that of the normal wave. This separation of more than an inch between the shock wave and the combustion wave is considerably more than the separation reported by Gross for his standing strong detonation. Further discussion of this problem was taken up by Dabora (21), who mentions the possibility of some burning of fuel ahead of the shock wave, preheating the gas and reducing the separation distance. Again, spectrographic analysis might help resolve this dilemma.

CONCLUSIONS

The spectrophotometer provides a useful tool for studying the structure of detonations, because in many cases it can follow accurately the course of fast chemical reactions. Unresolved radiation measurements may give misleading results.

Strong, unsteady, and decelerating detonations are all the same thing, provided that they consist of one shock front, followed by a combustion front. Strong detonations in a tube provide a handy source of high pressure shock waves and considerably extend the range of experiments with fast chemical reactions.

Knowledge of the nature and structure of strong and normal detonations should lead to a better understanding of standing normal detonations of both types, especially if spectrophotometric methods can be used.

Better understanding of standing, stabilized detonation waves may yet prove that they can be a superior mode of propulsion for hypersonic ramjets.

ACKNOWLEDGMENTS

The author wishes to express his grateful appreciation to John H. Ribbe and James R. Yeager for their valuable assistance in performing the experiments and for help with

data reduction, and to Raymon D. Garrett for carrying out the calculations and helping with data tabulation. Without such assistance this work could not have been done.

NOMENCLATURE

T	temperature
p	pressure
ρ	density
γ	ratio of specific heats
R	universal gas constant
M	average molecular weight
n	number of moles
y	p_2/p_1
μ	ρ_2/ρ_1
x	$1/\mu$
e	internal energy per mole
D	velocity of propagation of detonation wave into unburned gas

Subscripts 1 and 2 refer to conditions before and after detonation wave, respectively.

REFERENCES

1 G.L. Dugger: A Future for Hypersonic Ramjets. Astronautics, April 1959, vol. 4, pp. 38-39.

2 R.A. Gross and W. Chintz: Exploratory Studies of Combustion in Supersonic Flow, Parts I-IV. AFOSR TN 59-587, ASTIA AD 216 769, June 1959.

3 W.H. Sargent and R.A. Gross: Detonation Wave Hypersonic Ramjet. ARS Jour., June 1960, vol. 30, pp. 543-549.

4 R. Dunlap, R.L. Brehm and J.A. Nicholls: A Preliminary Study of the Application of Steady-State Detonative Combustion to a Reaction Engine. Jet Propulsion, July 1958, vol. 28, pp. 451-456.

5 J.A. Nicholls, E.K. Dabora and R.L. Gealer: Studies in Connection with Stabilized Detonation Waves. Seventh Symposium (International) on Combustion, pp. 144-150. Butterworths Scientific Publications, London, 1959.

6 W.E. Gilkerson and N. Davidson: On the Structure of a Detonation Front. Second ONR Symposium on Detonation.

Table 1 Summary of Calculated Values of Detonation Parameters AT $T_1 = 300°K$

Mixture	Initial Pressure	Density Ratio, ρ_2/ρ_1	Pressure Ratio, p_2/p_1	Velocity. fps	Final Temp., T_2 °K	Mole Ratio n_2/n_1	Composition of Burned Gas in Mole Fractions											Source
							H_2^0	H_2	O_2	OH	H	O	N_2	NO	A	CO_2	CO	
Stoichiometric Propane-Oxygen	0.10 atm	1.78	30.6	7310	3350°K	1.54	0.277	0.069	0.096	0.104	0.063	0.064	...	...	...	0.112	0.215	
Stoichiometric Hydrogen-Oxygen	0.25 atm 1.0	1.60	15.0 18.05	8200 9200	3300°K 3583°K	0.853	0.501	0.164	0.055	0.123 .253	0.109 .069	0.048	...	...	...	...	...	Lewis and von Elbe (18)
Stoichiometric Hydrogen-Air	0.25 atm	1.66	13.8	6040	2850°K	0.870	0.272	0.044	0.011	0.019	0.012	0.005	0.622	0.008	0.007	...	...	
Stoichiometric Hydrogen-Air	1.00 atm	1.81	15.8	6600	2960°K	0.852	0.293	0.033	0.009	0.016	0.006	0.002	0.626	0.008	0.007	....	...	Gross (2)
Stoichiometric Hydrogen-Air (Strong Detonation)	0.25 atm	3.84	40.0	7580	3330°K	0.941	0.217	0.065	0.016	0.041	0.050	0.013	0.576	0.015	0.007			

Table 2 Experimental Results of Propane-Oxygen Detonations

Propane in Mixture, %	Initial Pressure,	Velocity, fps		Pressure Ratio p_2/p_1		Rise of Radiation at 4312 A		
	in, Hg abs.	exp.	theor.	exp.	theor.	Time, μsec	Distance, mm	N
27.6	10.00	8330	...	41.8	...	0.90	2.31	8900
27.6	6.00	8220	...	44.9	...	1.30	3.27	7500
27.6	5.00	8520	...	55.4	...	1.30	3.38	6600
27.6	3.00	8330	...	52.3	...	1.33	3.39	3900
27.6	1.55	8570	...	51.3	...	2.00	5.22	2900
27.6	0.75	8830	...	81.5	...	1.30	3.52	1100
27.6	0.50	9680	...	104	...	1.35	3.99	900
16.7	6.00	7470	...	30.5		1.17	2.67	6200
16.7	3.00	7410	7310	33.6	30.6	0.97	2.17	2500
16.7	1.55	7280	...	32.4	...	1.27	2.82	1600
16.7	0.75	7430	...	47.0	...	1.66	3.86	1200
16.7	0.50	8540	...	72.8	...	1.14	3.01	600
16.7	0.30	9280	...	135	...	0.50	1.44	200

Table 3 Experimental Results of Stoichiometric Hydrogen-Oxygen Detonations (Spark Ignited)

Initial Pressure in. Hg abs.	Velocity, fps		Pressure Ratio, p_2/p_1		Rise of Radiation at 3065 A		
	exp.	theor.	exp.	theor.	Time, μsec	Distance, mm	N
6.00	9380	...	15.1	...	12.0	34.3	79,000
7.50	9010	8200	12.6	15.0	13.7	37.8	120,000
10.00	9350	...	20.1	...	9.00	25.7	98,800
15.00	9260	...	17.2	...	8.87	25.0	157,000
20.00	9390	...	14.4	...	6.00	17.2	145,000
30.00	9250	...	17.1	...	7.87	22.2	279,000

Table 4 Experimental Results of Hydrogen-Air Detonations

Initial Pressure, in. Hg abs	Ignition Source	Diaphragm Pressure Ratio p_4/p_1	Shock Wave Mach No., M_S	Velocity, fps		Pressure Ratio p_2/p_1		Rise of Radiation at 3065 Å		
				exp.	theor.	exp.	theor.	Time, μsec	Distance, mm	N
7.50	Shock	171	5.2	6440	6040	21.8	13.8	15.5	30.4	96500
7.50	Shock	75.7	3.4	7170	6040	27.4	13.8	10.3	22.6	71700
7.50		Strong Detonation		. . .	7580	. . .	40.0	. . .	. . .	. . .
15.00	Spark	. . .	. . .	7020	. . .	37.0	. . .	11.0	23.5	148000
15.00	Shock	31.8	2.7	7330	. . .	28.5	. . .	9.55	21.4	135000
15.00	Shock	94.5	3.6	6370	. . .	17.8	. . .	14.5	28.1	177000
15.00		Strong Detonation		7370	7880	36.6	40.0	15.4	34.7	218000

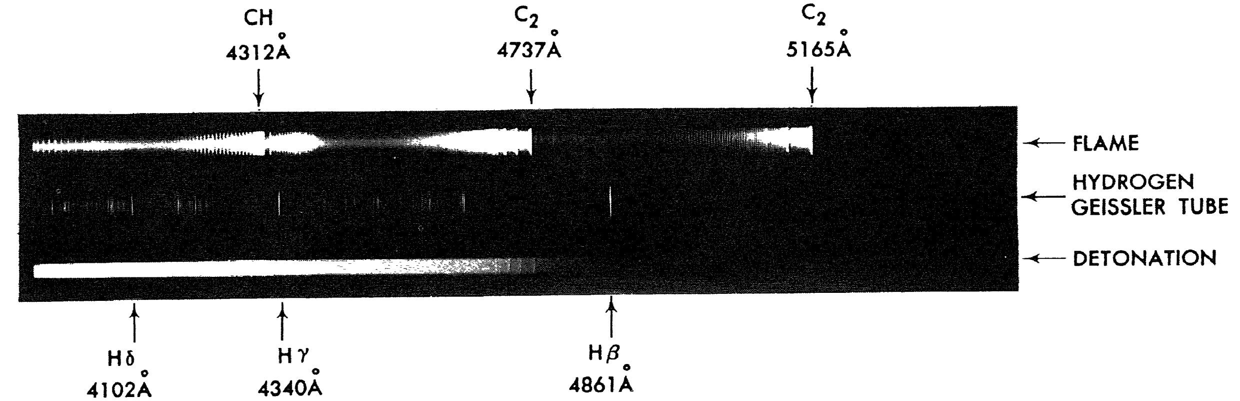

a. Propane — Oxygen

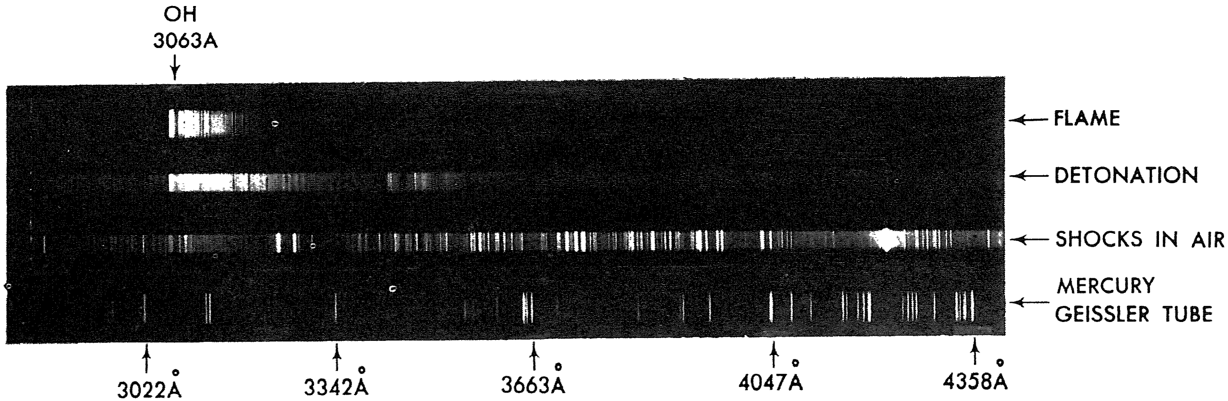

b. Hydrogen — Oxygen and Shocks

Fig. 1 Detonation, flame, and calibration spectra

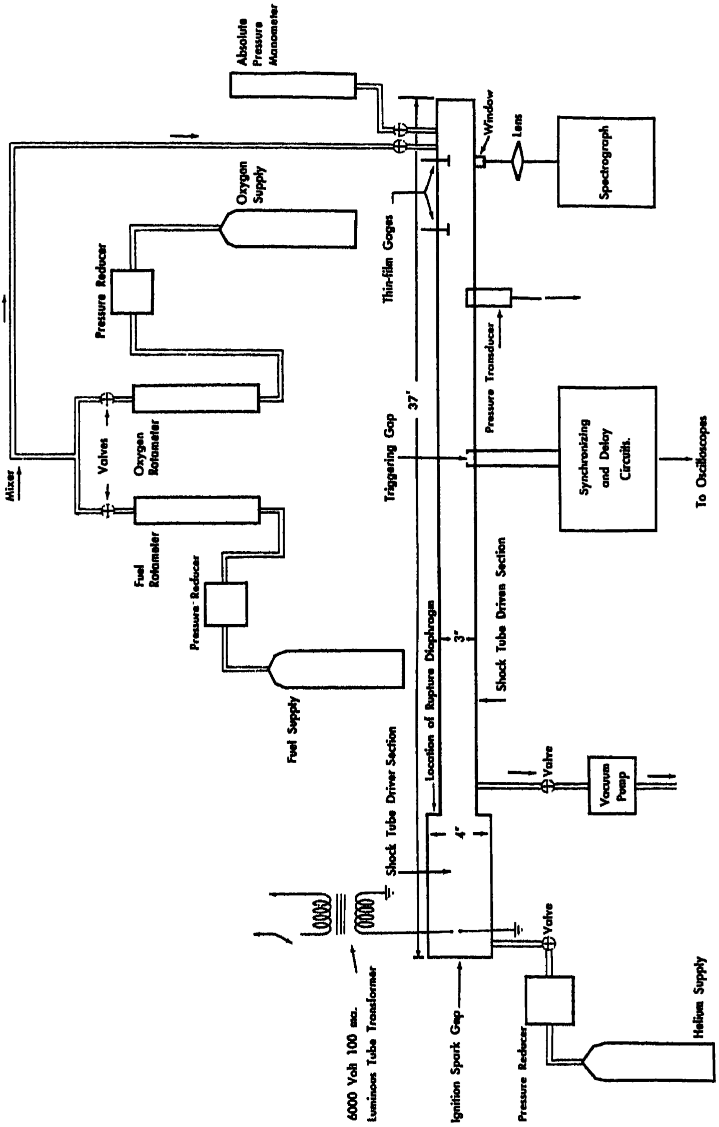

Fig. 2 Schematic of detonation experiments

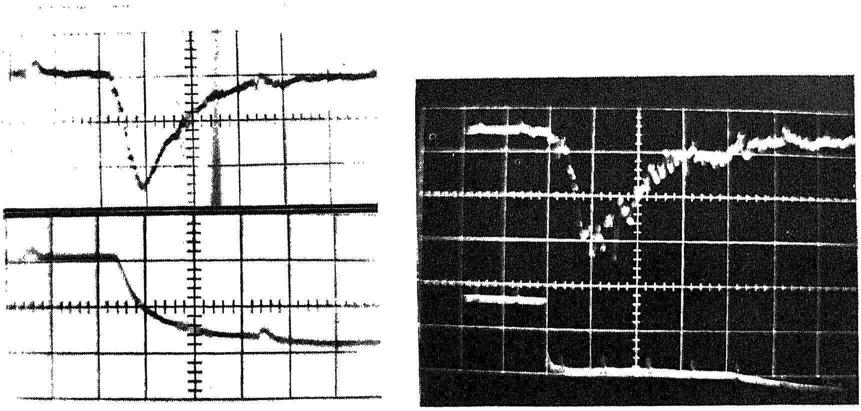

a. Propane - Oxygen
sweep speed 2 μsec/division
λ = 4312 A
p_1 = 3.0 inches Hg abs.
spark ignition

b. Hydrogen - Oxygen
sweep speed 10 μsec/division
λ = 3065 A
p_1 = 15.0 inches Hg abs.
spark ignition

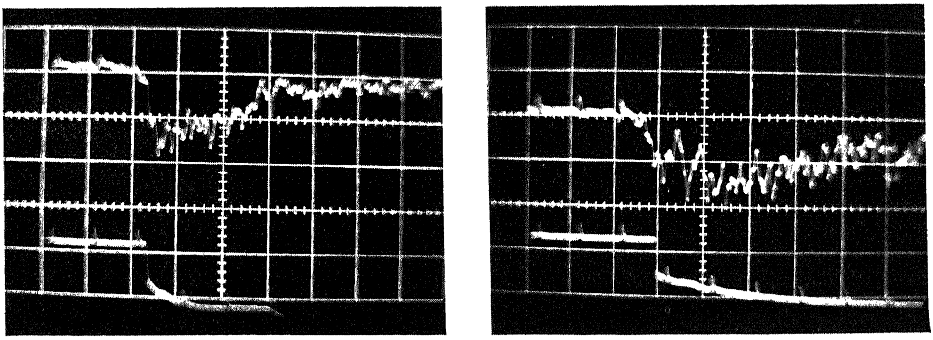

c. Hydrogen - Air
sweep speed 10 μsec/division
λ = 3065 A
p_1 = 15.0 inches Hg abs.
shock ignition

d. Hydrogen - Air
sweep speed 10 μsec/division
λ = 3065 A
p_1 = 15.0 inches Hg abs.
spark ignition

Fig. 3 Typical oscillograms of light emission and heat flux

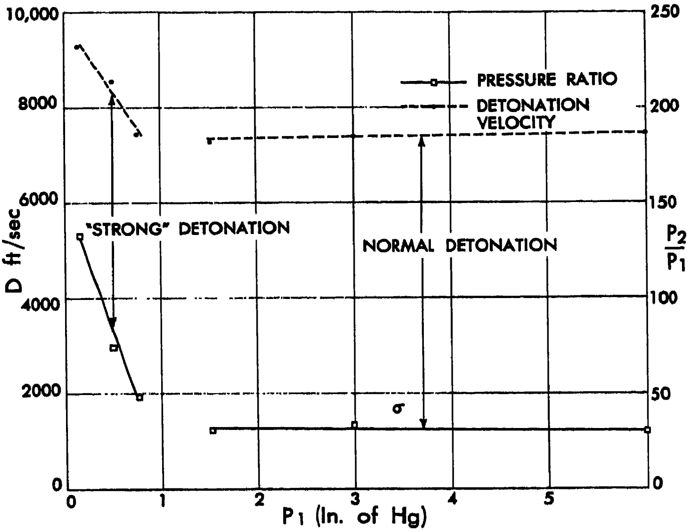

a. Velocity and Pressure Ratio Vs. Initial Pressure.

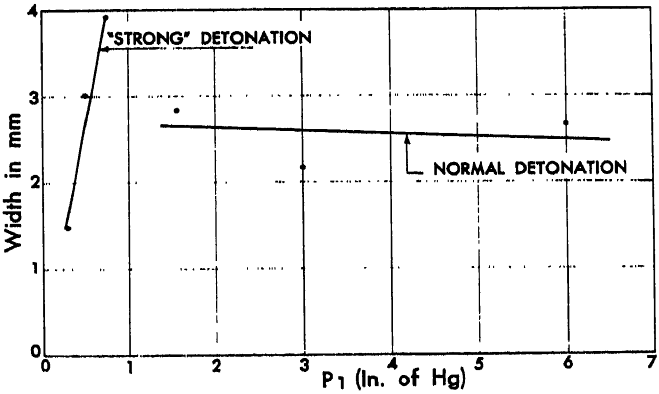

b. Width of Detonation Wave Vs. Initial Pressure.

Fig. 4 Experimental results of detonations of stoichiometric (16.7%) mixtures of propane and oxygen

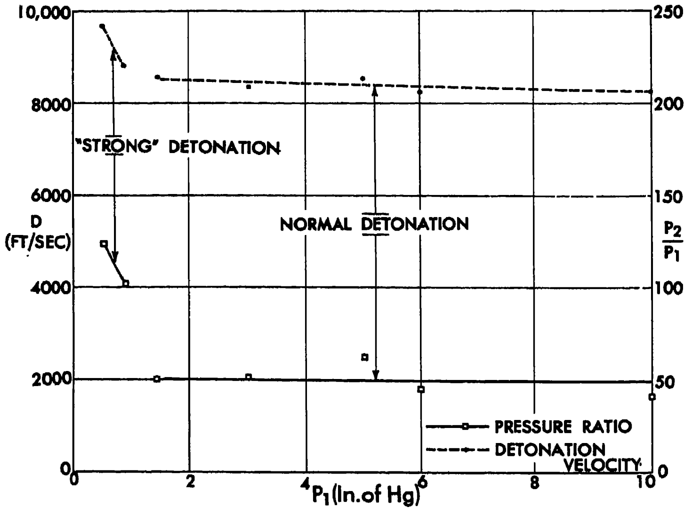

a. Velocity and Pressure Ratio Vs. Initial Pressure.

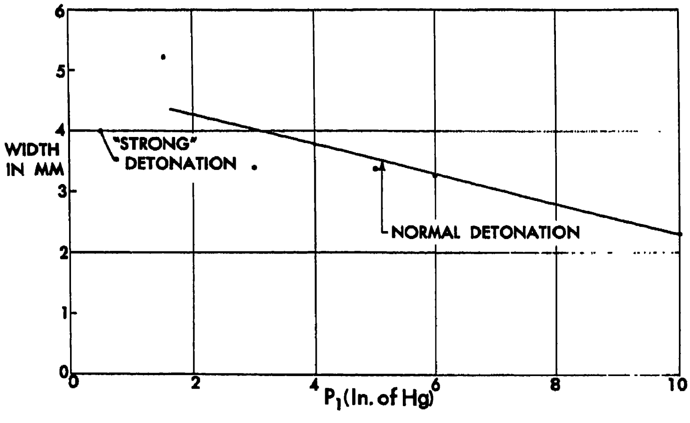

b. Width of Detonation Wave Vs. Initial Pressure.

Fig. 5 Experimental results of detonation of rich (27.6%) mixtures of propane and oxygen

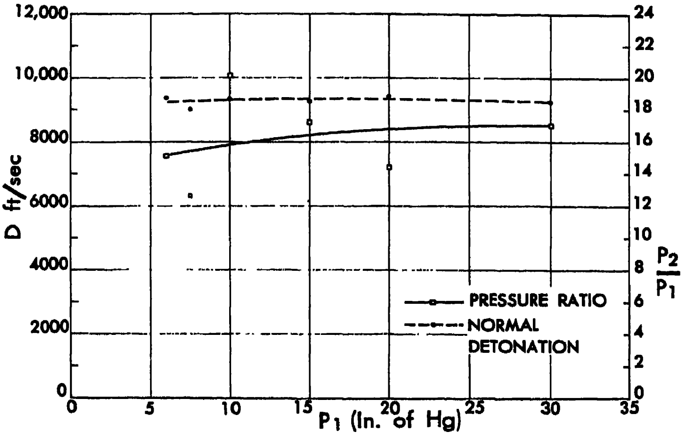

a. Velocity and Pressure Ratio Vs. Initial Pressure.

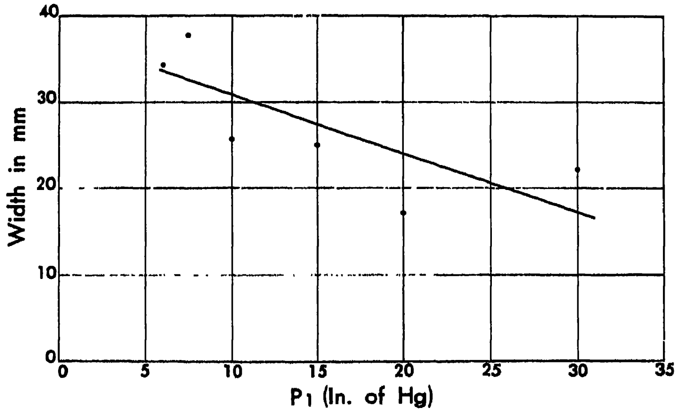

b. Width of Detonation Wave Vs. Initial Pressure.

Fig. 6 Experimental results of detonations of stoichiometric mixtures of hydrogen and oxygen

PARAMETRIC STUDIES OF STRONG GASEOUS DETONATIONS

K.M. Foreman, H. Pevney, and R. MacMillan

Republic Aviation Corp., Farmingdale, N.Y.

ABSTRACT

The real-gas thermodynamic properties and chemical composition of stationary, one-dimensional, strong detonations of oxygen-hydrogen and air-hydrogen mixtures for a wide range of laboratory and engineering application environments are calculated using an IBM 704 high speed digital computer. Reactant conditions are determined which theoretically result in equilibrium detonations of zero energy change.

INTRODUCTION

The net energy release of detonative processes equals the changes of enthalpy and kinetic energy of the reactants as they change to reaction products. As the wave velocity of strong detonations increases, the exothermic reactions become overriden by endothermic processes. Thus, a method of classification is suggested for the range of strong gaseous detonations by a composition (equivalence ratio)-velocity coordinate system for prescribed reactant temperature and pressure conditions. The lower velocity limit is the Chapman-Jouguet condition, whereas the upper velocity boundary is the zero energy release condition. Greater wave speeds are classified as strong shocks requiring additional processes to recombine the product species and make the overall system sufficiently exothermic to permit chemical energy extraction.

Parametric studies of equilibrium, one-dimensional, real-gas properties of oxygen-hydrogen and air-hydrogen detonations have been conducted for a range of initial temperatures between 270° and 1620°R and subatmospheric pressures to 10^{-3} atm using an IBM 704 digital

---

K.M. FOREMAN is Specialist, Scientific Research Engineer; H. PEVNEY is Engineering Assistant; R. MACMILLAN is Engineering Aide, all at the Plasma Propulsion Project. Paper presented at the ARS Propellants, Combustion, and Liquid Rockets Conference, Palm Beach, Fla. April 26-28, 1961. This work was partially supported by the Air Force Office of Scientific Research under Contract AF 49(638)-552.

computer program. Typical variations of product gas composition and thermodynamic properties with wave velocity are presented and discussed. It is seen that the coordinates that are used to classify strong oxygen-hydrogen detonations are broadened by higher reactant pressures and narrowed and shifted to lower velocities by higher reactant temperatures. Similar characteristics are displayed by air-hydrogen detonations, except that the energy release per unit quantity of fuel reaches a maximum at approximately an equivalence ratio of 4 rather than at the stoichiometric ratio.

HISTORICAL BACKGROUND

Since 1957, high speed digital computers have been applied to solve by numerical iterative techniques the several nonlinear simultaneous equations resulting from the formulation of the one-dimensional, steady flow, real-gas detonation problem. Developments in computer technology since then have increased the speed of calculation so as to make extensive parametric investigations physically and economically practical. As an indication of these improvements, a single dissociative case calculation now (1961) takes less than 1 sec (on an IBM 704) compared to 2-1/4 min in 1957 (on an IBM 650). A full determination of a Chapman-Jouguet condition can be accomplished in less than 30 sec for most conditions chosen to start the iteration, compared to some 3 to 5 hr in 1957.

THEORETICAL CONSIDERATIONS

The equations programmed solve the model of a one-dimensional inviscid, steady flow of a homogenous detonable gas mixture across a stationary detonation front. It is assumed that there is no heat transfer into or out of the frictionless flow channel. The reactant gas has known velocity, pressure, temperature and molar composition. The general form of the reaction is considered as

$$C_xH_y + \alpha_1 O_2 + \alpha_2 N_2 + \alpha_3 A \longrightarrow$$

$$\beta_1 CO_2 + \beta_2 H_2O + \beta_3 N_2 + \beta_4 O_2 + \beta_5 CO + \beta_6 OH + \beta_7 N + \beta_8 O$$

$$+ \beta_9 H + \beta_{10} NO + \beta_{11} H_2 + \beta_{12} A + \beta_{13} C + \beta_{14} O_3 + \beta_{15} NO_2 + \beta_{16} NO^+$$

The product gas composition is determined for chemical equilibrium. The subscripts x and y denote the number of carbon and hydrogen atoms respectively, based on one mole of fuel. Molar quantities of reactant and product species are denoted by α and β coefficients respectively. The special case of hydrogen fuel is accomodated by specifying a value of x that is extremely small compared to $y=2$; it has been found practical to use $x=10^{-6}$ or less for this type of case.

Similarly, a fuel reaction with only oxygen can be set up by specifying relatively small values of α_2 and α_3 as compared with α_1 and the one mole of fuel. Shock properties of unimolecular gas or gas mixtures without fuel can be determined in a similar manner.

Thermodynamic data required for the four conservation equations and 11 equilibrium reactions have been curve fitted by fifth-degree polynomials for temperatures between 0° and 6000°K. A complete description of the equations and thermodynamic data is found in Ref. 1 and discussed by Eisen in Ref. 2. For convenience, these basic equations are reproduced in the Appendix.

Nondissociative product gas calculations assume the existence only of CO_2, H_2O, O_2, N_2, and A. Results follow from the direct algebraic solution of the initial specified conditions. Dissociative product gas calculations are produced by a Newton-Raphson iterative procedure from initial specified conditions and estimates of specific strong and weak detonation final results.

DETONATION PROPERTIES

Computations were performed for the following initial conditions:

Temperature:	270°, 540°, and 1620°R
Pressure:	10^{-3}, 10^{-1}, and 1 atm
Velocity:	2000 fps, or the Chapman-Jouguet velocity, to 12,000 fps
Equivalence Ratio:	1, 2, 4, 8, and 16

Data for both weak and strong detonation branches were calculated since both are mathematically indicated, although only strong detonation results are considered realistic because the criteria of Damköhler's first ratio precludes the existence of one-dimensional, inviscid weak detonations for the considered gas mixtures.

Some typical thermodynamic properties of oxygen-hydrogen detonations are shown by Figs. 1, 2, and 3 for representative laboratory operating conditions.

These curves indicate that for any particular initial wave speed of strong shocks greater than the Chapman-Jouguet case, the velocity ratio (V_2/V_1) increases and the pressure ratio (P_2/P_1) decreases as the equivalence ratio decreases toward one. A single trend for the temperature ratio (T_2/T_1) is not similarly indicated. The interesting (and not at all initially obvious) result of the computation shows that although at wave speeds below about 9000 fps the temperature ratio and the temperature increase with decreasing equivalence ratio, this relation reverses in a transition regime between 9000 and 10,500 fps wave velocity so that, thereafter, leaner fuel mixtures produce higher product gas temperatures for comparable initial velocities.

Further investigation shows that the velocity transition zone shifts to higher values of velocity with increased initial pressure and falls to lower initial wave speed range with increased initial reactant temperatures. Although mixtures with equivalence ratios between 4 and 16 display nearly coincident transitional velocities, the full stoichiometric mixture has a decidedly lower wave velocity at which the temperature ratio trend becomes smaller. These temperature trends are attributable to the increasingly stronger endothermic reactions represented by the dissociation of molecular hydrogen and oxygen-hydrogen compounds at product gas temperatures above 5000°R.

Some further observations are worth noting. The Chapman-Jouguet condition represents the coalescense of the strong and weak detonation branches. This minimum wave velocity decreases as the fuel content of the mixture decreases, and the corresponding Chapman-Jouguet pressure and temperature decreases while the velocity ratio increases slightly. The general characteristics of nondissociative calculations are similar to the dissociative case except for the influence of initial pressure and the temperature ratio "cross over" effect noted at high product gas temperatures. More complete comparisons of these two cases are made in Ref. 3.

DETONATION COMPOSITION

An examination of the equilibrium concentration for strong stoichiometric oxygen-hydrogen detonations is shown in Fig. 4 and for the half stoichiometric mixture in Figs. 5 and 6. The former demstrates how the recombination product (H_2O) yield decreases with wave velocity and how the dissociative products, H and O, exhibit the greatest rate of increase. Similarly, the leaner detonable mixture products contain an increasing yield of dissociative products, H and O, with increased wave front velocity, whereas the recombination product, H_2O, and excess oxygen, O_2, decrease in absolute and relative concentrations (Figs. 5 and 6).

The variation of equilibrium product gas temperature with velocity is indicated at the principle divisions of the abscissa. The leaner mixture shows over 100° (or approximately 2%) higher temperature for the same detonation front velocity.

STRONG DETONATION REGIMES

Examination of the energy conservation equation shows that the macroscopic energy release of the detonation process is

$$Q = (h_2 - h_1) + \frac{(V_2^2 - V_1^2)}{2gJ}$$

that is, the enthalpy and kinetic energy changes between the reactants and products. For strong discontinuities, the kinetic energy change is always negative, whereas the static enthalpy change is positive. The variation of net energy release with mixture ratio for the oxygen-hydrogen real-gas system for a representative laboratory environment, over a velocity range of 4000 to 12,000 fps is shown in Fig. 7. It is evident that since the net energy release decreases with wave velocity increase, the kinetic energy change increases faster than the static enthalpy change. Thus, while energy-releasing chemical reactions continue to exist, the overall strong detonation process eventually becomes endothermic.

On the basis of classical detonation theory, this data suggests that one-dimensional equilibrium strong detonations can be classified as a regime of wave velocity and mixture ratio for certain given initial thermodynamic state conditions. One boundary of this regime is the Chapman-Jouguet condition of maximum energy release where the product gas velocity just equals the equilibrium sound speed. The other boundary is the condition of zero energy release. Larger wave velocities outside this regime are more properly classified as strong shocks.

In the sense of this classification, the regime of strong oxygen-hydrogen detonations is shown by Fig. 8 for two reactant pressures and a fixed initial temperature. As the pressure rises, the Chapman-Jouguet limit is slightly displaced to higher velocities, but the zero energy limit increases appreciably, thus broadening the regime.

The influence of reactant temperature, at a constant initial pressure level, on strong detonations is indicated by Fig. 9. In the six-fold range between 270° and 1620°R, the higher temperature results in lower wave velocity values at both boundaries of the strong detonation regime, and an overall reduction in extent.

A similar investigation for air-hydrogen detonations produces the additional information that the energy release based on a unit quantity of fuel becomes larger as the mixture becomes leaner (Fig. 10) and appears to approach an asymptote at an equivalence ratio of 4. On this basis, it becomes more efficient to use leaner than stoichiometric mixtures at wave velocities less than 8500 fps; the stoichiometric process appears desirable only between 8500 and 9600 fps. The best compromise from considerations of energy release and the extent of wave velocity appears to be the half stoichiometric mixture.

The regime of strong detonations for hydrogen-air mixtures is shown by Fig. 11 for a typical laboratory environment and is derived from the data of Fig. 10.

APPENDIX BASIC EQUATIONS FOR THE DETONATION COMPUTER PROGRAM

Species Conservation

$$x = \beta_1 + \beta_5$$

$$Y = 2\beta_2 + \beta_6 + \beta_9 + 2\beta_{11}$$

$$\alpha_1 = \beta_1 + \frac{1}{2}\beta_2 + \beta_4 + \frac{1}{2}\beta_5 + \frac{1}{2}\beta_6 + \frac{1}{2}\beta_8 + \frac{1}{2}\beta_{10} \qquad [A-1]$$

$$\alpha_2 = \beta_3 + \frac{1}{2}\beta_7 + \frac{1}{2}\beta_{10}$$

$$\alpha_3 = \beta_{12}$$

Mass Conservation

$$\rho_1 V_1 = \rho_2 V_2 \qquad [A-2]$$

Momentum Conservation

$$p_1 + \rho_1 V_1^2 = p_2 + \rho_2 V_2^2 \qquad [A-3]$$

Energy Conservation

$$\left(\sum_{i=0}^{3} \alpha_i m_i\right)\frac{V_1^2}{2} + \sum_{i=0}^{3} \alpha_i h_i(T_i) = \left(\sum_{j=1}^{16} \beta_j m_j\right)\frac{V_2^2}{2} + \sum_{j=1}^{16} \beta_j h_j(T_2) \qquad [A-4]$$

In practice it was found more practical to include only products β_1 through β_{13} in the energy equation. Determination of β_{14}, β_{15}, and β_{16} is made as an equilibrium reaction perturbation computation, changing the composition but not the thermodynamics of the product gas.

The heat reaction of the fuel ΔH_f is defined by [A-5]

$$\Delta H_f = \Delta H_{C_xH_Y} = h_{C_xH_Y} + \left(x + \frac{Y}{4}\right) h_{O_2} - x h_{CO_2} - \frac{Y}{2} h_{H_2O}$$

The equilibrium equations and their reactions are

$$K_{N_2}(T_2) = \frac{\beta_3 \Sigma\beta_j}{\beta_7^2 p_2} \qquad N_2 \rightleftharpoons 2N \qquad [A\text{-}6]$$

$$K_{H_2O}(T_2) = \frac{\beta_2 (\Sigma\beta_j)^2}{\beta_9^2 \beta_8 p_2^2} \qquad H_2O \rightleftharpoons 2H + O \qquad [A\text{-}7]$$

$$K_{O_2}(T_2) = \frac{\beta_4 \Sigma\beta_j}{\beta_8^2 p_2} \qquad O_2 \rightleftharpoons 2O \qquad [A\text{-}8]$$

$$K_{OH}(T_2) = \frac{\beta_6 \Sigma\beta_j}{\beta_8 \beta_9 p_2} \qquad OH \rightleftharpoons O + H \qquad [A\text{-}9]$$

$$K_{H_2}(T_2) = \frac{\beta_{11} \Sigma\beta_j}{\beta_9^2 p_2} \qquad H_2 \rightleftharpoons 2H \qquad [A\text{-}10]$$

$$K_{NO}(T_2) = \frac{\beta_{10} \Sigma\beta_j}{\beta_7 \beta_8 p_2} \qquad NO \rightleftharpoons N + O \qquad [A\text{-}11]$$

$$K_{CO_2}(T_2) = \frac{\beta_1^2 \Sigma\beta_j}{\beta_5^2 \beta_4 p_2} \qquad 2CO_2 \rightleftharpoons 2CO + O_2 \qquad [A\text{-}12]$$

$$K_C\ (T_2) = \frac{\beta_5 \Sigma\beta_j}{\beta_{13} \beta_8 p_2} \qquad CO \rightleftharpoons C + O \qquad [A\text{-}13]$$

$$K_{O_3}(T_2) = \frac{\beta_{14} (\Sigma\beta_j)^2}{\beta_8^3 p_2^2} \qquad O_3 \rightleftharpoons 3O \qquad [A\text{-}14]$$

$$K_{NO_2}(T_2) = \frac{\beta_{15}^2 \Sigma\beta_j}{\beta_3 \beta_4^2 p_2} \qquad 2NO_2 \rightleftharpoons N_2 + 2O_2 \qquad [A\text{-}15]$$

$$K_{NO^+}(T_2) = \frac{\beta_{10}\Sigma\beta_j}{\beta_{16}^{\,2}\, p_2} \qquad NO \rightleftharpoons NO^+ + e^- \qquad [A\text{-}16]$$

REFERENCES

1 C.L. Eisen, R. Gross, and T. Rivlin: Theoretical Calculations in Gaseous Detonation. AFOSR TN 58-326, Fairchild Engine Div., Deer Park, N.Y., March 15, 1958.

2 C.L. Eisen: Theoretical Calculations in Gaseous Detonation. Proc. Propellant Thermodynamics and Handling Conference, July 20-21, 1959, Ohio State University Spec. Rept. 12, June 1960, pp. 345-356.

3 W. Chinitz, K.M. Foreman, and L. Levin: Theoretical Studies for a Problem in Electromagnetically Induced Detonations. AFOSR TN 60-85, Republic Aviation Corp. PPL Rept. 121, Farmingdale, N.Y., Nov. 30, 1959.

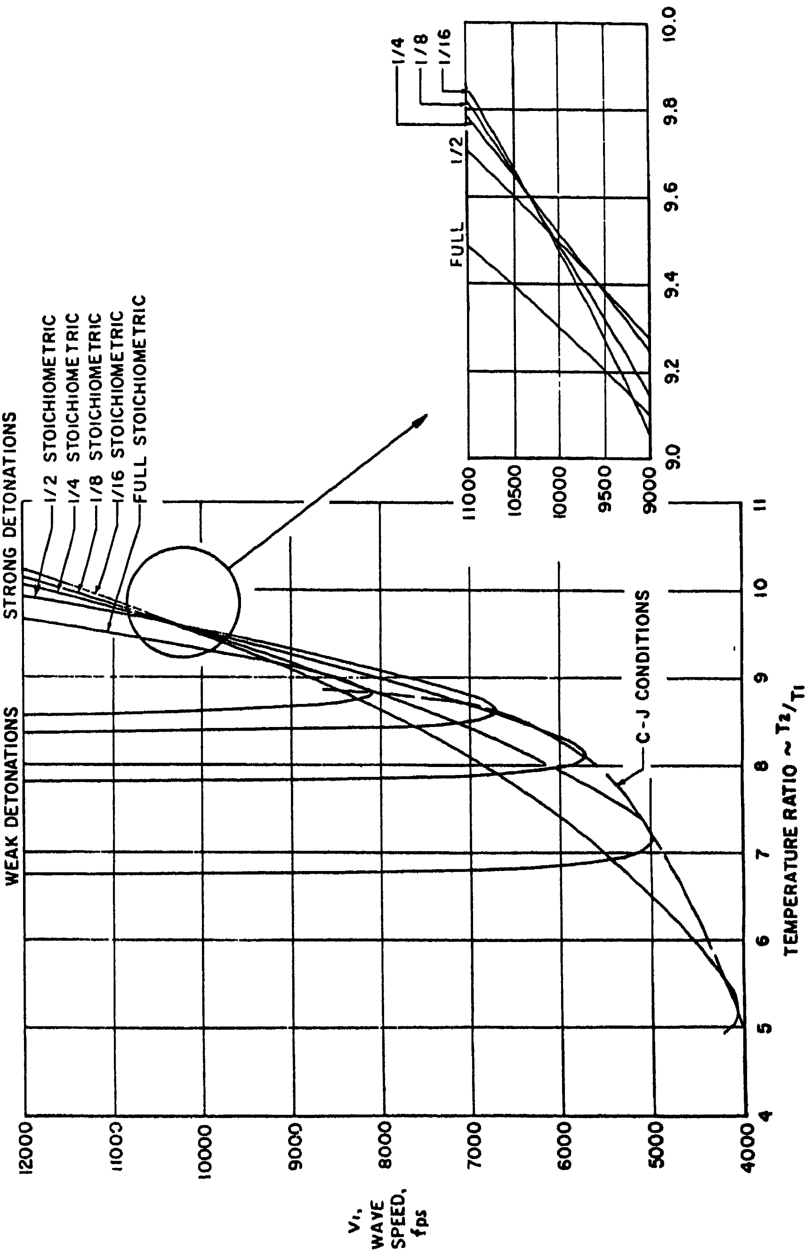

Fig. 1 Temperature ratio for oxygen-hydrogen detonation; $P_1 = 10^{-3}$ atm, $T_1 = 540°R$

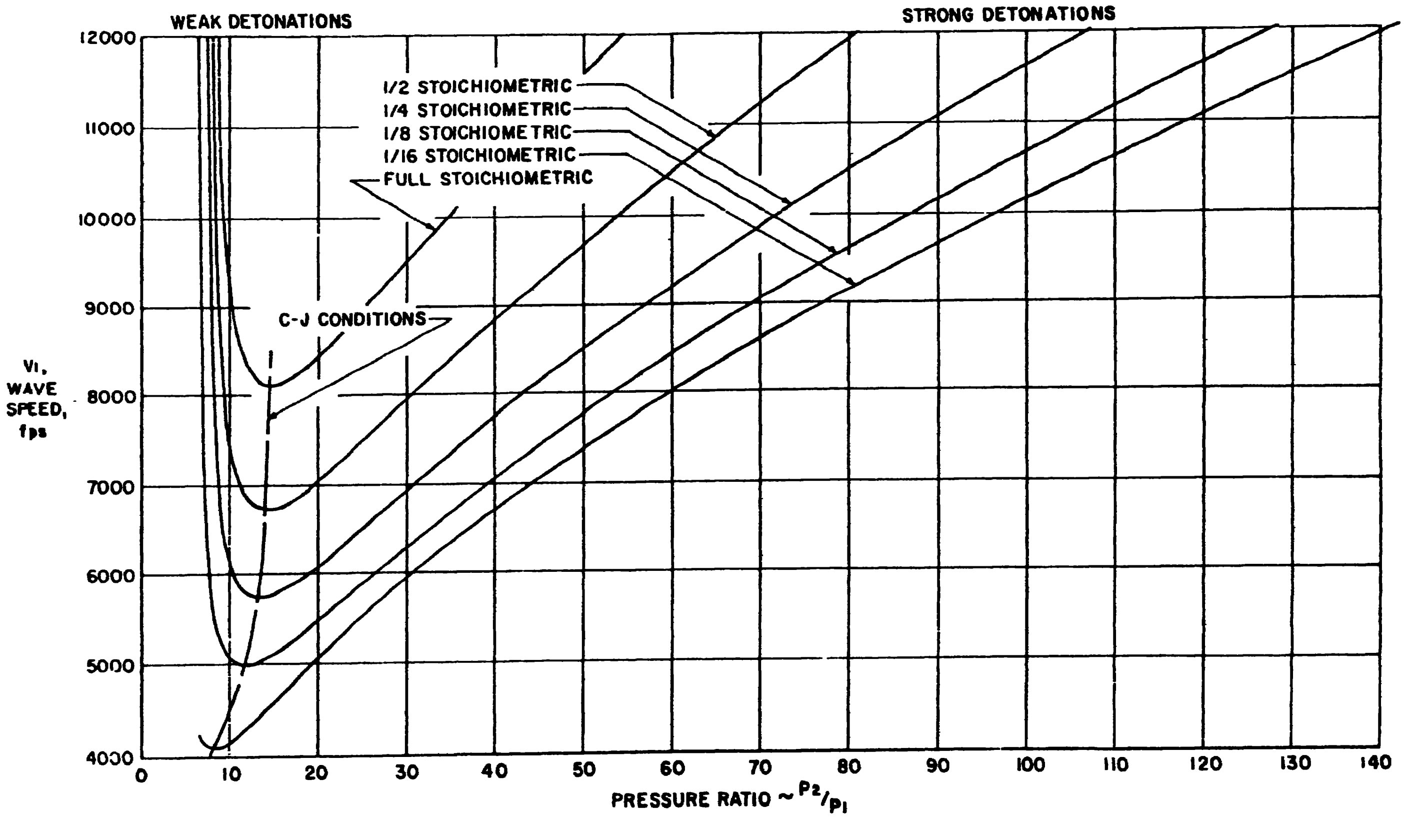

Fig. 2 Pressure ratio for oxygen-hydrogen detonation, $P_1 = 10^{-3}$ atm, $T_1 = 540°R$

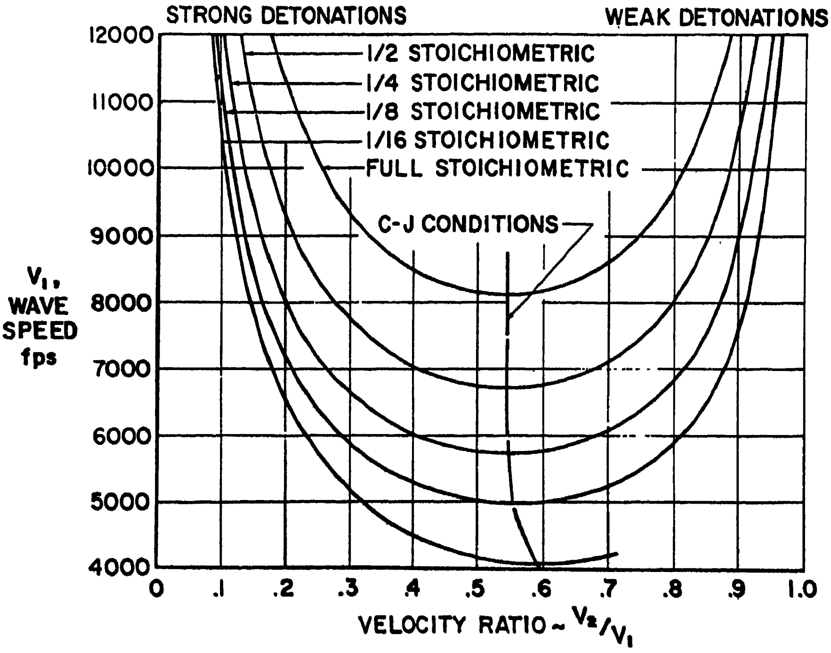

Fig. 3 Velocity ratio for oxygen-hydrogen detonation; $P_1 = 10^{-3}$ atm, $T_1 = 540°R$

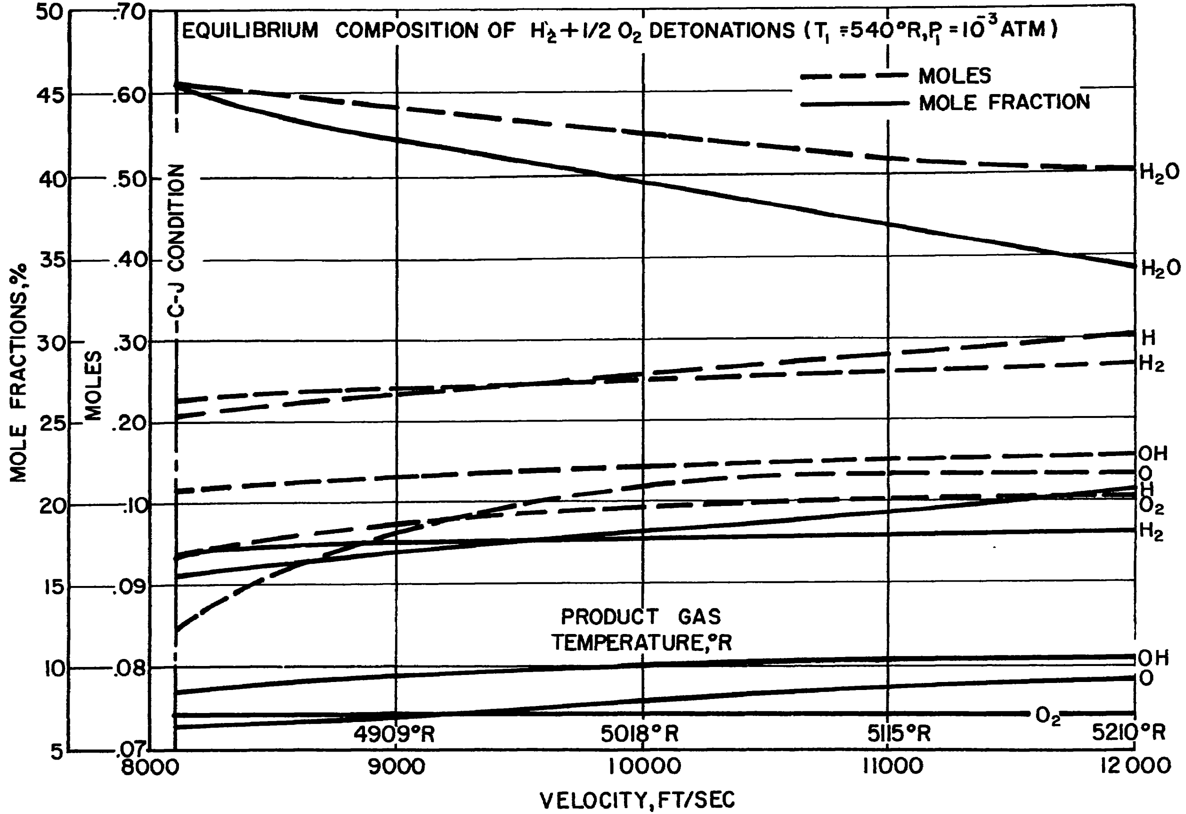

Fig. 4 Equilibrium composition of H_2 + (1/2) O_2 detonations; $T_1 = 540°R$, $P_1 = 10^{-3}$ atm

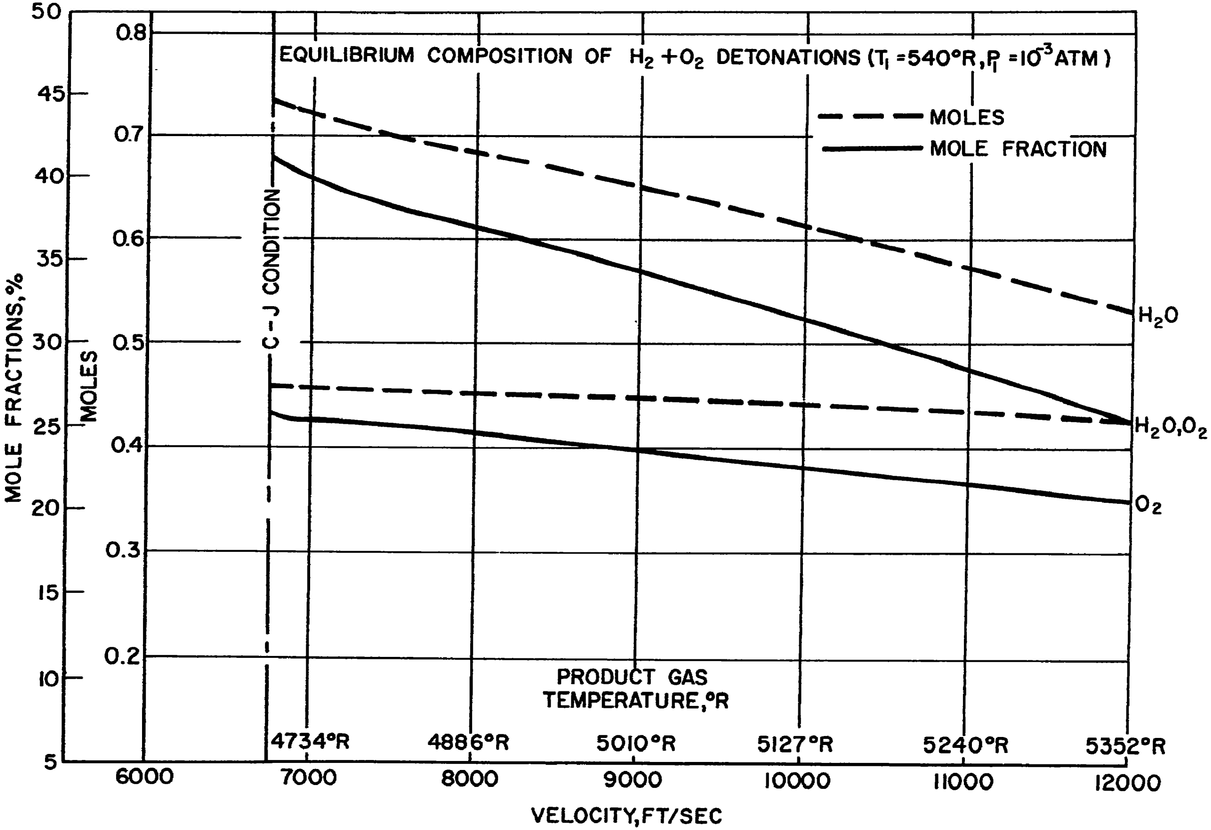

Fig. 5 Equilibrium composition of $H_2 + O_2$ detonations; $T_1 = 540°R$, $P_1 = 10^{-3}$ atm

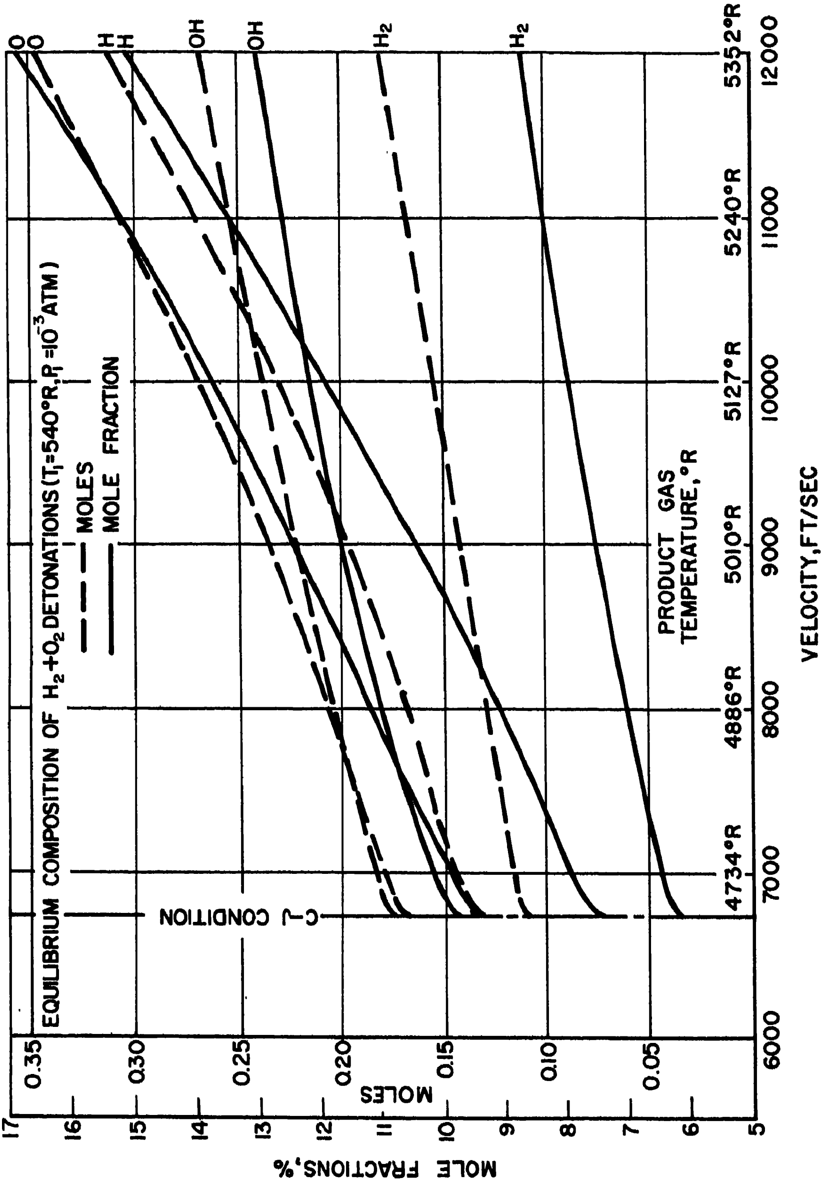

Fig. 6 Equilibrium composition of $H_2 + O_2$ detonations; $T_1 = 540°R$, $P_1 = 10^{-3}$ atm

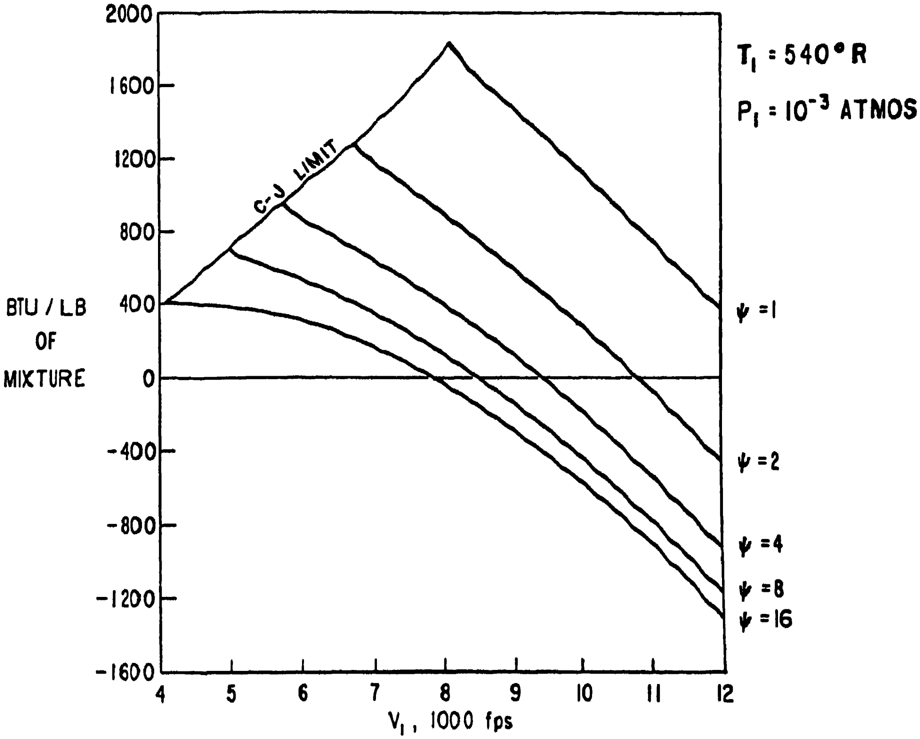

Fig. 7 Heat release of stationary H_2–O_2 detonations

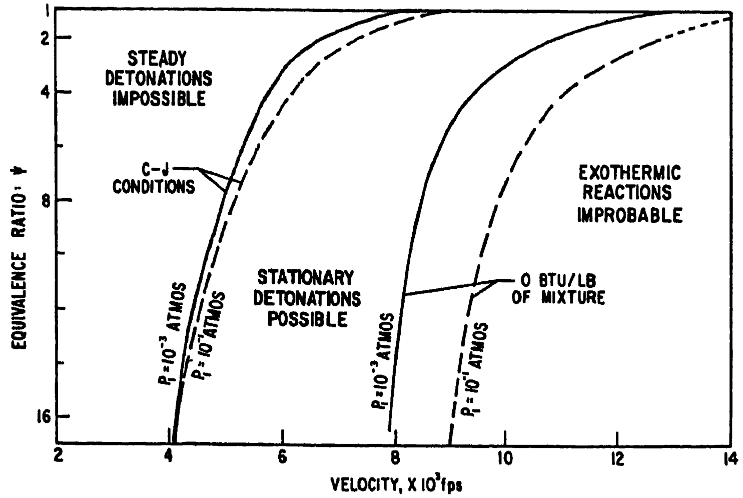

Fig. 8 Limits of stationary H_2+O_2 detonations; $T_1 = 540°R$

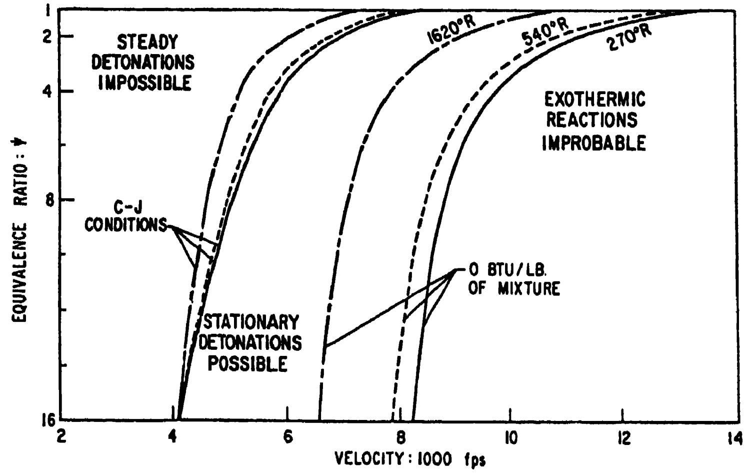

Fig. 9 Limits of stationary H_2+O_2 detonations; $P_1 = 10^{-3}$ atm

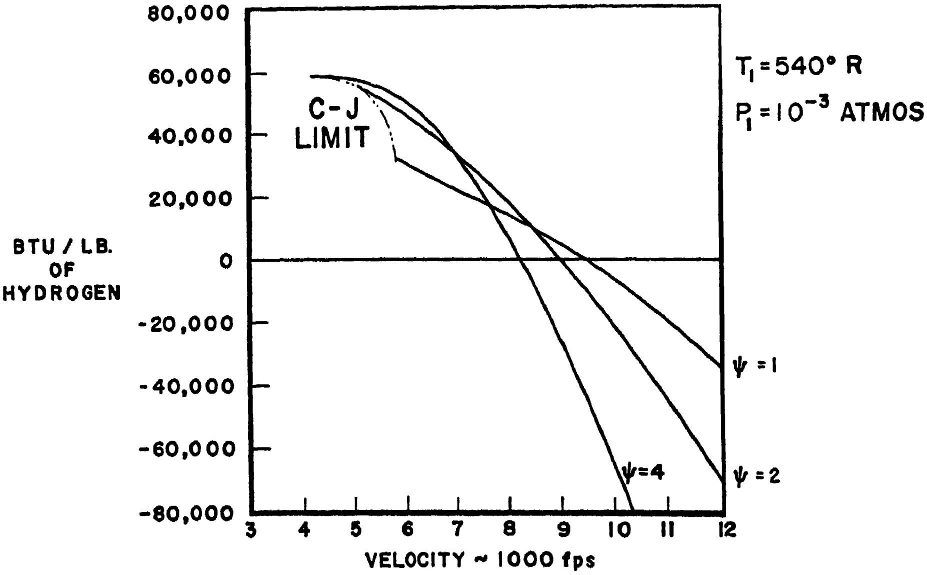

Fig. 10 Heat release of stationary H_2 + air detonations

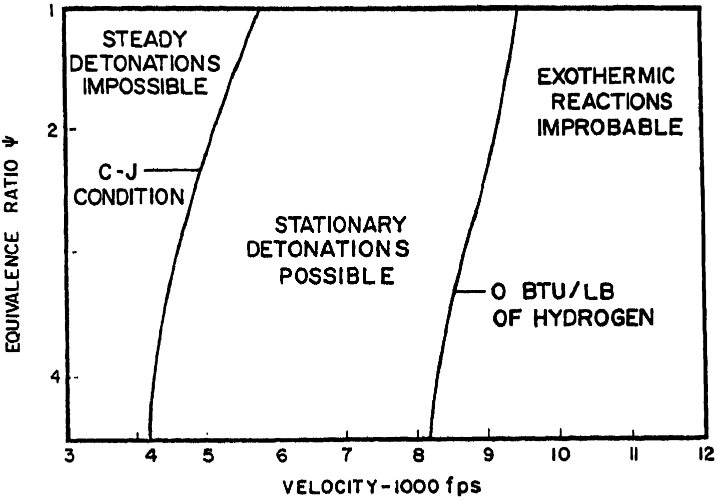

Fig. 11 Limits of stationary H_2 + air detonations; $T_1 = 540°R$, $P_1 = 10^{-3}$ atm

ESTIMATING CALORIC STATE BEHAVIOR IN CONDENSED-PHASE DETONATIONS

Riley O. Miller

NASA Lewis Research Center, Cleveland, Ohio

ABSTRACT

A method is proposed for estimating the adiabatic exponent γ for condensed-phase detonations in which loading density is at crystal densities or lower, down to critical. The overall expression is

$$\gamma - 1 = \gamma_G = \frac{1}{3} + \frac{1}{2}\frac{\rho_o}{\rho_{oc}}\frac{\sum_i \left[n_i(a \cdot r_e)_i\right]}{\sum_i n_i}$$

where γ_G is the Grüneisen parameter, ρ_o is the loading density, ρ_{oc} represents the crystal density of explosive, $a \cdot r_e$ are Morse parameters for each element i, and n is the number of atoms of type i. Values suggested for $a \cdot r_e$ are 3.04, 1.42, 3.40 and 3.22 for C, H, N, and O. The relation was checked by using available experimental and computed data for several explosives. At loading densities near crystalline the estimated values of γ agree well, for the most part, with those that have been measured experimentally. At loading densities less than crystalline the estimated values of γ, along with experimental values of detonation velocity, yield values of explosion energy Q which are in excellent to fair agreement with published values of Q that have been computed by detailed procedures. The technique is deemed satisfactory where rapidity of calculation outweighs the need for a high degree of certainty.

R. O. MILLER is Aeronautical Research Scientist, Chemistry and Energy Conversion Division. Paper presented at the ARS Propellants, Combustion and Liquid Rockets Conference, Palm Beach, Fla., April 26-28, 1961.

INTRODUCTION

During and after World War II considerable detailed work, reviewed in Refs. 1-3, was done on equations of state of condensed-phase detonation products. Some conclusions from these studies are that: 1) computed detonation velocities agree fairly closely with those obtained experimentally; 2) the form of the equation of state assumed was not critical in these calculations; and 3) little verifiable information about temperature can be learned from such calculations. Also, the arithmetic was tedious.

Important progress has been made in the last several years (1,4).[1] It has been realized that the original simplified equations of Chapman and Jouguet, in terms of γ, will work for a detonation at crystalline loading density, where $\gamma \sim 3$. The following relations (e.g., Refs. 2,5), which are very close approximations when $P \gg P_0$, constitute an expression for the Rankine-Hugoniot - Chapman-Jouguet conditions.

$$D^2 = 2(\gamma^2 - 1)Q \qquad [1]$$

$$\frac{D}{W} = \gamma + 1 \qquad [2]$$

$$\frac{V_0}{V} = \frac{\gamma + 1}{\gamma} \qquad [3]$$

$$PV = (\gamma - 1)E \qquad [4]$$

$$PV_0 = 2(\gamma - 1)Q \qquad [5]$$

where γ is the adiabatic exponent

$$\gamma = -\left(\frac{\partial \ln P}{\partial \ln V}\right)_S \qquad [6]$$

Experimental confirmation of these relations in condensed-phase detonation products recently has been made by Deal (6,7).

The relations of Eqs. 1-5 have the advantage that the hydrodynamic aspects of detonation may be analyzed without reference to temperature. If temperature is required, it can be estimated independently. The first five equations contain eight parameters, three of which must be known in order to solve the set. If an independent way to evaluate γ were available, then the set could be solved from the two experimental parameters most easily measured, D and $\rho_0 = 1/V_0$. Measurements of shock velocities in inert target materials would not be required. For example, an effective chemical energy Q would come from Eq. 1, which would aid in experimental explorations of chemical effects in condensed-phase detonation.

---

[1] Numbers in parentheses indicate References at end of paper.

The purpose of this presentation is to suggest a way to estimate γ values in detonations of explosives containing carbon, hydrogen, nitrogen, and oxygen. Estimating γ at near-crystalline loading densities will be considered first, and then a way to extend the estimated values of γ to lower densities will be proposed and appraised.

RELATION BETWEEN γ AND GRÜNEISEN PARAMETER - ESTIMATING γ AT CRYSTALLINE LOADING DENSITIES

Eqs. 1-5 were originally derived from the Rankine-Hugoniot - Chapman-Jouguet postulates and ideal gas theory. Andersen and Parlin (8), on the other hand, used the R-H - C-J postulates in a vibrational lattice model and obtained independently a set exactly equivalent to Eqs. 1-5 in which γ was replaced by $\gamma_G + 1$, γ_G being the Grüneisen parameter defined as

$$\gamma_G = -\frac{d \ln \nu}{d \ln V} \qquad [7]$$

The work of Andersen and Parlin thus shows that at the Chapman-Jouguet plane in a condensed-phase detonation

$$\gamma = \gamma_G + 1 \qquad [8]$$

It is now feasible to estimate γ from what is known about γ_G.

A simple way to estimate γ_G at crystalline loading densities will now be considered. Since the γ_G of this discussion is derived from a vibrational function, Eq. 7, empirical data of vibrational origin are used to estimate γ_G. The following interesting heuristic equation by Slater (9) is adapted to this purpose

$$\gamma_G = \frac{a \cdot r_e}{2} + \frac{1}{3} \qquad [9]$$

where a and r_e are Morse equation parameters. Here it is assumed that diatomic $a \cdot r_e$ data can be used to obtain an average γ_G in a dense gas lattice. An arithmetic average of the product $a \cdot r_e$ according to the number of atoms n of each element is proposed, thus

$$\gamma_{Gc} = \frac{\sum\limits_{i} \left[n_i (a \cdot r_e)_i \right]}{2 \sum\limits_{i} n_i} + \frac{1}{3} \qquad [10]$$

For the elements occurring in most high explosives the following values for the product $a \cdot r_e$ are suggested

Element	C	H	N	O
$a \cdot r_e$	3.04	1.42	3.40	3.22

These are optimized values from diatomic data tabulated by Slater.

An appraisal of the proposed method of estimating γ at crystalline loading density is shown by Table 1. Here values of γ for several explosives obtained experimentally by Deal (7,10), using Dural and air respectively as target materials, are compared with estimated values from Eqs. 8 and 10. The experimental γ values are generally a little higher than the estimates, but, with the exception of TNT-Dural, the differences are scarcely greater than expected experimental error. For some reason the data obtained with air as target showed the best agreement. The estimates are encouraging enough so that Eq. 10 can be used as a starting point for estimating γ at lower densities.

ESTIMATING γ AT LOADING DENSITIES LESS THAN CRYSTALLINE

A well-established experimental fact is that the detonation velocity varies linearly with loading density ρ_0, the mass of explosive in a unit volume

$$D = a + b\,\rho_0 \qquad [11]$$

The development of a simple rationale of this simple observation is an interesting challenge; but so far, elegant simplicity has been elusive (4,11).

The treatment proposed here, if lacking in elegance, is simple; γ in Eqs. 1-5 is assumed to be a linear function of loading density ρ_o. The work of Takahashi (12) indicates that γ_G in a quantized phonon field approaches a minimum value of 1/3. Reasoning similar to that of Eyring, Ree, and Hira (13) is now used when ρ_o is less than ρ_{oc}. The initial explosive is imagined to be in two phases: a lattice at crystal density in which γ_G is γ_{Gc}, and a hypothetical lattice at $\rho = 0$ in which γ_G is 1/3. This idea combined with Eqs. 8 and 10 results in the final expression

$$\gamma_G = \gamma - 1 = \frac{1}{3} + \frac{1}{2}\frac{\rho_o}{\rho_{oc}}\frac{\sum_i \left[n_i(a \cdot r_e)_i\right]}{\sum_i n_i} \qquad [12]$$

A further requirement is that the effective value of γ so computed will appear also at the Chapman-Jouguet plane.

Since the most immediate objective of this study is to find a way to obtain effective values of Q from experimental detonation velocity data, the following appraisal of Eq. 12 was made. For several explosives, indicated values of $Q = f(\rho_o)$ were obtained by use of Eq. 1, into which was inserted estimated values of γ from Eq. 12 and published experimental values of $D = f(\rho_o)$(Refs. 3, 14, and 15). The values of Q thus obtained were compared with available published values of Q that were obtained by detailed computations. This comparison is shown by Fig. 1. The theoretical $Q = f(\rho_o)$ values are those of several authors and are tabulated by Cook (3) and Taylor (2). The use of Q is a severe test for γ values because Q in Eq. 1 is a lower order term than are γ and D. The ρ_{oc} used in Eq. 12 was the true crystalline density of a given explosive.

The best agreement in Q is with RDX, Fig. 1a. The estimated curve falls on top of most of the points computed by Keyes, Filler, and Cook (3). The experimental D vs. ρ_o used in our computations came from Fickett, Wood, and Salsburg (14). It is interesting to note that good agreement in Q is obtained despite the fact that other parameters computed by Keyes et al. do not satisfy Eqs. 1-5 with the γ from Eq. 12 or any single value of γ for a single value of ρ_o.

The data for EDNA (Fig. 1b) are shown to be in best agreement at loading densities near 1.

Not many thermodynamic computations are available for tetryl (Fig. 1c). Those of Taylor (2) are higher than the estimated curve; the datum from Cook (3) is lower. The estimated curve seems to be a reasonable compromise.

The curve estimated for TNT (Fig. 1d) seems definitely low at the higher loading densities. This probably represents a true decrease in experimental efficiency.

For PETN (Fig. 1e) the estimated curve agrees well with detailed calculations at high loading densities. The estimates are low at lower densities; the maximum deviation, about 20%, is at $\rho_o = 1$, at which point a break occurs in our estimated curve. The break is the result of a break in the D vs. ρ_o data (Friederich in Ref. 15), which also occurs at $\rho_o = 1$.

A procedure for estimating γ_G that is even simpler than the one discussed here was proposed by Andersen and Parlin (8). They assumed a constant Q estimated by supposing all hydrogen in the explosive was oxidized to water; any balance of oxygen was then assumed to form CO first and then CO_2. A least-squares fit was made of γ_G for several explosives using Eqs. 1 and 8. The proposed equation for all explosives was

$$\gamma_G = 0.89\ \rho_o - 0.049 \qquad [13]$$

Values of Q, computed from Eqs. 1, 8, and 13 and the D vs. ρ_o data used previously in this discussion, are also plotted in Fig. 1. The results are not only high, as would be expected, but they also show a trend opposite to the detailed computations and the results of estimates made by the proposed procedure.

Results of some experiments at loading densities less than crystalline with water as target have recently been published by Cook, Keyes, and Ursenbach (16). They assumed that the Chapman-Jouguet pressure in the detonation products is given by the following impedance mismatch equation

$$P = \frac{P_t(\rho_{ot}D_t + \rho_o D)}{2\rho_{ot}D_t} \qquad [14]$$

Experimental values of P obtained in this way agree quite well with P obtained by their method of thermodynamic computation. Values of γ, however, computed by Eqs. 1 and 5 from the individual D, P, and V_o data of Ref. 16, show a large amount of scatter. The average values are about what would be expected from Eq. 12 for crystalline loading densities rather than for the lower densities used in the experiments.

A different viewpoint, held by Deal (6,7), is that the pressure sensed by an inert target is the pressure of the reflected wave in the detonation products. The Chapman-Jouguet pressure under certain conditions will then be above the indicated pressure on an isentrope. If the criteria of Ref. 7 are applied to the experimental velocity data of Ref. 16, the values of γ will approach a little closer those given by the proposed Eq. 12.

NOMENCLATURE

D = detonation velocity (or shock wave velocity)
W = particle velocity
V = volume
P = pressure
E = internal thermal energy
Q = chemical energy of reaction
ρ_o = loading density
γ = parameter defined in Eqs. 1-6
γ_G = Grüneisen parameter, defined in Eq. 7
ν = average vibration frequency
a, b = constants
$a \cdot r_e$ = Morse equation parameters
n = number of atoms

Subscripts

o = condition before detonation (or shock)
c = crystalline density
t = condition in an inert target that is in intimate contact with the detonating explosive

REFERENCES

1 S.J. Jacobs: Recent Advances in Condensed Media Detonations. ARS Jour., February 1960, vol. 30, pp. 151-158.

2 J. Taylor: Detonation in Condensed Explosives, pp. 33-110, Clarendon Press, Oxford, England, 1952.

3 M.A. Cook: The Science of High Explosives, pp. 44-90, 283-321, 376-407. Reinhold Publishing Corp., New York, 1958.

4 I.B. Zeldovich and A.S. Kompaneets: Theory of Detonation, pp. 206-246. Academic Press, New York, 1960 (English Translation).

5 J.O. Hirschfelder, C.F. Curtiss, and R.B. Bird: Molecular Theory of Gases and Liquids, pp. 783-805. John Wiley & Sons Inc., New York, 1954.

6 W.E. Deal: Measurement of the Reflected Shock Hugoniot and Isentrope for Explosive Reaction Products. Phys. Fluids, November-December 1958, vol. 1, pp. 523-527.

7 W.E. Deal: Low Pressure Points on the Isentropes of Several High Explosives. Third Symposium on Detonation, James Forrestal Research Center, Princeton Univ., ONR Symposium Rept. ACR-52, Sept. 26-28, 1960, vol. 2, pp. 386-395.

8 W.H. Andersen and R.B. Parlin: New Approaches to the Determination of the Thermodynamic-Hydrodynamic Properties of Detonation Processes. Tech. Rept. no. 38 (Research Contract N7-onr-45107), Inst. for Study of Rate Processes, University of Utah, Oct. 31, 1953.

9 J.C. Slater: Introduction to Chemical Physics, pp. 132, 450-5. McGraw-Hill Book Co. Inc., New York, 1939.

10 W.E. Deal: Measurement of Chapman-Jouguet Pressure for Explosives. Jour. Chem. Phys., September 1957, vol. 27, pp. 796-800.

11 W. Fickett and W.W. Wood: A Detonation Product Equation of State Obtained from Hydrodynamic Data. Phys. Fluids, November-December 1958, vol. 1, pp. 528-534.

12 Y. Takahashi: On the Thermal Expansion of Solids. Physica, 1958, vol. 24, pp. 857-867.

13 H. Eyring, T. Ree, and N. Hira: Significant Structures in the Liquid State. I. Proc. Nat. Acad. Sci., July 1958, vol. 44, pp. 683-688.

14 W. Fickett, W.W. Wood, and Z.W. Salsburg: Investigations of the Detonation Properties of Condensed Explosives with Equations of State Based on Intermolecular Potentials. I. RDX with Fixed Product Composition. Jour. Chem. Phys., December 1957, vol. 27, pp. 1324-1329.

15 W. Friederich: Detonation of Explosives. I. Zeit. für Gesamte Schiess und Spreng., vol. 28, 1933, pp. 2-6.

16 M.A. Cook, R.T. Keyes, and W.O. Ursenbach: Measurements of Detonation, Shock, and Impact Pressures. Third Symposium on Detonation, James Forrestal Research Center, Princeton Univ., ONR Symposium Rept. ACR-52, Sept. 26-28, 1960, vol. 2, pp. 357-385.

Table 1 Comparison of Estimated and Experimental γ at Crystalline Loading Densities

	RDX $C_3H_6N_6O_6$	TNT $C_7H_5N_3O_6$	64 RDX 36 TNT	77 RDX 23 TNT	77 HMX 23 TNT
Inert Target Experiments, Deal (7,10)					
Dural	2.90	3.17	2.77	2.80	2.84
Air	----	2.75	2.71	2.79	2.82
Estimate Based on Eqs. 8 and 10	2.70	2.71	2.70	2.70	2.70
Percent Deviation of Experiments From Estimate					
Dural	+7.4	+17.0	+2.6	+3.7	+5.2
Air	----	+1.5	+0.4	+3.3	+4.5

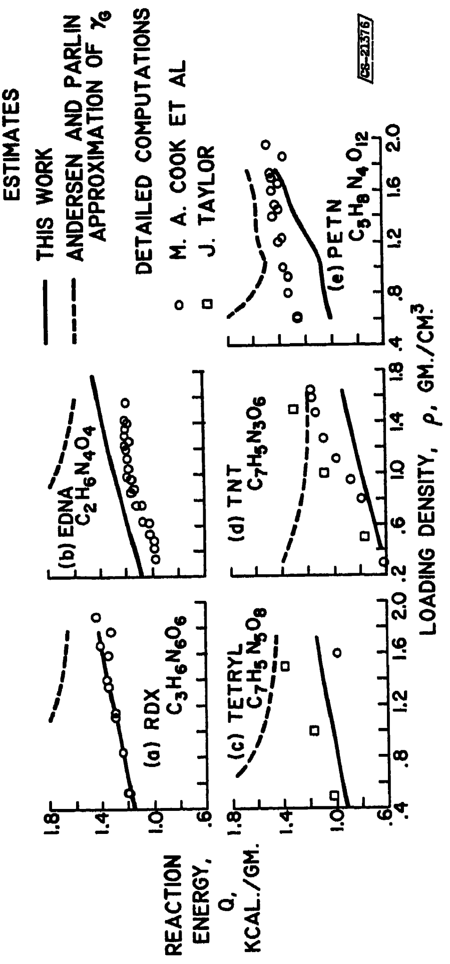

Fig. 1 Chemical energy values resulting from estimated γ from Eq. 12 and from Andersen and Parlin's Eq. 13 compared with values from detailed computations

THEORETICAL TREATMENT OF THE DETONATION BEHAVIOR OF COMPOSITE PROPELLANTS

M. H. Boyer and Ray Grandey

Aeronutronic
Division of Ford Motor Co.
Newport Beach, California

ABSTRACT

A mathematical model for the detonation process is described along the lines set forth by Hubbard and Johnson. This model is represented by a set of basic equations consisting of the hydrodynamic equations, the chemical rate equations, and the equations of state. The rate equations are based upon three different processes: an ignition reaction, one or more grain burning reactions and a diffusion controlled reaction having, respectively, the Arrhenius form, the Eyring grain burning form, and a form derived from diffusion theory. Solution of the set of basic equations is accomplished by numerical integration making use of an electronic computer (IBM 709). The results of some calculations are presented which show the dependence of detonation behavior upon propellant parameters. Correlation with experimentally observed detonation behavior is discussed.

INTRODUCTION

Deflagration and detonation processes are two different representations of a disturbance in a material capable of releasing energy. As such, they can be described mathematically by the Navier-Stokes equations together with two or more relations defining the equations of state and the energy release rate. In most cases energy release arises from chemical

---

M. H. BOYER is Section Supervisor, Physical and Analytical Chemistry, Chemistry Department, Research Laboratory.
R. GRANDEY is a Staff Scientist, Radiation Physics Department, Research Laboratory. Paper presented at the ARS Propellants, Combustion, and Liquid Rockets Conference, Palm Beach, Florida, April 26-28, 1961.

reaction so that the latter are expressions describing a chemical reaction rate.

The specific form assumed by these basic equations has been discussed in a previous paper (1).[1] It was shown that for treatment of detonation processes, the energy transport terms associated with thermal conduction can be deleted and that if geometry effects are not to be considered, the equations can be expressed in one-dimensional form. Numerical techniques involving the use of an electronic computer were presented for obtaining time dependent solutions to the simplified equations.

A primary objective of this work is to apply such computational techniques to the problem of detonation in composite propellants. In particular, it is desirable to extend them to treatment of problems relating to the effect of charge geometry on detonation behavior, i.e., to calculations of critical size. The form of the Navier-Stokes equations is independent of the material involved. Therefore a major problem in the theoretical treatment of the detonation behavior of propellants is the correct formulation of the chemical rate equations and the equation of state. The present paper is concerned with the rate equations.

THEORETICAL CONSIDERATIONS

The Rate Equations: Homogeneous Materials

The initial investigations were carried out using a single rate law of Arrhenius form, namely:

$$\frac{df}{dt} = (1-f)^n \, B \exp \left[-A/RT\right] \qquad [1]$$

Several different aspects of detonation behavior were studied during this initial phase. For example, there was demonstrated the existence of critical sets of values of intensity and duration of the pressure pulse used to initiate detonation which defined a boundary between regions of detonation and failure. A characteristic ignition delay was observed dependent upon the intensity and waveform of the incident pressure pulse and very sensitively upon the values of the parameters A and B. Finally the charge surface temperature was found to have a significant effect upon the ignition delay, and upon the apparent detonation sensitivity. These observations were all discussed in some detail in Ref. 1 and such behavior was shown to be closely related to the exponential form of the rate equation (Eq. 1).

---

[1] Numbers in parentheses indicate Reference at end of paper.

An additional series of calculations were carried out during this period which further illustrated behavior characteristic of an exponential rate law. They concerned the growth of a detonation wave from the point of initiation to the final steady state value. Fig. 1 shows a typical example of such a growth process. The wave is initiated in a semi-infinite charge of explosive by the application of a pressure of 100 kilobars to the free surface. In the figure, the free surface is located at the point x=o at zero time. The situation is then shown at five successive times after application of pressure, starting at 49.8 μsec.

The positions of the shock front at 49.8, 54.0 and 58.1 μsec are shown by the plateaus at the bottom of the figure. The sharp peak first appearing some distance behind the front represents over-pressure developed as a consequence of chemical reaction in the shocked material. This over-pressure grows in intensity and rapidly overtakes the shock front, merging with it at about 60 μsec, at which point a steady state detonation is established. The propagation velocity of this reaction wave is about 20 mm/μ sec.

In all of the foregoing cases, the behavior described is analagous to behavior which has been observed experimentally and discussed in various treatises on detonation phenomena. In particular, very high speed disturbances resembling the reaction wave of Figure 1 have been described by Ginsburgh (2), and appear to be analagous to a phenomena called flashcross by M. A. Cook (3). This resemblance between computed and experimental waves constitutes supporting evidence for Eq. 1 as properly descriptive of the ignition process.

In one very important respect, however, the computed waves were found to be unrealistic. Calculations of reaction zone thickness (4) gave values of the order of 10^{-5} to 10^{-6}cm, whereas experimental values in the range of 0.01 to 2.0 cm are reported for high explosives such as TNT. This finding together with the observations described in the foregoing suggested that whereas an Arrhenius form was correct for a description of ignition phenomena in detonation processes, it was not suitable for representation of the reaction following ignition. Accordingly it became necessary to consider in more detail the question of the proper form of the rate equations.

The best documented concept of reaction in the solid state under detonation conditions is provided by the grain burning model of Eyring (5). The corresponding rate law is of the form

$$\frac{df}{dt} = (1-f)^{2/3} \frac{aB}{Z} \exp(-A/RT_f) \qquad [2]$$

where T_f is a constant temperature generally taken as the theoretical detonation temperature. Eq. 2 has been successful in describing various aspects of steady state detonation phenomena. It is, however, not useful in describing initiation or other transient phenomena, since in this form it is decoupled from the pressure and energy density conditions in the wave. An additional equation is needed to describe the process by which the surface burning of the grain can be initiated. This requirement, together with the evidence as mentioned in the foregoing, that the ignition process conforms to a rate law of Arrhenius form has led to the dual zone concept of the grain burning process.

The dual zone model conceives of a grain of reactive material as divided into two zones: an outer zone, consisting of a relatively thin layer on the surface of the grain, and an inner zone that includes the remainder of the grain. The surface material is postulated to be different from the interior such that reaction can take place uniformly throughout its bulk, as in a gas. Accordingly it is assumed to react adiabatically following an Arrhenius rate law and, on reaching maximum temperature, it serves to initiate the material in the inner zone which then reacts according to the standard Eyring formulation.

For such a composite process, the overall reaction rate is given by the following expression

$$\frac{df}{dt} = F_1B_1(1-f_1)^n \exp(-A_1/RT) + F_2(1-f_2)^{2/3} \frac{aB_2}{Z} \exp(-A_2/RT) \qquad [3]$$

Necessary coupling between the two zones is obtained by defining T as the temperature in the surface zone. Computations carried out for a reactive material conforming to Eq. 3 with reasonable values of the parameters gave detonation waves that had approximately the correct reaction zone thickness, and simultaneousl y showed values of ignition delay very close to the experimental values of Majowicz and Jacobs (6). (See also Ref. 1.) The data are shown in Table 1.

Table 1. Comparison of Calculated and Experimental Values of Ignition Delay and Reaction Zone Thickness (r) of the Steady State Wave for TNT

P, megabar	τ, μ sec		r, mm	
	Calc	Exp	Calc	Exp
0.0811	0.22	0.27[a]	0.2	0.3 - 3[b]
0.108	0.08	0.07	0.2	0.3 - 3

---

a Defined according to Majowicz and Jacobs.

b Experimental values cover a rather wide range(5,7,8).

The Rate Equations: Composite Propellants

A composite material is conceived to be a collection of reaction units, each consisting of an oxidizer granule surrounded by a fuel matrix. Initiation of reaction in such a unit is assumed to occur at the interface between fuel and oxidizer. This is followed by erosive processes at the oxidizer and fuel surfaces which cause a change in phase from solid to gaseous state. The fuel and oxidizer solid surfaces therefore recede and become separated by a distance that increases with time. The process is shown by the sequential diagram of Fig. 2, time increasing on proceeding from top to bottom.

In order to react, the gaseous fuel and oxidizer species must diffuse into the space between the two surfaces. Presumably this leads to something analagous to a diffusion flame. The rate of heat flow from this flame back to the solid surfaces will in turn affect the rate of the surface erosive processes. The detailed treatment of this overall system constitutes a very formidable mathematical problem involving considerations of moving boundaries and spherical geometry. For present purposes it is desirable to introduce some assumptions that will simplify the formulation of the problem.

First, the transport of thermal energy from the diffusion flame zone to the solid surfaces is assumed to be substantially faster than the transport of material by diffusion. This is reasonable at high density, since the diffusion of heat by collisional transfer of energy or lattice vibrations should predominate over molecular diffusion processes. It follows that the solid surfaces will regress more rapidly than gaseous material will diffuse away. In such cases, the diffusion of reactive material into the flame zone proceeds at the same rate as by diffusion from an infinite gas, and the problem of the moving boundaries is avoided.

Second, it is assumed that the reaction zone is of infinitesimal thickness and that the concentration of reactive material is zero in this region. The problem then becomes the rate of transport of material from an infinite gas past a boundary at which the concentration is held equal to zero. A one dimensional diagram illustrating this conception of the reaction process is shown in Fig. 3.

It is assumed that the reaction unit is approximately spherical and it is therefore necessary to treat the problem in spherical form. The model is represented as a sphere of oxidizer gas surrounded by a shell of fuel gas with the diffusion flame located at the spherical surface. The problem is then the diffusion of material from a sphere, the surface concentration always being zero. For the case where the shell is thick relative to the spherical radius, a reduction in flame radius would take place with time. However, with actual propellants the volume ratio of fuel to oxidizer is small; i.e., the average shell thickness will be small relative to the spherical diameter. This suggests that an assumption of constant flame radius equal to the original grain radius is acceptable.

The problem of the rate of diffusion of material from a sphere of constant radius with zero concentration at the surface has been solved in series form (9). Using the first two terms of this series, the following expression is obtained for the fractional completion of reaction

$$f = 1 - \left[0.8 \exp\left(-\frac{D\pi^2 t}{z^2}\right) + 0.2 \exp\left(-\frac{4D\pi^2 t}{z^2}\right)\right] \qquad [4]$$

As in the case of homogeneous materials, it is still necessary to define the process by which reaction is initiated. It has been stated that initiation occurs at the fuel oxidizer interface. The assumption is made that the interfacial zone in which this occurs is narrow enough so that diffusion processes across it are rapid compared to chemical reaction rates. Under these conditions, the zone material behaves like a molecularly dispersed mixture of fuel and oxidizer and as in the case of homogeneous materials, it is assumed to react in accordance with an Arrhenius rate equation, i.e., Eq. 1.

In cases where thermal effects at the gas-solid interface are small and the surface erosion rates are wholly dependent on the transfer of heat from the diffusion flame, the combination of Eqs. 1 and 4 would be expected to represent the overall reaction. However, if either fuel or oxidizer is capable of an independent exothermic decomposition reaction, it represents an additional source of energy that must be described by an additional rate equation. It has already been explained that under detonation conditions, the rates of such processes are defined by a grain burning equation of the form of Eq. 2. Since nearly all composite propellants of interest use either ammonium perchlorate or a nitrated binder or both as the oxidizer, and such materials are capable of undergoing exothermic decomposition, the addition of one or more grain burning equations is necessary for complete definition of the overall rate process.

MATHEMATICAL CONSIDERATIONS AND CALCULATIONS

The considerations of the previous section have resulted in the interpretation of reaction in a composite propellant in terms of the following processes

Interface Ignition Reaction
unreacted solid → gaseous products (Step 1)

Burning Reaction
unreacted solid → reactive vapor (Step 2)
reactive vapor → gaseous products (Step 3)

Step 1 is the reaction of a molecularly dispersed mixture of fuel and oxidizer. The heat of reaction is that corresponding to conversion of the propellant material to completely reacted products. Step 2 represents the grain burning processes with a heat of reaction defined by the oxidizer and fuel vaporization processes. Step 3 is the diffusion reaction. Its heat of reaction is that for the reaction of the products of oxidizer and fuel decomposition to form final products. This three-step representation has a practical advantage because its mathematical formulation will also represent the reaction of homogeneous material merely by insertion of zero for the rate parameter of Step 3 and the use of appropriate heats of reaction. A computer program written around this model can thus be used for both homogeneous and composite materials merely by a change in input data.

The temperature T in Eq. 1 which describes the ignition reaction is not a constant, and the problem requires its expression in terms of the other parameters of the system. This is done by means of an equation which relates it to the sum of the energy change due to chemical reaction and that due to the volume and entropy changes resulting from hydrodynamic motion.

The temperature T_f which appears in Eq. 2 is also not regarded as strictly constant. If the grain decomposition occurs effectively as a surface reaction, then T_f should be the temperature attained as a consequence of this reaction. The process is regarded as taking place at constant pressure, so that the expression for T_f becomes

$$T_f = \frac{1}{C_v} \left(e_s + \frac{Q_2}{\gamma_g}\right)$$

It is therefore dependent on the solid energy density, e_s, and γ_g which are variables throughout the problem.

The following are thus obtained for the complete set of equations upon which calculation of the detonation behavior of composite propellants is based. Because of uncertainties as to the distribution of energy between thermal and potential forms at high pressures, all equations have been expressed in terms of energy density rather than temperature.

Conservation Equations

Momentum
$$\frac{du}{dt} + \frac{1}{\rho} \frac{\delta p}{\delta x} = 0$$

Mass
$$\frac{d\rho}{dt} + \rho \frac{\delta u}{\delta x} = 0$$

Energy
$$\frac{de}{dt} - \frac{p}{\bar{\rho}^2} \frac{d\bar{\rho}}{dt} + F_1 Q_1 \frac{df_1}{dt} + Q_2 \frac{df_2}{dt} + Q_d \frac{df_d}{dt}$$

Equations of State

Solid
$$(p + B)v_s = (\gamma_s - 1)e_s + C$$

Gas
$$pv_g = (\gamma_g - 1)e_g$$

Chemical Rate Equations

Ignition
$$\frac{df_1}{dt} = (1-f_1)B_1 \exp\left[- \frac{C_v A_1}{k(e + Q_1 f_1)}\right]$$

Vaporization
$$\frac{df_2}{dt} = (1-f_2)^{2/3} \frac{aB_2}{Z} \exp\left[- \frac{C_v A_2}{k\left(e_s + \frac{Q_2}{\gamma_g}\right)}\right]$$

Diffusion
$$f_d = 1 - \left\{0.8 \exp\left(- \frac{D\pi^2(t-\tau)}{Z^2}\right) + 0.2 \exp\left(- \frac{4D\pi^2(t-\tau)}{Z^2}\right)\right]$$

Other

$$\gamma_g = \gamma_o + \frac{P}{p+B} (\gamma_s - \gamma_o)$$

$$D = D_s + \frac{D_o}{p}$$

A discussion of the methods by which the basic equations are integrated is beyond the scope of this paper. However, it is of interest to consider some examples of computed waves and the dependence of their behavior on initial conditions and material parameters. In all of the problems described, a charge of 20 cm length and infinite lateral dimension was initiated by applying to one surface a pressure pulse of specified intensity and duration with zero rise and cutoff times. Unless otherwise noted, the input data were as shown in Table 2. They were chosen to represent a hypothetical material analagous in some but not all respects to an ammonium perchlorate-polymer binder composite propellant. The calculations gave pressures, velocities, specific volumes, energy densities, and degree of completion of each of the three reaction processes at all points in the charge and as function of time. From this information, wave velocities, reaction profiles, particle trajectories, etc. were obtained.

Fig. 4 shows data on a series of computations carried out for the purpose of investigating the effect of propellant grain size and initial pressure on wave behavior. The curves are plots of wave velocity vs. linear position in the charge. At the extreme left the indicated velocity in each case is that of the initial unreactive shock. As the wave progresses into the charge, a sharp increase in velocity is observed due to the occurrence of the ignition reaction and appearing more quickly with an initiation pressure of 0.1 megabar than with 0.04 megabar. Subsequent behavior depends primarily on the grain size of the material.

With a grain radius of 30 μ, a smooth and rapid increase in velocity is obtained to a final value of about 6.4mm/μ sec. With a 0.3 μ radius, a similar rise occurs to a much higher value of about 10 mm/μ sec. Finally, at 200 μ, it is found that the velocity remains constant at about 4 mm/μ sec.

The explanation for these final velocities is shown by Figs. 5-7, which consist of plots of reaction profiles through the different waves. The situation after attainment of final velocity is shown in all cases. Pressure profiles are also indicated as a dashed curve.

Fig. 5 shows the wave progressing through material of 30 μ grain radius. It is noted that completion of the ignition reaction is coincident with the wave front and that the grain burning reaction is complete within a distance of about 1.5cm behind the front. The diffusion reaction, however, has proceeded to a negligible extent. It becomes clear that the observed velocity of 6.4 mm/μsec for this case corresponds to support of the wave only by the energy release from the ignition and grain burning reactions.

Fig. 6 shows a similar set of profiles for the wave in material of 0.3 μ grain radius. In this case, both the ignition and grain burning reaction go to completion coincidently with the wave front, and the diffusion reaction is complete within about 2 cm of the front. The velocity of 10 mm/μ sec corresponds to complete release of chemical energy in the material and is the maximum value possible.

Fig. 7 shows profiles of a wave in material of 200μ radius. In this case not only is the diffusion reaction negligible, as in Fig. 5, but also the grain burning reaction is only partially complete. It is deduced that the energy release from the ignition reaction combined with the contribution from the grain burning process is just enough to maintain the wave at its initial value, with neither acceleration or decay.

Fig. 8 shows data on velocity histories of some additional waves computed to examine the effect of the parameter F_1. The grain radius was taken to be 200 μ for all three curves. It is observed first that the value of F_1 has a strong effect on the initial jump in velocity. This is to be expected since it determines the amount of energy released in the ignition reaction. It is also observed to affect the subsequent wave growth and final velocity. At the lowest value of $F_1 = 0.01$, the wave decays. At the larger value of 0.10 the wave remains in its initial state. Finally, at $F_1 = 0.25$ growth to a final velocity of 7.5 mm/μ sec occurs. This behavior is consistent with the fact that the rate of the grain burning reaction is a function of the energy density of the solid phase. The latter depends on the energy deposited in the solid by the shock front and the chemical reaction associated with the ignition process.

A final set of computations was carried out to show the effect of variation in A_1. The data are presented in Table 3 as ignition delay (time from initial application of incident pressure to first completion of ignition reaction at any point) vs. A_1. Applied pressures were 0.04 megabar in all cases.

The ignition delay represents the duration that an initial pulse must have in order to initiate detonation in a material. The data show it to be extremely sensitive to the value of A_1 for the propellant. The general relationship between A_1 and the intensity and duration of the applied pressure was discussed in some detail in Ref. 1.

Table 2. Input Data for Calculations

$\rho = 1.6$ gm/cm^3

$a = 4.0 \times 10^{-8}$cm

$Q_1 = 1000$ cal/gm

$Q_2 = 304$ cal/gm

$Q_d = 696$ cal/gm

$k = 0.02$ cal/gm-deg

$C_v = 0.3$ cal/gm-deg

$D_s = 10^{-4}$ cm^2/sec

$Z = 3 \times 10^{-3}$cm

$L = 20$ cm

$B = 5 \times 10^4$ atm

$C = 31$ cal/gm

$\gamma_o = 1.3$

$\gamma_s = 2.8$

$B_1 = 5 \times 10^{13}$

$B_2 = 5 \times 10^{13}$

$A_1 = 124$ cal/gm

$A_2 = 210$ cal/gm

$F_1 = 0.10$

Table 3. Variation of Ignition Delay With the Parameter A_1

A_1, cal/gm	τ, μ sec
119	1.94
124	4.0
131	7.4
139	> 20

DISCUSSION AND CONCLUSIONS

The formulation of the detonation process presented in the foregoing sections and its usefulness in the treatment of real cases depends on information as to a number of parameters that represent different properties of the material or define the initiation conditions. With the exception of F_1, all are relatively familiar and, at least in theory, capable of evaluation by independent measurement. The quantity F_1 has been specifically related to the material in the surface zone of a grain. Since the zone concept may appear to be somewhat contrived, additional considerations as to the meaning of F_1 are of interest.

A well-documented fact in connection with the initiation of detonation is that sensitivity increases with porosity(8,10,11) i.e., lower density. An explanation commonly advanced for this phenomenon is that compressional heating of gas occluded in the pores induces ignition in the surrounding material. Estimates have been made of the temperatures to which the material surrounding a pore could be raised (12,13) and have led to some question as to the possibility of ignition by such a process. An alternative explanation can be based upon the fact that porous material itself should be more compressible and that therefore more work will be done when it is subjected to a given pressure pulse.

The compression resulting from the application of a high pressure to a material would tend to collapse any porosity present so that with increasing pressure the equation of state should approach that of the nonporous material. The effect of porosity on physical properties should therefore manifest itself primarily in the low pressure region. The increase in internal energy under shock heating is dependent upon the initial specific volume and the equation of state at the high pressure end of the Hugoniot. It follows that increasing porosity can be effectively simulated merely by increasing the initial specific volume (v_o). The same effect can be simulated by decreasing γ .

A few calculations were carried out to investigate this point during the early phases of the program. A rate law of Arrhenius form and a co-volume equation of state, i.e., $p(v-\alpha) = (\gamma-1)e$, were assumed to apply. Results of the calculation are shown in Table 4.

Table 4. Effect of Physical Properties on Ignition Delay

γ	V_o, cm^3	τ, μ sec
3.00	0.625	39.8
2.75	0.625	8.1
3.00	0.650	7.8

Mechanically, the increase in shock heating of a material with porosity occurs as a consequence of high speed viscous flow, shearing strains, or other dissipative effects in the region of the pores as they collapse. It follows that heating is concentrated in regions of material surrounding the pores. Shearing and flow together with elevated temperature are effects expected to lead to reaction in accordance with an Arrhenius rate law. Such a mechanism produces a point source type of ignition leading to progressive internal surface burning model rather than the external surface burning model from which Eq. 3 is derived. It is readily shown, however, that the appropriate rate equation for an internal burning process is identical to Eq. 3 if f is defined as the fraction of material unreacted.

Regions surrounding a pore constitute a reasonable alternative interpretation of the parameter F_1. If it is assumed that the volume of material to be included in such a region is approximately equal to the pore volume, then F_1 defines the overall fractional porosity. Furthermore, in this case the energy density deposited in the vicinity of a pore by passage of a shock is just twice that deposited in bulk material at some distance from a pore. Kinetically, the consequences of this fact can be simulated by use for A_1 of a value one half the true value.

For the purposes of the mathematical problem a detailed physical concept of the ignition zone is in any case unnecessary. All that must be known about F_1 is the quantity of heat released by the material that it represents and the rate equation that describes the release. It will be necessary to obtain this information from direct experimental observation in order to apply the computational methods that have been described to the treatment of real materials.

Two additional points should be mentioned. First, whatever physical interpretation is preferred for the quantity F_1, it is very likely that it should be represented as a function of Z. Thus, as the surface region of a grain, it would be expected to constitute a larger fraction of the total material for smaller Z. The same conclusion follows from its conception as the effective volume of material surrounding a void.

Second, the reaction kinetics in the various ignition regions are not likely to be uniform throughout the material because of difference in disorder, concentrations of impurities, etc. There are therefore expected to be significant differences in the level of shock intensity at which different ignition sites are activated. The consequence is a dependence of Z upon shock intensity. Such a dependence is particularly to be anticipated with homogeneous explosives since at some extreme level of shock intensity the overall rate equation for homogeneous materials should reduce to an Arrhenius form. This occurs, according to the present mathematical formulation, when $Z=0$; $F_1=1$.

An important consequence of the present work has been the demonstration from purely theoretical considerations that a number of different, apparently stable, detonation velocities are obtainable with the same material merely by changing material properties. Experimentally, such behavior is well known and has been extensively discussed by Cook (3) and Taylor (8) as well as by Bowden and Yoffee (10,11). Its theoretical justification, however, has thus far been lacking. The data that have been presented show that the so-called ideal velocity is readily obtained only when reaction rates are rapid and strongly coupled to the pressure disturbance. Large grain sizes or small F_1 tend to decouple these two processes.

The theoretical justification of the existence of low level stable detonation waves in which only a small fraction of the maximum theoretical energy yield is obtained, is of considerable importance to an understanding of the behavior of propellant materials. Low-yield detonations are likely to be the rule rather than the exception if detonation occurs at all, particularly with propellants having a non-selfreactive binder. However, for purposes of hazard and reliability evaluation, they must be regarded equally as dangerous as detonations of ideal intensity.

ACKNOWLEDGEMENT

The authors are indebted to D. A. Schermerhorn for programming and carrying out the calculations. This program is supported by the Special Projects Office, Bureau of Naval Weapons, Contract NOrd 17945. The work described was carried out over the period of June 1957 to December 1960 and originally reported in Progress Reports One to Fourteen.

NOMENCLATURE

R = gas constant

T = temperature

T_m = temperature after reaction

t = time

τ = ignition delay

e = energy density

p = pressure

P = pressure pulse applied to surface

v = specific volume

ρ = density

u = material velocity

f = fraction of complete reaction

D = diffusion coefficient

A,B,n = rate parameters

r = reaction zone thickness

t_p = duration of initial pulse

$\alpha,\gamma C,B$ = equation of state parameters

C_v = specific heat

Q = heat of reaction

F = fraction of material in zone

a = molecular diameter

Z = grain radius

L = charge length

Subscripts

o = ambient conditions

1 = ignition zone

2 = grain burning zone

d = diffusion reaction

g = gas phase

s = solid phase

Bar = average value

REFERENCES

1. H. W. Hubbard and M. H. Johnson: Initiation of Detonation. *Jour. Appl. Phys.*, 1959, Vol. 30, p. 765-769.

2. D. Ginsburgh: Abnormally High Detonation Pressures in a Shock Tube. *Jour. Appl. Phys.*, 1958, Vol. 29, p. 1381-1382.

3. M. A. Cook: *The Science of High Explosives*, p. 88, 50-59, Reinhold Publishing Corp., New York, 1958.

4. Fourth Quarterly Report Concerning Study of Detonation Behavior of Solid Propellants. Aeronutronic Rept. No. U-253, Bureau of Weapons Contract No. NOrd 17945, August 15, 1958.

5. H. Eyring, R. E. Powell, G. H. Duffy and R. B. Parlin: The Stability of Detonation. *Chem. Rev.*, 1949, Vol. 45, p. 69-181.

6. J. M. Majowicz and S. J. Jacobs: Preprint, Tenth Annual Meeting of Division of Fluid Dynamics of the American Physical Society, Lehigh Univ., Bethlehem, Pa., November, 1957.

7. R. E. Duff and E. Houston: Measurement of the Chapman-Jouguet Pressure and Reaction Zone Length in a Detonating High Explosive. *Jour. Chem. Phys.*, 1955, Vol. 23, p. 1268-1273.

8. J. Taylor: Detonation in Condensed Explosives, Chap. 10, Oxford Press, Amen House, London E.C. 4, 1952.

9. J. Crank: The Mathematics of Diffusion, Chap. VI, Oxford Press, Amen House, London E.C. 4, 1956.

10. F. P. Bowden and A. D. Yoffee: Initiation and Growth of Explosion in Liquids and Solids, p. 89-92, Cambridge Press, Cambridge, 1952.

11. F. P. Bowden and A. D. Yoffee: Fast Reactions in Solids, p. 130-133, Academic Press, New York, 1958.

12. C. H. Johansson: The Initiation of Liquid Explosives by Shock and the Importance of Liquid Breakup. Proc. Roy. Soc., 1958, Vol. A246, p. 160-167.

13. C. H. Johansson and H. L. Selberg: The Ignition Mechanism of High Explosives. Appl. Sci. Res., 1955, Vol. A5, p. 439-449.

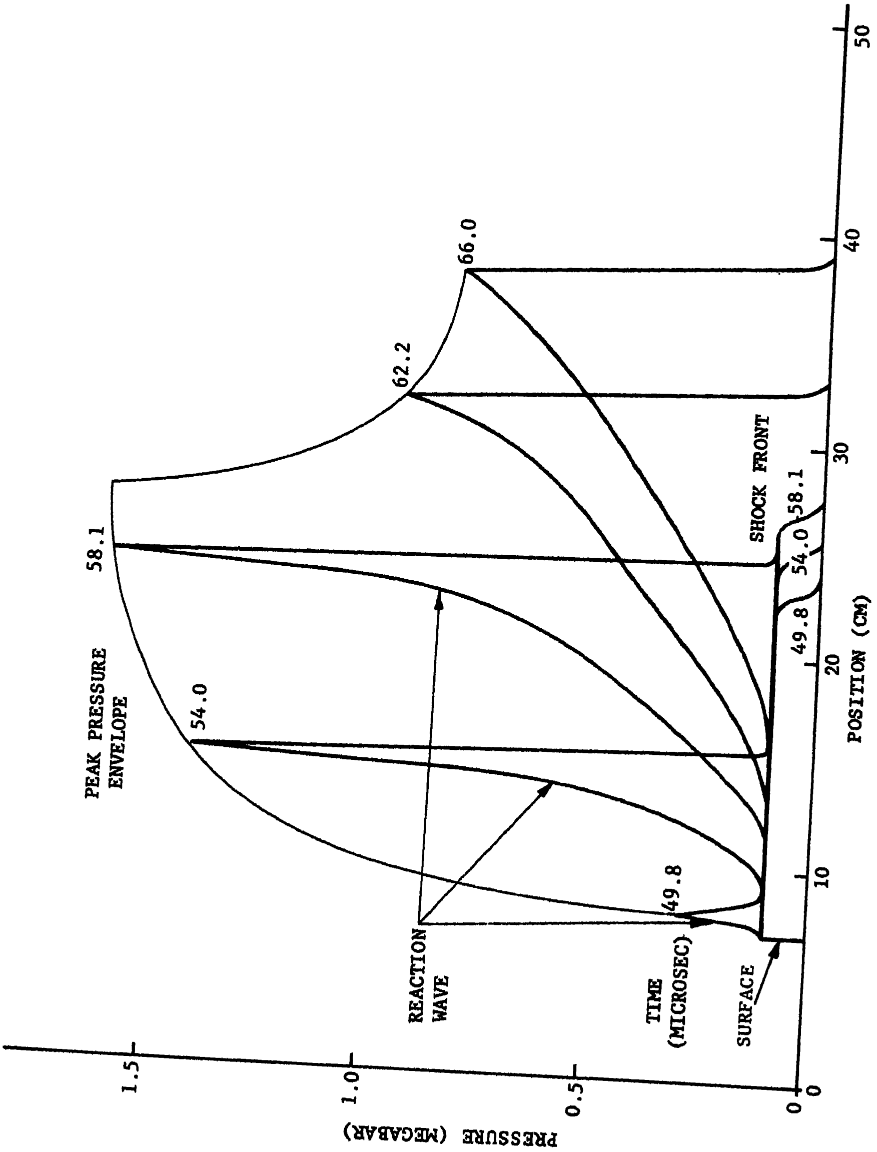

Fig. 1 Growth of detonation in reactive material

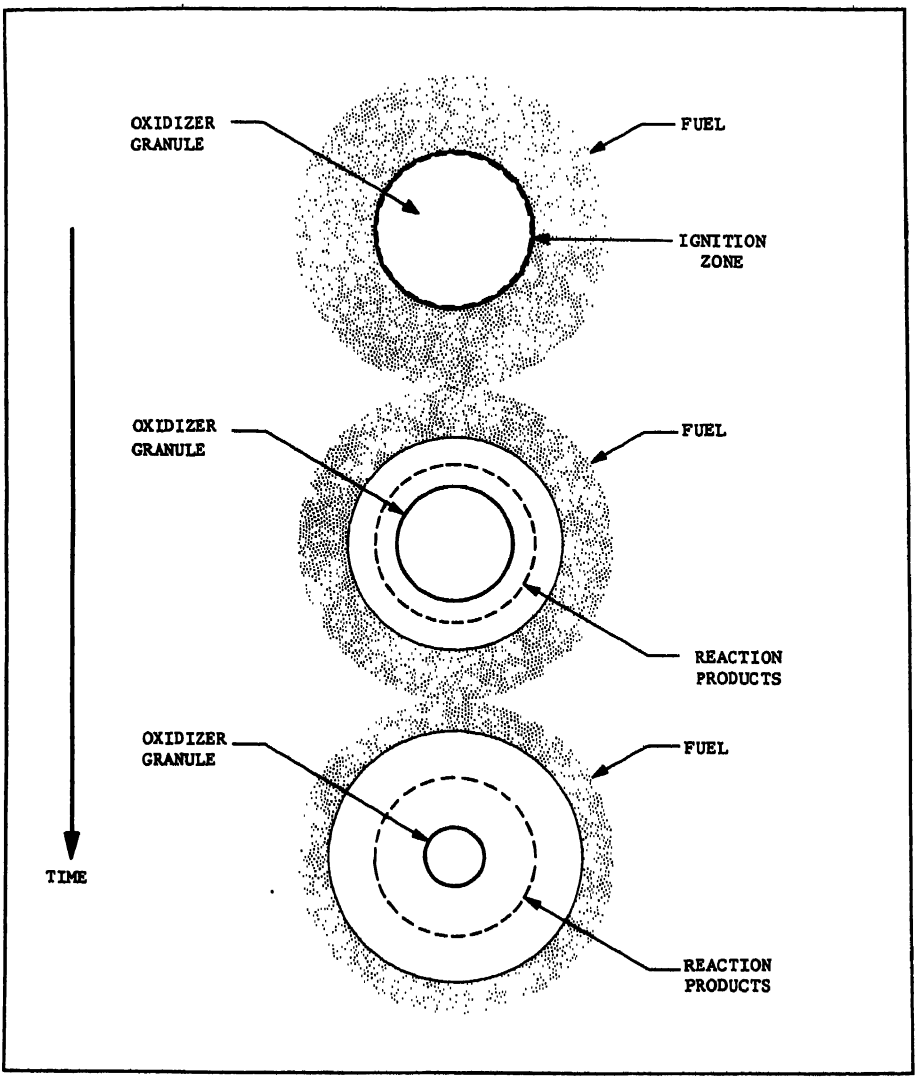

Fig. 2 Burning of an oxidizer granule surrounded by fuel

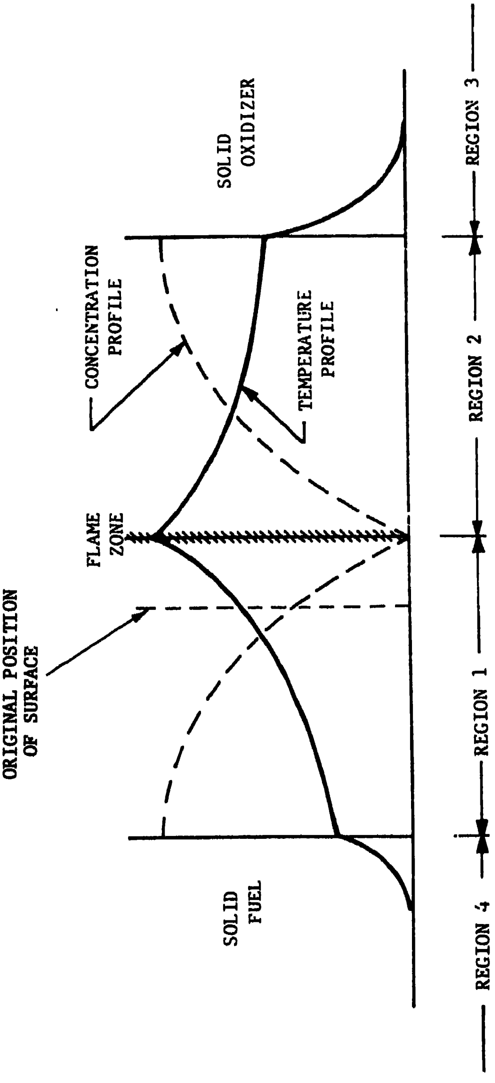

Fig. 3 One-dimensional model for combustion of oxidizer granule surrounded by fuel

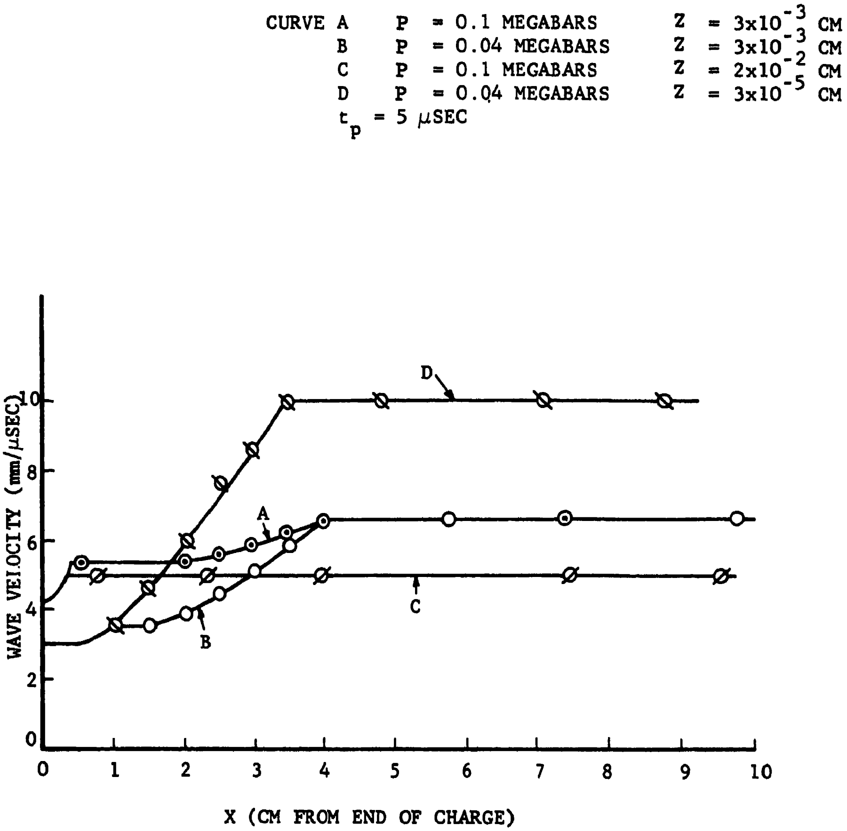

Fig. 4 Initiation and growth of detonation as a function of grain size

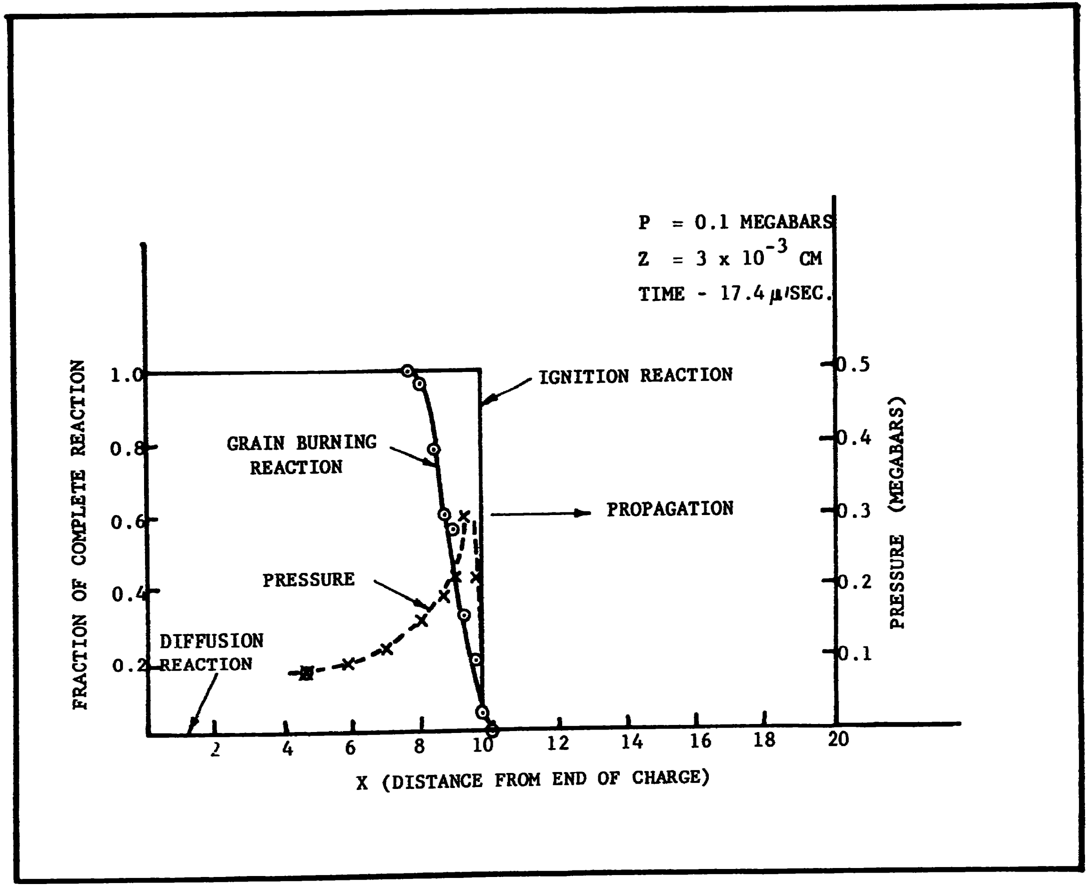

Fig. 5 Reaction profile through detonation wave

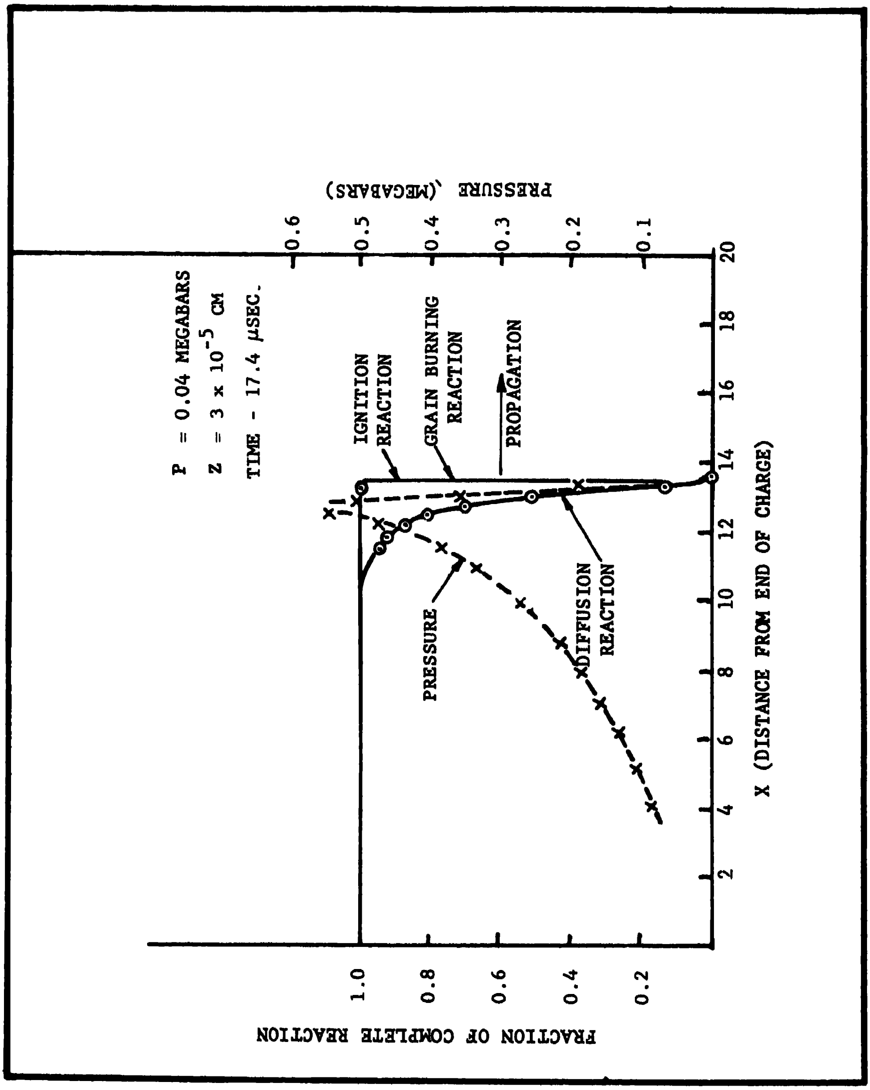

Fig. 6 Reaction profiles through detonation wave

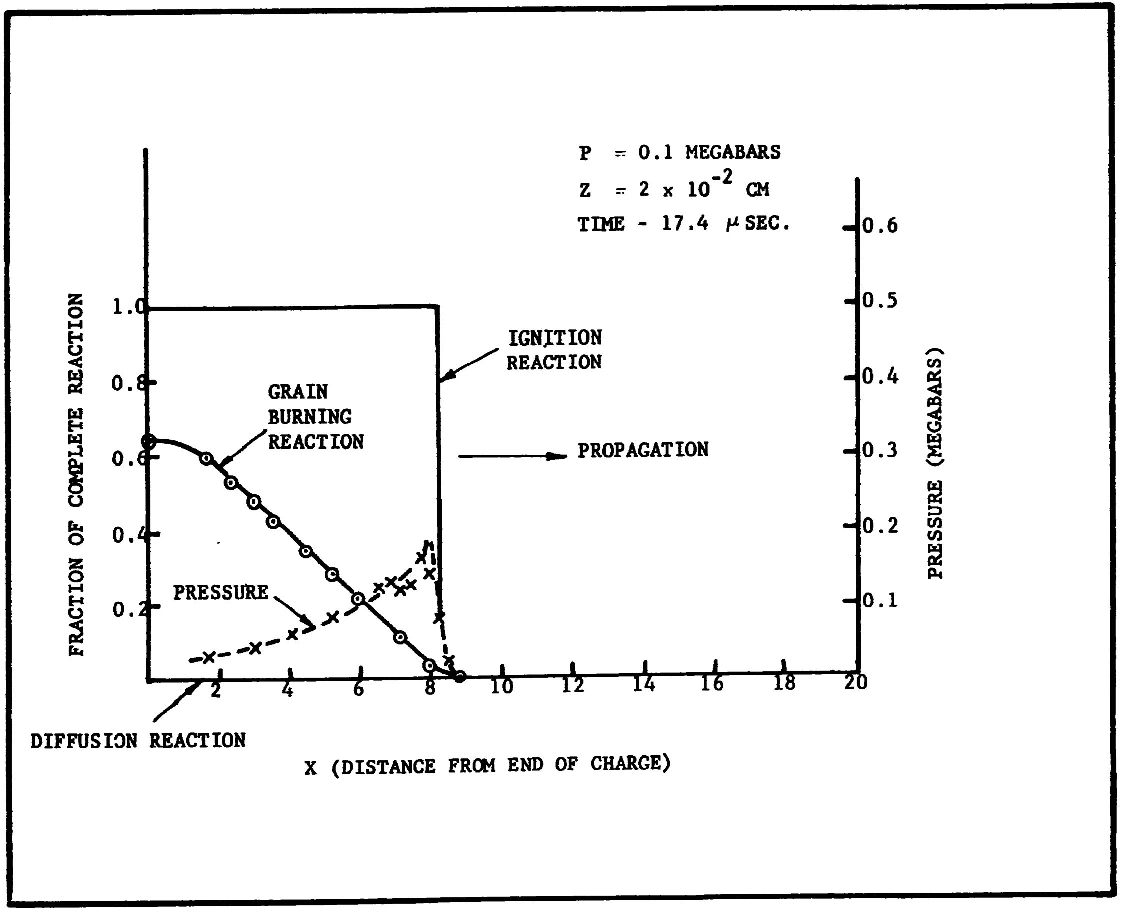

Fig. 7 Reaction profiles through detonation wave

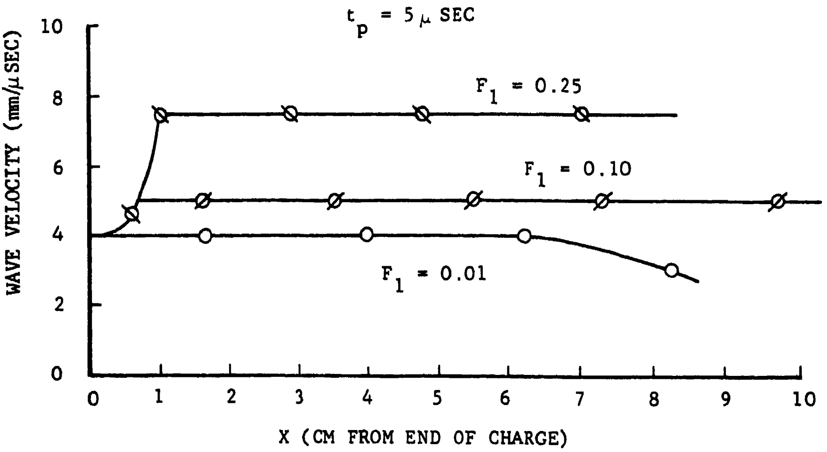

Fig. 8 Initiation and growth of detonation as a function of F_1

DETONATIONS IN DILUTE SPRAYS

F. A. Williams

Harvard University, Cambridge, Mass.

ABSTRACT

Previously developed conservation equations for mixtures of reacting gases and liquid droplets are applied to the study of properties of detonations in sprays. The modified forms of the conservation equations which appear to be most appropriate for studying detonations are presented. The Rankine-Hugoniot equations for spray detonations are derived and analyzed in detail. It is shown that, compared with a gaseous detonation with the same total heat release per unit mass, a Chapman-Jouguet detonation in a spray travels at a slightly higher Mach number with a pressure ratio that is roughly 10% larger.

INTRODUCTION

Detonations in mixtures of combustible gases have been studied extensively. The Rankine-Hugoniot equations relating properties on the upstream and downstream sides of steady-state gaseous detonations have long been known (1-3),[1] and the von Neumann-Zeldovich-Doring theory of the structure of these waves (see Refs. 2, 3) has recently been improved by investigations initiated by Hirschfelder (4). However, it appears that no theoretical studies or results of well-controlled experiments on detonations in sprays have been reported in the literature. In view of recent success in stabilizing gaseous detonations (5, 6) and the fact that fuel is injected as a liquid in practical combustion chambers, it would seem that questions concerning the existence and properties of detonations in sprays are of basic importance in determining whether an operational propulsive device based on a standing detonation principle can be developed. This paper is principally devoted to a theoretical analysis of the Rankine-Hugoniot equations

---

F.A. WILLIAMS is an Assistant Professor in Engineering and Applied Physics. Paper presented at the ARS Propellants, Combustion, and Liquid Rockets Conference, Palm Beach, Fla., April 26-28, 1961.

[1] Numbers in parentheses indicate References at end of paper.

for steady-state detonation in dilute sprays; investigations of the existence, structure, and stability of spray detonations are planned for the future.

The background material used in the present study has been given in Ref. 7; only dilute sprays will be considered in the present paper, since most hydrocarbon fuel sprays in air are dilute (as defined in Ref. 7)[2] whenever the mixture is within the rich flammability limit. In the section on governing equations, the basic conservation equations (7) are cast into forms that appear to be most useful for studying spray detonations. The Rankine-Hugoniot relations are derived in the section on general Rankine-Hugoniot equations, and analogies with the corresponding expressions for gaseous detonations are discussed in the section on comparison with purely gaseous detonations.

GOVERNING EQUATIONS

In the absence of sources of droplets and droplet collisions, the basic equations governing the steady-state motion of dilute sprays (7) may be written in the form

$$\frac{\partial}{\partial r}(R_j f_j) + \nabla_x \cdot (\vec{v} f_j) + \nabla_v \cdot (\vec{F}_j f_j) = 0, \quad j = 1,\ldots,M \qquad [1]$$

$$\nabla_x \cdot [\rho_f(\vec{u} + \vec{U}_k) Y_k] =$$

$$\omega_k - \sum_{j=1}^{M} \iint \rho_{l,j}\, 4\pi r^2\, R_j \epsilon_{k,j} f_j \, dr d\underset{\sim}{v}, \quad k = 1,\ldots,N \qquad [2]$$

$$\nabla_x \cdot [\rho_f \vec{u} + \sum_{j=1}^{M} \iint \rho_{l,j} \frac{4}{3}\pi r^3 \vec{v} f_j \, dr d\underset{\sim}{v}] = 0 \qquad [3]$$

$$\nabla_x \cdot [\rho_f(\vec{u}\vec{u}) +$$

$$\sum_{j=1}^{M} \iint \rho_{l,j} \frac{4}{3}\pi r^3 (\vec{v}\vec{v}) f_j \, dr d\underset{\sim}{v} + p\underline{\underline{U}} + \underline{\underline{T}}] = 0 \qquad [4]$$

---

[2] The ratio of the volume occupied by liquid to the volume occupied by gas is small compared to unity.

$$\nabla_x \cdot [\rho_f \vec{u}(h_f + \frac{u^2}{2}) +$$

$$\sum_{j=1}^{M} \iint \rho_{\ell,j} \frac{4}{3} \pi r^3 \vec{v}(h_{\ell,j} + \frac{v^2}{2}) f_j \, dr d\underset{\sim}{v} + \vec{q} + \underline{\underline{\tau}} \cdot \vec{u}] = 0 \qquad [5]$$

and

$$p = \rho_f \mathbb{R} T_f \sum_{K=1}^{N} (Y_k / W_k) \qquad [6]$$

where the notation is the same as that defined in Ref. 7 and is restated in the Nomenclature.

Eq. 1 is the spray conservation equation, which is merely a statistical rule for counting droplets. Eq. 2 expresses the conservation of mass of chemical species k in the gas; the terms on the right-hand side of Eq. 2 account for the production of species k by homogeneous gaseous reactions and by heterogeneous processes, respectively. Eqs. 3, 4, and 5 are, respectively, the over-all mass, momentum, and energy conservation equations for the gas-droplet mixture. The ideal gas equation of state is given in Eq. 6. The asymmetries with respect to liquid and gas in Eqs. 1-6 arise from the spray. (The equation of state of the liquid is unimportant in dilute sprays.)

Some of the relations given in Eqs. 1-6 are not written in the same form as the corresponding expressions in Ref. 7. However, the form given here appears to be the most convenient one for the present application. Demonstration of how Eqs. 1-6 can be derived from Ref. 7 would seem unnecessary because the present forms actually might have been written down a priori; if the definitions of the symbols in Eqs. 1-5 are used to translate these equations into verbal statements, then these statements are the phenomenological conservation laws. Nevertheless, for the sake of completeness, a formal derivation of Eqs. 1-6 from Ref. 7 is outlined (and illustrated in detail for Eq. 5) in the Appendix.

In considering plane detonations, the one-dimensional forms of Eqs. 2-5 are appropriate ($\vec{x} \rightarrow x$, $\nabla_x \rightarrow d/dx$, $\vec{u} \rightarrow u$, $\vec{v} \rightarrow v$, $\vec{F}_j \rightarrow F_j$, $\vec{U}_k \rightarrow U_k$, $\vec{q} \rightarrow q_x$, $\underline{\underline{\tau}} \rightarrow \tau_{xx}$, $\underline{\underline{U}} \rightarrow 1$), and Eqs. 3-5 may be integrated immediately, showing that the quantities inside the brackets in these three equations are constants. These constants will be denoted by m, P, and E, respectively.

GENERAL RANKINE-HUGONIOT EQUATIONS

The general equations relating properties on the upstream (subscript o) and downstream (subscript ∞) sides of the detonation wave may be obtained formally from Eq. 6 and the integrated forms of Eqs. 3-5 by using the fact that conditions are spacially uniform at positions o and ∞. Since $\vec{U}_k$, $\vec{q}$, and $\underline{\underline{T}}$ are proportional to gradients of the flow variables, these quantities are zero at positions o and ∞, and it is found from Eqs. 3-6, respectively, that

$$\dot{m} = \rho_{f\infty} u_\infty + \sum_{j=1}^{M} \iint \rho_{\ell,j\infty} \frac{4}{3} \pi r^3 \, v f_{j\infty} \, drdv$$

$$= \rho_{fo} u_o + \sum_{j=1}^{M} \iint \rho_{\ell,jo} \frac{4}{3} \pi r^3 \, v f_{jo} \, drdv \qquad [7]$$

$$P = \rho_{f\infty} u_\infty^2 + \sum_{j=1}^{M} \iint \rho_{\ell,j\infty} \frac{4}{3} \pi r^3 \, v^2 f_{j\infty} \, drdv + p_\infty$$

$$= \rho_{fo} u_o^2 + \sum_{j=1}^{M} \iint \rho_{\ell,jo} \frac{4}{3} \pi r^3 \, v^2 f_{jo} \, drdv + p_o \qquad [8]$$

$$E = \rho_{f\infty} u_\infty (h_{f\infty} + \frac{u_\infty^2}{2}) +$$

$$\sum_{j=1}^{M} \iint \rho_{\ell,j\infty} \frac{4}{3} \pi r^3 \, v(h_{\ell,j\infty} + \frac{v^2}{2}) f_{j\infty} \, drdv$$

$$= \rho_{fo} u_o \, (h_{fo} + \frac{u_o^2}{2}) +$$

$$\sum_{j=1}^{M} \iint \rho_{\ell,jo} \frac{4}{3} \pi r^3 \, v(h_{\ell,jo} + \frac{v^2}{2}) f_{jo} \, drdv \qquad [9]$$

and[3]

$$p_\infty/[\rho_{f\infty}T_{f\infty}\sum_{k=1}^{N}(Y_{k\infty}/W_k)] = p_o/[\rho_{fo}T_{fo}\sum_{k=1}^{N}(Y_{ko}/W_k)] \qquad [10]$$

From Eq. 2 it follows that $\omega_{ko} = 0$, $\omega_{k\infty} = 0$, $R_{jo} = 0$, and $R_{j\infty} = 0$. In general for a detonation propagating at a known velocity into a spray with known properties, Eqs. 7-10 plus the equilibrium conditions $\omega_{k\infty} = 0$, $R_{j\infty} = 0$ and the thermodynamic properties of the system determine completely all flow variables downstream.

In physically realistic detonations in dilute sprays, all droplets will vaporize ($f_{j\infty} = 0$); initially, all droplets will have essentially the same velocity as the gas ($f_{jo} \sim \delta(v - u_o)$ with $\delta \equiv$ Dirac delta function); and the initial enthalpy per unit mass $h_{\ell,j}$ of droplets of any type will be independent of the droplet radius. Eqs. 7-9 then simplify considerably, yielding

$$\rho_{f\infty}u_\infty = (\rho_{fo} + \sum_{j=1}^{M}\rho_{s,jo})u_o \qquad [11]$$

$$\rho_{f\infty}u_\infty^2 + p_\infty = (\rho_{fo} + \sum_{j=1}^{M}\rho_{s,jo})u_o^2 + p_o \qquad [12]$$

$$\rho_{f\infty}u_\infty(h_{f\infty} + \frac{u_\infty^2}{2}) = \rho_{fo}u_o(h_{fo} + \frac{u_o^2}{2}) + \sum_{j=1}^{M}\rho_{s,jo}u_o(h_{\ell,jo} + \frac{u_o^2}{2}) \qquad [13]$$

respectively, where the spray densities are defined by

$$\rho_{s,j} \equiv \iint \rho_{\ell,j}\,\frac{4}{3}\pi r^3 f_j \,drdv, \quad j = 1,\ldots M \qquad [14]$$

---

[3] If the gaseous constituents of the system do not obey the ideal gas law, then Eq. 10 is, of course, replaced by the actual equation of state of the gas.

If, further, $\rho_s \equiv \sum_{j=1}^{M} \rho_{s,j}$, the total density is defined as $\rho \equiv \rho_f + \rho_s$, the mass flux fraction of spray j is defined as $Z_j \equiv \iint \rho_{\ell,j} (\frac{4}{3}) \pi r^3 f_j v \, dr dv / \dot{m}$, and $Z \equiv \sum_{j=1}^{M} Z_j$, then Eqs. 10-13 become

$$p_\infty / [\rho_\infty T_{f\infty} \sum_{k=1}^{N} (Y_{k\infty}/W_k)] = p_o / [\rho_o (1 - Z_o) T_{fo} \sum_{k=1}^{N} (Y_{ko}/W_k)] \quad [15]$$

$$\rho_\infty u_\infty = \rho_o u_o \quad [16]$$

$$\rho_\infty u_\infty^2 + p_\infty = \rho_o u_o^2 + p_o \quad [17]$$

$$h_{f\infty} + \frac{u_\infty^2}{2} = (1 - Z_o) h_{fo} + \sum_{j=1}^{M} Z_{jo} h_{\ell,jo} + \frac{u_o^2}{2} \quad [18]$$

which, except for the factor $(1 - Z_o)$ in Eq. 15, are essentially the same as the Rankine-Hugoniot equations for an ordinary ideal gas mixture. The Chapman-Jouguet condition

$$u_\infty^2 = [(\partial p / \partial \rho_f)_{S, Y_k = Y_{k,e}}]_\infty$$

where S is entropy and $Y_{k,e}$ is the value of Y_k at chemical equilibrium, may be added to Eqs. 15-18 in order to determine the detonation velocity of Chapman-Jouguet waves.

COMPARISON WITH PURELY GASEOUS DETONATIONS

To illustrate the properties of Eqs. 15-18 in greater detail, attention may be focused on the special case in which the initial and final average molecular weights of the gas are equal $[\sum_{k=1}^{N} (Y_{k\infty}/W_k) = \sum_{k=1}^{N} (Y_{ko}/W_k)]$ and the specific heats of all gaseous species are constant and equal over a temperature range including T_{fo}, $T_{f\infty}$, and a standard reference temperature T^o. Denoting the common specific heat of all species by c_p, the relation

$$h_f = \sum_{k=1}^{N} [h_k^o + c_p(T_f - T^o)]Y_k \qquad [19]$$

is then valid, where h_k^o is the standard enthalpy of formation per unit mass for gaseous species k at temperature T^o. In view of Eq. 19 and the identity $\sum_{k=1}^{N} Y_k = 1$, Eq. 18 becomes

$$c_p T_{f\infty} + \frac{u_\infty^2}{2} = c_p(1 - Z_o)T_{fo} + \frac{u_o^2}{2} + Q \qquad [20]$$

where

$$Q \equiv \sum_{j=1}^{M} Z_{jo} h_{\ell,jo} + \sum_{k=1}^{N} [h_k^o + c_p(T_{fo} - T^o)]\,[Y_{ko}(1 - Z_o) - Y_{k\infty}]$$

$$+ Z_o c_p T_{fo} \equiv \hat{Q} + Z_o c_p T_{fo} \qquad [21]$$

equals $Z_o c_p T_{fo}$ plus the total heat released per unit mass of mixture $\hat{Q}$.

The purpose of defining Q as in Eq. 21 is to make Eqs. 15-17 plus 20 formally identical to the Rankine-Hugoniot equations for purely gaseous detonations in an ideal gas with constant specific heats. Explicitly, if $u' \equiv u$, $\rho' \equiv \rho$, $p' \equiv p$, $T' \equiv (1 - Z)T_f$, and $Q' \equiv Q$, then Eqs. 15-17 and 20 become

$$p'_\infty/(\rho'_\infty T'_\infty) = p'_o/(\rho'_o T'_o)$$

$$\rho'_\infty u'_\infty = \rho'_o u'_o$$

$$\rho'_\infty u'^2_\infty + p'_\infty = \rho'_o u'^2_o + p'_o$$

$$c_p T'_\infty + u'^2_\infty/2 = c_p T'_o + u'^2_o/2 + Q'$$

which are the Rankine-Hugoniot equations for a detonation in an ideal gas with constant heat capacity c_p, density ρ', pressure p', temperature T', velocity u', and total heat release per unit mass Q'. Thus it is clear that the entire interpretation of these ideal gas relations (1-3) may be transcribed for the present case of spray detonations.

Instead of translating the discussion and analysis of Rankine-Hugoniot equations for ideal gases given elsewhere in the literature (e.g., in Refs. 1-3), a few of the more important results that can be obtained in this manner will be stated. For the detonation branch of the spray Hugoniot curve it can be shown that

$$\frac{\rho_o}{\rho_\infty} = \frac{u_\infty}{u_o} = \Big\{(H + 1)(\gamma M_\infty^2 + 1) - [H^2(\gamma M_\infty^2 + 1)^2 + 2H(\gamma M_\infty^4 + 1) + (M_\infty^2 - 1)^2]^{1/2}\Big\}/[2 + (\gamma - 1)M_\infty^2] \qquad [22]$$

$$\frac{T_{f\infty}}{(1 - Z_o)T_{fo}} = \left(\frac{u_\infty}{u_o}\right)^2 / \left[\left(\frac{u_\infty}{u_o}\right)(\gamma M_\infty^2 + 1) - \gamma M_\infty^2\right] = \frac{p_\infty}{p_o}\,\frac{u_\infty}{u_o} = \frac{M_o^2}{M_\infty^2(1 - Z_o)}\left(\frac{u_\infty}{u_o}\right)^2 \qquad [23]$$

where a dimensionless measure of the effective heat of reaction is

$$H \equiv Q/[(1 - Z_o)c_pT_{fo}] = (\hat{H} + Z_o)/(1 - Z_o) \qquad [24]$$

$[\hat{H} \equiv \hat{Q}/(c_pT_{fo})]$, the specific heat ratio of the gas is

$$\gamma \equiv c_p/[c_p - \mathcal{R}\sum_{K=1}^{N}(Y_{ko}/W_k)] \qquad [25]$$

and the Mach number is

$$M \equiv u/[(\gamma - 1)c_pT_f]^{1/2} \qquad [26]$$

For Chapman-Jouguet detonations ($M_\infty = 1$), it can be shown from Eqs. 22 and 23 that

$$\frac{\rho_o}{\rho_\infty} = \frac{u_\infty}{u_o} = H + 1 - [H^2 + (\frac{2}{\gamma+1}) H]^{1/2} \qquad [27]$$

$$\frac{p_\infty}{p_o} = \gamma\left\{H + \frac{1}{\gamma} + [H^2 + (\frac{2}{\gamma+1})H]^{1/2}\right\} \qquad [28]$$

$$\frac{T_{f\infty}}{T_{fo}} = (1 - Z_o)(\gamma-1)\left\{(\frac{\gamma^2+1}{\gamma^2-1})H + \frac{1}{\gamma-1} + [H^2 + (\frac{2}{\gamma+1})H]^{1/2}\right\} \qquad [29]$$

$$M_o^2 = (1 - Z_o)(\gamma+1)\left\{H + \frac{1}{\gamma+1} + [H^2 + (\frac{2}{\gamma+1})H]^{1/2}\right\} \qquad [30]$$

The predictions of Eqs. 27-30 are plotted in Figs. 1-4 for various values of the dimensionless actual total heat release $\hat{H}$ with $\gamma = 1.4$. Since H increases as Z_o increases for a given total heat release per unit mass, it follows from Eqs. 27-30 that a Chapman-Jouguet detonation in a spray propagates at a slightly higher Mach number M_o and has a higher pressure and temperature downstream than does a gaseous detonation with the same heat release and the same initial pressure, temperature, and gas density. From Figs 1-4, however, it is seen that for reasonable values of $\hat{H}$ and Z_o these differences are almost negligibly small for all quantities except p_∞/p_o, which may be increased by roughly 10%.

It should be emphasized that, since the present comparison refers to a constant $\hat{H}$, these differences result only from the changes in the equation of state and in the effective heat of reaction caused by the presence of the droplets; if comparison is made between systems involving gaseous and liquid (spray) forms of the same fuel at the same initial temperature, then the decrease in the total heat release caused by the latent heat of vaporization of the fuel tends to counteract these effects.

CONCLUSION

The Rankine-Hugoniot equations for detonations in dilute sprays differ from those for gaseous detonations mainly in the effective heat of reaction and the equation of state. In ideal systems these two sets of equations become identical if the definitions of the temperature and the heat of reaction are suitably modified for the spray.

APPENDIX: DERIVATION OF CONSERVATION EQUATIONS

In the section on governing equations the spray equation, the gaseous species conservation equation, and the ideal gas equation of state (Eqs. 1, 2, and 6, respectively) are in exactly the same form used in Ref. 7. Eq. 3 may be obtained from the over-all mass conservation equation of Ref. 7 by multiplying Eq. 1 by $\rho_{\ell,j}(4/3)\pi r^3$, integrating over r and $\vec{v}$, integrating the first term by parts, and using the facts that $\rho_{\ell,j}(4/3)\pi r^3 \vec{F}_j f_j$ rapidly approaches zero as $|\vec{v}| \to \infty$ and $\rho_{\ell,j}(4/3)\pi r^3 R_j f_j$ goes to zero as $r \to \infty$ or $r \to 0$ in order to solve for $\iint \rho_{\ell,j}\, 4\pi r^2 R_j f_j \, dr d\underset{\sim}{v}$. Eq. 4 is derived from the momentum conservation equations of Ref. 7 by multiplying Eq. 1 by $\rho_{\ell,j}(4/3)\pi r^3 \vec{v}$ and performing similar integrations using Eq. 3 and the identity $\nabla_x \cdot [\rho_f(\vec{u}\vec{u})] = \rho_f \vec{u} \cdot \nabla_x \vec{u} + \vec{u} \cdot \nabla_x(\rho_f \vec{u})$ and solving for

$$\sum_{j=1}^{M} \iint \rho_{\ell,j}(4/3)\pi r^3 \vec{F}_j f_j \, dr d\underset{\sim}{v}.$$

In order to derive Eq. 5 from the energy conservation equation given by Williams (Eq. 22 of Ref. 7) it is necessary to make the additional hypothesis that total enthalpy is neither created nor destroyed in droplet surface layers; carrying out operations similar to those described above and using a treatment of the type given in the second section of Ref. 8 for a less general case then yields Eq. 5, as shown in the following paragraph.

Multiplying Eq. 1 by $\rho_{\ell,j}(4/3)\pi r^3 (h_{\ell,j} + \frac{v^2}{2})$ and integrating over r and $\vec{v}$ yields

$$
\begin{aligned}
&\iint \frac{\partial}{\partial r}\left[\rho_{\ell,j}\,\frac{4}{3}\,\pi r^3\left(h_{\ell,j}+\frac{v^2}{2}\right)R_j f_j\right]dr\,d\underset{\sim}{v}\;- \\
&\qquad\iint \rho_{\ell,j}\,4\pi r^2\left(h_{\ell,j}+\frac{v^2}{2}\right)R_j f_j\;dr\,d\underset{\sim}{v} \\
&-\iint \rho_{\ell,j}\,\frac{4}{3}\,\pi r^3\,R_j\,\frac{\partial h_{\ell,j}}{\partial r}\,f_j\;dr\,d\underset{\sim}{v}\;+ \\
&\qquad\nabla_x\cdot\iint \rho_{\ell,j}\,\frac{4}{3}\,\pi r^3\left(h_{\ell,j}+\frac{v^2}{2}\right)\vec{v}\,f_j\;dr\,d\underset{\sim}{v} \\
&-\iint \rho_{\ell,j}\,\frac{4}{3}\,\pi r^3\,\vec{v}\cdot\nabla_x h_{\ell,j}f_j\;dr\,d\underset{\sim}{v}\;+ \\
&\qquad\iint \nabla_v\cdot\left[\rho_{\ell,j}\,\frac{4}{3}\,\pi r^3\left(h_{\ell,j}+\frac{v^2}{2}\right)\vec{F}_j f_j\right]\;dr\,d\underset{\sim}{v} \\
&-\iint \rho_{\ell,j}\,\frac{4}{3}\,\pi r^3\,\vec{F}_j\cdot\nabla_v h_{\ell,j}f_j\;dr\,d\underset{\sim}{v}\;- \\
&\qquad\iint \rho_{\ell,j}\,\frac{4}{3}\,\pi r^3\,\vec{v}\cdot\vec{F}_j f_j\;dr\,d\underset{\sim}{v} = 0 \qquad [\text{A-1}]
\end{aligned}
$$

after performing a few integrations by parts and using the identity $\nabla_v\cdot(v^2/2) = \vec{v}$.[4] The first and sixth terms in Eq. A-1 vanish by virtue of the conditions at $r = 0$, $r = \infty$, and $|\vec{v}| = \infty$. If there is no production of total enthalpy in the droplet surface layer, then from the definition of h_j given in Ref. 7 ($h_j \equiv$ total enthalpy added to the gas per unit mass of material vaporized from a droplet of kind j) it follows that

---

[4] For simplicity, $\rho_{\ell,j}$ is assumed constant.

$$\rho_{\ell,j}\, 4\pi r^2\, R_j h_j = \frac{d}{dt}\left(\rho_{\ell,j}\, \frac{4}{3}\, \pi r^3 h_{\ell,j}\right) =$$

$$\left(R_j \frac{\partial}{\partial r} + \vec{v}\cdot\nabla_x + \vec{F}_j\cdot\nabla_v\right)\left(\rho_{\ell,j}\, \frac{4}{3}\, \pi r^3 h_{\ell,j}\right)$$

$$= \rho_{\ell,j}\, 4\pi r^2 R_j h_{\ell,j} + \rho_{\ell,j}\, \frac{4}{3}\pi r^3 \left(R_j \frac{\partial h_{\ell,j}}{\partial r} + \vec{v}\cdot\nabla_x h_{\ell,j} + \vec{F}_j\cdot\nabla_v h_{\ell,j}\right) \qquad [A-2]$$

from which it is seen that the third, fifth, and seventh terms in Eq. A-1 together reduce to $\iint \rho_{\ell,j}\, 4\pi r^2 (h_{\ell,j} - h_j) R_j f_j \, dr d\underset{\sim}{v}$. Hence, Eq. A-1 may be written in the form

$$\iint \rho_{\ell,j}\, 4\pi r^2\, R_j \left(h_j + \frac{v^2}{2}\right) f_j \; dr d\underset{\sim}{v} + \iint \rho_{\ell,j}\, \frac{4}{3}\, \pi r^3\, \vec{F}_j \cdot \vec{v}\, f_j \; dr d\underset{\sim}{v}$$

$$= \nabla_x \cdot \iint \rho_{\ell,j}\, \frac{4}{3}\, \pi r^3 \left(h_{\ell,j} + \frac{v^2}{2}\right) \vec{v}\, f_j \; dr d\underset{\sim}{v} \qquad [A-3]$$

Eq. 5 is finally obtained by summing Eq. A-3 over j and substituting the result into the right-hand side of the expression

$$\nabla_x \cdot \left[\rho_f \vec{u}\left(h_f + \frac{u^2}{2}\right)\right] = -\nabla_x \cdot \vec{q} - \nabla_x \cdot \left(\underline{\underline{\tau}} \cdot \vec{u}\right) -$$

$$\sum_{j=1}^{M} \iint \rho_{\ell,j}\, \frac{4}{3}\, \pi r^3 \left(\vec{F}_j \cdot \vec{v}\right) f_j \; dr d\underset{\sim}{v}$$

$$- \sum_{j=1}^{M} \iint \rho_{\ell,j}\, 4\pi r^2\, R_j \left(h_j + \frac{v^2}{2}\right) f_j \; dr d\underset{\sim}{v}, \qquad [A-4]$$

which is Eq. 22 of Ref. 7.

ACKNOWLEDGMENT

This work was supported in part by the National Science Foundation under Research Grant No. 12146.

NOMENCLATURE

$d\underset{\sim}{v}$ = abbreviation for a three-dimensional volume element in velocity space

f = droplet distribution function (the number of droplets at r, $\vec{x}$, $\vec{v}$) per unit range of r, $\vec{x}$ and $\vec{v}$)

$\vec{F}$ = acceleration of an individual droplet at (r, $\vec{x}$, $\vec{v}$)

h_f = enthalpy per unit mass for the gas

h_ℓ = enthalpy per unit mass for a liquid

p = hydrostatic pressure

$\vec{q}$ = heat flux vector (accounting for thermal conduction and the diffusion of chemical enthalpy)

r = droplet radius

R = time rate of increase of r for an individual droplet at (r, $\vec{x}$, $\vec{v}$)

$\mathcal{R}$ = universal gas constant

T_f = temperature of the gas

$\vec{u}$ = (mass average) velocity of the gas

$\underline{\underline{\underline{U}}}$ = unit tensor

$\vec{U}_k$ = diffusion velocity of species k

$\vec{v}$ = velocity vector of a droplet

W_k = molecular weight of species k

$\vec{x}$ = position vector in physical space

Y_k = mass fraction of species k in the gas

$\epsilon_{k,j}$ = mass of species k added to the gas by a droplet of kind j per unit mass of droplet material vaporized

ρ_f = mass of gas per unit volume

ρ_ℓ = specific gravity of liquid

ω_k = mass rate of production of species k by homogeneous gaseous chemical reactions

$\underline{\underline{\underline{\tau}}}$ = shear stress tensor

Symbols such as ($\vec{u}\vec{u}$) represent the dyadic product of the two vectors (i.e., a tensor).

Subscripts

j = identifies droplets of different composition (there are a total of M different droplet compositions)

k = identifies different chemical species in the gas (there are N different chemical species in the gas)

v, x = on the gradient operator ∇ distinguish position and velocity derivatives

REFERENCES

1 S. S. Penner: Chemistry Problems in Jet Propulsion, Pergamon Press, New York, 1957

2 S. S. Penner and B. P. Mullins: Explosions, Detonations, Flammability and Ignition, Pergamon Press, New York, 1959.

3 J. O. Hirschfelder, C. F. Curtiss, and R. B. Bird: Molecular Theory of Gases and Liquids, pp 797-814, John Wiley and Sons, Inc., New York, 1954.

4 J. O. Hirschfelder and C. F. Curtiss: Theory of Detonations - I. Irreversible Unimolecular Reaction, Jour. Chem. Phys., 1958, Vol. 28, pp. 1130-1146.

5 J. A. Nicholls, E. K. Dabora, and R. L. Gealer: Studies in Connection with Stabilized Gaseous Detonation Waves, Seventh International Symposium on Combustion, pp. 766-772, Butterworths Scientific Publications, London, 1958.

6 R. A. Gross: Research on Supersonic Combustion, ARS Jour., Jan. 1959, Vol. 29, pp. 63-64.

7 F. A. Williams: Eighth International Symposium on Combution, Williams and Wilkins Co., Baltimore, 1961 (in press).

8 F. A. Williams: Spray Combustion Theory, Combustion and Flame, 1959, Vol. 3, pp 215-228.

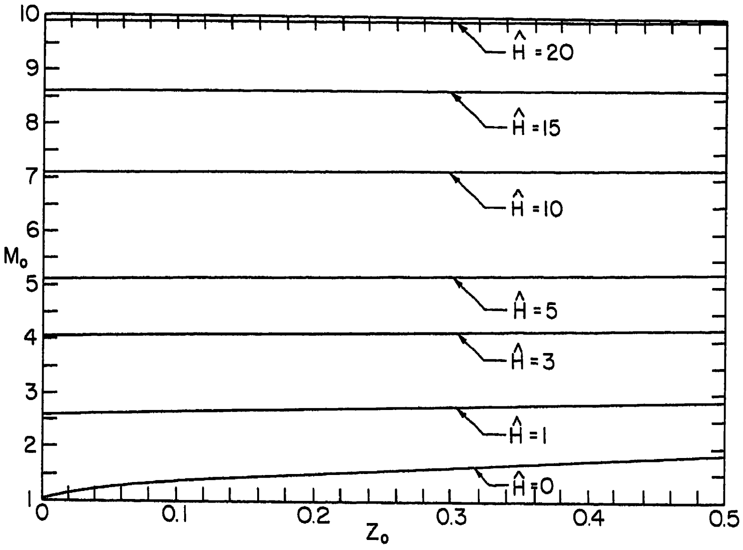

Fig. 1 Dependence of Mach number on mass flux fraction of the spray for Chapman-Jouguet detonations with $\gamma = 1.4$

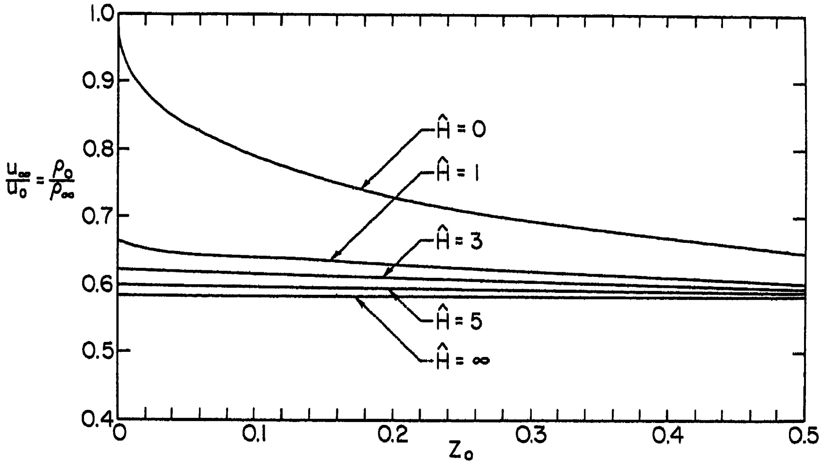

Fig. 2 Dependence of velocity and density ratios on mass flux fraction of spray for Chapman-Jouguet detonations with $\gamma = 1.4$

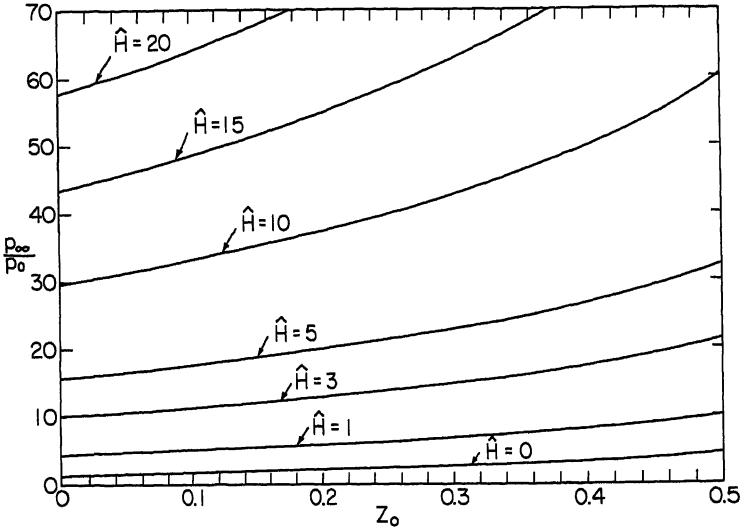

Fig. 3 Dependence of pressure ratio on mass flux fraction of spray for Chapman-Jouguet detonations with $\gamma = 1.4$

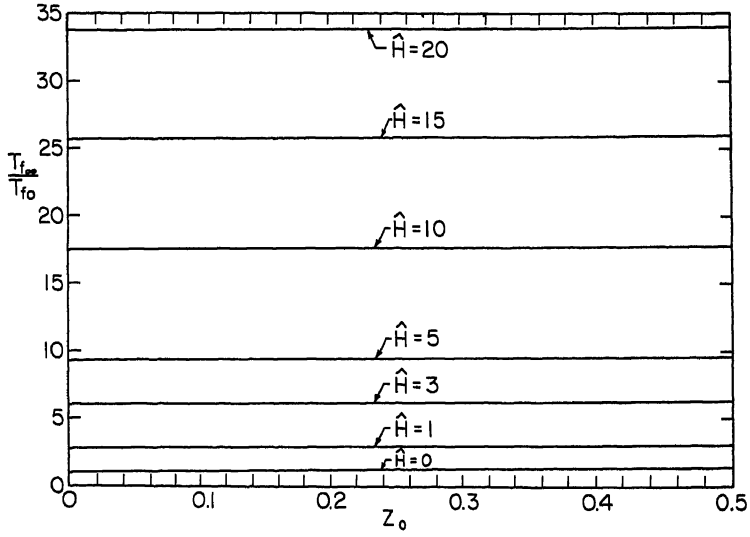

Fig. 4 Dependence of gas temperature ratio on mass flux fraction of spray for Chapman-Jouguet detonations with $\gamma = 1.4$

PART 2

TWO-PHASE FLOW

A. Two-Phase Nozzle Flow

PERTURBATION ANALYSIS OF ONE-DIMENSIONAL HETEROGENEOUS FLOW IN ROCKET NOZZLES

W. D. Rannie

California Institute of Technology, Pasadena, Calif.

ABSTRACT

A perturbation analysis of the velocity and temperature lags in two-phase flow in rocket nozzles is developed and applied to the calculation of specific impulse and other performance characteristics of nozzles of arbitrary shape. Within the limitations of the one-dimensional flow approximation, the analysis is valid for distributions of particle diameters that are in a practical range.

INTRODUCTION

The development of high energy propellants, with products of combustion partially in the form of finely divided particles, has increased interest in the effects of the heterogeneous flows on performance. The particles, swept through the nozzle by gas flow, lag behind the gas in temperature drop as well as velocity increase, both lags degrading performance and partially defeating the purpose of the high energy propellants.

Analysis of the heterogeneous flow in the rocket nozzle is necessarily complex because of the large number of separate parameters required to specify particle characteristics and the nozzle contour. Most previous investigations (e. g., Refs. 1-4) have required numerical procedures at an early stage of the analysis, thus tending to conceal the influence of individual parameters and making necessary a great number of specific calculations. Clearly an analytical solution of the problem, even if complex in form, has the advantage that the

---

W. D. RANNIE is Robert H. Goddard Professor of Jet Propulsion, Daniel and Florence Guggenheim Jet Propulsion Center, Kármán Laboratory of Fluid Mechanics and Jet Propulsion. Submitted for publication to the American Rocket Society, Jan. 3, 1962.

influence of each parameter can be traced relatively easily.

The perturbation procedure developed here is confined to the one-dimensional hydraulic approximation, which is known to be satisfactory for the flow of a homogeneous fluid in a nozzle. The magnitude of the error that is introduced with the same approximation for heterogeneous flow is difficult to estimate, since the boundary conditions appropriate to particles impinging on the nozzle wall are not known. The additional simplifying assumptions, that the particle conductivity is very high compared with the gas and that radiative heat transfer between particles is small, compromise the solution much less seriously.

The perturbation solution requires that velocity and temperature lags be small compared with the velocity and temperature of the unperturbed flow without lag. Although this requirement introduces some restrictions on nozzle shape and particle size, it appears that the method will be valid (as far as the one-dimensional analysis can be valid) for most practical applications. For instance, the error in the perturbation solution ordinarily will be small for particle diameters up to 5×10^{-4} cm, the upper limit depending on nozzle dimensions and shape as well as on the stagnation conditions in the rocket chamber. The range of size of particles under actual operating conditions is not yet firmly established; however, the evidence at hand indicates that the diameters of most of the particles will not exceed the forementioned figure.

The perturbation analysis is formulated in terms of pressure as the independent variable. This choice of independent variable has advantages that do not seem to have been exploited sufficiently in the previous investigations. With pressure as the independent variable, the dependence of nozzle cross-sectional area on axial distance does not appear explicitly in the unperturbed solution with no lag, and hence the area can be chosen arbitrarily in the perturbed solution. With axial distance as the independent variable, the usual choice in earlier investigations, the cross-sectional area appears in the solution without lag as well as in the solution with lag. When lags are introduced, the area dependence on axial distance must be changed to satisfy required throat conditions. Hence direct comparison of the same nozzle shape with and without lag is not possible. With pressure as the independent variable this difficulty does not arise.

The major complication in the analysis is evaluation of the drag and heat transfer between particles and gas. In the Stokes' regime of flow, this is quite simple, but particles satisfying the conditions for Stokes' flow have negligible lags. When the lags are appreciable, the Reynolds number of the relative flow becomes large in the neighborhood of the nozzle throat, and slip flow phenomena become important near the nozzle exit. Both of these effects have strong influence on drag and heat transfer and increase the difficulty of scaling to different conditions and dimensions.

In the sections following, the equations governing the one-dimensional heterogeneous flow are established (cf., also Refs. 3-4) and are put in the most suitable form for perturbation analysis. Solutions for the first and second approximations are obtained, where the first approximation corresponds to flow with no lag. General expressions are derived for the second approximations to the mass flow rate, specific impulse, and thrust for an arbitrary nozzle shape in terms of a single numerical integration. The parameter defining the nozzle contour and the correction parameters for drag and heat transfer outside the Stokes' regime are discussed in some detail. A specific example for particles of a single diameter illustrates the method and forms a basis for estimation of the range of validity and certain general conclusions. A simple means of extending the analysis to a distribution of particle size is derived.

GOVERNING EQUATIONS

Let α be the mass fraction of particles in the heterogeneous mixture, ρ_g the gas density, ρ_s the density of the solid (or liquid) material of the particles, and ρ the density of the mixture. Then

$$\frac{1}{\rho} = \frac{1-\alpha}{\rho_g} + \frac{\alpha}{\rho_s} \qquad [1]$$

where $(1-\alpha)\rho$ is the density of gas per unit volume of mixture and $\alpha\rho$ is the density of particles per unit volume of mixture. The mass fraction of particles in the mixture when both gas and particles have the same velocity (i.e., no lag) will be denoted α_0. In general, $\alpha = \alpha_0$ only at stagnation conditions in the rocket chamber.

Let A denote the area of cross section of the nozzle at any point along its axis, and let $\dot{m}$ be the constant mass flow rate of the mixture. Then the conservation of mass flow rates for gas and particles separately lead to the equations

$$(1-\alpha)\rho u_g A = (1-\alpha_0)\dot{m} \qquad [2]$$

$$\alpha \rho u_s A = \alpha_0 \dot{m} \qquad [3]$$

where u_g is the velocity of the gas and u_s is the velocity of the particles. All particles are assumed to be of the same size and to have the same velocity at any cross section.

The momentum equation for the mixture, neglecting friction on the walls, is

$$\frac{d}{dx}\left[(1-\alpha)\rho u_g A u_g\right] + \frac{d}{dx}\left[\alpha \rho u_s A u_s\right] = -\frac{d}{dx}(pA) + p\frac{dA}{dx}$$

where p is the pressure in the gas and x is the distance along the nozzle axis, positive downstream. Applying Eqs. 2 and 3, the momentum equation becomes

$$(1-\alpha)\rho u_g \frac{du_g}{dx} + \alpha \rho u_s \frac{du_s}{dx} + \frac{dp}{dx} = 0 \qquad [4]$$

This equation is quite general, whatever the force interaction between particles and gas.

The energy equation for steady flow of a homogeneous fluid with no heat addition is

$$\rho A u \left(e + \frac{1}{2}u^2\right) + A p u = \text{constant}$$

where e is the internal energy per unit mass. The corresponding equation for the mixture is

$$(1-\alpha)\rho A u_g \left(e_g + \frac{1}{2}u_g^2\right) + \alpha \rho A u_s \left(e_s + \frac{1}{2}u_s^2\right) + Ap\left[u_g \frac{(1-\alpha)\rho}{\rho_g} + u_s \frac{\alpha \rho}{\rho_s}\right] = \dot{E}_c \qquad [5]$$

where $\dot{E}_c$ is the total rate of energy flow from the chamber. The rate of working of the pressure force per unit area (pu for the homogeneous fluid) must be weighted by the ratio of component volume to mixture volume when applied to components of the mixture. Again, this equation is quite general, whatever the force interaction and heat transfer processes between particles and gas.

The particles will be approximated by small spheres of radius a , and the drag law will be based on Stokes' formula with a correction factor to allow for conditions outside the Stokes' regime of flow. Assuming that the steady state drag law is applicable to the accelerated motion, the force balance for a single particle is represented by

$$\frac{4}{3}\pi a^3 \rho_s u_s \frac{du_s}{dx} = 6\pi a \mu (u_g - u_s)\frac{1}{f_d} - \frac{4}{3}\pi a^3 \frac{dp}{dx} \qquad [6a]$$

where μ is the viscosity of the gas. The second term on the right is the contribution of the pressure gradient in the gas. The factor f_d is the correction factor to the drag and, in general, is a function of Reynolds number and Mach number of the relative flow; $f_d = 1$ in the Stokes' regime. Eq. 6a can be written in more convenient form as

$$u_g - u_s = \frac{2}{9}\;\frac{a^2 \rho_s}{\mu} f_d \left(u_s \frac{du_s}{dx} - \frac{1}{\rho_s}\frac{dp}{dx}\right) \qquad [6b]$$

In the range of Reynolds number where Stokes' formula is applicable, heat is transferred primarily by conduction. The rate at which heat is conducted from a sphere of radius a and temperature T_s to a fluid at temperature T_g far from the sphere is $k(T_s - T_g)/a$ per unit area, where k is the gas conductivity. Hence the heat balance for a single particle is

$$\frac{4}{3}\pi a^3 \rho_s C u_s \frac{dT_s}{dx} = -\frac{k}{a}(T_s - T_g)\,4\pi a^2 \frac{1}{f_k} \qquad [7a]$$

where C is the specific heat of the particle material. The factor f_k is a correction factor similar to f_d and depends on Reynolds number and Mach number in much the same way as f_d. Rearranging Eq. 7a

$$T_g - T_s = \frac{1}{3}\;\frac{a^2 \rho_s}{k} C f_k u_s \frac{dT_s}{dx} \qquad [7b]$$

In most applications the volume occupied by the particles is much smaller than the volume occupied by the gas and can be neglected in comparison. The gas density at stagnation conditions will seldom be larger than 0.4 lb/ft^3; if the particle material has a density of 240 lb/ft^3, for instance, the error in the approximation

$$\rho_g \cong (1-\alpha)\rho \qquad [8]$$

to Eq. 1 is less than one percent with a particle mass fraction α as high as 0.8. Correspondingly small errors are introduced by dropping the second term in the brackets in Eq. 5 and the second term in parentheses in Eq. 6b.

The variable particle mass fraction α may be eliminated from the equations with the relation

$$\alpha u_s = (1-\alpha)\, u_g \frac{\alpha_0}{1-\alpha_0} \qquad [9]$$

obtained from Eqs. 2 and 3. From Eq. 9 and the approximations introduced by Eq. 8, the equations for conservation of mass, momentum, and energy (i.e., Eqs. 2, 4, and 5) become, respectively

$$\rho_g u_g A = (1-\alpha_0)\dot{m} \qquad [10]$$

$$u_g \frac{du_g}{dx} - \alpha_0 u_g\left(\frac{du_g}{dx} - \frac{du_s}{dx}\right) + \frac{1-\alpha_0}{\rho_g}\frac{dp}{dx} = 0 \qquad [11]$$

$$(1-\alpha_0)e_g + \alpha_0 e_s + \frac{1}{2}u_g^2 - \frac{1}{2}\alpha_0\left(u_g^2 - u_s^2\right) + \frac{1-\alpha_0}{\rho_g}p = \frac{\dot{E}_0}{\dot{m}} \qquad [12]$$

The gas will be assumed perfect with constant specific heats; if the gas constant is $\mathcal{R}$, then

$$p = \mathcal{R}\rho_g T_g \qquad [13]$$

and if c_v and c_p are the specific heats of the gas

$$e_g + \frac{p}{\rho_g} = c_v T_g + \mathcal{R} T_g = c_p T_g \qquad [14]$$

It is convenient to introduce the specific heat c_{p_0} for the mixture with particle mass fraction α_0

$$c_{p_0} = (1-\alpha_0)c_p + \alpha_0 c \qquad [15]$$

and a modified gas constant $\mathcal{R}_0$ defined as

$$\mathcal{R}_0 = (1-\alpha_0)\mathcal{R} \qquad [16]$$

Then $\dot{E}_0/\dot{m} = c_{p_0}T_c$, where T_c is the stagnation temperature for the mixture. Further, the dependent variables will be reduced to dimensionless form by the definitions

$$u = \sqrt{\mathcal{R}_0 T_c}\,\phi \qquad T = T_c\,\tau \qquad p = p_c\,\varsigma \qquad [17]$$

where p_c is the stagnation pressure in the chamber. Then Eqs. 10-12 can be written

$$A = \dot{m}\frac{\sqrt{\mathcal{R}_0 T_c}}{p_c}\,\frac{\tau_g}{\varsigma\phi_g} \qquad [18]$$

$$\phi_g \frac{d\phi_g}{d\varsigma} + \frac{\tau_g}{\varsigma} = \alpha_0\phi_g\left(\frac{d\phi_g}{d\varsigma} - \frac{d\phi_s}{d\varsigma}\right) \qquad [19]$$

$$\tau_g + \frac{1}{2}\frac{\mathcal{R}_0}{c_{p_0}}\phi_g^2 = 1 + \frac{1}{2}\alpha_0\frac{\mathcal{R}_0}{c_{p_0}}\left(\phi_g^2 - \phi_s^2\right) + \alpha_0\frac{c}{c_{p_0}}\left(\tau_g - \tau_s\right) \qquad [20]$$

In deriving Eq. 19 from Eq. 11, the independent variable was changed from x to $p = p_c\,\varsigma$. There is no difficulty in doing so because x appears explicitly only in Eq. 11, and there only through the factor dx in the denominator.

The gas viscosity μ occurring in Eq. 6b depends on the gas temperature and will vary appreciably through the length of the nozzle. This variation can be approximated satisfactorily by a power law of the form

$$\mu = \mu_c\left(\frac{T_g}{T_c}\right)^n = \mu_c \tau_g^n \tag{21}$$

where $n \cong 0.6$ for the temperature range of interest. The gas conductivity varies in the same way, since the Prandtl number $P_r = \mu c_p/k$ is very nearly constant in a gas over a wide temperature range; hence it can be assumed that

$$k = \frac{c_p}{P_r}\mu_c \tau_g^n \tag{22}$$

It is convenient to introduce a dimensionless parameter ϵ depending on particle size and stagnation conditions; this parameter is defined by the relation

$$\epsilon = \frac{2}{9} a^2 \frac{\rho_s\sqrt{R_\circ T_c}}{r_t \mu_c} \tag{23}$$

where r_t is the nozzle throat radius. Defining a dimensionless length coordinate ξ along the nozzle axis by

$$x = r_t \xi \tag{24}$$

and another dimensionless constant β by the definition

$$\beta = \frac{3}{2}\frac{C}{c_p}P_r \tag{25}$$

Eqs. 6b and 7b become

$$\phi_g - \phi_s = \epsilon f_d \frac{1}{\tau_g^n} \phi_s \frac{d\phi_s}{d\zeta}\frac{1}{\xi'} \tag{26}$$

$$\tau_g - \tau_s = \epsilon\beta f_k \frac{1}{\tau_g^n} \phi_s \frac{d\tau_s}{d\zeta}\frac{1}{\xi'} \tag{27}$$

where $\xi' = d\xi/d\zeta$. Since A is a prescribed function of ξ, i.e.

$$A = A(\xi) \tag{28}$$

there are now six equations (Eqs. 18-20 and 26-28) for the six unknowns (ϕ_g, ϕ_s, τ_g, τ_s, A, and ξ) as functions of ζ.

FIRST APPROXIMATION: ZERO VELOCITY AND TEMPERATURE LAGS

An examination of Eqs. 26 and 27 shows that for $a \rightarrow 0$ (i.e., $\epsilon \rightarrow 0$), $\phi_g \rightarrow \phi_s$ and $\tau_g \rightarrow \tau_s$, since all other factors in the equations are of order unity. In particular, ξ' is always negative, corresponding to a monotonic pressure drop through the nozzle. Hence, with subscript zero denoting zero lag, Eqs. 26 and 27 reduce to

$$\phi_g = \phi_s = \phi_0 \qquad \tau_g = \tau_s = \tau_0 \tag{29}$$

for sufficiently small particles, and Eqs. 19 and 20 become

$$\phi_0 \phi_0' + \tau_0 / \zeta = 0 \tag{30}$$

$$\tau_0 + \frac{1}{2} \frac{\gamma_0 - 1}{\gamma_0} \phi_0^2 = 1 \tag{31}$$

The ratio of specific heats γ_0 is introduced by analogy with the perfect gas relation from the definition

$$\frac{\gamma_0}{\gamma_0 - 1} = c_{p_0} / R_0 \tag{32}$$

since $c_{p_0} - c_{v_0} = R_0$.

The solution of Eqs. 30 and 31 is well known, and results are listed for future reference:

$$\tau_0 = \zeta^{\frac{\gamma_0}{\gamma_0 - 1}} \tag{33}$$

$$\phi_0 = \sqrt{\frac{\gamma_0}{\gamma_0 - 1}} \left(1 - \zeta^{\frac{\gamma_0 - 1}{\gamma_0}} \right)^{1/2} \tag{34}$$

$$\frac{A'}{A} = - \frac{1 - \frac{\gamma_0 + 1}{2} \zeta^{\frac{\gamma_0 - 1}{\gamma_0}}}{\gamma_0 \zeta \left(1 - \zeta^{\frac{\gamma_0 - 1}{\gamma_0}} \right)} \tag{35}$$

$$\frac{A}{A_t} = \sqrt{\frac{\gamma_0 - 1}{2\gamma_0}} \, \frac{1}{\Gamma_0} \, \frac{1}{\zeta^{1/\gamma_0} \left(1 - \zeta^{\frac{\gamma_0 - 1}{\gamma_0}} \right)^{1/2}} \tag{36}$$

$$A_t = \Gamma_0 \frac{\dot{m} \sqrt{R_0 T_c}}{p_c} \tag{37}$$

$$\Gamma_0 = \frac{1}{\sqrt{\gamma_0}} \left(\frac{\gamma_0 + 1}{2} \right)^{\frac{\gamma_0 + 1}{2(\gamma_0 - 1)}} \tag{38}$$

where A_t is the area of cross section at the throat.

SECOND APPROXIMATION: SMALL VELOCITY AND TEMPERATURE LAGS

As the radius a of the particles is increased, Eqs. 26 and 27 show that the velocity difference $\phi_g - \phi_s$ and the temperature difference $\tau_g - \tau_s$ will increase in absolute value from zero. Expansions in powers of the parameter ϵ proportional to a^2 seem appropriate; hence it is assumed that

$$\phi_g(\zeta) = \phi_0(\zeta) + \epsilon\, \phi_{g_1}(\zeta) + \cdots \qquad [39a]$$

$$\phi_s(\zeta) = \phi_0(\zeta) + \epsilon\, \phi_{s_1}(\zeta) + \cdots \qquad [39b]$$

$$\tau_g(\zeta) = \tau_0(\zeta) + \epsilon\, \tau_{g_1}(\zeta) + \cdots \qquad [39c]$$

$$\tau_s(\zeta) = \tau_0(\zeta) + \epsilon\, \tau_{s_1}(\zeta) + \cdots \qquad [39d]$$

$$\xi(\zeta) = \xi_0(\zeta) + \epsilon\, \xi_1(\zeta) + \cdots \qquad [39e]$$

The criterion for the validity of such expansions is that

$$\frac{\phi_g - \phi_0}{\phi_0} = \epsilon\, \frac{\phi_{g_1}}{\phi_0} << 1 \qquad [40]$$

and corresponding inequalities for the other functions. The parameter ϵ need not be small compared with unity provided that inequalities of the type given by Eq. 40 are satisfied; that is, ϵ is an indicator of a small quantity rather than a small quantity in its own right. The rate of convergence of the expansions in Eqs. 39 and estimates of error in truncating at any particular term can be estimated in a straightforward way when the coefficients of powers of ϵ in the expansion are themselves independent of a. This will be true in the Stokes' regime of flow, where $f_d = f_h = 1$, but outside of this regime, f_d and f_h depend on a and estimates of error become more involved. The analysis here is confined to the second term in the expansions above; confidence in the validity of the results is based on how well inequalities similar to Eq. 40 are satisfied.

Substituting the expansions, Eqs. 39, into Eqs. 26 and 27 and retaining only first order terms in ϵ

$$\phi_{g_1} - \phi_{s_1} = f_d \frac{1}{\tau_0^n} \phi_0 \phi_0' \frac{1}{\xi_0'} \qquad [41]$$

$$\tau_{g_1} - \tau_{s_1} = \beta f_h \frac{1}{\tau_0^n} \phi_0 \tau_0' \frac{1}{\xi_0'} \qquad [42]$$

With these expressions and substitution of the expansions into Eqs. 19 and 20, the second approximation is obtained by equating coefficients of ϵ in the equations to zero, giving

$$(\phi_0 \phi_{g_1})' + \tau_{g_1}/\zeta = \alpha_0 \phi_0 \frac{d}{d\zeta}\left(f_d \frac{1}{\tau_0^n} \phi_0 \phi_0' \frac{1}{\xi_0'}\right) \qquad [43]$$

$$\tau_{g1} + \frac{\gamma_0-1}{\gamma_0}\phi_0\phi_{g1} = \alpha_0\frac{\gamma_0-1}{\gamma_0} f_d \frac{1}{\tau_0^n}\phi_0^2\phi_0'\frac{1}{\xi_0'} + \alpha_0\frac{C}{c_{p_0}}\beta f_h\frac{1}{\tau_0^n}\phi_0\tau_0'\frac{1}{\xi_0'} \qquad [44]$$

Eliminating τ_{g1} between these equations

$$\begin{aligned}
&(\phi_0\phi_{g1})' - \frac{\gamma_0-1}{\gamma_0}\frac{1}{\varsigma}(\phi_0\phi_{g1}) \\
&= \varsigma^{\frac{\gamma_0-1}{\gamma_0}}\frac{d}{d\varsigma}\left(\frac{1}{\varsigma^{\frac{\gamma_0-1}{\gamma_0}}}\phi_0\phi_{g1}\right) \\
&= \tau_0\frac{d}{d\varsigma}\left(\frac{\phi_0\phi_{g1}}{\tau_0}\right) \\
&= \alpha_0\phi_0\frac{d}{d\varsigma}\left(f_d\frac{\phi_0\phi_0'}{\tau_0^n}\frac{1}{\xi_0'}\right) - \alpha_0\frac{\gamma_0-1}{\gamma_0}f_d\frac{\phi_0^2\phi_0'}{\varsigma\tau_0^n}\frac{1}{\xi_0'} - \alpha_0\frac{C}{c_{p_0}}\beta f_h\frac{\phi_0\tau_0'}{\varsigma\tau_0^n}\frac{1}{\xi_0'}
\end{aligned}$$

and integrating by parts

$$\frac{\phi_{g1}}{\phi_0} = \alpha_0 f_d\frac{\phi_0'}{\tau_0^n}\frac{1}{\xi_0'} - \alpha_0\frac{\tau_0}{\phi_0^2}\int_{\varsigma_i}^{\varsigma}\left(f_d\phi_0'^2 + \frac{C}{c_{p_0}}\beta f_h\frac{\tau_0'}{\varsigma}\right)\frac{\phi_0}{\tau_0^{n+1}}\frac{d\varsigma}{\xi_0'} \qquad [45]$$

Substituting this expression for ϕ_{g1}/ϕ_0 into Eq. 44

$$\frac{\tau_{g1}}{\tau_0} = \alpha_0\frac{C}{c_{p_0}}\beta f_h\frac{\phi_0\tau_0'}{\tau_0^{n+1}}\frac{1}{\xi_0'} + \alpha_0\frac{\gamma_0-1}{\gamma_0}\int_{\varsigma_i}^{\varsigma}\left(f_d\phi_0'^2 + \frac{C}{c_{p_0}}\beta f_h\frac{\tau_0'}{\varsigma}\right)\frac{\phi_0}{\tau_0^{n+1}}\frac{d\varsigma}{\xi_0'} \qquad [46]$$

It is assumed that the velocity and temperature lags are zero as the flow enters the convergent section of the nozzle where $\varsigma = \varsigma_i$ and $1/\xi_0' = 0$. Although here the analysis is restricted to this initial condition, there is no particular difficulty in extending it to any prescribed lags at the entrance to the nozzle provided that care is taken in defining p_i correctly. Clearly the pressure is not suitable as an independent variable for ducts of constant cross-sectional area, so calculation of lags in a cylindrical rocket chamber preceding the nozzle must be made in a different way.

It is convenient to introduce new notation to take advantage of similarities in the expressions for ϕ_{g1}/ϕ_0 and τ_{g1}/τ_0. Let $G(\varsigma)$ be defined as

$$G(\varsigma) = -\alpha_0\left(f_d\phi_0'^2 + \frac{C}{c_{p_0}}\beta f_h\frac{\tau_0'}{\varsigma}\right)\frac{\phi_0}{\tau_0^{n+1}} \qquad [47]$$

The function $G(\varsigma)$ is positive since ξ_0' is negative for all values of ς, and the remaining terms are positive. With substitutions from Eqs. 33-38, $\mathcal{G}(\varsigma)$ can be expressed as

$$\mathcal{G}(\varsigma) = \alpha_0 T_0' \left[f_d \varsigma^{\frac{\gamma_0-1}{\gamma_0}} + 2 \frac{\sigma}{c_{p_0}} \beta f_h \left(1-\varsigma^{\frac{\gamma_0-1}{\gamma_0}}\right) \right] \frac{A}{A_t} \frac{1}{\varsigma^{(n+1)\frac{\gamma_0-1}{\gamma_0}}} \left(-\frac{1}{\xi_0'}\right) \quad [48]$$

where the factor A/A_t is introduced directly because its magnitude is more immediately evident than is the equivalent form expressed as a function of ς . Except the factor $1/\xi_0'$, which depends on nozzle shape and will be discussed later, and the factor A/A_t , the only other variable in the expression for $\mathcal{G}$ is $\varsigma^{\frac{\gamma_0-1}{\gamma_0}} = \tau_0$. This quantity usually will have a small range of variation, from slightly less than unity at the nozzle entrance to 0.5 or so at the nozzle exit.

The fractional contribution of heat transfer to the function $\mathcal{G}(\varsigma)$ will be represented by $\psi(\varsigma)$, where

$$\psi(\varsigma) = \frac{2 \frac{\sigma}{c_{p_0}} \beta f_h \left(1-\varsigma^{\frac{\gamma_0-1}{\gamma_0}}\right)}{f_d \varsigma^{\frac{\gamma_0-1}{\gamma_0}} + 2 \frac{\sigma}{c_{p_0}} \beta f_h \left(1-\varsigma^{\frac{\gamma_0-1}{\gamma_0}}\right)} \quad [49]$$

Introducing the functions $\mathcal{G}(\varsigma)$ and $\psi(\varsigma)$ into the expressions for ϕ_{g1}/ϕ_0 and τ_{g1}/τ_0 given by Eqs. 45 and 46

$$\frac{\phi_{g1}}{\phi_0} = \left[1-\psi(\varsigma)\right] \mathcal{G}(\varsigma) - \frac{\gamma_0-1}{\gamma_0} \frac{\varsigma^{\frac{\gamma_0-1}{\gamma_0}}}{1-\varsigma^{\frac{\gamma_0-1}{\gamma_0}}} \int_{\varsigma_i}^{\varsigma} \mathcal{G}(\varsigma)\, d(\ln 1/\varsigma) \quad [50]$$

$$\frac{\tau_{g1}}{\tau_0} = -\psi(\varsigma)\, \mathcal{G}(\varsigma) + \frac{\gamma_0-1}{\gamma_0} \int_{\varsigma_i}^{\varsigma} \mathcal{G}(\varsigma)\, d(\ln 1/\varsigma) \quad [51]$$

The qualitative behavior of the velocity and temperature lags is demonstrated clearly by these equations. Near the nozzle entrance, the first terms dominate since the contributions of the integrals are small. The velocity of the gas increases above the velocity of the mixture with no lag, and the gas temperature drops below the temperature of the mixture with no lag. Further downstream, however, the trends are reversed, as the contribution of the integrals becomes larger. The heat stored in the particles feeds back directly into the gas, and kinetic energy deficiency stored in the particles is transferred to the gas by dissipation. The effects are parallel, and both tend to increase the gas temperature and lower the gas velocity. If the heat capacity of the particles is zero, i.e., $\mathcal{C} = 0$ and hence $\Psi = 0$, the mechanism of transfer of energy is entirely dissipative, then the velocity lag exhibits the same trends as for finite particle heat capacity, but the gas temperature increment increases monotonically.

EFFECT OF VELOCITY AND TEMPERATURE LAGS ON PERFORMANCE

The effect of the particle lags on performance will be determined as a correction to the performance of a rocket nozzle of identical shape with the same mass fraction of particles but without lag. The stagnation temperature T_c in the rocket chamber is assumed to be the same with and without lags. Expanding the terms in Eq. 18 up to and including the first order in ϵ

$$\frac{p_c}{\dot{m}}\frac{A}{\sqrt{R_0T_c}} = \frac{\Upsilon_g}{\varsigma\Phi_g} \cong \frac{\Upsilon_0}{\varsigma\Phi_0}\left[1+\epsilon\left(\frac{\Upsilon_{g1}}{\Upsilon_0}-\frac{\Phi_{g1}}{\Phi_0}\right)\right] \qquad [52]$$

Let ς_{t_0} be the throat pressure ratio without lag and ς_t the value with lag; it is assumed that $(\varsigma_t - \varsigma_{t_0})/\varsigma_{t_0}$ is of order ϵ. The throat pressure ratio is determined by the condition $A' = 0$, hence equating the differential of the logarithm of the right hand side of Eq. 52 to zero and expanding to order ϵ

$$\frac{\varsigma_t-\varsigma_{t_0}}{\varsigma_{t_0}} = -\epsilon\left[\frac{\Upsilon/\varsigma\Phi}{\varsigma(\Upsilon/\varsigma\Phi)''}\right]_{t_0}\left(\frac{\Upsilon_{g1}}{\Upsilon_0}-\frac{\Phi_{g1}}{\Phi_0}\right)'_{t_0}$$

or evaluating the terms in the brackets explicitly

$$\frac{\varsigma_t-\varsigma_{t_0}}{\varsigma_{t_0}} = -\epsilon\,\frac{\gamma_0^2}{2}\left(\frac{2}{\gamma_0+1}\right)^{\frac{2\gamma_0-1}{\gamma_0-1}}\left(\frac{\Upsilon_{g1}}{\Upsilon_0}-\frac{\Phi_{g1}}{\Phi_0}\right)'_{t_0} \qquad [53]$$

Now A_t and $\sqrt{R_0T_c}$ are the same with and without lag, so an expansion of Eq. 52 around $\varsigma_t = \varsigma_{t_0}$ leads to the relation

$$\frac{p_c/\dot{m}}{p_{c_0}/\dot{m}_0} = 1+\epsilon\left(\frac{\Upsilon_{g1}}{\Upsilon_0}-\frac{\Phi_{g1}}{\Phi_0}\right)_{t_0} \qquad [54]$$

The throat pressure ratio ς_t is not needed to find $p_c/\dot{m}$ because of the condition $(\Upsilon/\varsigma\Phi)'_{t_0} = 0$, peculiar to the throat. Substituting from Eqs. 50 and 51 and recalling that

$$\varsigma_{t_0}^{\frac{\gamma_0-1}{\gamma_0}} = 2/(\gamma_0+1)$$

$$\frac{p_c/\dot{m}}{p_{c_0}/\dot{m}_0} = 1 - \epsilon\left[G(\varsigma_{t_0}) - \int_{\varsigma_i}^{\varsigma_{t_0}} G(\varsigma)\, d\left(\ln\frac{1}{\varsigma}\right)\right] \qquad [55]$$

The quantity in the brackets is positive, as will become clear when the behavior of $G(\varsigma)$ is examined later; hence $p_c/\dot{m}$ always decreases as a result of the lags. Only the ratio $p_c/\dot{m}$ is determined in the flow with lag; some additional information must be supplied to determine p_c and $\dot{m}$ separately. For a solid propellant rocket this normally would be a burning rate law relating $\dot{m}$ and p_c .

The vacuum thrust F_v for the nozzle is given by

$$F_v = A_e\left[p + (1-\alpha)\rho u_g^2 + \alpha\rho u_s^2\right]_e$$

where the subscript e denotes the nozzle exit. The vacuum specific impulse is defined by

$$I_v = F_v/\dot{m}g$$

These expressions are exact, within the limitations of one-dimensional flow, as is the derived form

$$I_v = A_e\frac{p_c}{\dot{m}}\varsigma_e\left[1 + \frac{\phi_g^2}{\tau_g} - \alpha_0\frac{\phi_g}{\tau_g}(\phi_g - \phi_s)\right]_e$$

Substituting the expansions for ϕ_g , τ_g , and ϕ_s and retaining terms of order ϵ

$$I_v \cong A_e\frac{p_c}{\dot{m}}\varsigma_e\left[1 + \left(\frac{\phi_0^2}{\tau_0}\right)_e + \epsilon\left\{\frac{\phi_0^2}{\tau_0}\left(2\frac{\phi_{g1}}{\phi_0} - \frac{\tau_{g1}}{\tau_0}\right) - \alpha_0\frac{\phi_0}{\tau_0}(\phi_{g1} - \phi_{s1})\right\}_e\right] \qquad [56]$$

The exit pressure can be determined from the continuity equation

$$\frac{p_c}{\dot{m}}\frac{A_e}{\sqrt{R_0T_c}} = \left(\frac{\tau_g}{\varsigma\phi_g}\right)_e \cong \left(\frac{\tau_0}{\varsigma\phi_0}\right)_e + \epsilon\left[\frac{\tau_0}{\varsigma\phi_0}\left(\frac{\tau_{g1}}{\tau_0} - \frac{\phi_{g1}}{\phi_0}\right)\right]_{e_0}$$

Expanding the expression for $(\tau_0/\varsigma\phi_0)_e$ to the first power in $(\varsigma_e - \varsigma_{e_0})/\varsigma_{e_0}$, which is assumed to be of order ϵ , and substituting for $p_c/\dot{m}$ from Eq. 54

$$\frac{\varsigma_e - \varsigma_{e_0}}{\varsigma_{e_0}} = \epsilon\gamma_0\frac{1 - \varsigma_{e_0}^{\frac{\gamma_0-1}{\gamma_0}}}{1 - \frac{\gamma_0+1}{2}\varsigma_{e_0}^{\frac{\gamma_0-1}{\gamma_0}}}\left[\left(\frac{\tau_{g1}}{\tau_0} - \frac{\phi_{g1}}{\phi_0}\right)_{e_0} - \left(\frac{\tau_{g1}}{\tau_0} - \frac{\phi_{g1}}{\phi_0}\right)_{t_0}\right] \qquad [57]$$

The quantity $\varsigma_e[1+\phi_0^2/\gamma_0]_e$ in the expression for I_v, Eq. 56, is expanded to the first power in $(\varsigma_e-\varsigma_{e_0})/\varsigma_{e_0}$, and with substitutions from Eqs. 41, 50, and 51 the specific impulse can be expressed as

$$\frac{I_v}{I_{v_0}} = 1 - \epsilon\,\frac{\frac{\gamma_0-1}{2\gamma_0}\,\varsigma_{e_0}^{\frac{\gamma_0-1}{\gamma_0}}}{1-\frac{\gamma_0+1}{2\gamma_0}\,\varsigma_{e_0}^{\frac{\gamma_0-1}{\gamma_0}}}\left[G(\varsigma_{t_0}) + \int_{\varsigma_{t_0}}^{\varsigma_{e_0}} G(\varsigma)\,d\left(\ln\frac{1}{\varsigma}\right)\right] \qquad [58]$$

This formula shows that the vacuum specific impulse is quite independent of conditions upstream of the throat, a result that does not appear obvious.

The thrust can be determined only if p_c or $\mathring{m}$ or a relation between them is prescribed. For instance, in a solid propellant rocket with $\mathring{m}/\mathring{m}_0 = (p_c/p_{c_0})^N$

$$\frac{F_v}{F_{v_0}} = \frac{I_v}{I_{v_0}} - \frac{1-N}{N}\left(1-\frac{p_c/\mathring{m}}{p_{c_0}/\mathring{m}_0}\right) \qquad [59]$$

where I_v/I_{v_0} and $(p_c/\mathring{m})/(p_{c_0}/\mathring{m}_0)$ are given by Eqs. 55 and 58 respectively. The percentage reduction of thrust is always greater than the percentage reduction of specific impulse as a result of velocity and temperature lags.

NOZZLE SHAPE PARAMETER ξ_0'

The nozzle shape appears in the analysis through the parameter ξ_0' only. This parameter occurs directly as a factor in the function $G(\varsigma)$ defined by Eq. 48 and indirectly, with weaker effect, through the coefficients f_d and f_h, also occurring in $G(\varsigma)$. If θ is the angle between the tangent to the nozzle contour and the nozzle axis, with θ positive downstream of the throat

$$\tan\theta = \frac{dr}{dx} = \frac{d(r/r_t)}{d\xi_0} = \frac{d(A/A_t)^{1/2}}{d\varsigma}\,\frac{d\varsigma}{d\xi_0}$$

and hence

$$-\frac{1}{\xi_0'} = -\frac{d\varsigma}{d\xi_0} = -2\sqrt{\frac{A_t}{A}}\,\frac{\tan\theta}{A'/A}$$

or, substituting from Eq. 35

$$-\frac{d\varsigma}{d\xi_0} = 2\gamma_0\sqrt{\frac{A_t}{A}}\,\varsigma\left(1-\varsigma^{\frac{\gamma_0-1}{\gamma_0}}\right)\frac{\tan\theta}{1-\varsigma^{\frac{\gamma_0-1}{\gamma_0}}} \qquad [60]$$

where $\varsigma_{t_0} = [2/(\gamma_0+1)]^{\frac{\gamma_0}{\gamma_0-1}}$ is the throat pressure ratio. Proceeding downstream from the throat, the quantity

$$\left(1-\varsigma^{\frac{\gamma_0-1}{\gamma_0}}\right) \Big/ \left\{1-(\varsigma/\varsigma_{t_0})^{\frac{\gamma_0-1}{\gamma_0}}\right\}$$

decreases as do the factors $\sqrt{A_t/A}$ and ς, the latter very rapidly. Hence $-d\varsigma/d\xi_0$ decreases rapidly after θ reaches its maximum value downstream of the throat. The trend is more marked for a bell-shaped nozzle (θ decreasing) than for a conical nozzle (θ = constant).

The value of $-d\varsigma/d\xi_0$ at the throat is indeterminate as given by Eq. 60. An expansion in powers of $(\varsigma_t-\varsigma_{t_0})/\varsigma_{t_0}$ near the throat yields the relation

$$-\frac{d\varsigma}{d\xi_0} \longrightarrow \frac{1}{\sqrt{b_t}}\,\gamma_0\left(\frac{2}{\gamma_0+1}\right)^{\frac{3\gamma_0-1}{2(\gamma_0-1)}}\left(1-\frac{3-2\gamma_0}{3\gamma_0}\,\frac{\varsigma-\varsigma_{t_0}}{\varsigma_{t_0}}+\cdots\right) \qquad [61]$$

where $b_t r_t$ is the radius of curvature of the nozzle contour at the throat. Since $-d\varsigma/d\xi_0$ is increasing downstream at the throat, the maximum value of $-d\varsigma/d\xi_0$ must occur somewhere downstream of the throat.

If the nozzle entrance joins a cylindrical rocket chamber with a continuous slope and a discontinuity in curvature, the behavior of $-d\varsigma/d\xi_0$ near the entrance can be determined by an expansion that gives

$$-\frac{d\varsigma}{d\xi_0} \longrightarrow \frac{1}{\sqrt{b_i}}\left(\frac{A_t}{A_i}\right)^{5/4}\sqrt{\frac{\gamma_0-1}{\gamma_0}}\left(\frac{2}{\gamma_0+1}\right)^{\frac{3\gamma_0-1}{2(\gamma_0-1)}}\frac{\sqrt{(\varsigma_i-\varsigma)/\varsigma_i}}{1-(\varsigma_{t_0}/\varsigma_i)^{\frac{\gamma_0-1}{\gamma_0}}} \qquad [62]$$

where A_i is the cross-sectional area of the nozzle entrance and $b_i r_i$ is the radius of curvature of the nozzle contour immediately downstream of the entrance. This relation shows that $-d\varsigma/d\xi_0$ remains finite but has an infinite slope at the nozzle entrance.

The general behavior of $-d\varsigma/d\xi_0$ as a function of $\ln\frac{1}{\varsigma}$, say, can be deduced from Eqs. 60, 61, and 62. For a typical nozzle, the value of $-d\varsigma/d\xi_0$ increases sharply from zero at the nozzle entrance, then rather slowly to a maximum downstream of the throat, and decreases to a small quantity at the nozzle exit. The maximum is quite close to the value at the throat; hence the contour radius at the throat is the primary influence on the magnitude of $-d\varsigma/d\xi_0$.

A discontinuity in radius of curvature at the throat produces a discontinuity in $-d\gamma/d\xi_0$. Elsewhere on the nozzle contour a discontinuity in curvature with continuous slope produces only a discontinuity in the derivative of $-d\gamma/d\xi_0$. It is unrealistic, in a one-dimensional approximation, to prescribe a nozzle contour that produces discontinuities in $-d\gamma/d\xi_0$; such discontinuities would be smoothed out by the real three-dimensional flow.

DRAG AND HEAT TRANSFER COEFFICIENTS f_d AND f_h

The drag and heat transfer coefficients introduced in Eqs. 6 and 7 to allow for departures from Stokes' regime for drag and simple conduction for heat transfer are the most difficult parameters to evaluate in the analysis. Below a Reynolds number of unity, for the Mach number sufficiently low, the Stokes' drag formula and conduction theory ($f_d = f_h = 1$) are adequate. However, this regime of relative flow is applicable only to very small particles and leads to negligible lags in most examples of practical interest. The magnitude of the drag coefficient of spheres at very low Mach number has been well established by measurement over a wide range of Reynolds numbers and hence can be evaluated from the relation $f_d = 24/(C_D \mathcal{R}_e)$, where $C_D \, (= 2\mathcal{D}/\pi a^2 \rho u^2)$ is the measured drag coefficient and $\mathcal{R}_e$ is the Reynolds number based on sphere diameter. The heat transfer coefficient for spheres, usually presented as the Nusselt number $N_u \, (= 2/f_h)$, has also been measured over a wide range of Reynolds numbers at low Mach number, although the magnitude is not quite as well established as that of the drag coefficient.

These remarks apply to continuum flow, which occurs only when the ratio of the mean free path of the molecules is very small compared with the particle dimension. The criterion for continuum flow is that the value of $M/\mathcal{R}_e$, where M is the Mach number of the flow relative to the particle, should be very small compared with unity. This condition is not satisfied for typical particles in a rocket nozzle; hence dependence of f_d and f_h on $M/\mathcal{R}_e$ must be investigated.

Measurements of the heat transfer to spheres in the slip flow regime have been made by Kavanau (5).[1] His measurements covered the Mach number range from 0.1 to 0.7 and the Reynolds number range from 2 to 100. To represent the results of the experiments in a simple form, Kavanau proposed a semi-empirical interpolation formula, which can be written in the present notation as

---

[1] Numbers in parenthesis indicate References at end of paper.

$$f_k = f_k^{(0)} + K \frac{M}{Re\,Pr}$$

where $f_k^{(0)} (= 2/Nu^{(0)})$ is the value of f_k for continuum flow (M = 0) and K is a constant; Kavanau found that $K = 6.84$ gave the best agreement with his measurements. The second term on the right-hand side was suggested by free molecular flow theory, with the reasonable assumption that if the formula gives the correct value of f_k in continuum flow when the second term is zero and in free molecular flow when the second term is dominant, the formula may well give a good approximation in the slip and transition regimes between the two extremes.

If the expression for heat transfer to a sphere in free molecular flow (e. g., Ref. 6) is expanded in a power series in M^2, the leading terms for $f_k = 2/Nu$ are given by

$$f_k = \frac{2\sqrt{2\pi}}{\bar{\alpha}} \frac{\gamma^{3/2}}{\gamma+1} \frac{M}{Re\,Pr}\left(1 - \frac{\gamma}{6} M^2 + \cdots\right) \qquad [63]$$

where $\bar{\alpha}$ is the accommodation coefficient. Taking $\gamma = 1.4$ to compare with Kavanau's experiments in air and assuming that $\bar{\alpha} = 1.0$, the numerical factor in Eq. 63 is 6.92, very close to the value 6.84 that was determined experimentally. Kavanau used the results of an approximate theory of Sauer (7) to evaluate $f_k^{(0)}$, and this agreed well with his experiments at the lowest Mach number. The analytical expression for $f_k^{(0)}$ is complex, but it can be represented reasonably well by an empirical relation

$$\begin{aligned} \log_{10} \frac{1}{f_k^{(0)}} &= 0.108 \left(\log_{10} Re + 0.5\right)^{1.86} & Re > 10^{-0.5} \\ &= 0 & Re < 10^{-0.5} \end{aligned} \qquad [64]$$

where the dependence on Prandtl number is ignored. For application to a rocket nozzle, a value of $\gamma = 1.28$ in Eq. 63 seems more appropriate; hence it will be assumed that the heat transfer correction factor is

$$f_k = f_k^{(0)} + 6.35 \frac{M}{Re\,Pr} \qquad [65]$$

with $f_k^{(0)}$ given by Eq. 64. This formula is expected to be sufficiently accurate as long as M is not much larger than unity.

The drag of spheres apparently has not been measured in the slip flow regime at subsonic Mach numbers. It seems reasonable, however, to use the same procedure for estimating drag as for heat transfer. Expanding the expression for drag in terms of f_d for the regime of free molecular flow in powers of M^2, it is found that, with reflection coefficients equal to unity and with the ratio of gas temperature to sphere temperature close to unity

$$f_d = \frac{18\sqrt{2\pi}}{\pi + 8}\sqrt{\gamma}\,\frac{M}{\mathcal{R}_e}\left[1 - \frac{4\gamma}{5(\pi+8)}M^2 + \cdots\right]$$

For $\gamma = 1.28$, the numerical factor of $M/\mathcal{R}_e$ is 4.58, so it is assumed that

$$f_d = f_d^{(0)} + 4.58\,\frac{M}{\mathcal{R}_e} \qquad [66]$$

where $f_d^{(0)}$ is the value of f_d for continuum flow. This latter coefficient has been measured by several independent investigators (e.g., Ref. 8), and the results can be approximated for Reynolds numbers up to 10^4 by the empirical formula

$$\begin{aligned} \log_{10}\frac{1}{f_d^{(0)}} &= 0.1025\left(\log_{10}\mathcal{R}_e + 0.5\right)^2 & \mathcal{R}_e &> 10^{-0.5} \\ &= 0 & \mathcal{R}_e &< 10^{-0.5} \end{aligned} \qquad [67]$$

The combination of Eqs. 66 and 67 should give, by analogy with the heat transfer findings, a satisfactory representation of f_d as a function of $\mathcal{R}_e$ and $M/\mathcal{R}_e$, at least for $M < 1$.

The parameters $\mathcal{R}_e$ and $M/\mathcal{R}_e$, which determine the coefficients f_d and f_h, must be evaluated first. The ratio $M/\mathcal{R}_e$ is, by definition

$$\frac{M}{\mathcal{R}_e} = \frac{\mu}{\rho_g \cdot 2a \cdot \sqrt{\gamma \mathcal{R} T_g}}$$

Substituting from Eqs. 13, 21, and 33 and keeping only the first approximation

$$\frac{M}{\mathcal{R}_e} = \frac{\delta}{\sqrt{1-\alpha_0}\sqrt{\gamma}}\left(\frac{1}{\xi}\right)^{1-\left(n+\frac{1}{2}\right)\frac{\gamma_0 - 1}{\gamma_0}} \qquad [68]$$

where δ is a new dimensionless parameter defined by

$$\delta = \frac{\mu_c\sqrt{\mathcal{R}_0 T_c}}{2a\,p_c} \qquad [69]$$

The Reynolds number $\mathcal{R}_e$ is defined by the equation

$$\mathcal{R}_e = (u_g - u_s)\,2a\,\rho_g/\mu$$

Substituting from Eqs. 13, 21, 33, 34, and 41 and retaining only the first approximation

$$\frac{R_e}{f_d} = \frac{\epsilon}{\delta}(1-\alpha_0)\left(\frac{1}{\rho}\right)^{2n\frac{\gamma_0-1}{\gamma_0}}\left(\xi - \frac{1}{\xi_0'}\right) \qquad [70]$$

Because the combination R_e/f_d rather than R_e alone is determined by the particle and nozzle characteristics, it is convenient to have f_d as a function of R_e/f_d and M/R_e so that f_d can be found directly without iteration. From Eqs. 66 and 67 it is a simple matter to plot f_d vs. R_e/f_d with M/R_e as a parameter, as is shown in Fig. 1. The line corresponding to $M = 1$ is shown in the figure; values of f_d for points falling to the right of this line may not be reliable. After f_d is read from the chart, the value of R_e can be found and f_h calculated directly from Eqs. 64 and 65.

The value of R_e/f_d for ϵ and δ fixed depends on a power of the pressure ratio that has limited variation and on the shape parameter ξ_0'. From the discussion in the previous section it is apparent that R_e/f_d will have a maximum somewhat downstream of the nozzle throat. The value of M/R_e, on the other hand, is independent of the nozzle shape and increases monotonically from entrance to exit; hence the effects of slip flow are most pronounced near the exit. Since M/R_e is inversely proportional to particle radius, the factors f_d and f_h can become large for sufficiently small particles. However, the lags are proportional to the combinations ϵf_d and ϵf_h, which become small as the particle radius is reduced.

Example

The large number of parameters entering the calculation of particle lags makes a general discussion difficult, so an examination of one or more specific examples is almost essential as a starting point. Calculations have been carried out for the following arbitrary, but it is hoped reasonable, choice of characteristics.

$c_p = 0.500$ Btu/lb-°F
$R = 0.110$ Btu/lb-°F
$C = 0.550$ Btu/lb-°F
$\rho_s = 210$ lb/ft.^{3}

$p_c = 1000$ psi
$T_c = 6000$ °R
$\mu_c = 1.5 \times 10^{-6}$ lb-sec/ft.^{2}
$r_t = 3.00$ in.

$a \doteq 2.5 \times 10^{-4}$ cm
$\alpha_0 = 0.40$
$P_r = 0.74$

Dimensionless parameters required in the analysis are then

$\gamma = 1.282$ $\epsilon = 0.817$ $\delta = 2.00 \times 10^{-3}$

$\gamma_0 = 1.1454$ $C/C_{p_0} = 1.058$ $\beta = 1.222$

The nozzle contour chosen for the example is shown in Fig. 2. The nozzle is made up of three sections, as follows:

(i) $r/r_t = 1.468 - (1 - \cos\theta)$ $0 \leq |\theta| \leq 40^\circ$

(ii) $r/r_t = 1 + (1 - \cos\theta)$ $-40^\circ \leq \theta \leq 28^\circ$

(iii) $r/r_t = 3.438 - 8.21 \tan^2\theta$ $28^\circ \geq \theta \geq 13^\circ$

The first two sections are circular arcs ($b_c = b_t = 1$) and the third is a two-parameter curve. For this contour $A_i/A_t = 2.155$ and $A_e/A_t = 9.0$; the length of the convergent part is 1.29 r_t, and the length of the divergent part is 5.42 r_t. Without lag, the vacuum thrust and specific impulse would be 50,000 lb and 271 sec respectively, with constant thermodynamic properties, and the exit pressure ratio $p_c/p_{e_0} = 59.6$.

A graph of the shape parameter $-d\delta/d\xi_0$ plotted against $\ln(1/\delta)$ is shown in Fig. 3. The kinks occur at the two points where the radius of curvature of the nozzle contour changes. In the same figure, the function defined by Eq. 48 is shown. The value of the Reynolds number rises to 56 immediately downstream of the throat and decreases to 2 at the nozzle exit. The coefficient f_d drops to 0.32 at the throat and increases to 1.22 at the exit, whereas f_h has a minimum of 0.36 near the throat and rises to 1.52 at the exit.

The functions $\epsilon\phi_{g_1}/\phi_0$, $\epsilon\phi_{s_1}/\phi_0$, $\epsilon\tau_{g_1}/\tau_0$, and $\epsilon\tau_{s_1}/\tau_0$ are plotted against $\ln(1/\delta)$ in Fig. 4. The criterion for validity of the analysis is that these quantities should be small compared with unity, a condition that is fairly well satisfied in this particular example. Appreciably larger diameters of the particles would give less reliable results. For instance, doubling the partitle radius to 5.0×10^{-4} cm increases the value of R_e/f_d by a factor of 8, and this, in the throat region, reduces f_d and f_h by a factor of 2 or so. Since the lags are linear in ϵf_d and ϵf_h, the values of the perturbation quantities above are doubled in the neighborhood of the throat.

The quantities that are required for performance estimation are listed below with their numerical values.

$$\mathcal{G}(\xi_{t_0}) = 0.1605 \qquad \int_{\xi_i}^{\xi_{t_0}} \mathcal{G}(\xi)\, d\left(\ln \frac{1}{\xi}\right) = 0.0680$$

$$\mathcal{G}(\xi_{e_0}) = 0.0994 \qquad \int_{\xi_{t_0}}^{\xi_{e_0}} \mathcal{G}(\xi)\, d\left(\ln \frac{1}{\xi}\right) = 0.6803$$

Substituting these into Eqs. 55 and 58

$$\frac{p_0/p_{c_0}}{\dot{m}/\dot{m}_0} = 1 - 0.0753 \qquad I_v/I_{v_0} = 1 - 0.0538 \tag{71}$$

so that the lags are responsible for a reduction of 5.4 percent in specific impulse in this particular example.

DISTRIBUTED PARTICLE SIZE

The particles in the rocket chamber apparently are formed in a variety of sizes rather than a single size, to which the analysis so far has been restricted. Let $\lambda(a)\,da$ be the weight fraction of the total mixture (including gas) which is in the form of particles with radii between a and $a+da$. Then

$$\int_0^\infty \lambda(a)\, da = \overline{\alpha} \qquad \int_0^\infty \lambda_0(a)\, da = \alpha_0 \tag{72}$$

where α is the total weight fraction of particles and the subscript 0 refers to no lag. Then Eq. 1 is still valid, as is the continuity equation for the gas, Eq. 2. The particle velocity u_s is now a function of a; hence the continuity equation for particles of radius between a and $a+da$ is

$$\lambda(a)\, \rho\, u_s(a)\, A = \lambda_0(a)\, \dot{m} \tag{73}$$

which replaces Eq. 3. Dividing Eq. 73 by Eq. 2 gives

$$\lambda\, u_s = \frac{1-\alpha}{1-\alpha_0}\, \lambda_0\, u_g \tag{74}$$

which is the counterpart of Eq. 9.

The momentum equation for the mixture is now

$$(1-\alpha)\rho\, u_g \frac{du_g}{dx} + \rho \int_0^\infty \lambda\, u_s \frac{du_s}{dx}\, da + \frac{dp}{dx} = 0$$

the extension of Eq. 4. Substituting for λu_s from Eq. 74 and replacing $(1-\alpha)\rho$ by ρ_g, the momentum equation becomes

$$u_g \frac{du_g}{dx} - u_g \int_0^\infty \lambda_0 \left(\frac{du_g}{dx} - \frac{du_s}{dx}\right) da + \frac{1-\alpha_0}{\rho_g} \frac{dp}{dx} = 0$$

or, in terms of the dimensionless variables, to compare with Eq. 19

$$\phi_g \frac{d\phi_g}{d\xi} + \frac{\tau_g}{\xi} = \phi_g \int_0^\infty \lambda_0 \left(\frac{d\phi_g}{d\xi} - \frac{d\phi_s}{d\xi}\right) da \qquad [75]$$

The energy equation can be extended in the same way to give

$$\tau_g + \frac{1}{2}\frac{\gamma_0 - 1}{\gamma_0}\phi_g^2 = 1 + \frac{\gamma_0 - 1}{2\gamma_0}\int_0^\infty \lambda_0 (\phi_g^2 - \phi_s^2) da + \frac{c}{c_{p_0}} \int_0^\infty \lambda_0 (\tau_g - \tau_s) da \qquad [76]$$

which replaces Eq. 20; Eq. 18 of course does not change. The relations for drag and heat transfer, Eqs. 26 and 27, were derived for single particles and hence are still valid. All of these equations are exact, within the limitations of the one-dimensional flow approximation.

The first approximation to the solution of the new equations is the same as before because no lags are involved. The parameter ϵ depends on the particle radius a, so it is not suitable as an expansion parameter; it can be replaced by ϵ_m where

$$\epsilon_m = \frac{2}{9} a_m^2 \frac{\rho_s \sqrt{R_0 T_c}}{\gamma_c \mu_c} \qquad [77]$$

and a_m is some arbitrary mean particle radius used as a reference. Then

$$\phi_g = \phi_0 + \epsilon_m \phi_{g_1} + \cdots$$

$$\tau_g = \tau_0 + \epsilon_m \tau_{g_1} + \cdots$$

but in Eqs. 26 and 27 the ϵ is replaced by $\epsilon_m (a/a_m)^2$, so that Eqs. 41 and 42 become

$$\phi_{g_1} - \phi_{s_1} = \left(\frac{a}{a_m}\right)^2 f_d \frac{\phi_0 \phi_0'}{\tau_0^n} \frac{1}{\xi_0'} \qquad [78]$$

$$\tau_{g_1} - \tau_{s_1} = \left(\frac{a}{a_m}\right)^2 f_h \beta \frac{\phi_0 \tau_0'}{\tau_0^n} \frac{1}{\xi_0'} \qquad [79]$$

Substituting the expansions into Eqs. 75 and 76 and picking out the coefficients of ϵ_m, it is seen that ϕ_{s_1} and τ_{s_1} appear only in the combinations

$$\int_0^\infty \lambda_0(\phi_{g_1}-\phi_{s_1})\,da \qquad \int_0^\infty \lambda_0(\tau_{g_1}-\tau_{s_1})\,da$$

In Eqs. 78 and 79 only the first two factors on the right-hand sides depend on a. Defining two new coefficients F_d and F_k by the equations

$$F_d = \int_0^\infty \lambda_0\left(\frac{a}{a_m}\right)^2 f_d\,da \qquad F_k = \int_0^\infty \lambda_0\left(\frac{a}{a_m}\right)^2 f_k\,da \qquad [80]$$

it is seen that it is merely necessary to replace f_d by F_d, f_k by F_k, and ϵ by ϵ_m to make the entire analysis applicable to flow with particles of any distribution of size.

Eqs. 80 can be interpreted in terms of a single particle radius that is equivalent in effect to the distribution at each axial station. For the Stokes' regime of flow the result is very simple, because $f_d = f_k = 1$; then the effective radius is constant through the nozzle and is determined by the second moment of the particle weight distribution function. Outside of the Stokes' regime, however, the equivalent single particle radius is not constant through the nozzle. It has been seen that f_d and f_k decrease with increasing a in the neighborhood of the throat where the Reynolds number is high. Hence the equivalent single particle radius corresponds to a moment of some power less than 2 in the throat region. Near the nozzle exit slip flow phenomena can become important, and, because f_d and f_k increase with decreasing size of the particles, the equivalent single particle radius is again less than that determined from the second moment.

The numerical evaluation of F_d and F_k is straightforward. At each value of $\ln(1/\gamma)$ chosen for computation, M/Re and Re/f_d are determined from Eqs. 68 and 70 as before, but for several different values of a. Then f_d and f_k are found for each of the values of a and the integrations indicated in Eq. 80 are performed. After F_d and F_k have been determined as functions of $\ln(1/\gamma)$, the method of calculation is the same as for uniform particle radii.

CONCLUDING REMARKS

The perturbation analysis of particle lags in a rocket nozzle has been shown to lead to reasonably simple expressions for the specific impulse and other performance characteristics of the nozzle for sufficiently small particles. The expansion parameter ϵ (or ϵ_m for distributed particle size) is proportional to the square of the particle radius and inversely proportional to the radius of the nozzle throat. Because the flow relative to the particles is outside the Stokes' regime in practice, the lags are not as strongly dependent on particle radius and throat radius as the proportionality with ϵ would indicate. The influence of the nozzle shape on particle lags has been shown to depend primarily on the ratio of the radius of curvature of the nozzle contour at the throat to the throat radius. The lags are inversely proportional to the square root of this ratio in the region of the throat, although again, through the effect of deviations from Stokes' regime of flow, the influence is weaker than direct proportionality with the inverse square root of the radius ratio would indicate.

Recent measurements of particle size distributions in rocket nozzles made by Sehgal (9) indicate that the practical range of particle size lies within the scope of the perturbation analysis if the rocket delivers more than 10,000 to 15,000 lb thrust. For instance, Sehgal reports that 50 percent of the mass fraction of particles is contained in the particles with radii between 1.35×10^{-4} cm and 2.05×10^{-4} cm at 500 psi chamber pressure. If the effective single particle radius is about 1.7×10^{-4} cm, the value of ϵ in the example is the same if the throat radius is reduced from 3 in. to 1.5 in., i.e., the thrust is reduced to 12,500 lb. Geometrically similar rockets of larger size would have smaller lags and the accuracy of the perturbation analysis would improve correspondingly.

REFERENCES

1 M. Gilbert, L. Davis, and D. Altman: Velocity Lag of Particles in Linearly Accelerated Combustion Gases. Jet Propulsion, January 1955, vol. 25, pp. 25-30.

2 M. Barrère, A. Jaumotte, B. F. de Veubeke, and J. Vandenkerchove: Rocket Propulsion, p. 103, Elsevier, Amsterdam, 1960.

3 J. R. Kliegel: One-Dimensional Flow of a Gas-Particle System. IAS Paper No. 60-3, presented at the 28th annual meeting of the IAS, New York, January 1960.

4 W. S. Bailey, E. N. Nilson, R. A. Serra, and T. F. Zupnik: Gas Particle Flow in an Axisymmetric Nozzle. ARS Jour., June 1961, vol. 31, pp. 793-798.

5 L. L. Kavanau: Heat Transfer from Spheres to a Rarefied Gas in Subsonic Flow. Trans. ASME, July 1955, vol. 77, pp. 617-623.

6 S. A. Schaaf and L. Talbot: Handbook of Supersonic Aerodynamics, Section 16, Mechanics of Rarefied Gases, Superintendent of Documents, U. S. Government Printing Office, February 1959.

7 R. M. Drake, F. M. Sauer, and S. A. Schaaf: Forced Convection Heat Transfer from Cylinders and Spheres in a Rarefied Gas Flow. Rept. HE-150-74, Univ. of Calif. Engineering Projects, November 1950.

8 S. Goldstein (ed.): Modern Developments in Fluid Dynamics, Vol. II, pp. 492-493, Oxford University Press, Oxford, 1938.

9 R. Sehgal: Personal communication. Jet Propulsion Laboratory, Pasadena, Calif., January 30, 1962.

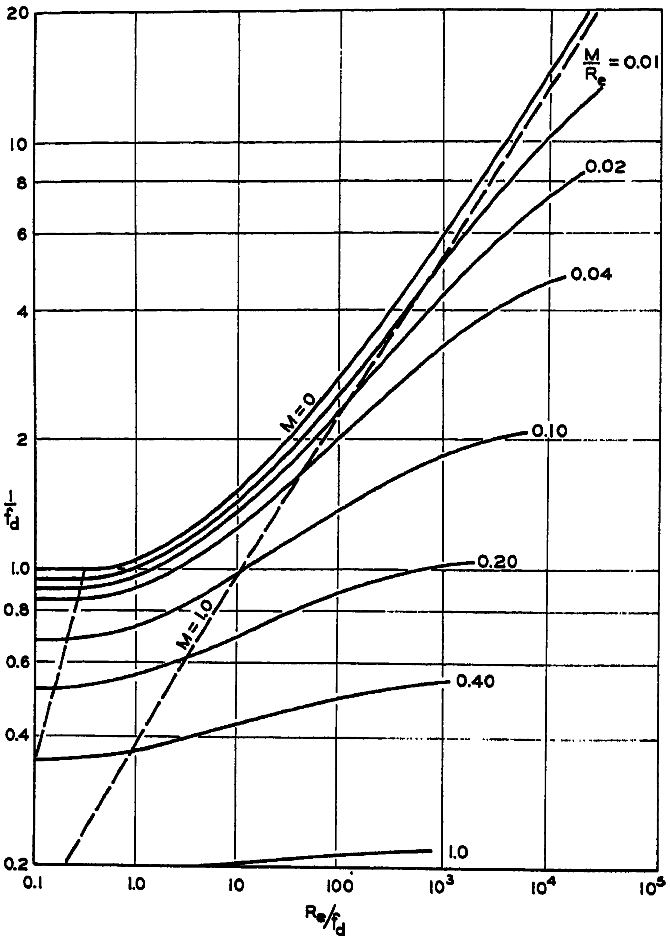

Fig. 1 Drag correction factor f_d

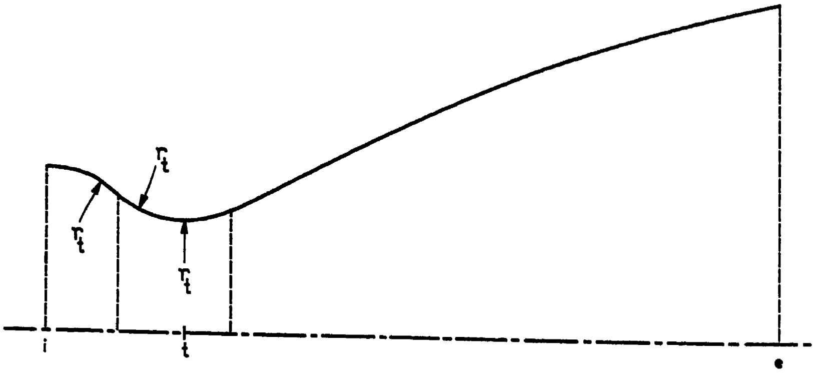

Fig. 2 Nozzle contour

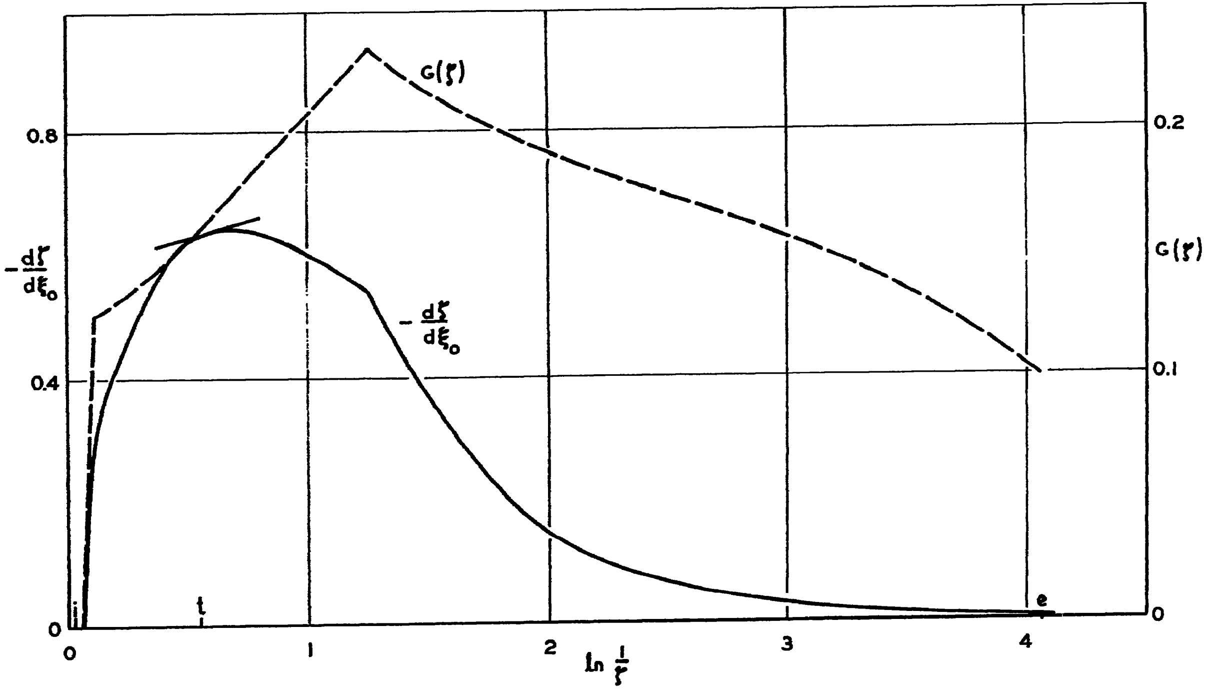

Fig. 3 Shape parameter $-d\zeta/d\xi_0$ and function $G(\zeta)$

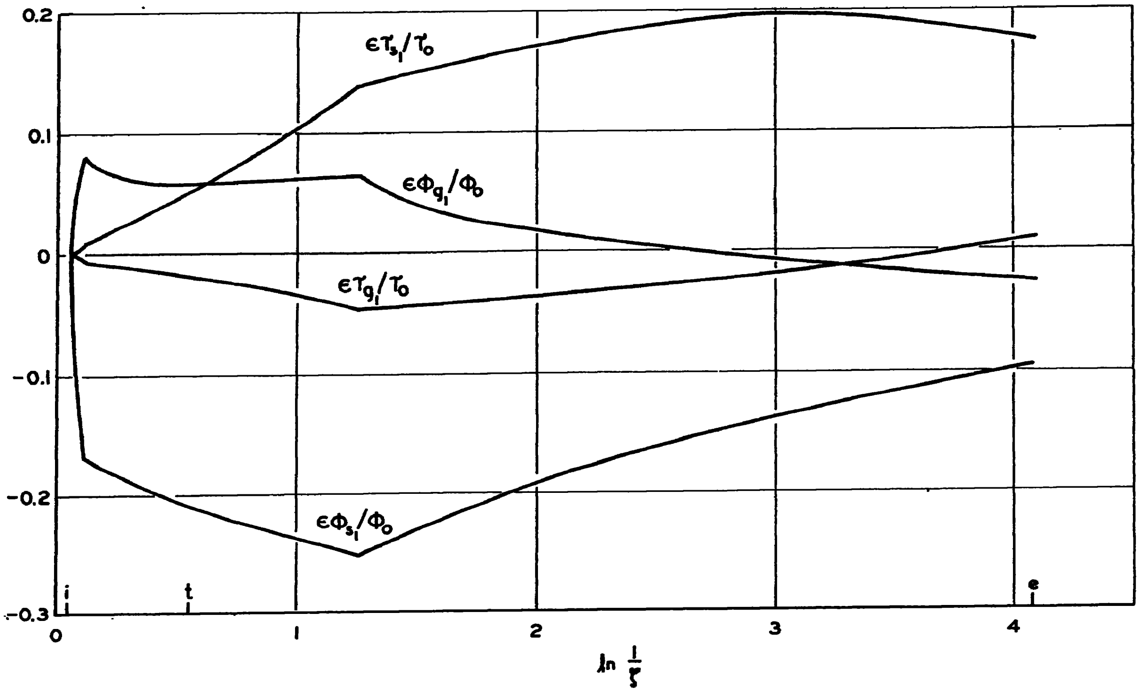

Fig. 4 Perturbation velocities and temperatures for gas and particles

ANALYSIS OF TWO-PHASE FLOW IN SUPERSONIC EXHAUSTS

John H. Morgenthaler

Atlantic Research Corp., Alexandria, Va.

ABSTRACT

A theoretical and experimental investigation of the effect of solids on the characteristics of two-phase supersonic exhausts is presented for systems containing up to 30% by weight aluminum oxide and air. In the experimental program, solids were metered into a high pressure air stream with a paddle-wheel feeder valve prior to flow through a two-dimensional supersonic nozzle. The angle of the oblique shock wave, attached to a wedge located at the exit plane of the nozzle, was determined with shadowgraph techniques. For a particle size of 0.1μ, these angles were in good agreement with theoretical predictions made assuming complete interchange of heat and momentum between phases in the nozzle, but no interphase interchange in the shock wave. For expansions in which the gas phase may be considered perfect, and the particle size of the solid phase is large enough so that the presence of the solids does not significantly change the shock wave angle, the exhaust velocity and temperature of each phase may be experimentally determined. Measurements required for these determinations are wedge angle, shock wave angle, the flow rate of each phase, and axial pressure distribution along the nozzle. The theoretical analysis for these determinations is presented.

INTRODUCTION

Interest has increased in the last few years in the general field of two-phase flow. Gas-solid expansions through supersonic nozzles and the characteristics of the resulting two-phase exhaust have become important. When calculations of particle impingement on wedges suspended in a two-phase exhaust

---

J.H. MORGENTHALER is Project Engineer. Paper presented at the ARS Propellants, Combustion, and Liquid Rockets Conference, Palm Beach, Fla., April 26-28, 1961. This work was supported by the Bureau of Naval Weapons and the Advanced Research Projects Agency under contract NOrd-15536.

were begun two years ago, very little information was found in the literature concerning the effect of solids on the characteristics of a two-phase supersonic exhaust. Especially lacking was any work predicting the effect of entrained solids on attached, oblique shock wave angles, such as those formed on the leading edge of a wedge. The present work was undertaken in an effort to gain a better understanding of two-phase exhausts, to characterize this flow through shock waves, and to establish if possible a simple experimental technique for determining the velocity and temperature of each phase in a supersonic two-phase exhaust.

In the theoretical portion of this work, the conditions at the exhaust of a supersonic nozzle were computed for various limiting assumptions of interphase heat and momentum interchange during expansion. The conditions immediately downstream of the oblique shock wave attached to a wedge (located at the exit plane of the nozzle) were also computed, using the same set of limiting assumptions to delimitate the two-phase region. Using computed exit conditions, the extent of interphase equilibrium attained while traversing a shock wave was estimated.

In the experimental portion of the program, solid particles were introduced into a high pressure air stream with a paddle-wheel feeder valve. A double wedge was placed at the exit of a two-dimensional supersonic nozzle, and shadowgraphs of the attached, oblique shock waves taken. Comparisons between the theoretically predicted and experimentally measured shock wave angles appeared to confirm theoretical predictions.

METHOD OF ANALYSIS

Calculation of Nozzle Exit Conditions

The importance of the assumptions concerning heat and momentum interchange between solid and gas phases during expansion in a supersonic nozzle and in the exhaust was determined in the following manner. Exhaust velocities of the two-phase system at the exit plane of the nozzle were calculated for the two limiting conditions of interchange of heat and momentum: 1) complete interphase interchange, i.e., equilibrium between phases; and 2) no interphase interchange, i.e., neglecting the solid phase. The conditions of this first assumption would be approached for very small particle sizes of the solid phase. The second assumption was obviously a poor one since in this case the solids would neither accelerate nor change temperature during flow through the nozzle and so would exhaust at their chamber velocity and temperature. However, calculations based on this assumption were of value in establishing one of the limits.

Since chamber temperatures of about room temperature were considered, i.e., 80 to 90°F, and chamber pressures of about 80 psig, no problems concerning dissociation or recombination of air were encountered. A constant specific heat of 0.2415 Btu/lbm-°R was used for air, which was considered a good average value (1).[1]

Aluminum oxide grinding abrasive was the solid used in these two-phase studies. Its specific heat per mole was expressed as a function of temperature (Kelvin) in the range from 180 to 300°K by the equation

$$\left(C_p\right)_s = 7.3035 + 0.045179\,T - 1.6323 \times 10^5/T^2 \qquad [1]$$

The constants in this equation were obtained from a least squares fit of tabulated specific heats for alpha aluminum oxide (2).

When the assumption of complete interphase interchange between phases during expansion in the nozzle was made, the temperature at the exit plane was calculated from the equation for an isentropic expansion

$$\Delta S = \int_{T_0}^{T_1} \frac{\left(C_p\right)_t \, dT}{T} - \int_{P_0}^{P_1} \frac{n_g R}{J} \frac{dP}{P} = 0 \qquad [2]$$

where $\left(C_p\right)_t = A_t + B_t T - C_t/T^2$

In this case $\left(C_p\right)_t$ was determined for the two-phase mixture per unit mass of gas plus solid, and n_g was the moles of gas per unit mass of gas plus solid mixture; the reciprocal of n_g may be considered an effective molecular weight.

When the assumption of no interphase transfer during the expansion was made, the temperature at the exit plane was calculated from the equation

$$\Delta S = \int_{T_0}^{T_1} \frac{\left(C_p\right)_g \, dT}{T} - \int_{P_0}^{P_1} \frac{R}{JMW} \frac{dP}{P} = 0 \qquad [3]$$

---

[1] Numbers in parentheses indicate References at end of paper.

where $(C_p)_g$ was evaluated per unit mass of gas and MW was the molecular weight of the gas.

Eqs. 2 and 3 were readily integrated to give, respectively

$$\frac{n_g R}{J} \ln \frac{P_o}{P_1} = A_t \ln \frac{T_o}{T_1} + B_t (T_o - T_1) + \frac{C_t}{2} \left(\frac{1}{T_o^2} - \frac{1}{T_1^2} \right) \qquad [4]$$

$$\frac{R}{JMW} \ln \frac{P_o}{P_1} = \left(C_p\right)_g \ln \frac{T_o}{T_1} \qquad [5]$$

Eq. 4 was solved for T_1 by an iterative procedure on a digital computer.

Once the exhaust temperature was computed, the exhaust velocity was obtained from a total energy balance

$$\int_{V_o}^{V_1} \frac{V\,dV}{g_c J} + \int_{T_o}^{T_1} C_p dT = 0 \qquad [6]$$

This equation was integrated and solved directly for V_1. Two different values of the exhaust velocity V_1 resulted, depending on whether the specific heat and exhaust temperature T_1 of the two-phase mixture or those of the gas phase alone were considered.

Calculation of Shock Wave Angles

The following equation of gas dynamics relates the angle of the oblique shock wave which forms on a wedge to the semiapex angle of the wedge, for adiabatic flow of a perfect gas (3)

$$\cot \sigma = \tan \theta \left\{ \frac{(\gamma + 1) M_1^2}{2 (M_1^2 \sin^2 \theta - 1)} - 1 \right\} \qquad [7]$$

The terms γ and M_1 were defined differently depending on whether or not interphase equilibrium in the shock wave was assumed. When the assumption was made that no interphase transfer occurs between phases, the speed of sound a and the specific heat ratio γ were calculated from the normal relations for a perfect gas

$$a_g = \sqrt{\frac{\gamma_g \, g_c RT}{MW}} \qquad [8]$$

$$\gamma_g = \left(\frac{C_p}{C_v}\right)_g = \left[1 - \frac{R}{J(C_p)_g\ MW}\right]^{-1} \qquad [9]$$

When the assumption of complete interphase interchange between phases was made, the molecular weight of the gas in these equations was replaced by the term $1/n_g$, which represents the total mass of gas plus solid mixture per mole of gas. In this case the specific heat used was $(C_p)_t$, the total specific heat of the two-phase mixture per unit mass of gas plus solid. Eqs. 8 and 9 become in this case

$$a_t = \sqrt{n_g\ \gamma_t\ g_c\ RT} \qquad [10]$$

$$\gamma_t = \left[1 - \frac{n_g R}{J(C_p)_t}\right]^{-1} \qquad [11]$$

The Mach number of the exhaust just upstream of the shock wave may be calculated from the relation

$$M_1 = \frac{V_1}{a_1} \qquad [12]$$

Since both V_1 and a_1 vary depending on the assumptions made concerning the interphase interchange of heat and momentum in the nozzle and in the shock wave, four different Mach numbers can be computed, one for each combination of assumptions.

The following conditions were constant for these calculations: 1) 30% aluminum oxide by weight in air; 2) a chamber pressure of 94.7 psia; 3) a chamber temperature of 85°F; 4) an exit pressure of 14.7 psia; and 5) a wedge with a semiapex angle of 10° immersed in the exhaust stream at the exit plane of the nozzle, with centerline of the wedge parallel to the flow. In addition, the assumption was made that the chamber velocity was negligible compared to that of the supersonic exhaust.

The four sets of assumptions and the results computed for each set are presented in Table 1. The characteristics of the exhaust and the shock wave angle vary considerably depending on the set of assumptions used. Comparing set 1 with set 2 and set 3 with set 4, it can be seen that the assumption of no heat or momentum interchange in the shock wave results in larger values of shock wave angle. Comparing set 1 with 3 and 2 with 4, it can be seen that the assumption of no heat or momentum interchange in the nozzle results in lower values of shock wave angle.

The relative importance of the heat and momentum effects can be separated by consideration of the case in which complete interphase thermal equilibrium is attained in the shock wave with no interphase momentum interchange and, alternatively, the case of complete interphase momentum equilibrium in the shock wave with no interphase thermal interchange. In the former case, the speed of sound was computed from Eq. 8 using γ_t defined by Eq. 11 and in the latter case, the speed of sound was determined using Eq. 10 with γ_g defined by Eq. 9. Four different Mach numbers were again computed at the nozzle exit, since both V_1 and a_1 varied depending on the set of assumptions; these results are presented in Table 2. Comparing set 5 with set 6 and set 7 with set 8 shows that the assumption of complete thermal equilibrium in the shock wave with no momentum interchange results in larger shock wave angles than does the assumption of complete momentum equilibrium in the shock wave with no thermal interchange.

Calculations of Extent of Equilibrium Attained in Shock Wave

An effort was made to predict the magnitude of the extent of interphase equilibrium achieved between the solid and gas phases while traversing a shock wave. The following assumptions were made in these calculations:

1) The shock waves were two-dimensional oblique attached shock waves, such as those which form on the leading edge of a wedge.

2) At the exit plane of the nozzle, just upstream of the shock wave, the velocity and temperature of the solid and gas phases were constant and equal, and the velocity was parallel to the centerline of the wedge.

3) Immediately downstream of the shock wave, the velocity and temperature of the gas phase were constant, and the velocity was parallel to the surface of the wedge.

4) Shock wave thickness was not significantly affected by the presence of solids at concentrations below 50% by weight (50% aluminum oxide corresponds to a fraction voids of 0.9996 at the conditions considered), and there were no interactions between the solid particles.

5) Shock wave thickness for the gas phase alone was of the order of six mean free paths of the gas molecules at the exhaust conditions (4).

6) The solid particles were spherical in shape.

7) The force of gravity was negligible in comparison to the drag forces.

8) The gas-phase conditions within the shock wave were constant and equal to those immediately downstream of the shock wave.

The first seven assumptions appear to be reasonable approximations, especially since estimates rather than exact calculations were desired. The last assumption is obviously not correct but was made because it greatly simplified the calculations; consideration of the variable gas-phase conditions that actually exist within the shock wave was avoided. The assumption is a conservative one; by assuming that the gas-phase conditions were instantaneously changed to their downstream values instead of gradually changing within the shock wave, the maximum value of the driving force between particle and gas was employed over the entire region of the shock wave. Particle velocities and temperatures computed at the downstream edge of the shock wave in this manner were closer to the gas-phase conditions at that point than if the actual but unknown gas phase conditions within the shock wave had been used. The results of the calculations (shown in Table 3) justified this assumption.

The relationship between the wedge and the supersonic exhaust stream is shown in Fig. 1. Assumptions 1, 2, 3, and 8 guaranteed that no matter where a particle entered the shock wave, it would be subjected to identical conditions. The determination of the temperature and velocity of the solids after entering the shock wave was simplified by adopting a coordinate system moving at the constant velocity of the gases V_2 downstream of the shock wave. In this frame of reference, the initial vector velocity of the solids $\vec{U}_i$ relative to the gases behind the shock wave is $\vec{U}_i = \vec{V}_1 - \vec{V}_2$. By this method, the problem was reduced to the determination of the motion and temperature of a particle projected into still air. This method of analysis is similar to that used by Serafini in his analysis of the impingement of water droplets on wedges (5).

1 Calculation of Residence Time in Shock Wave

The time for the particle to traverse the shock wave was estimated using assumptions 4 and 5 as

$$t = \frac{6\lambda_m}{V_1} \qquad [13]$$

The mean free path of the gas molecules λ_m was computed from the relation (6)

$$\lambda_m = \frac{3\mu}{\rho\sqrt{8g_c RT/\pi MW}} \qquad [14]$$

The exhaust velocities in Table 1 show that regardless of the set of assumptions concerning interphase heat and momentum interchange during expansion, particle residence times in the shock wave will be about 10^{-9} sec. Using this value as an estimate, very little interphase interchange was computed in the shock wave. Therefore exact calculations were made using the exhaust conditions of set 1 in Table 1. Results presented in Table 3 justify this assumption.

Conditions immediately downstream of the shock wave were calculated using relations for adiabatic flow of a perfect gas (3); solutions were obtained on a digital computer. Obviously, further downstream of the shock wave equilibrium conditions between phases will be attained regardless of the particle size; however, results presented in Table 3 show that the distance required to attain equilibrium conditions will be large compared to the shock wave thickness.

2 Velocity Equilibrium

The velocity of a particle relative to the gas behind an oblique shock wave attached to a wedge was computed using Newton's second law

$$F_D = C_D \frac{1}{2} \frac{\rho_g}{g_c} U^2 \;(\pi r^2) = -\frac{4}{3} \pi r^3 \frac{\rho_s}{g_c} \frac{dU}{dt} \qquad [15]$$

or

$$\frac{dU}{dt} = -\frac{3}{8} \frac{\rho_g U^2}{\rho_s r} C_D \qquad [16]$$

The Stokes-Cunningham law was used to evaluate the drag coefficient, since relative particle Reynolds numbers were less than two for the small wedge angles and particle sizes considered. Therefore, the drag coefficient was evaluated as

$$C_D = \frac{24}{k_m Re_p} = \frac{12\mu}{k_m r U \rho_g} \qquad [17]$$

where (6)

$$k_m = 1 + k_{me}\left(\frac{\lambda_m}{2r}\right) \qquad [18]$$

and

$$k_{me} = 1.644 + 0.552 \exp(- 0.656(2r/\lambda_m)) \qquad [19]$$

Combining Eqs. 16 and 17

$$\frac{dU}{dt} = U \frac{dU}{dx} = - \frac{9\mu\ U}{2\ k_m\ r^2 \rho_s} \qquad [20]$$

or

$$\frac{dU}{dx} = - \frac{9\mu}{2\ k_m\ r^2 \rho_s} = - B \qquad [21]$$

where B is a constant. Integrating this equation twice and substituting the initial conditions

$$\begin{aligned} x(0) &= 0 \\ U(0) &= U_i \end{aligned} \qquad [22]$$

the relative velocity U was obtained as a function of time as

$$U = U_i \exp(- Bt) \qquad [23]$$

The value of U corresponding to a calculated residence time of 0.815×10^{-9} sec was obtained from this equation.

The particle velocity V_s at the downstream edge of the shock wave was calculated by solving the triangles shown in Fig. 2. Angle C remains constant because the direction of U, the relative velocity, is always perpendicular to the shock wave. This fact is easily seen from the equations of continuity $(\rho_1\ V_{N_1} = \rho_2\ V_{N_2})$ and tangential momentum $(\rho_1\ V_{N_1}\ V_{T_1} = \rho_2 V_{N_2}\ V_{T_2})$ across the oblique shock wave; tangential components must be equal, so that the change in velocity downstream of the shock wave is only in the normal direction. Therefore, the direction of the relative velocity will be normal to the shock wave. Angle C was determined from Fig. 2a with the law of sines and V_s from Fig. 2b with the law of cosines. Results are summarized in Table 3.

3 Thermal Equilibrium: Heat Transfer Coefficient Correlation

The heat transfer by convection between a solid particle and the gas phase was computed from an energy balance by equating the rate of increase of sensible heat of the particle to the rate of heat transfer from the gas to the particle

$$\left(\frac{4}{3}\pi r^3\rho_s\right)C_s\,\frac{dT_s}{dt} = h\;(4\pi r^2)\;(T_g - T_s) \qquad [24]$$

or

$$\frac{dT_s}{dt} = \frac{3h}{r\rho_s C_s}\,(T_g - T_s) \qquad [25]$$

Convective heat transfer to spheres has been correlated by the following equation (7)

$$Nu = 2 + 0.6\ Pr^{1/3}\ Re_p^{\ 1/2} \qquad [26]$$

Substituting for Nu and Re_p

$$h = \frac{k_g}{r}\left[1 + 0.3\ Pr^{1/3}\left(\frac{2r\rho_g U}{\mu}\right)^{1/2}\right] \qquad [27]$$

Using Eqs. 23 and 27 and assumptions 3 and 8, Eq. 25 may be integrated directly. However, it is more convenient to carry out the integration by defining a time-average value $\tilde{h}$ by the equation

$$\tilde{h} = \frac{1}{t}\int_0^t h\,dt \qquad [28]$$

Eq. 28 was integrated by combining Eqs. 23 and 27 to give

$$\tilde{h} = \frac{k_g}{r}\left[1 + \frac{0.6}{Bt}\ Pr^{1/3}\ Re_{p,i}^{1/2}\left(1 - \exp\left(-\frac{Bt}{2}\right)\right)\right] \qquad [29]$$

Eq. 25 was then readily integrated as

$$\frac{T_s - T_g}{T_{s_i} - T_g} = \exp\left(-\frac{3\tilde{h}}{r\rho_s\tilde{C}_s}\ t\right) \qquad [30]$$

where $\tilde{C}_s$ is the average value of the specific heat of the particle. This equation was used to estimate the extent of thermal equilibrium attained by a particle within the shock wave. Results are presented in Table 3.

4 Thermal Equilibrium: Molecular Collision Model

The heat transferred between molecules of a gas and a solid surface due to a molecular collision may be written as (8)

$$dQ = \alpha S N_s\ C_v{'}(T_s - T_g)dt \qquad [31]$$

where α is the thermal accommodation coefficient defined as the ratio of the average energy transfer per collision to the energy transfer corresponding to attainment of thermal equilibrium between solid and gas. N_s, the number of molecular collisions with a surface per second per unit area, is obtained from kinetic theory as (9)

$$N_s = \frac{n\bar{c}}{4} = \frac{nC\sqrt{8/3\pi}}{4} \qquad [32]$$

since

$$P = \frac{1}{3}\frac{\rho_g}{g_c}C^2 \qquad [33]$$

$$N_s = n\left[\frac{g_c P}{2\pi\rho_g}\right]^{1/2} \qquad [34]$$

Substituting Eq. 34 into Eq. 31 and using the perfect gas law and the relations

$$C_v' = \frac{C_v'' MW}{A_o}\ ; \qquad n = \frac{\rho_g A_o}{MW} \qquad [35]$$

there results[2]

$$dQ = \alpha r^2 C_v'' P\left[\frac{8g_c\pi MW}{RT_g}\right]^{1/2}(T_s - T_g)dt \qquad [36]$$

The heat lost by the solid

$$dQ = -\left(\frac{4}{3}\pi r^3\rho_s\right)C_s dT_s \qquad [37]$$

is equal to the heat gained by the gas. Setting Eqs. 36 and 37 equal and integrating where T_g and P are constant (assumptions 3 and 8) gives

$$\frac{T_s - T_g}{T_{s_i} - T_g} = \exp\left(-\frac{3\alpha C_v'' P}{4r\rho_s\tilde{C}_s}\left[\frac{8g_c MW}{\pi RT_g}\right]^{1/2} t\right) \qquad [38]$$

where $\tilde{C}_s$ is the average value of the specific heat of the solid. This equation also was used to estimate the extent of thermal equilibrium attained by a particle within the shock wave; results are presented in Table 3.

---

[2] This is Eq. 2-2 of Ref. 8.

5 Discussion of Results

The percent thermal and momentum equilibrium predicted when 0.1 μ particles traverse a shock wave is presented in Table 3. Calculations were based on the exhaust conditions of set 1 in Table 1. These results show that for this particle size, considered the smallest size of practical interest, only 1% or less of the equilibrium value is predicted.

The thermal equilibrium predicted using the heat transfer coefficient correlation is considerably larger than any of the other equilibrium values computed. These results suggest that extrapolation of the heat transfer coefficient correlation to particle sizes in the submicron range may not be justified.

In the computation of thermal equilibrium using the molecular collision model, calculations were made using both a large and small value of the accommodation coefficient α. The results show that even an order of magnitude variation in the value of α did not significantly affect the calculated equilibrium.

The analyses show that the equilibrium attained will decrease with increasing particle size; therefore, for particle sizes larger than 0.1μ, considerably less than 1% of the equilibrium value is predicted while traversing a shock wave.

EXPERIMENTAL SHOCK WAVE ANGLE DETERMINATIONS

A series of experimental shock wave angle determinations was made with the experimental apparatus shown in Fig. 3. In a portion of these determinations, aluminum oxide grinding abrasive[3] was added to the high pressure air stream from a conical feed hopper with a paddle-wheel feeder valve. The hopper with an attached vibrator was enclosed in the pressure vessel shown in Fig. 3, thus equalizing pressure on both sides of the feeder valve. The feeder valve was powered with a variable speed Graham drive and a 1/2 hp motor. Air was supplied by two Ingersoll-Rand horizontal air compressors each with a capacity of approximately 0.25 lb/sec at 100 psig.

Shadowgraphs were made of the oblique, attached shock waves that formed on a double wedge supported at the exit plane of the nozzle in the supersonic exhaust, using a 100-w concentrated zirconium arc lamp. Final finishing of the wedge surfaces was accomplished by hand lapping; the double wedge angle was determined by optical measurement. A new steel wedge was used for each run so that the sharpest possible edge would be available. Wedges were generally first exposed to air alone and then to the two-phase exhaust. Each run lasted just long enough to expose a negative (generally less than 15 sec).

---

[3] Obtained from Buehler Ltd., Evanston, Ill.

Typical shadowgraphs are shown in Fig. 4. Shock wave angles were measured on an Ex-Cell-O Contour projector (optical comparator) at a magnification of 10. Negatives of runs in which no solids were present were read directly. In runs in which solids were present, positive transparencies made from the negatives were required for projection.

Shock wave angles for the most successful runs with air alone are presented in Table 4. Computed shock wave angles, calculated by the procedure described in the section on method of analysis, are tabulated for comparison. The data show that measured angles were within approximately one degree of the predicted values. Lack of more precise agreement was probably caused by the difficulty in obtaining truly sharp uniform wedges, variation in air flow rate, and errors in measurement of pressure and temperatures used for computing shock wave angles. In addition, some error occurred in the determination of wedge semiapex angles. Each of these angles was determined by measurement of shadowgraphs on the optical comparator using the exit plane of the nozzle for reference. However, this error was small since double wedge angles computed from these measurements generally agreed with the optical measurements of the double angles.

Shock wave angles, determined for the most successful two-phase runs, are presented in Table 5. Angles computed assuming complete interphase heat, momentum interchange between phases in the nozzle, and no interchange in the shock wave (assumption set 1 in Table 1) are tabulated for comparison. As shown in Table 1, angles computed for the other equilibrium assumptions differ greatly from those computed for set 1; for the conditions considered, the assumption of complete interphase equilibrium in the shock wave lowered the predicted shock wave angle almost 14° from the value predicted for no interchange in the shock wave. As would be anticipated, agreement between the experimentally determined and theoretically computed angles was not as good as that obtained with air alone. Part of this difference may be attributed to the fact that interphase equilibrium during expansion was not completely attained; however, particles as small as 0.1μ would be expected to closely approach equilibrium.

In addition to the experimental difficulties previously discussed for air, measurement of shock wave angles in the two-phase exhaust was considerably more difficult, as can be seen from the shadowgraphs in Fig. 4. Also, maintaining constant solid feed rates of up to 0.25 lb/sec and accurately determining them proved difficult. The fine grinding abrasives used in many of the runs costs $15.00 per pound, so long runs to establish certain steady-state conditions were not feasible. Additional experimental difficulties encountered during solids addition were fluctuation in static pressure (up to 3 psi) and air flow rate and erosion of the leading edge of the wedge.

The reasonably successful runs presented in Table 5 represent almost one third the total made with solids. Normally where large deviations in predicted and measured angles occurred, good agreement could be obtained by assuming a lower solids concentration than that computed from the rpm of the feeder valve and the measured bulk density of the solids—the method adopted as best for the short run intervals involved.

An important objective of the experimental program was to confirm or disprove the theoretical predictions concerning the interphase interchange that occurs between phases in shock waves. The agreement between measured and predicted shock wave angles obtained in some of the runs supports the reasonable theoretical predictions. Experimental problems can readily explain the lack of close agreement in the other runs; however, additional data will be required to conclusively prove the predictions.

Modification of the feeder valve to allow direct calibration and more uniform operation is currently in progress. More accurately determined solids concentrations should result from this modification.

METHOD FOR EXPERIMENTAL DETERMINATION OF VELOCITIES AND TEMPERATURES IN TWO-PHASE SUPERSONIC EXHAUST

The velocity and temperature of each phase at the exhaust plane of the nozzle may be experimentally determined for particle sizes large enough so that essentially no interphase interchange of heat or momentum occurs in the shock wave. Measurements required are the pressure distribution along the nozzle, the semiapex angle of the wedge positioned at the exhaust plane of the nozzle, the angle of the attached shock wave formed on the wedge in the supersonic two-phase exhaust, and the flow rate of each phase.

The gas-phase Mach number, defined as the velocity of the gas divided by the speed of sound in the gas, may be determined for a perfect gas from Eq. 7 by solving for the Mach number

$$M_1 = \left[\sin^2\theta - \frac{\gamma+1}{2}\left(\frac{\tan\theta}{\cot\sigma + \tan\theta}\right)\right]^{-1/2} \qquad [39]$$

since the shock wave angle is measured and the wedge angle and γ of the gas are known. This equation is applicable as long as the solid phase does not influence shock wave angles. If the static pressure at the exit plane of the nozzle is measured, the velocity of the gas V_{g_1} may be calculated using the perfect gas law, continuity, and the definition of gas-phase Mach number.

The perfect gas law may be written

$$P_1 = \frac{\rho_1 R T_{g_1}}{MW} \qquad [40]$$

The equation of continuity for the gas phase is[4]

$$\dot{m}_g = \rho_1 V_{g_1} A_1 \qquad [41]$$

Eliminating ρ_1 from these equations gives

$$P_1 = \left(\frac{\dot{m}_g R}{A_1 MW}\right)\frac{T_{g_1}}{V_{g_1}} \qquad [42]$$

Using the definition of gas-phase Mach number gives for a perfect gas

$$M_1{}^2 = \frac{V_{g_1}{}^2}{a_1{}^2} = \frac{V_{g_1}{}^2 MW}{\gamma g_c R T_{g_1}} \qquad [43]$$

Eqs. 42 and 43 can be solved for V_{g_1} by eliminating T_{g_1}; there results

$$V_{g_1} = \gamma g_c M_1{}^2 P_1\left(\frac{A_1}{\dot{m}_g}\right) \qquad [44]$$

The gas-phase temperature can then be computed using Eq. 43.

---

[4] The negligible decrease in cross-sectional area due to the presence of the solids is neglected.

Measurement of the static pressure distribution along the nozzle allows calculation of the solid-phase temperature and velocity from momentum and total energy balances. The integrated form of the momentum equation is

$$\frac{\dot{m}_g}{g_c}\left(V_{g_1} - V_{g_0}\right) + \frac{\dot{m}_s}{g_c}\left(V_{s_1} - V_{s_0}\right) = - \int_{P_0}^{P_1} AdP \qquad [45]$$

The right-hand side may be evaluated as

$$- \int_{P_0}^{P_1} AdP = - P_1 A_1 + P_0 A_0 + \int_{A_0}^{A_1} PdA \qquad [46]$$

if the static pressure is a known function of the area. Alternatively, either integral may be evaluated by graphical integration. The only unknown in Eq. 45 is V_{s_1}, the velocity of the solid phase at the exit plane, for which the equation may be solved.

The total energy balance allows calculation of the temperature of the solid phase. The integrated form of the energy equation is

$$\frac{\dot{m}_g}{2g_c J}\left(V_{g_1}{}^2 - V_{g_0}{}^2\right) + \dot{m}_g (C_p)_g \left(T_{g_1} - T_{g_0}\right) + \frac{\dot{m}_s}{2g_c J}\left(V_{s_1}{}^2 - V_{s_0}{}^2\right)$$
$$+ \dot{m}_s\left[A_s\left(T_{s_1} - T_{s_0}\right) + \frac{B_s}{2}\left(T_{s_1}^2 - T_{s_0}^2\right) + C_s\left(\frac{1}{T_{s_1}} - \frac{1}{T_{s_0}}\right)\right] = 0 \qquad [47]$$

The solid's temperature T_{s_1} is the only unknown in this equation. Solution of these equations is facilitated by the use of a digital computer.

The effect of small changes in shock wave angle on the Mach number, velocity, and temperature of the gas phase at the exit plane of the nozzle was determined using Eqs. 39, 43, and 44. Shock wave angles, slightly different from those calculated for an equilibrium expansion (assumption set 1, Table 1), were assumed. In calculating velocities and temperatures, the additional assumptions were made that the pressure at the exit plane remained constant at 14.7 psia and that the gas flow rate per unit area remained equal to its value in the equilibrium expansion. These assumptions appear reasonable approximations for shock wave angles close to those of the equilibrium expansion. Results are presented in Table 6.

The results show that for the 10-deg wedge angle approximately 2% variation in gas-phase velocity and temperature would result from a one-degree change in shock wave angle. Larger wedge angles, up to the point of shock wave detachment, would result in even less variation in gas-phase conditions for a one-degree variation in shock wave angle. These results are encouraging, since shock wave angles determined to an accuracy of within one degree in a two-phase exhaust appear possible.

A theoretical program in which the velocity and temperature of each phase at the exit plane of the nozzle is computed has recently been completed. Assuming one-dimensional flow, expansion of a two-phase system through a supersonic nozzle is solved by a stepwise numerical integration. The major objective of future work is to obtain confirmation of experimentally determined conditions in a supersonic exhaust with this theoretical program. Uncertainties as to the validity of the heat transfer and drag correlations may be resolved in this manner. Perhaps improved correlations, applicable to the small particle sizes present in rocket exhausts, will be obtained.

NOMENCLATURE

A = cross-sectional area of nozzle, ft^2
A_o = Avogadro's number, molecules/lb-mole
a = speed of sound, fps
A_s, B_s, C_s = constants in specific heat equation
A_t, B_t, C_t = constants in specific heat equation
B = constant defined in Eq. 21, sec^{-1}
C = root-mean square molecular velocity, fps
$\bar{c}$ = mean molecular velocity, fps
C_D = drag coefficient, dimensionless
C_p = specific heat at constant pressure, Btu/(lbm-°R)
C_s = specific heat of solid, Btu/(lbm-°R)
C_v = specific heat at constant volume, Btu/(lbm-°R)
C_v' = translational specific heat of gas molecules at constant volume, Btu/(molecule-°R)
C_v'' = translational specific heat of gas at constant volume, 3R/2JMW Btu/(lbm-°R)
F_D = drag forces on a particle, lbf
g_c = dimensional constant, 32.174 (lbm-ft)/(lbf-sec^2)
h = heat transfer coefficient, Btu/(sec-ft^2-°R)
$\tilde{h}$ = time-average heat transfer coefficient, Btu/(sec-ft^2-°R)
J = mechanical equivalent of heat, 778.2 (ft-lbs)/Btu

k = thermal conductivity, Btu/(sec-ft-°R)
k_m = Cunningham correction factor to Stokes Law, dimensionless
M = Mach number, dimensionless
$\dot{m}$ = mass flow rate, lbm/sec
MW = molecular weight of gas, lbm/(lb-mole)
n = number of molecules per unit volume, molecules/ft^3
n_g = moles of gas per unit mass of gas plus solid, (lb-moles)/lbm
Nu = Nusselt number, dimensionless
N_s = number of molecular collisions with a surface per unit time per unit area, molecules/(sec-ft^2)
P = absolute pressure, lbf/ft^2
Pr = Prandtl number, dimensionless
Q = heat transferred between gas molecules and a surface, Btu
R = universal gas constant, 1545.4 (ft-lbf)/(lb-mole-°R)
Re_p = particle Reynolds number, dimensionless
r = particle radius, ft
S = surface area of solid particle, ft^2
ΔS = entropy change, Btu/(lbm-°R)
T = absolute temperature, °R
t = time, sec
U = velocity of particles relative to gas phase downstream of shock wave, fps
V = velocity, fps
x = perpendicular distance from shock wave, ft

α = thermal accommodation coefficient, dimensionless
γ = specific heat ratio C_p/C_v, dimensionless
θ = shock wave angle, deg
λ_m = mean free path of gas molecules, ft
μ = viscosity of gas, lbm/sec-ft
ρ = density, lbm/ft^3
σ = semiapex angle of wedge, deg

Subscripts

0 = chamber
1 = exit plane of nozzle
2 = immediately downstream of shock wave
g = gas phase
i = initial, when entering shock wave
N = normal to shock wave
s = solid phase
T = tangent to shock wave
t = gas and solid phases considered together

REFERENCES

1 J. Hilsenrath, C.W. Beckett, W.S. Benedict, L. Fano, H.J. Hoge, J.F. Masi, R.L. Nuttall, Y.S. Touloukian, H.W. Woolley: Tables of Thermal Properties of Gases. National Bureau of Standards Circular 564, 1955, pp. 25-62.

2 C.W. Beckett: Preliminary Report on the Thermodynamic Properties of Lithium, Beryllium, Magnesium, Aluminum, and Their Compounds with Hydrogen, Oxygen, Nitrogen, Fluorine, and Chlorine. National Bureau of Standards Rept. 6484, 1959, Table 2-2.

3 Ames Research Staff: Equations, Tables, and Charts for Compressible Flow. National Advisory Committee for Aeronautics Rept. 1135, 1953, p. 9.

4 E.F. Greene and D.F. Hornig: The Shape and Thickness of Shock Fronts in Argon, Hydrogen, Nitrogen, and Oxygen. Jour. Chem. Phys., April 1953, vol. 21, no. 4, pp. 617-624.

5 J.S. Serafini: Impingement of Water Droplets on Wedges and Double-Wedge Airfoils at Supersonic Speeds. National Advisory Committee for Aeronautics Rept. 1159, 1954.

6 J.H. Perry: Chemical Engineers' Handbook, 3rd Ed., p. 1019. McGraw-Hill Book Co. Inc., New York, 1950.

7 W.E. Ranz and W.R. Marshall Jr.: Evaporation from Drops, Part II. Chemical Engineering Progress, April 1953, vol. 48, pp. 173-180.

8 P.L. Dillon and L.E. Line Jr.: Heat Transfer Between Solid Particles and Gas in a Rocket Nozzle, Jet Propulsion, December 1956, vol. 26, p. 1091.

9 L. Loeb: Kinetic Theory of Gases, 1st Ed., p. 96. McGraw-Hill Book Co. Inc., New York, 1927.

Table 1 Effect of Equilibrium Assumptions on Characteristics of 30% Al_2O_3 in Air Flowing Over 10-Deg Wedge: Chamber Pressure = 94.7 psia, Chamber Temperature 545°R (85°F), Exhaust Pressure 14.7 psia

Characteristics	Complete Heat and Momentum Interchange Between Phases in Nozzle		No Heat or Momentum Interchange Between Phases in Nozzle	
	No Heat or Momentum Interchange in Shock Wave	Complete Heat and Momentum Interchange in Shock Wave	No Heat or Momentum Interchange in Shock Wave	Complete Heat and Momentum Interchange in Shock Wave
Set number	1	2	3	4
Gas temperature,[a] T_1, °R	360	360	320	320
Specific heat ratio, γ_1	1.396	1.306	1.396	1.318
Molecular weight, MW or $\frac{1}{n_g}$	29.0	41.4	29.0	41.4
Speed of sound, a_1, fps	928	751	876	712
Gas velocity, V_1, fps	1415	1415	1645	1645
Mach number, M_1	1.525	1.884	1.878	2.310
Shock wave angle, θ	55°1'	41°22'	41°59'	33°49'

---

[a] Subscript 1 refers to conditions at exit plane of nozzle.

Table 2 Effect of Equilibrium Assumptions on Characteristics of 30% Al_2O_3 in Air Flowing Over 10-Deg Wedge: Chamber Pressure = 94.7 psia, Chamber Temperature 545°R (85°F), Exhaust Pressure 14.7 psia

	Complete Heat and Momentum Interchange Between Phases in Nozzle		No Heat or Momentum Interchange Between Phases in Nozzle	
Characteristics	Complete Thermal Equilibrium in Shock Wave with no Momentum Interchange	Complete Momentum Equilibrium in Shock Wave with no Thermal Interchange	Complete Thermal Equilibrium in Shock Wave with no Momentum Interchange	Complete Momentum Equilibrium in Shock Wave with no Thermal Interchange
Set number	5	6	7	8
Gas temperature,[a] T_1, °R	360	360	320	320
Specific heat ratio, γ_1	1.306	1.396	1.318	1.396
Speed of sound, a_1, fps	898	777	851	733
Gas velocity, V_1, fps	1415	1415	1645	1645
Mach number, M_1	1.577	1.822	1.934	2.244
Shock wave angle, θ	51°24'	43°26'	40°18'	35°6'

---

[a] Subscript 1 refers to conditions at exit plane of nozzle.

Table 3 Estimate of Percent Equilibrium Attained when 0.1μ Al_2O_3 Particles Traverse a Shock Wave

Type of Equilibrium Considered	Percent Equilibrium Attained in Shock Wave
Velocity	0.05
Thermal	
Heat transfer coefficient correlation	1.18
Molecular collision model	
$\alpha = 1.0$	0.27
$\alpha = 0.1$	0.03

Table 4 Comparison of Measured and Computed Shock Wave Angles for Air Alone

Wedge[a] Angle	Measured Shock Wave Angle	Computed[b] Shock Wave Angle	Wedge[a] Angle	Measured Shock Wave Angle	Computed[b] Shock Wave Angle
5°39'	38°11'	37°54'	4°43'	36°31'	36°58'
6°31'	39°0'	38°47'	5°9'	38°11'	37°23'
13°34'	47°16'	46°59'	12°13'	45°12'	45°8'
9°50'	42°42'	42°9'	11°14'	45°46'	43°52'
7°4'	40°1'	39°23'	12°44'	45°12'	45°33'
2°50'	35°50'	35°11'	12°13'	45°15'	44°52'
11°13'	44°37'	43°50'	12°28'	45°18'	45°12'
13°8'	45°50'	46°22'	12°44'	44°40'	45°33'
5°45'	38°5'	38°0'	12°28'	44°13'	45°12'
3°59'	37°9'	36°15'	12°44'	45°4'	45°33'

---

[a] Each group of two is for a single run with a double wedge.

[b] Chamber pressures, 93 to 95 psia; exhaust pressures, 14.7 psia.

Table 5 Comparison of Measured and Computed Shock Wave Angles for Two-Phase Systems Containing 0.1μ Al_2O_3[a]

Concentration Al_2O_3, %	Wedge Angle[b]	Measured Shock Wave Angle	Computed[c] Shock Wave Angle
29.0	5°53' 4°45'	48°15' 46°52'	47°55' 46°23'
22.0	6°26' 4°54'	45°12' 44°22'	46°27' 44°30'
11.3	5°25' 4°41'	38°49' 38°41'	40°20' 39°34'
28.9	5°26' 4°32'	44°18' 42°47'	46°44' 45°48'
22.8	5°46' 6°10'	44°15' 43°21'	45°1' 45°30'
16.8	5°25' 4°41'	40°49' 37°28'	42°6' 41°17'
27.0	5°45' 3°59'	47°15' 41°32'	46°51' 44°36'
22.7	5°46' 6°10'	41°18' 42°8'	44°56' 45°27'
28.8	12°31' 12°42'	54°8' 55°30'	60°34' 61°21'

---

[a] Nominal size specified by supplier.

[b] Each group of two is for a single run with a double wedge.

[c] Assuming complete heat and momentum interchange between phases in nozzle and no interchange in the shock wave. Chamber pressure, 93 to 95 psia; exhaust pressures, 14.7 psia.

Table 6 Effect of Shock Wave Angle on Mach Number, Velocity, and Temperature of Gas Phase for 10-Deg Wedge Angle and 30% Al_2O_3 in Air[a]

Shock Wave Angle, deg	Gas-Phase Mach Number	Gas-Phase Velocity, fps	Gas-Phase Temperature, °R	Change in Velocity & Temperature from Equilibrium Expansion, %
		Equilibrium Expansion		
55[b]	1.525	1418	360	-
		Nonequilibrium Expansion		
54	1.542	1450	368	2.3
53	1.561	1485	377	4.7
56	1.509	1389	353	2.0
57	1.495	1362	346	4.0

---

[a] Exhaust pressure assumed to be 14.7 psia; gas-phase mass flow rate per unit area assumed constant.

[b] This angle has been rounded off so that the equilibrium conditions differ slightly from those of assumption set 1 in Table 1.

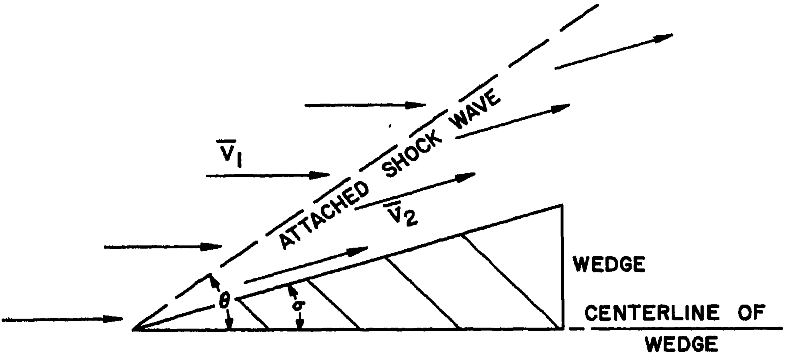

Fig. 1 Schematic diagram showing gas-phase velocities upstream and downstream of a two-dimensional wedge in supersonic exhaust: shock wave angle, θ; semiapex wedge angle, σ

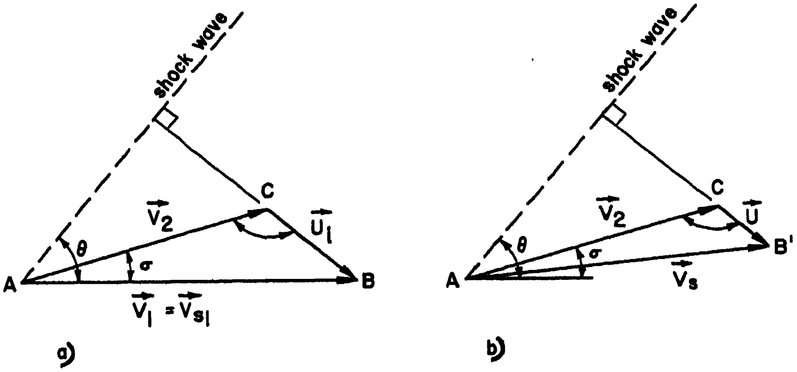

Fig. 2 Relationship between gas-phase velocities and particle velocity. a) Entering shock wave; b) downstream of shock wave

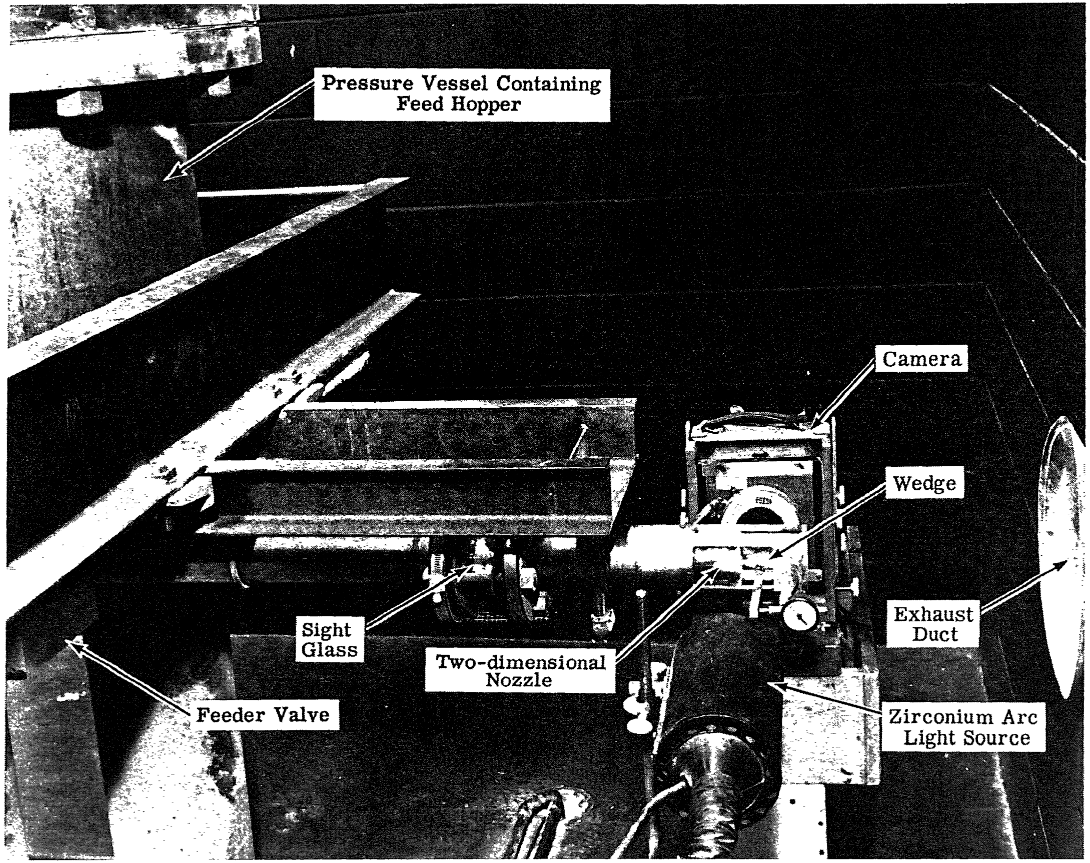

Fig. 3 Experimental apparatus for determining shock wave angles in supersonic exhaust

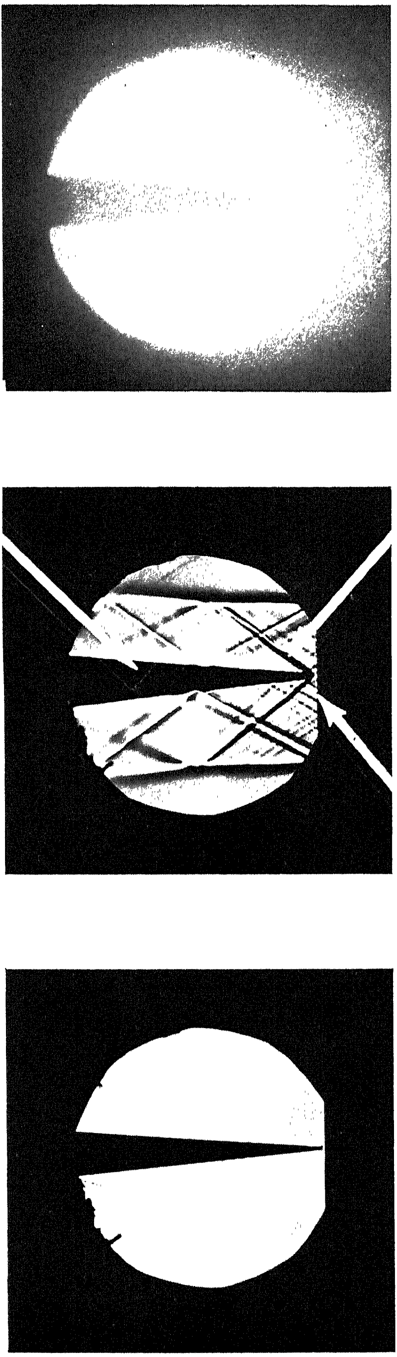

No flow

Attached shock wave with air alone

Attached shock wave with 27% 0.1μ Al_2O_3 and air

Fig. 4 Typical shadowgraphs showing double wedge positioned at exit plane of nozzle

FLOW OF GAS-PARTICLE MIXTURES IN AXIALLY SYMMETRIC NOZZLES

James R. Kliegel and Gary R. Nickerson

Space Technology Laboratories Inc., Los Angeles, Calif.

ABSTRACT

A previous study of one-dimensional gas-particle nozzle flows has been expanded to treat axially symmetric nozzle flows. Comparisons between calculated and experimentally measured nozzle efficiencies are given for a metallized double base propellantswhose exhaust contains 38% condensed oxides. It is shown that the theory predicts the performance of this propellant in nozzles of greatly different size, shape and expansion ratio, within the limits of the experimental measurements. It is concluded that the theory adequately describes the flow of gas-particle mixtures in axially symmetric nozzles.

INTRODUCTION

Experience has shown that the efficiency of metallized propellants (delivered impulse/theoretical impulse) is lower than the efficiency of nonmetallized propellants. This decreased efficiency has been found to be approximately proportional to the particle weight fraction in the exhaust gases. In addition, performance losses have been observed when using optimum contoured nozzles (calculated assuming gas-particle equilibrium) with metallized propellants. These facts suggest that nonequilibrium gas-particle effects should be considered when making performance predictions for metallized propellants. A study (1)[1] was first made of one-dimensional gas-particle nozzle flows. It was found that gas-particle nonequilibrium effects become important in metallized propellants if the

---

J. R. Kliegel and G. R. Nickerson are Members of the Technical Staff. Paper presented at the ARS Propellants, Combustion and Liquid Rockets Conference, Palm Beach, Fla., April 26-28, 1961. This research sponsored by Air Force Ballistic Missile Division Contract No. AF 04(694)-1.

[1] Numbers in parentheses indicate references at end of paper.

particle diameter is greater than 1μ. For larger particle sizes, the predicted nonequilibrium effects were in qualitative agreement with experimental results. The present investigation is essentially an extension of the above study to axially symmetric gas-particle nozzle flows.

CHARACTERISTIC RELATIONSHIPS OF GAS-PARTICLE SYSTEMS

The equations governing the flow of a gas-particle mixture have been previously derived (2) and are given below for axially symmetrical flows

$$(\rho_g u_g)_z + \frac{1}{r}(r\rho_g v_g)_r = 0 \qquad [1]$$

$$(\rho_p u_p)_z + \frac{1}{r}(r\rho_p v_p)_r = 0 \qquad [2]$$

$$\rho_g\left[u_g(u_g)_z + v_g(u_g)_r\right] + \frac{9}{2}\frac{\mu_g \rho_p f_p}{m_p r_p^2}(u_g - u_p) + (P_g)_z = 0 \qquad [3]$$

$$\rho_g\left[u_g(v_g)_z + v_g(v_g)_r\right] + \frac{9}{2}\frac{\mu_g \rho_p f_p}{m_p r_p^2}(v_g - v_p) + (P_g)_r = 0 \qquad [4]$$

$$u_g(P_g)_z + v_g(P_g)_r - \gamma_g R T_g\left[u_g(\rho_g)_z + v_g(\rho_g)_r\right]$$

$$- \frac{9}{2}\frac{\mu_g \rho_p f_p}{m_p r_p^2}(\gamma_g - 1)\left[(u_g - u_p)^2 + (v_g - v_p)^2 + \frac{2}{3}\frac{g_p}{f_p}\frac{c_{pg}}{Pr}(T_p - T_g)\right] = 0 \qquad [5]$$

$$P_g = \rho_g R T_g \qquad [6]$$

$$u_p(u_p)_z + v_p(u_p)_r = \frac{9}{2}\frac{\mu_g f_p}{m_p r_p^2}(u_g - u_p) \qquad [7]$$

$$u_p(v_p)_z + v_p(v_p)_r = \frac{9}{2}\frac{\mu_g f_p}{m_p r_p^2}(v_g - v_p) \qquad [8]$$

$$u_p(h_p)_z + v_p(h_p)_r = -3\frac{\mu_g g_p}{m_p r_p^2}\frac{c_{pg}}{Pr}(T_p - T_g) \qquad [9]$$

where

$$T_p = T_{pm} + \frac{h_p - h_{pl}}{c_{pl}} \qquad h_p \geqslant h_{pl} \qquad [10a]$$

$$T_p = T_{pm} \qquad h_{pl} > h_p \geqslant h_{ps} \qquad [10b]$$

$$T_p = \frac{h_p}{c_{ps}} \qquad h_{ps} > h_p \qquad [10c]$$

For simplicity of presentation, only one particle size will be considered in the derivation of the characteristic relationships of gas-particle systems in this report. Complete details of the theoretical treatment of gas-particle flows, including consideration of a particle size distribution in the flow, are given in Ref. 2. Unless otherwise noted, the calculations presented in this paper consider the measured particle size distribution (3) present in the flow.

The basic assumptions made in deriving Eqs. 1-10 are: 1) there are no mass or energy losses from the system; 2) the particles do not interact; 3) the thermal (Brownian) motion of the particles does not contribute to the pressure of the system; 4) the internal temperature of the particles is uniform; 5) energy exchange occurs between the particles and the gas only by convection; 6) the gas is considered to be a perfect gas of constant composition; 7) the gas is inviscid except for the drag it exerts on the particles; 8) the thermal heat capacities of the gas and particles are constant; and

9) the volume occupied by the particles is negligible.

These same assumptions have been used in previous studies (1, 4) of the one-dimensional flow of gas-particle systems.

It has been found (2) that the complete system of characteristics of Eqs. 1-10 are as follows.

Along Gas Streamlines

$$\frac{dr}{dz} = \frac{v_g}{u_g} \qquad [11]$$

$$\rho_g\left[u_g\,du_g + v_g\,dv_g\right] + dP_g = -\frac{9}{2}\,\frac{\mu_g\rho_p f_p}{m_p r_p^2}\left[(u_g-u_p)\,dz + (v_g-v_p)\,dr\right] \qquad [12]$$

$$\frac{dP_g}{P_g} - \gamma_g\frac{d\rho_g}{\rho_g} = -\frac{9}{2}\,\frac{\mu_g\rho_p f_p}{m_p r_p^2}\,\frac{(\gamma_g-1)}{P_g u_g}\left[(u_g-u_p)^2+(v_g-v_p)^2+\frac{2}{3}\,\frac{g_p}{f_p}\,\frac{C_{pg}}{Pr}(T_p-T_g)\right]dz \qquad [13]$$

Along Gas Mach Lines

$$\frac{dr}{dz} = \frac{u_g v_g \pm \gamma_g R T_g\sqrt{M^2-1}}{u_g^2-\gamma_g R T_g} \qquad [14]$$

$$\left(u_g\frac{dr}{dz}-v_g\right)\left\{\frac{9}{2}\,\frac{\mu_g\rho_p f_p}{m_p r_p^2}(\gamma_g-1)\left[(u_g-u_p)^2+(v_g-v_p)^2+\frac{2}{3}\,\frac{g_p}{f_p}\,\frac{C_{pg}}{Pr}(T_p-T_g)\right]dz - u_g\,dP_g\right\}$$

$$+\gamma_g R T_g\left\{\frac{9}{2}\,\frac{\mu_g\rho_p f_p}{m_p r_p^2}\left[(u_g-u_p)\,dr-(v_g-v_p)\,dz\right]+\rho_g\left[v_g\,du_g-u_g\,dv_g\right.\right.$$

$$\left.\left.-\frac{v_g}{r}(u_g\,dr-v_g\,dz)\right]+dP_g\frac{dr}{dz}\right\} = 0 \qquad [15]$$

Along Particle Streamlines

$$\frac{dr}{dz} = \frac{v_p}{u_p} \qquad [16]$$

$$u_p \, du_p = \frac{9}{2} \frac{\mu_g f_p}{m_p r_p^2} (u_g - u_p) \, dz \qquad [17]$$

$$v_p \, dv_p = \frac{9}{2} \frac{\mu_g f_p}{m_p r_p^2} (v_g - v_p) \, dr \qquad [18]$$

$$u_p \, dh_p = -3 \frac{\mu_g g_p}{m_p r_p^2} \frac{c_{pg}}{Pr} (T_p - T_g) \, dz \qquad [19]$$

$$d\psi_p = 0 \qquad [20]$$

where ψ_p is the particle stream function defined by

$$(\psi_p)_r = r \rho_p u_p \quad , \quad (\psi_p)_z = - r \rho_p v_p \, .$$

It is seen that all the characteristics of the equations governing the flow of a gas-particle system are real if the flow is supersonic ($M > 1$). Using Eqs. 11-20, the supersonic flow of a gas-particle mixture may be computed using the method of characteristics. Fig. 1 illustrates the characteristic mesh.

It is interesting to note that one of the characteristic directions of Eqs. 11-20 is identical with the gas Mach lines and is independent of the presence of the particles. This result is similar to the situation found in reacting gas mixtures (5) in which one of the characteristic directions is also identical with the gas Mach lines and is independent of chemical reactions occurring in the flow.

TRANSONIC FLOW OF A GAS-PARTICLE SYSTEM

To solve the equations governing the transonic flow of a gas-particle mixture is an extremely formidable task. For perfect gas flows, approximate transonic solutions can be obtained by taking perturbations about the sonic velocity (6, 7). This method is applicable for perfect gas flows because the throat conditions are essentially determined by the nozzle geometry in the immediate neighborhood of the throat and are quite in-sensitive to the nozzle inlet geometry. This is not true for gas-particle flows, because the throat conditions are determined by the nozzle inlet geometry (1). Thus to obtain initial conditions to start a characteristic calculation for a gas-particle system, the equations for the complete subsonic and transonic flow field in the nozzle inlet and throat regions must be solved.

Interesting qualitative information about the transonic flow of a gas-particle mixture can be obtained by such a perturbation method, however. A gas-particle nozzle flow that is essentially in equilibrium will now be considered. The gas properties in the transonic throat region can be approximated by (1, 6)

$$\frac{u_g}{u_g^*} = 1 + \alpha \frac{z}{r^*} + \frac{\bar{\gamma}+1}{8} \alpha^2 \frac{r^2}{r^{*2}} \qquad [21]$$

$$\frac{v_g}{u_g^*} = \frac{\bar{\gamma}+1}{4} \alpha^2 \frac{zr}{r^{*2}} + \frac{(\bar{\gamma}+1)^2}{16} \alpha^3 \frac{r^3}{r^{*3}} \qquad [22]$$

where $\alpha = \sqrt{\frac{2}{\bar{\gamma}+1} \frac{r^*}{R^*}}$ and the nozzle throat location is given by

$$\frac{z^*}{r^*} = -\sqrt{\frac{\bar{\gamma}+1}{32} \frac{r^*}{R^*}} \qquad [23]$$

From Eqs. 7 and 8 it is found that to Sauer's order of approximation

$$\frac{u_p}{u_g^*} = K\left(1 + \alpha \frac{z}{r^*} + \frac{\bar{\gamma}+1}{8} \alpha^2 \frac{r^2}{r^{*2}}\right) \qquad [24]$$

$$\frac{v_p}{u_g^*} = K\left[\frac{\bar{\gamma}+1}{4} \alpha^2 \left(\frac{z}{r^*} - \frac{2}{9} \frac{m_p r_p^2}{\mu_g^* \rho_{bp}^*} \frac{u_g^*}{r^*}\right) \frac{r}{r^*} + \frac{(\bar{\gamma}+1)^2}{16} \alpha^3 \frac{r^3}{r^{*3}}\right] \qquad [25]$$

where $K = 1 - \frac{2}{9} \frac{m_p r_p^2}{\mu_g^* \rho_{bp}^*} \frac{u_g^*}{r^*} \alpha$, $\frac{2}{9} \frac{m_p r_p^2}{\mu_g^* \rho_{bp}^*} \frac{u_g^*}{r^*} << 1$.

Examination of Eqs. 24 and 25 shows that the particle and gas streamlines diverge in the throat region for all particle sizes even though the flow may be essentially in equilibrium. Thus the particles concentrate along the nozzle axis, greatly complicating the calculation of the gas-particle flow properties in the nozzle throat. This divergence is illustrated in Fig. 2.

It has been shown (1) that the Mach number in a gas-particle nozzle flow is less than one at the nozzle throat. For typical metallized propellants, calculations show that the Mach number is approximately 0.8 at the throat. Hence, the transonic zone in a gas-particle flow extends downstream of the throat. A discontinuity in the wall radius of curvature at the throat will therefore have a great influence on the flow. It will be extremely difficult to calculate the gas-particle flow properties in a throat region of a nozzle having different wall radii of curvatures upstream and downstream of the throat.

From this discussion, it is evident that only approximate solutions to the equations governing the transonic flow of a gas-particle system can be obtained. In order to reduce the complexity of the calculations, the nozzle inlet and throat geometry considered in this study consisted of a conical inlet section joined smoothly to a constant radius of curvature throat section. This geometry is shown in Fig. 3. It is believed that this simplified geometry adequately represents the inlet and throat geometry for nozzle configurations of interest.

APPROXIMATE METHOD FOR OBTAINING GAS-PARTICLE TRANSONIC FLOW CONDITIONS

The following method was used to obtain approximate initial conditions for the characteristic calculations. In the conical inlet section, the flow was assumed to be a one-dimensional sink flow. The equations governing the one-dimensional flow of a gas-particle system were solved to obtain the flow properties on the sink line. The gas properties in the throat region were approximated by the perfect gas relationships, and particle trajectories were calculated through the throat region to determine the particle properties along the initial line. An average expansion coefficient was used which approximated the gas-particle expansion, including the effects of gas-particle nonequilibrium (1).

The initial conditions thus determined were self-consistent as was evidenced by the fact that the characteristic calculations proceeded smoothly away from the initial line. Comparison of the nozzle weight flows obtained by the above method with those obtained by one-dimensional calculations shows that the two-dimensional weight flows are slightly less than the one-dimensional weight flows. This agrees with the results obtained (8) for perfect gases. In addition, the above method of obtaining the gas-particle flow properties along the initial line is exact for the case of gas-particle equilibrium. It is concluded that the gas-particle flow properties determined along the initial line by the above method are an adequate representation of the true flow properties for nozzle calculations.

COMPARISON OF EXPERIMENTAL NOZZLE FIRINGS WITH CALCULATED NOZZLE PERFORMANCE

The experimental nozzle firings that will be compared with the calculations are firings conducted by the Hercules Powder Co. The altitude nozzle firings were conducted at the Arnold Engineering Development Center, and the sea level nozzle firings were conducted at the Hercules facility in Baccus, Utah. Similar firings were made at both facilities, which allows direct comparison of firings at either site. Most of the altitude nozzle firings have been previously reported (9).

All of the firings were of short duration and were made with engines containing a metallized double base propellant whose combustion products contain 38% condensed metal oxides. Most of the firings were made with 40-lb charge (FPC) engines whose configuration is shown in Fig. 4. Various nozzle configurations were tested, and the parameters used to identify the nozzles are shown in Fig. 5.

All comparisons of experimental and calculated nozzle performances are made on the basis of engine efficiency (delivered or calculated impulse/theoretical impulse). It has been assumed that the calculated theoretical impulse is correct, and no allowance has been made for possible inaccuracies in this calculation.

In order to separate expansion losses from engine heat losses and nozzle friction, these quantities were calculated following the method suggested by Bartz (10). The calculated heat and friction losses, as well as the experimentally measured engine efficiencies, are given in Table 1 for a series of conical nozzles. The difference between the calculated heat and friction losses and the measured engine losses was assumed to be expansion loss due to gas-particle nonequilibrium in the nozzle.

Calculations of the expansion losses in these nozzles due to gas particle nonequilibrium in the nozzles are given in Table 2. These calculations were made assuming various particle size distributions present in the flow. The particle size distributions considered were the nominal particle size distribution measured during these firings (3) and possible particle size distributions (1σ light and 1σ heavy) within the accuracy of the measurements.

It is seen that within the accuracy with which the various quantities are known, the calculated losses due to gas-particle nonequilibrium in the nozzle are in reasonable agreement with the experimental measurements if the 1σ light particle size distribution is assumed present in the flow. Although the theory seems to overestimate the gas-particle nonequilibrium losses on the basis of nominal estimates of all quantities, it is felt that the agreement between the calculations and the experimental measurements is quite good, especially when it is considered that no allowance has been made for possible inaccuracies in the calculated theoretical impulses. In all further comparisons between the calculations and experimental measurements, it has been assumed that the 1σ light particle size distribution is present in the flow. In addition, the calculations have been adjusted slightly (less than 0.5% in all cases) to fit one of the experimental measurements in the set of nozzles being compared.

One of the more interesting predictions of the previous one-dimensional study (1) is that the throat conditions for a gas-particle exhaust mixture are fixed by the nozzle inlet geometry and that nozzle performance can be changed by changing only the nozzle inlet geometry. Table 3 compares the experimental and calculated performance for a set of cutoff nozzles ($\epsilon = 1$) in which only the wall radius of curvature in the throat section was varied. Table 4 compares the experimental and calculated performance of a set of nozzles in which only the nozzle inlet angle was varied. It is seen that the predicted variation of performance with changes in nozzle inlet geometry is confirmed by experiment.

Table 5 compares the performance of similar nozzles of different throat size with the calculated scaling effects. (The TPC engine is essentially a 1/3 scale FPC, and the Be-1 engine is similar to the ABL-X248 engine. Although these nozzles do not have identical inlets, calculations show that the performances of the TPC and Be-1 nozzles are identical with geometrically scaled FPC nozzles.) It is seen that the predicted scaling effects are confirmed by experiment.

Table 6 and 7 compare the experimental and calculated performance of conical and contoured nozzles of the same length and expansion ratio. It is seen that the calculations adequately predict the performance of the contoured nozzles. It is of interest to note that particle impingement occurred on the lips of the two contoured nozzles in Table 6. The calculations predicted particle impingement on the lip of the more highly contoured nozzle.

Table 8 compares one-dimensional and the axially symmetric calculations for a set of conical nozzles. It is seen that the one-dimensional calculations underestimate the expansion losses due to gas-particle nonequilibrium by approximately 0.75%. It appears that gas-particle nonequilibrium losses can be estimated adequately for conical nozzles through use of one-dimensional gas-particle calculations.

CONCLUSIONS

From the forementioned comparisons of experimental and calculated nozzle efficiencies of metallized propellants, it is concluded that the efficiency of these propellants can be predicted by considering engine heat and friction losses and expansion losses due to gas-particle nonequilibrium in the nozzle.

It has been shown that the theoretical predictions of the effects of the nozzle inlet and throat section, nozzle contouring, and nozzles size on performance are in reasonable agreement with experiment. It is concluded that present theoretical treatment adequately describes axially symmetric gas-particle nozzle flows.

ACKNOWLEDGMENTS

The authors would like to thank the Hercules Powder Co. for allowing the use of their experimental nozzle firings as examples in this report. The work of Loren Morey, Billings Brown, and Robert Barry in planning and conducting these nozzle tests is gratefully acknowledged.

NOMENCLATURE

C_D = particle drag coefficient
C_{pg} = gas heat capacity
C_{pl} = particle heat capacity ($T_p > T_{pm}$)
C_{ps} = particle heat capacity ($T_p < T_{pm}$)
f_p = ratio, $C_D/(C_D)_{Stokes}$
g_p = ratio, $Nu/(Nu)_{Stokes}$
h = film heat transfer coefficient
h_p = particle enthalpy
h_{pl} = particle enthalpy after melting ($T_p = T_{pm}$)
h_{ps} = particle enthalpy before melting ($T_p = T_{pm}$)
k_g = gas thermal conductivity
L = nozzle length
M = gas Mach number, $\sqrt{(u_g^2 + v_g^2)/\gamma_g R T_g}$
m_p = particle density
Nu = particle Nusselt number, $2hr_p/k_g$
P_g = gas pressure
Pr = gas Prandtl number $\mu_g C_{pg}/k_g$
R = gas constant
R^* = nozzle wall radius of curvature at nozzle throat
r = radial coordinate
r_p = particle radius
r^* = nozzle throat radius
T_g = gas temperature
T_p = particle temperature
T_{pm} = particle solidification temperature
U_g = gas axial velocity
U_p = particle axial velocity
V_g = gas radial velocity
V_p = particle radial velocity
z = coordinate in flow direction
γ_g = gas adiabatic expansion coefficient

$\bar{\gamma}$ = equilibrium expansion coefficient for gas-particle system

ϵ = nozzle expansion ratio

θ = conical nozzle cone angle

θ_e = nozzle exit lip angle

θ_i = nozzle inlet angle

θ_j = nozzle initial expansion angle

μ_g = gas viscosity coefficient

ρ_g = gas density

ρ_p = particle density in the gas (based on gas volume)

ψ_p = particle stream function

Superscript

$*$ = throat conditions

REFERENCES

1 J.R. Kliegel: One Dimensional Flow of a Gas-Particle System. Paper No. 60-S, IAS 28th Annual Meeting, New York, January 1960.

2 J.R. Kliegel and G.R. Nickerson: Calculation of Gas-Particle Flows in Axially Symmetric Nozzles. Space Technology Laboratories Rept. 7106-0017-RU-000. To be issued.

3 B. Brown: Particle Size of Condensed Oxides from Combustion of Metalized Solid Propellants. 8th International Combustion Symposium, Pasadena, Calif., September 1960.

4 G.F. Carrier: Shock Waves in a Dusty Gas. Jour. Fluid Mech., July 1958 Vol. 4, p. 376.

5 W.G. Vincenti: Non-equilibrium Flow Over a Wavy Wall. Jour. Fluid Mech. Nov. 1958, Vol. 6, p. 481.

6 R. Sauer: General Characteristics of the Flow Through Nozzles at Near Critical Speeds. NACA TN 147, June 1947.

7 J.R. Kliegel: Higher Order Approximations to the Transonic Flow in a Nozzle Throat. Space Technology Laboratories Rept. 7106-0016-RU-000. To be issued.

8 K.W. Emmons: The Theoretical Flow of a Frictionless, Adiabatic, Perfect Gas Inside of a Two-Dimensional Hyperbolic Nozzle. NACA TN 1003, May 1946.

9 R. Winer and L. Morey: Nozzle Design for Solid Propellant Rockets. Preprint 1046-60, ARS Solid Propellant Rocket Research Conference, Princeton, N.J., Jan. 28-29, 1960.

10 D.R. Bartz: A Simple Equation for Rapid Estimation of Rocket Nozzle Convective Heat Transfer Coefficients. Jet Propulsion, January 1957, vol. 27, p. 49.

Table 1 Measured Gas-Particle Nonequilibrium Expansion Losses in Conical Nozzles

ϵ	3.5	20	24
No. Firings	2	3	8
r^*	1.32 in.	1.32 in.	1.32 in.
R^*/r^*	2	2	2
θ_i	30°	30°	30°
θ	25.2°	21.5°	24°
Calculated Heat Losses	$0.6 \pm .2\%$	$0.8 \pm .2\%$	$0.9 \pm .3\%$
Calculated Friction Losses	$0.7 \pm .2\%$	$1.5 \pm .5\%$	$1.4 \pm .4\%$
Measured Engine Efficiency	$95.4 \pm .3\%$	$94.7 \pm .3\%$	$94.7 \pm .6\%$
Measured Expansion Losses	$3.3 \pm .7\%$	$3.0 \pm 1.0\%$	$3.0 \pm 1.3\%$

Table 1a Measured Gas-Particle Nonequilibrium Expansion Losses in Conical Nozzle

ϵ	24	24	24
No. Firings	3	2	2
r^*	1.32 in.	1.32 in.	1.32 in.
R^*/r^*	5	5	5
θ_i	30°	30°	30°
θ	12°	18°	24°
Calculated Heat Losses	1.3±.4%	1.1±.3%	1.0±.3%
Calculated Friction Losses	2.9±.9%	2.0±.6%	1.6±.5%
Measured Engine Efficiency	95.1±.3%	95.1±.3%	95.1±.3%
Measured Expansion Losses	0.7±1.6%	1.8±1.2%	2.3±1.1%

Table 2 Calculated Gas-Particle Nonequilibrium Expansion Losses in Conical Nozzles

ϵ	3.5	20	24
No. Firings	2	3	12
r^*	1.32 in.	1.32 in.	1.32 in.
R^*/r^*	2	2	2
θ_i	30°	30°	30°
θ	25.2°	21.5°	24°
Calculated Expansion Losses	5.0±1.0%	4.8±1.0%	4.9±1.0%

Table 2a Calculated Gas-Particle Nonequilibrium Expansion Losses in Conical Nozzles

ϵ	24	24	24
No. Firings	3	2	2
r^*	1.32 in.	1.32 in.	1.32 in.
R^*/r^*	5	5	5
θ_i	30°	30°	30°
θ	12°	18°	24°
Calculated Expansion Losses	3.5±1.0%	4.1±1.0%	4.6±1.0%

Table 3 Comparison of The Experimental and Calculated Effect of Changes in The Nozzle Throat Geometry

ϵ	1	1	1
No. Firings	1	3	3
r^*	1.32 in.	1.45 in.	1.32 in.
R^*/r^*	1	2	3
θ_i	30°	30°	30°
Measured Efficiency	91.5%	90.5±.4%	92.2±.4%
Calculated Efficiency	90.6%	91.3%	91.8%

Table 3a Comparison of The Experimental and Calculated Effect of Changes in The Nozzle Throat Geometry

ϵ	1	1	1	1
No. Firings	3	3	3	3
r^*	1.32 in.	1.32 in.	1.32 in.	1.32 in.
R^*/r^*	5	7	9	15
θ_i	30°	30°	30°	30°
Measured Efficiency	91.6±.3%	92.3±.5%	92.9±.3%	93.1±.5%
Calculated Efficiency	92.3%	92.6%	92.9%	93.2%

Table 4 Comparison of The Experimental and Calculated Effect of Changes in The Nozzle Inlet Angle

ϵ	3.5	3.5	3.5
No. Firings	1	3	3
r^*	1.32 in.	1.32 in.	1.32 in.
R^*/r^*	2	2	2
θ_i	5°	15°	30°
θ	15°	15°	15°
Measured Efficiency	96.0±.5%	95.4±.5%	95.0±.5%
Calculated Efficiency	95.7%	95.4%	95.2%

Table 5 Comparisons of Calculated and Experimental Effects of Changes in Nozzle Throat Radii

ϵ	3.5	3.5	24	24
Engine	TPC	FPC	BE-1[a]	FPC
No. Fired	3	3	2	8
r^*	0.47 in.	1.32 in.	2.50 in.	1.32 in.
R^*/r^*	2	2	2	2
θ_i	27.6°	30°	90°	30°
θ	15°	15°	24°	24°
Measured Efficiency	93.0±.3%	95.4±.3%	95.5±.3%	94.7±.5%
Calculated Efficiency	93.0%	95.4%	95.3%	94.7%

---

[a] Efficiency corrected for rubber liner loss.

Table 6 Comparison of Calculated and Experimental Effects of Nozzle Contouring

ϵ	24	24	24
No. Fired	8	8	3
r^*	1.32 in.	1.32 in.	1.32 in.
R^*/r^*	2	2	2
L/r^*	9.02	9.02	9.02
θ_i	30°	30°	30°
Contour	Cone	Rao	Mod. Rao
θ_j	24°	33.6°	45°
θ_e	24°	14.2°	12.4°
Measured efficiency[a]	100.0%	99.9%[b]	98.1%[b]
Calculated efficiency[b]	100.0%	100.1%	98.8%[b]

---

[a] Based on cone efficiency.

[b] Particle impingement on nozzle lip.

Table 7 Comparison of Calculated and Experimental Effects of Nozzle Contouring

ϵ	20	20	20
No. Fired	4	3	3
r^*	1.32 in.	1.32 in.	1.32 in.
R^*/r^*	2	2	2
L/r^*	9.21	9.21	9.21
θ_i	30°	30°	30°
Contour	Cone	Arc	Arc
θ_j	21.5°	23.5°	25.0°
θ_e	21.5°	19.5°	18.0°
Measured Efficiency[a]	100.0%	100.4%	100.7%
Calculated Efficiency[a]	100.0%	100.3%	100.5%

---

[a] Based on cone efficiency.

Table 7a Comparison of Calculated and Experimental Effects of Nozzle Contouring

ϵ	20	20
No. Fired	3	3
r^*	1.32 in.	1.32 in.
R^*/r^*	2	2
L/r^*	9.21	9.21
θ_i	30°	30°
Contour	Arc	Arc
θ_j	26.0°	27.0°
θ_e	17.0°	16.0°
Measured Efficiency[a]	100.7%	100.2%
Calculated Efficiency[a]	100.6%	100.3%

---

[a] Based on cone efficiency.

Table 8 Comparison of One-Dimensional and Two-Dimensional Calculated Conical Nozzle Efficiencys

ϵ	3.5	20	24
No. Firings	2	3	12
r^*	1.32 in.	1.32 in.	1.32 in.
R^*/r^*	2	2	2
θ_i	30°	30°	30°
θ	25.2°	21.5°	24°
Efficiency - 1D	100.5%	100.8%	100.8%
Efficiency - 2D			

Table 8a Comparison of One-Dimensional and Two-Dimensional Calculated Conical Nozzle Efficiencys

ϵ	24	24	24
No. Firings	3	2	2
r^*	1.32 in.	1.32 in.	1.32 in.
R^*/r^*	5	5	5
θ_i	30°	30°	30°
θ	12°	18°	24°
Efficiency - 1D	100.5%	100.7%	100.8%
Efficiency - 2D			

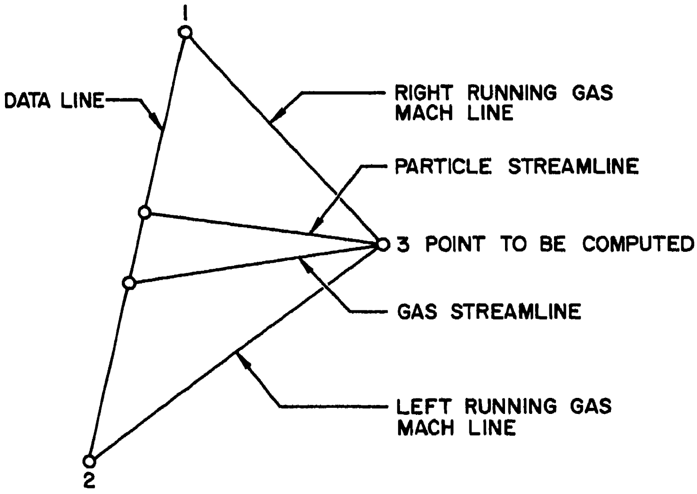

Fig. 1 Gas-particle characteristic mesh

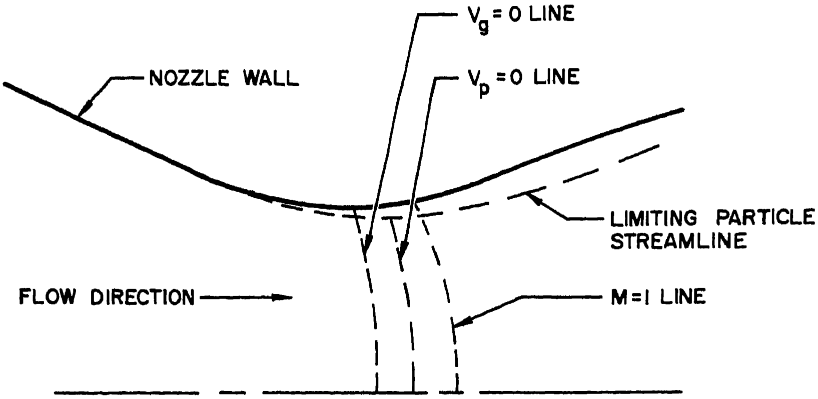

Fig. 2 Gas-particle transonic flow

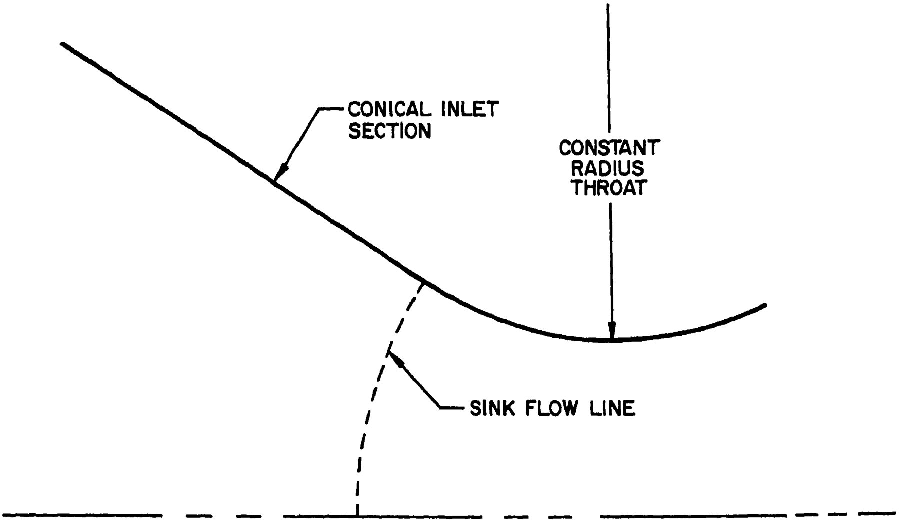

Fig. 3 Nozzle inlet and throat geometry

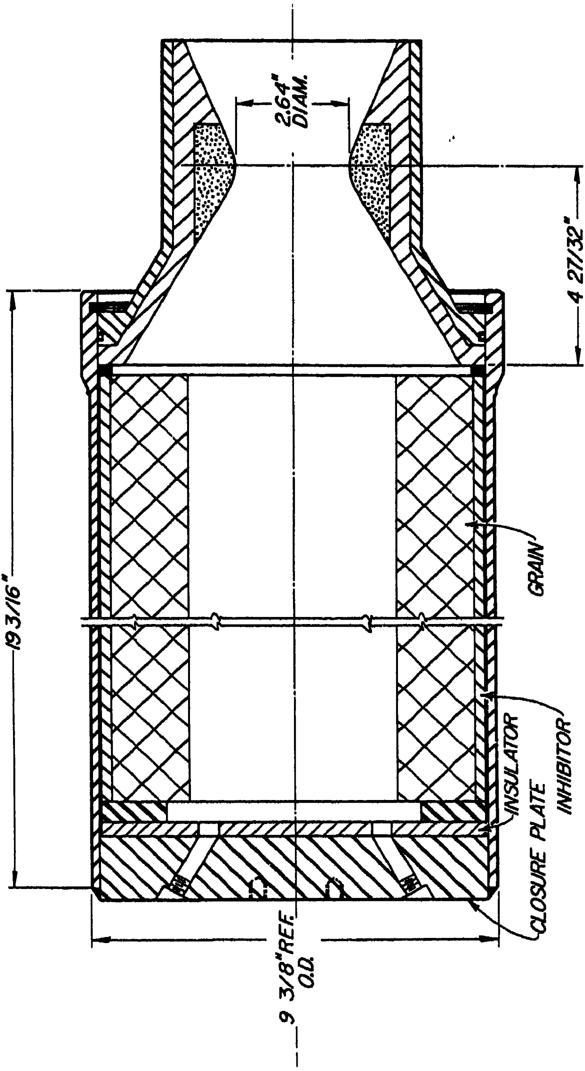

Fig. 4 Hercules FPC engine assembly

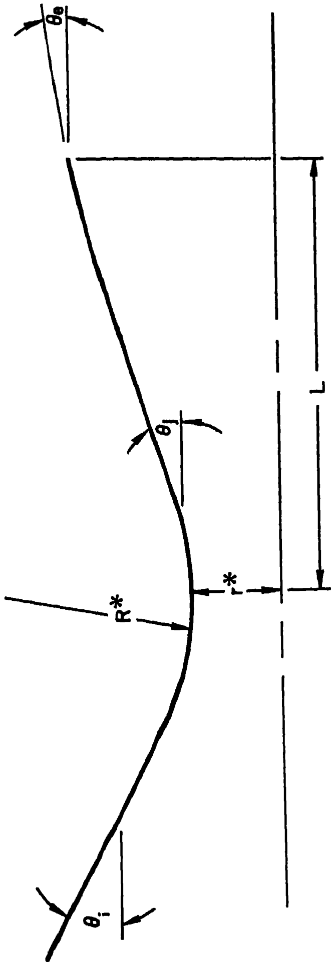

Fig. 5 Nozzle contour parameters

PARTICLE VELOCITY LAG IN METALIZED PROPELLANTS

B. Brown

Hercules Powder Co., Magna, Utah

ABSTRACT

The velocity of the condensed phase has been measured at the nozzle exit plane of small solid propellant rocket motors. It has been determined that the velocity lag is appreciable. The velocity lag and heat loss to the nozzle can account for the observed inefficiency of such rocket motors.

INTRODUCTION

Many solid propellants in use today contain metal powders as high impulse additives, which result in substantial quantities of metal oxides appearing as a condensed phase or phases in the exhaust products. Recently it has become of interest to increase the efficiency of solid propellant rocket motors, even though some are currently operating near the 95% efficiency level. It has been experimentally determined that the delivered specific impulse of metalized solid propellants begins to fall significantly below the calculated value as the percentage of metal is increased.

One plausible cause for reduced specific impulse is that the particles or droplets of condensed oxide do not achieve velocity equilibrium with the gases during their passage through the nozzle. This effect has been studied analytically by several authors, including Gilbert, Davis, and Altman (1),[1] Kliegel (2), and, most recently, Lype (3).

An equally plausible reason for the loss in specific impulse is combustion inefficiency, here defined as the nonachievement

---

B. Brown is Supervisor, Engineering Development, Bacchus Works. Paper presented at the ARS Solid Propellant Rocket Conference, Salt Lake City, Utah, Feb. 1-3, 1961.

[1] Numbers in parentheses indicate references at end of paper.

of chemical equilibrium among the combustion products.

The purpose of this investigation was to determine, if possible, which of these factors was most likely responsible for the observed inefficiency. It appeared that difficulties in the experimental techniques involved in determining the departure from chemical equilibrium (including frozen flow and relaxation phenomena) were almost insurmountable; hence it was decided to investigate the particle velocity lag first.

EXPERIMENTAL

In any consideration of particle velocity lag, the particle or droplet diameter is an important parameter. It was established in the first part of this investigation (and reported in Ref. 4) that the particles or droplets were smaller than had formerly been thought. A particle size distribution found to be typical of all solid propellant motors investigated is shown in Fig. 1. The mass mean diameter is seen to be somewhat less than 3 μ .

The firings in which velocity lag of the condensed phase was measured were performed at the Tooele Ordnance Depot, Tooele, Utah. A Miller-type framing camera operating at 10^6 frames per second and using Super Anscochrome 35 mm film was used. The camera is owned by the Navy and operated by personnel of the Intermountain Research Corp.

The equipment is illustrated schematically in Fig. 2. Backlighting was provided by light bombs formed from cardboard cylinders which confined the air shock resulting from the detonation of 3.5 lb of composition B explosive.

An assembly drawing of 40-lb charge (FPC) motor is shown in Fig. 3. This motor has a neutral burning grain and was developed primarily for ballistic evaluation. The nozzle has conical entrance and exit sections. The entrance cone has a half angle of 30^o and the exit cone, 15^o. The radius of curvature of the nozzle wall at the throat is twice the throat diameter. The throat diameter is varied to accommodate propellants having different burning rates. The exit cone in the nozzles used in these experiments was cut off at an expansion ratio $\epsilon = 3.5$.

The 10-lb charge (TPC) motor is similar, being scaled down in all dimensions from the FPC.

The modified FPC (FPC-BT) motor was identical to the standard model except for the approach section of the nozzle, which had a half angle of 5° instead of 30°, forming a short blast tube. The entrance to this section was rounded, using a 1-in. radius; consequently, the entrance presented a sudden constriction to flow, rather than the gradual transition of the conical approach section. The propellant used was a double base matrix containing aluminum.

Flame temperatures outside the nozzle were measured both by a two-color optical pyrometer (Shawmeter) and by interpreting the color temperature of the framing camera film. Care was taken to insure that measurements were made well upstream of the first shock wave. The shock raises the flame temperature several hundred degrees Kelvin. The error in these measurements is probably 100° K. Agreement between the two methods employed was usually closer.

Heat loss to the nozzle was measured in a third independent experiment by dropping the entire motor into a water calorimeter within one second after the end of burning and noting the temperature rise of the water. This simple method, which includes heat loss to the entire motor but neglects radiation loss from the nozzle both during and following firing, is capable of giving the order of magnitude results required.

A framing camera exposes approximately 23 frames per firing. Typical frames are shown in Fig. 4 for a 10-lb (propellant charge weight) motor (TPC) and in Fig. 5 for a 40-lb motor (FPC). Inhomogeneities or striations in the flame are more apparent in Fig. 4 but are discernible in all firings. When the position of any striation is tracked from frame to frame, it is seen to be moving at a substantial fraction of the calculated exit gas velocity. The striations are interpreted as being denser portions of the flame in which the concentration of the condensed phase is unusually high.

When the position of a striation is plotted vs. time for a TPC, data of Fig. 6 result. The slope of the curve is interpreted as particle or droplet velocity. The average velocity shown here is 4150 fps.

The change in slope is attributed to the acceleration of the particles, which is still taking place outside the nozzle. The acceleration indicated in Fig. 6 is of the order of 10^7 times gravity.

The longer FPC nozzle yields higher particle velocities, achieving 70% of the gas velocity with a standard (30° half angle) convergent nozzle section and up to 95% with a 5° half angle entrance section.

Flame temperatures as measured by optical methods outside the nozzle were only slightly higher than the calculated gas temperatures. The two-color optical pyrometer and the color temperature of the framing camera film gave concordant results. Both methods depend on radiation. Since the gas has negligible emissivity at the wavelengths used, whereas the condensed phase is highly opaque, the radiation temperature measured is nearly that of the condensed phase. It is concluded that the condensed phase, as observed outside the nozzle, is substantially in thermal equilibrium with the gas, and little thermal lag obtains.

Nozzle heat losses for the FPC motors were found to account for 1% of the loss of efficiency in motors using phenolic nozzles with graphite throat inserts and for 2% in motors having all carbon nozzles. The TPC motor has not been thus tested; however, because the smaller motor contains one fourth as much propellant but exposes one eighth as much nozzle area to the exhaust gases as does the FPC motor, it is expected that the heat losses of the two motors will be comparable.

DISCUSSION

The specific impulse for two-phase flow is given by the momentum balance

$$I = \frac{1}{g_c\,(\dot{w}_p + \dot{w}_g)} \quad (\dot{w}_g u_g + \dot{w}_p u_p) \qquad [1]$$

For a clean gas, this reduces to

$$I^* = \frac{u_g}{g_c} \qquad [2]$$

These equations are discussed by Altman (6). From these relations, it follows that the nozzle efficiency for two-phase flow in which the exit velocity of the condensed phase is lagging that of the gas is given by

$$\text{Eff} = \frac{I}{I^*} = 1 - \frac{\dot{w}_p}{\dot{w}_p + \dot{w}_g} \quad (1 - K_e) \qquad [3]$$

The important assumptions are that the flow is isentropic and that no temperature difference exists between particles and gas.

The experimental data are plotted in Fig. 7 for the conditions of the present investigation according to Eq. 3. The ordinate intercept has been moved down to 0.99 which represents the experimentally determined heat loss of the FPC nozzle. No allowance was made for wall friction, since its magnitude remains undetermined.

As might be expected, the longer nozzles resulted in higher particle exit velocities. Clearly, the TPC and standard FPC nozzles are too short to handle two-phase flow efficiently. A small improvement is noted in the efficiency in going from the TPC to the longer, though geometrically similar, FPC nozzle, with concurrent improvement in the condensed phase exit velocity. The contour of these nozzles was developed and standardized prior to the use of metal as an additive. The nozzles performed well with the nonmetalized propellants.

A greater increase in particle exit velocity is obtained by reducing the nozzle entrance angle, thus providing more time for particle acceleration. It should not be concluded that the present FPC-BT design illustrates the optimum contour for efficiency. The change has probably been too drastic. Further experiments are indicated. It is evident that the simple analysis based on the momentum balance alone is qualitatively correct. The agreement would be somewhat better if the enthalpy of the condensed phase were made available to the gas by considering heat transfer from particle to gas.

The analyses of Kliegel and Lype include the heat transfer process. Also considered are the irreversibilities associated with particle drag. Because of these effects, isentropic flow cannot be assumed. However, making the assumptions of Stokes flow, adiabatic expansion, and constant system physical properties (frozen flow), it is possible to arrive at a set of first order, nonlinear differential equations that may be integrated by iteration using machine computation. The particle and gas velocities are related by the drag equation

$$u_p \frac{du_p}{d_x} = \frac{3}{8} \frac{C_D \rho_g}{r_p \rho_p} (u_g - u_p)^2 \qquad [4]$$

in which the drag coefficient C_D may be approximated for nozzles of interest by the Stokes flow relation $C_D = 24/Re$. Particle or droplet size is assumed uniform and constant. Although by analogy to Setze's (5) work on jet engines the particles are expected to grow in size by accretion, this has not been observed in solid propellant rocket motors (4).

The results of such a computer program are compared with the experimental values in Table 1. The experimentally determined 3 μ particle diameter was used in the calculations. The neglect of heat transfer to the nozzle and losses associated with wall friction are felt to be nearly compensated by the equally invalid assumption of frozen flow. The nozzle efficiencies are seen to be predicted very well by the concept of velocity lag. The lack of agreement in exit velocity ratios is not unexpected in view of the many assumptions made in the derivation of the equations.

Table 1

Exit Velocity Ratios and Nozzle Efficiencies

Motor	Nozzle Length, cm	K_e Calculated	K_e Experiment	Efficiency, % Calculated	Efficiency, % Experiment
TPC	13.5	0.79	0.53	91.5	91
FPC	24	0.85	0.70	94	93
FPC-BT	21	0.85	0.95	94	95

CONCLUSIONS

Although perhaps not conclusive, the evidence presented herein indicates that the observed inefficiency of small solid propellant rocket motors using metalized fuels may be attributed to a combination of nozzle heat losses and momentum lag of the condensed phase metal oxides. The latter appears to be numerically more important. It is apparent that all of the nozzles in this investigation were too short to properly evaluate the ballistics of metalized propellant. These results do not apply to large rocket nozzles where there is adequate time for condensed phase acceleration to occur. Proper attention to nozzle design with emphasis on the approach contour may raise the efficiency slightly above present values. Reduction of the particle or droplet size, however, or reduction in amount or elimination of the condensed phase from the exhaust appear to afford the really fruitful approaches to the problem.

ACKNOWLEDGMENT

The framing camera results were obtained and reduced by J.W. Walker. The Shawmeter results were obtained by Ralph Blake. Much assistance was given in the experiments by W. A. Schroeder and J. L. Judkins. Many discussions of the subject with M. A. Cook and N. W. Ryan of the University of Utah and J. R. Kliegel of Space Technology Laboratories were invaluable.

NOMENCLATURE

C_D = drag coefficient

I = specific impulse for two-phase flow

I* = specific impulse of clean gas

K = ratio of particle velocity to gas velocity

r = particle or droplet radius

Re = Reynolds number, based on particle dimension

u = velocity

w = mass flow rate

x = nozzle length

ρ = density

g_c = conversion factor

Subscripts

g = gas phase

p = condensed phase

e = exit plane

REFERENCES

1 M. Gilbert, L. Davis, and D. Altman: Velocity Lag of Particles of Linearly Accelerated Combustion Gases. Jet Propulsion, 1955, vol. 25, p. 26.

2 J. R. Kliegel: One-Dimensional Flow of a Gas-Particle System. IAS Meeting, Princeton Univ., January 1960.

3 E. F. Lype: One-Dimensional Analysis of Non-Isentropic Two-Phase Flow. ARS Solid Propellant Rocket Conference, Salt Lake City, Feb. 1-3, 1961.

4 B. Brown and K. P. McCarty: Particle Size of Condensed Oxides from Combustion of Metalized Solid Propellants. Proc. International Combustion Symposium, Pasadena, Calif., 1960, to be published.

5 A Review of the Physical and Thermodynamic Properties of Boric Oxide, NASA RM E57B14, 1957.

6 D. Altman and J. M. Carter: *High Speed Aerodynamics and Jet Propulsion Combustion Processes, Section B - Expansion Processes*, vol. 2, p. 54. Princeton Univ., Princeton, N. J.

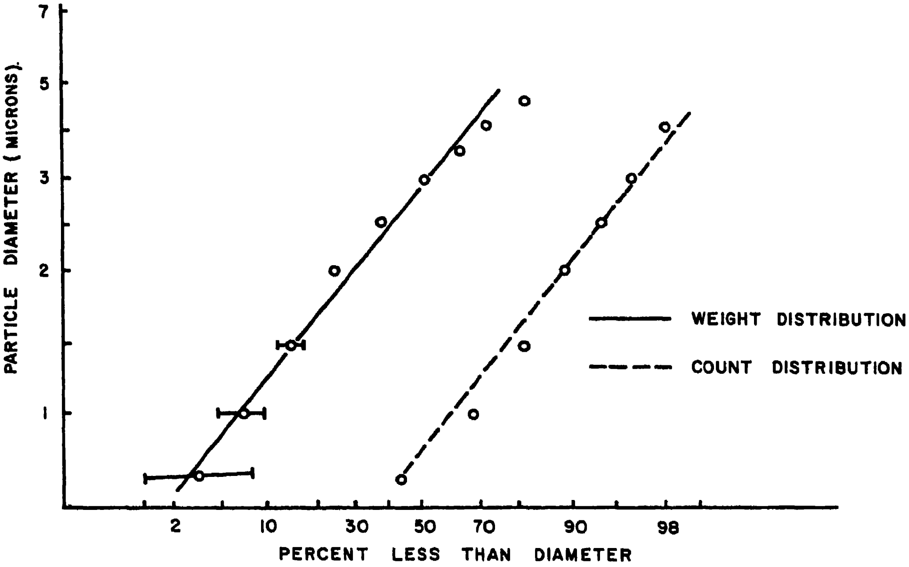

Fig. 1 Size distribution of aluminum oxide particles

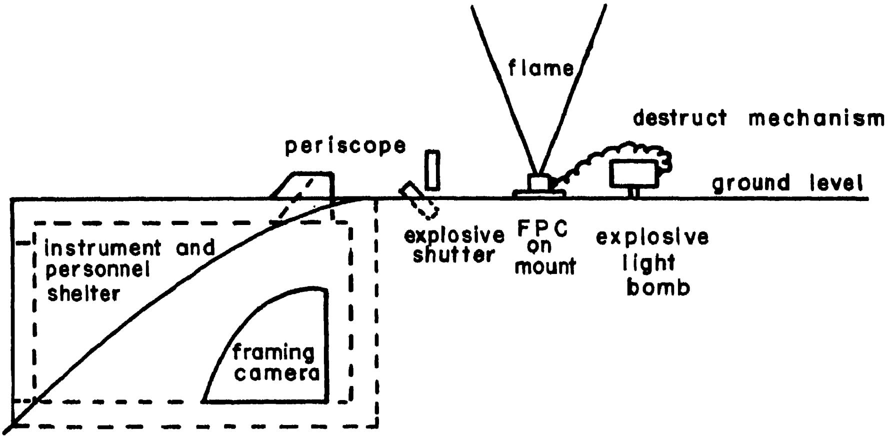

Fig. 2 Shelter and firing arrangement for Miller framing camera

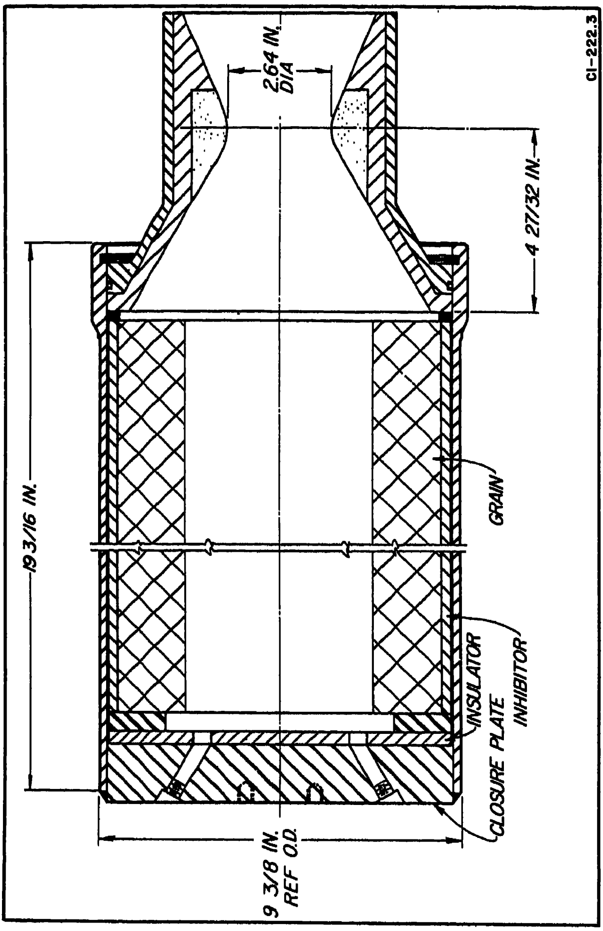

Fig. 3 FPC motor assembly

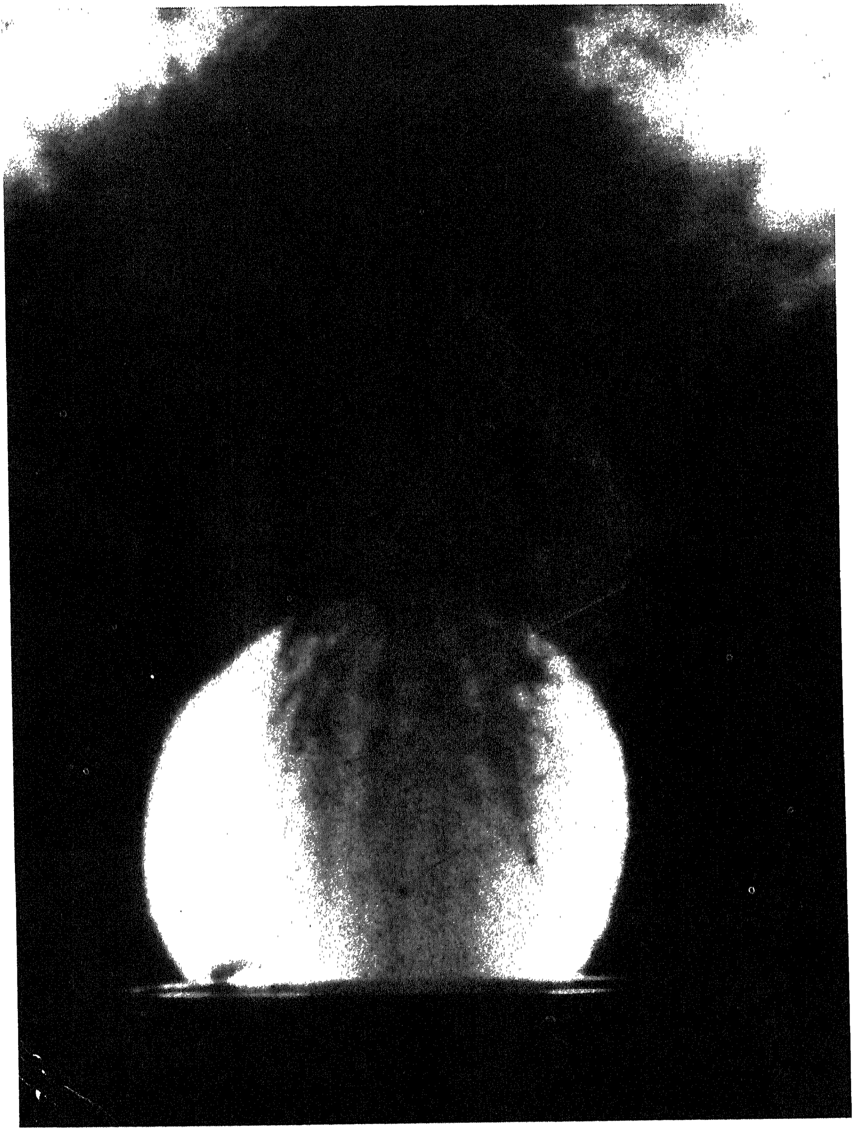

Fig. 4 Back lighted TPC rocket motor flame

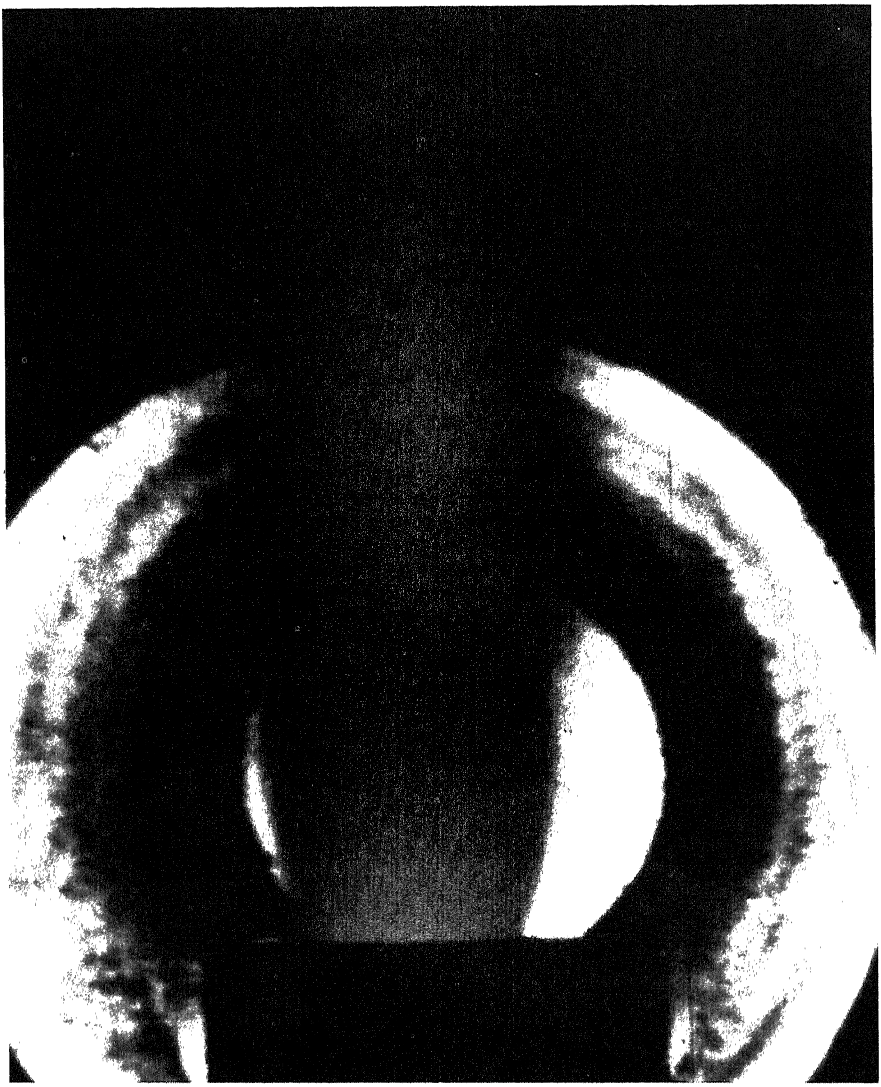

Fig. 5 Back lighted FPC rocket motor flame

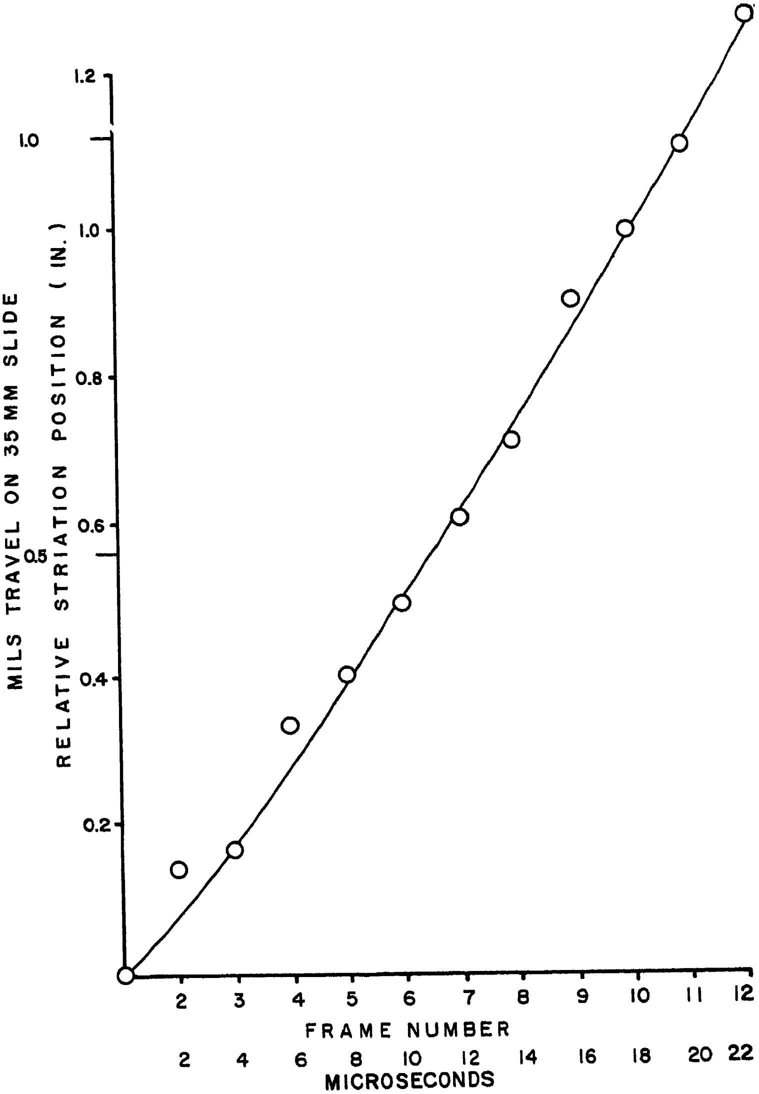

Fig. 6 Striation position vs. time for a TPC motor

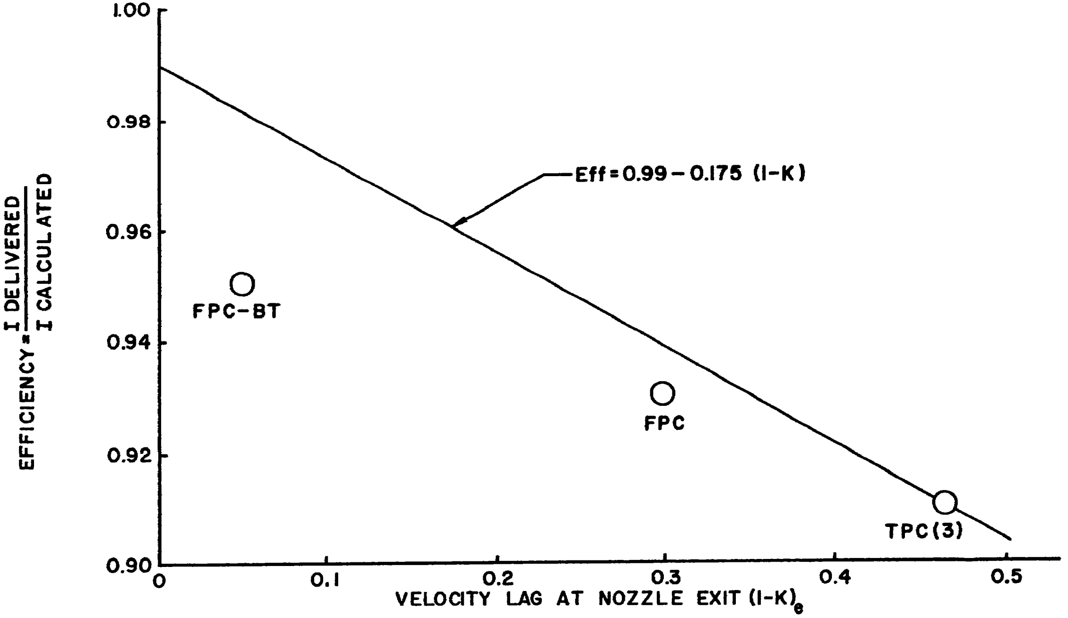

Fig. 7 Nozzle efficiency as a function of the momentum lag observed at the exit plane

EQUILIBRIUM BETWEEN PHASES IN CONVERGING-DIVERGING NOZZLES

Bruce A. Reese and Louis P. Richard

Jet Propulsion Center, Purdue University, Lafayette, Ind.

ABSTRACT

An analytical and experimental investigation has been conducted to determine if it is possible to achieve nonequilibrium (thermal) expansion in a single component two-phase flow, and also in two component two-phase flow through a converging-diverging nozzle. In the cases investigated the phases were gas and liquid, with the liquid phase predominating. The method of investigation was to calculate the exit velocity for two ideal cases (no temperature difference between the phases and no heat transfer from the gas to the liquid) and then compare the calculated and measured nozzle velocities. Two liquid-gas combinations were employed; liquid nitrogen-gaseous nitrogen and liquid nitrogen-gaseous helium. It was concluded that: the two-phase mixtures approach thermal equilibrium, even though the contact times in the nozzles were less than one millisecond; condensation of the gaseous phase occurs in the liquid nitrogen-gaseous nitrogen system and reduces the exit velocity from the nozzle; and the tendency towards thermal equilibrium is increased if the liquid has high vapor pressure and the gas has high thermal conductivity.

INTRODUCTION

During the last five years considerable research effort has

B. A. REESE, Professor of Mechanical Engineering and currently on leave, is the Deputy Chief, Antimissile Missile Division, AOMC, Redstone Arsenal, Huntsville, Ala. L. P. RICHARD, formerly Research Assistant, is currently Research Engineer, The Martin Co., Denver, Colo. Paper presented at the ARS Propellants, Combustion, and Liquid Rockets Conference, Palm Beach, Fla., April 26-28, 1961. The research reported herein was sponsored by the Office of Naval Research, Navy Department, under Contract N onr 1100-(07).

been devoted to the flow of two-phase, two-component mixtures in the converging-diverging nozzles of rocket motors. The problems of the velocity lag between the two phases have been investigated both analytically and experimentally (11-13 and 17)[1] and those problems concerned with the heat transfer between the phases, primarily neglecting the effects of velocity lag, have been studied analytically (4, 6-9, 14-16).

The work described herein considers the heat transfer problem between the phases of a two-phase flow from both the analytical and experimental viewpoints. The object was to determine whether or not nonequilibrium (thermal) expansion can be achieved in a single component two-phase flow and in a two component, two-phase flow through a converging-diverging nozzle. A secondary objective was to determine the effect on the nozzle exit velocity of a single component two-phase mixture where the gas would condense in the liquid that was pumped. In the investigations the liquid phase was always the predominant one, and varied from 86 to 99% of the weight of fluid entering the nozzle.

The problem discussed is related to a research program being conducted at the Jet Propulsion Center, Purdue University, which is concerned with pumping liquid propellants with a two-phase jet pump (1-3).

Fig. 1 is a schematic diagram illustrating the basic elements of a two-phase jet pump. They are a two-phase nozzle, wherein a high pressure liquid and gas are accelerated to high velocity, an induction-acceleration device termed a mixer, wherein the mixture discharged by the two-phase nozzle accelerates a suction liquid to a high velocity, a separator for removing the gas from the high velocity mixture, and a diffuser for converting the kinetic energy of the high velocity liquid into a static pressure rise. The work to be discussed is concerned with the problems of flow in the two-phase nozzle of a jet pump employed for pumping cryogenic liquids by means of high pressure, high temperature gases. To pump a cryogenic liquid with the aforementioned type of jet pump, the two-phase nozzle must operate with substantially nonequilibrium thermal conditions. This is necessary so that the cryogenic liquid will not be vaporized; the vapors cannot be conveniently recovered in the pumping system. Moreover, nonequilibrium thermal conditions between the hot gas (the driving fluid) and the cold liquid (the pumped fluid) increase the exit velocity of the two-phase mixture leaving the nozzle.

---

[1] Numbers in parentheses indicate References at end of paper.

For determining whether nonequilibrium thermal conditions were achieved, the exit velocity from the two-phase nozzle was measured and compared with the calculated values of exit velocity based on two ideal flow models: 1) isentropic[2] flow with no internal[3] temperature differences between the liquid and gas; and 2) isentropic flow with no internal heat transfer. The basis for calculating the nozzle exit velocity for the forementioned two ideal flows will be presented later. The previously given procedure was selected since it was not possible to measure or calculate the deviation from equilibrium directly. Such basic data as the temperatures of the two phases, the droplet size, the droplet size distribution through the nozzle, and the instantaneous heat transfer rates to the droplets could not be obtained experimentally.

Fig. 2 is a sectional view of the nozzle assembly which consists of a two-phase injector and a conical converging-diverging nozzle. A single tube of the injector is also drawn on the figure. It is seen that the exit from the injector was located very close to the nozzle throat to keep the stay time of the two-phase mixture in the nozzle smaller than 1 m sec in all of the experiments. The experiments were conducted with two different converging-diverging nozzles, hereafter designated as Nozzle 1 and Nozzle 2; their respective throat diameters were 0.1955 in. and 0.266 in. The liquid entered the nozzle through 61 similar plexiglass tubes (0.026 in. ID) having outside tapered walls. (The wall thickness at the exit section was 0.002 in.) The gas entered the nozzle through the spaces around the exit of the tubes.

Two different two-phase systems were investigated: 1) a single component two-phase system, consisting of liquid nitrogen and gaseous nitrogen; and 2) a two component two-phase system consisting of liquid nitrogen and gaseous helium. In all of the experiments the liquid nitrogen entered the injector at approximately 500 psig and -305°F, the gaseous nitrogen at varying pressures and approximately 70°F, and the helium gas at varying pressures and approximately 85°F. Measurements were made of the thrust of the nozzle system and the flow rates of the liquid and the gas. It should be noted that the initial temperature difference between the gas and the liquid was approximately 400° F, and that helium cannot be condensed by liquid nitrogen, whereas the nitrogen gas was condensible in the liquid nitrogen.

---

[2] For two-phase flow, the term isentropic will be understood to mean either constant total entropy of the two-phase mixture or constant entropy of the individual flow constituents. Its usage will be explained in the text.

[3] Throughout this paper the word internal will be understood to mean interphase, or between the gaseous and liquid phases.

Fig. 3 is a schematic diagram of the experimental apparatus. The gas and liquid flow rates were measured with calibrated orifice meters, and the thrust was measured with a Wiancko force transducer. A correction to the thrust measurement was made to account for the influence of the liquid in the unsymmetrical tank. Ref. 1 describes this correction, the details of the apparatus, the method of calibration, and the experimental procedure.

THEORETICAL ANALYSIS

The following factors influence the flow of a two-phase mixture in a converging-diverging nozzle: 1) physical properties of the gas; 2) physical properties of the liquid; 3) mixture ratio (mass flow rate ratio of gas to liquid); 4) liquid droplet size; 5) drag characteristics of the droplets; 6) time required for the mixture to expand through the nozzle (contact time); 7) vaporization characteristics of the liquid; 8) condensibility of the gaseous phase in the liquid; and 9) temperature difference between the gas and the liquid at the inlet to the nozzle.

The investigation was concerned primarily with studying the effects of temperature difference between the gas and liquid, and gas condensibility on the exit velocity of the two-phase mixture. To date there has been no rigorous analytical treatment of the mechanics of two-phase nozzle flow, and one was not attempted here. The only internal phenomena that was considered in detail was the rate of heat transfer between the phases in the exit plane of the injector. This was done to obtain an insight into the intermediate nozzle processes (see Discussion of Results).

General Equations for Isentropic Two-Phase Flow in Nozzles

It was assumed that the overall flow process in the nozzle can be separated into the three subprocesses illustrated in Fig.4. These processes are: 1) separate isentropic acceleration of the gas and liquid phases in the injector; 2) constant pressure mixing of the two phases; and 3) isentropic expansion of the mixture in the nozzle.

In the actual nozzle, no separate chamber was provided for the constant pressure mixing process. The following additional assumptions were made:

1) Steady, one-dimensional flow with no wall friction or droplet drag.

2) No heat transfer across the boundaries of the nozzle.

3) Gas and liquid are uniformaly mixed and travel at the same velocity downstream of station 3 (see Fig. 4) in the "no temperature difference" case.

4) Only pressure forces act on the fluid.

5) The gas is perfect and has a constant specific heat.

6) Liquid specific heat, thermal expansion coefficient, adiabatic compressibility, and isothermal compressibility are all constant.

7) Entropy and enthalpy of the gas phase are equal to zero at 0°R.

8) Entropy and enthalpy of the liquid phase are equal to zero for saturation conditions at 14.7 psia.

9) The velocity of the liquid and of the gas entering the injector are negligible.

The following paragraphs present the basis for the derivation of the equations for the exit velocity from the nozzle for the two ideal cases of two-phase flow described earlier; the Appendix presents a summary of the derivations that are presented in detail in Ref. 1.

The injection process was assumed to be identical for the two ideal two-phase flows. The liquid nitrogen was assumed to be accelerated isentropically from the inlet conditions (500 psi and -305°F) to a known pressure at the outlet of the injector, designated as P_2. The nitrogen or the helium entered the injector at ambient temperature and was assumed to be accelerated isentropically from the inlet pressure, which was dependent on the desired mixture ratio[4] to the outlet pressure P_2.

In deriving the equations for the ideal case of isentropic flow with no internal temperature difference, hereafter referred to as the NTD case, it was assumed that in the mixing process: 1) the momentum of the fluid was conserved; and 2) the amounts of each phase (gas, vapor, and liquid) could be calculated by employing the energy equation, and in the case of the two-component, two-phase system the relationship for the partial pressures of the phases. In the expansion process it was assumed that the heat transfer between the liquid droplets and the gas occurred reversibly with no velocity lag between the gas and the liquid droplets. The calculation resulted in the determination of the exit velocity from the two-phase nozzle as a function of mixture ratio. The exit velocity $(V_4)_{NTD}$ is given by a form of Eq. A-15:[5]

---

[4] Ratio of gas phase to liquid phase, by weight.

$$\frac{M_T(V_4)^2_{NTD}}{2gJ} = M_{G_3} h_{G_3} + M_{V_3} h_{V_3} + M_{L_3} h_{L_3} + M_T \frac{V_3^2}{2gJ} - M_{G_4} h_{G_4} - M_{V_4} h_{V_4} - M_{L_4} h_{L_4} \qquad \text{A-15}$$

For the case of isentropic flow with no internal heat transfer, hereafter denoted as the NHT case, it was assumed that in the mixing process the decrease in the total kinetic energy of the mixture was transformed into a temperature rise for the gas The two phases were then assumed to expand independently and isentropically. The exit velocity (V_4) was calculated by means of the energy equation. The NHT result is:

$$(V_4)_{NHT} = \left\{ V_3^2 + \frac{2gJ}{M_T}\left[M_G\,(h_{G_3} - h_{G_4}) + M_L\,(h_{L_3} - h_{L_4})\right]\right\}^{1/2} \qquad \text{A-21}$$

Application of Isentropic Exit Velocity Equations to Nozzles With Specific Gas-Liquid Combinations

The comparison between the isentropic exit velocities and the experimental exit velocities was based on calculations employing Eqs. A-15 and A-21 and the measured values of the nozzle inlet conditions (P_{L_1}, P_{G_1}, T_{L_1}, T_{G_1}) and the injector outlet pressure P_2; two nozzles having different throat diameters were employed, and the mixture ratios were varied from 0.006 to 0.13. In all of the experiments the liquid pressure entering the injector P_{L_1} was held constant at 500 psig ± 13 psi, and the inlet gas pressure P_{G_1} was changed to vary the mixture ratio. Fig. 5 presents the measured value of P_{G_1} and P_2 as a function of the mixture ratio M_G/M_L for the two nozzles and two liquid-gas combinations.

---

[5] There is a list of Nomenclature at the end of the paper and the equations are derived in the Appendix.

Fig. 6 presents the calculated exit velocities, $(V_4)_{NTD}$ and $(V_4)_{NHT}$ as functions of mixture ratio for the two ideal flows and the two fluid systems. Only the flow of the helium-liquid nitrogen system was investigated in both nozzles. It is seen that the ideal discharge velocities of the two-phase mixtures varied from approximately 400 to 1100 fps, depending on the two-phase system and the mixture ratio. Increasing the mixture ratio increases the calculated exit velocity. For a given two-phase system, $(V_4)_{NHT}$ is larger than $(V_4)_{NTD}$, and the exit velocities for the helium-liquid nitrogen system are larger than those for the single-component (nitrogen) system. There is no difference between the ideal exit velocities obtained from Nozzles 1 and 2.

EXPERIMENTAL INVESTIGATION

In the experiments the exit velocity denoted by V_4 of the mixture was determined from the thrust of the nozzle system. Thus

$$V_4 = \frac{F}{M_G + M_L} \qquad 1$$

V_4 is an effective exit velocity because it has been shown that the liquid droplets lag or lead the gas velocity (11, 17, 18). The calculated exit velocity $(V_4)_{NHT}$ is likewise an effective exit velocity, since it was calculated from the mean momentum of the mixture (a relative velocity exits at the exit of the nozzle), whereas the exit velocity $(V_4)_{NTD}$ assumes that two phases travel at the same velocity. Since the mass flow rate of the gas was always a small percentage of the total mass flow (1 to 13%), the exit velocity V_4 is not materially different from the liquid droplet velocity (18).

Physical Considerations in Two-Phase Flow.

Before presenting the results of the investigation, some general observations concerning two-phase nozzle flow appear appropriate. The limiting cases of the helium and liquid nitrogen system are 100% liquid nitrogen (-305°F, 500 psig inlet condition) and 100% helium gas (85°F, 500 psig). For the first limiting case (100% liquid), the isentropic exit velocity when expanding to atmospheric pressure is approximately 370 fps. For the second limiting case (100% helium gas), the corresponding exit velocity would be approximately 4840 fps. Thus the exit velocity of the mixture increases as its percentage gas is increased.

An insight into the influence of the physical properties of the liquid and gas on the equilibrium thermal conditions during the flow through the two-phase nozzle can be obtained by calculating the initial rate of heat transfer between the gas and the liquid. In calculating the diameters of the liquid droplets, the empirical equations of Nukiyama and Tanasawa (5) were used, even though they were developed from experiments with a single tube injector. It is recognized that the proximity of other injector tubes, as in the injector employed in this investigation, probably changes the droplet size. For the mixture ratios and fluid combinations used in this investigation, the dimensionless group $\rho_G/r\rho_L$ (where ρ_G is the density of the gas, ρ_L is the density of the liquid, and r is the mixture ratio) had the most significant effect on droplet diameters (10). Nusselt numbers based on droplet diameter were calculated from the experimental work of Ingebo (4) and of Williams (19). From the calculated values of Nusselt number and droplet diameters, the instantaneous rates of change of gas temperature at the nozzle inlet were calculated; the detailed calculations are presented in Ref. 1, and the results are summarized in Table 1.

Table 1 Instantaneous Heat Transfer Parameters at the Nozzle Inlet

Parameter	Fluid Combination	
	He-LN	N-LN
$(V_4)_{NTD}$	600	600
r, %	1.39	14.0
d_o, in.	0.0335	0.0312
Nu	540	853
h, B/hr-ft^2-°F	15,870	4620
$\frac{dT_G}{d\tau}$, °F/m sec	3,930	386

Table 1 shows that for the helium-liquid nitrogen system the rate of change in temperature $dT_G/d\tau$ is large, 3930°F/m sec. The initial rate of change of gas temperature is a significant parameter that is helpful in interpreting experimental results.

For two-phase flow, Ingebo (4) postulates that a vapor film surrounds each liquid droplet and the gaseous constituent surrounds the vapor layer. Through its intermediate position the vapor acts as an effective carrier of thermal energy from the gas to the liquid. Bimolecular collisions between gas molecules or between a gas molecule and a vapor molecule result in a net heat flux to the surface of the liquid. Thus, liquids having high vapor pressures tend to reduce the resistance to heat transfer and thus favor thermal equilibrium between the liquid and gas.

The properties of the gas that exert the greatest importance on the gas temperature during the two-phase expansion process are the thermal conductivity, the constant pressure specific heat, and the density.

The inlet mixture ratio influences exit velocity not only by virtue of the difference in the expansion characteristics of the gas and liquid phases, but also because of the effect of the mixture ratio on the liquid droplet diameter and on the contact time. Considering the effect of mixture ratio on droplet size and contact time, calculations based on Ref. 5 indicate that as the mixture ratio for an air-water system was increased from $r = 5$ to 20%, the initial droplet size decreased from 0.101 in. (2565μ) to 0.0141 in. (358μ), respectively.[6] The corresponding calculation for the contact times, made by the authors, were 0.7 m sec for $r = 5$ and 0.4 m sec for $r = 20$. The aforementioned results indicate that increasing the mixture ratio decreases the droplet diameters and the contact time; from the heat transfer point of view, the latter two effects tend to cancel each other. The smaller droplets increase the surface area, thus increasing the total heat transferred, whereas the decrease in the contact time has the opposite effect.

Losses due to wall friction in the injector and nozzle decrease the exit velocity. Chenoweth and Martin (20) conclude the following regarding frictional losses in two-phase flow:

1) Frictional losses under the conditions of their investigation were higher than for single-phase flow; they ascribed the larger losses with two-phase flow to the increased turbulence.
2) For equal values of the parameter $\rho_G/r\rho_L$ (when the value

---

[6] Experiments by Crabtree (18), also for the air-water system, indicate that the droplets continue to break up as they flow through the nozzle and that the final droplet size is between 0.0001 (2.54μ) and 0.005 in. (127μ) in nozzles similar to those employed in this investigation.

of the parameter is less than 0.000417) the frictional losses for helium-liquid nitrogen and nitrogen-liquid nitrogen are approximately the same.

The configuration of the injector-nozzle combination also exerts an influence on the exit velocity. In this investigation two nozzles with different diameters -- $D_t = 0.1955$ and 0.266 in.--were employed with the same injector. The smaller mozzle had a longer contact time since the injector was located further upstream from the throat.

Experimental Results

Fig. 7 represents the measured nozzle exit velocity V_4 as a function of mixture ratio for the helium-liquid nitrogen system for Nozzles 1 and 2. For comparison the curves of $(V_4)_{NHT}$ and $(V_4)_{NTD}$ from Fig. 6 are also shown. Fig. 8 presents the measure exit velocity V_4 as a function of mixture ratio for the nitrogen-liquid nitrogen system for Nozzle 1. Also shown are the curves for $(V_4)_{NHT}$ and $(V_4)_{NTD}$. It is apparent from the fugures that the curves for V_4 lie below those for $(V_4)_{NHT}$ and $(V_4)_{NTD}$.

Discussion of Results

Fig. 9 presents the nozzle velocity coefficients as a function of the mixture ratio for the helium-liquid nitrogen and nitrogen-liquid nitrogen cases for Nozzle 1.[7] It should be note that the velocity coefficients vary from 0.95 to 0.71 for the "no temperature difference" case and from 0.79 to 0.50 for the "no heat transfer" case. Fig. 10 presents the nozzle velocity coefficients as a function of mixture ratio for the helium-liquid nitrogen combination in Nozzle 2. In Nozzle 2, the mean value of the nozzle coefficient is approximately 0.9 for the "no temperature" case and 0.75 for the "no heat transfer" case.

It is seen from Fig. 9 that for the liquid nitrogen-gaseous helium system, the exit velocity V_4 was 5 to 11% below the ideal value $(V_4)_{NTD}$; this decrease is attributed to friction and drag losses. The high initial rate of change of gas temperature (see Table 1) for the helium-liquid nitrogen case (3930 °F/m sec) indicates that the expansion of the helium liquid nitrogen system is a "no temperature difference" expansion.

---

[7] The nozzle velocity coefficient is defined as the ratio of the measured exit velocity V_4 to either the calculated exit velocit $(V_4)_{NTD}$ or $(V_4)_{NHT}$ and is denoted by ϕ with an appropriate subscript.

Fig. 9 shows that ϕ_{NTD} and ϕ_{NHT} are 10 to 20% higher for the helium-liquid nitrogen system than for the nitrogen-liquid nitrogen system. For the same exit velocities V_4, the inlet gas and liquid temperatures, the contact time, the droplet diameters, and the friction losses are approximately the same for the two systems. It is inferred, therefore, that the difference in the values of exit velocity of the two systems are due to differences in the properties of the gas phase.

Calculations (see Appendix, Eq. A-6 and A7) indicate that for the nitrogen-liquid nitrogen system most of the gaseous nitrogen condenses during the mixing process. In the actual case, if gaseous nitrogen failed to condense during its flow through the nozzle, the values of ϕ_{NTD} and ϕ_{NHT} would be equal to values for the liquid nitrogen-helium system. Consequently failure of the nitrogen gas to condense is not an explanation for smaller values of ϕ for the liquid nitrogen-nitrogen system. Calculations (see Appendix, Eq A-15) also indicate that the liquid nitrogen, which enters the nozzle in a subcooled state, reaches a saturated condition (due to the reduction in pressure) at some station between the nozzle inlet and exit sections. Vaporization of a portion of the liquid nitrogen is, therefore, necessary for achieving the calculated value of (V_4). The explanation offered for the decrease in the exit velocity of the nitrogen-liquid nitrogen system as compared to the helium-liquid nitrogen combination is that the actual expansion in the diverging section is so rapid that the vaporization process is incomplete. That hypothesis is not unreasonable when it is noted that the condensation occurs where the velocity is low, whereas vaporization must occur where the velocities are high. For the calculated values of the exit velocity to be correct, the liquid must be saturated at the exit conditions (-320°F), which requires a drop in temperature of approximately 50°F during the drop in pressure from 160 psia to atmospheric pressure in less than 0.5 m sec.

It should be noted that the same lag in vaporization rate probably occurs in the expansion of the helium-liquid nitrogen system. The gaseous helium, however, does not condense during the expansion process and is, therefore, the major contributor to the attainment of a high mixture velocity at the nozzle exit. Thus the vaporization of liquid nitrogen in the diverging section of the nozzle is of less importance in achieving high exit velocities in the helium-nitrogen case.

Reference to Figs. 9 and 10 shows that the nozzle velocity coefficients for helium-liquid nitrogen and nitrogen-liquid nitrogen systems varied 5 to 10% as the mixture ratio changed; in general, they tend to increase with an increase in the mixture ratio, and this variation in ϕ is not surprising. As pointed out earlier, the mixture ratio affects the droplet size, the contact time, and frictional losses.

Figs. 9 and 10 show that the values of the nozzle coefficient for the helium-liquid nitrogen system are slightly higher for Nozzle 1 than for Nozzle 2. The difference cannot be explained by the approximately 15% shorter contact time for Nozzle 2. A shorter contact should increase the exit velocity. Since the flow rates were larger in Nozzle 2, there was more pressure drop across the injector (the same injector was employed for both nozzles), and the velocity differences between the helium and the liquid nitrogen were much larger than for Nozzle 1. The larger flow velocities and velocity difference between the two-phase flow through the nozzle cause the friction and drag losses to increase, and thus, the nozzle velocity coefficient to decrease.

CONCLUSIONS

Calculation and experiment indicate that the flow of two-phase mixtures (liquid-gas) in converging-diverging nozzles (with the liquid in the form of small droplets) approaches thermal equilibrium even with contact times of the order of 1 m sec.

The expansion of a mixture of helium gas (initially at 85°F) and liquid nitrogen (initially at -305°F) in a convergent-divergent nozzle from 500 psig to atomospheric pressure occurs with substantially no temperature difference between the phases.

In the expansion of a mixture of nitrogen gas (initially at 70°F) and liquid nitrogen (initially at -305°F) in a convergent-divergent nozzle, the nitrogen gas condenses in the liquid nitrogen in the converging section of the nozzle. Condensation of the gas phase materially reduces the exit velocity. Calculations indicate that the nitrogen should vaporize at some section in the diverging portion of the nozzle to maintain phase equilibrium. It is believed that the lack of phase equilibrium in the nitrogen-liquid nitrogen system is responsible for the decrease in its exit velocity.

The tendency toward thermal equilibrium is increased if the liquid has high vapor pressure and if the gas has high thermal conductivity.

ACKNOWLEDGMENTS

The authors are indebted to M. J. Zucrow for his guidance in conducting the research work and for his assistance in preparing the paper. Appreciation is also expressed to D. G. Elliott for his technical advice and personal interest during the research project.

APPENDIX: Equations for the Discharge Velocity From Two-Phase Converging-Diverging Nozzles Assuming Isentropic Flow With No Internal Heat Transfer and Isentropic Flow with No Temperature Difference.

Introduction

The nozzle discharge velocities were calculated assuming that the flow process was divided into three stages: injection, constant pressure mixing, and expansion. The injection process was common for the two ideal cases - no internal heat transfer and no temperature difference - whereas different assumptions were made for the two ideal cases when considering the mixing and expansion processes.

Injection Process

In the injector, the liquid is assumed to be accelerated isentropically from zero velocity and a known static pressure P_{L_1} (500 psig) and temperature T_{L_1} to a known pressure P_2. The enthalpy change for the liquid is calculated for $dh = vdp$ in terms of the specific volume at saturated conditions at the inlet, and the compressibility factors β_T and β_S; thus[8]

$$h_{L_1} - h_{L_2} = \frac{v_{L_{sat}} (P_{L_1} - P_2)}{1 + \beta_T (P_{L_1} - P_{sat})} \left[1 + \frac{\beta_S}{2} (P_{L_1} - P_2) \right] \frac{1}{J} \qquad \text{A-1}$$

The liquid injection velocity V_{L_2} may be calculated from the relationship

---

[8] See Ref. 1 for details of the derivation.

$$V_{L_2} = \left[2g\,J\,(h_{L_1} - h_{L_2})\right]^{1/2} \qquad \text{A-1}$$

For a perfect gas, the enthalpy change is given by

$$h_{G_1} - h_{G_2} = c_p\,T_{G_1}\left[1 - \left(\frac{P_2}{P_{G_1}}\right)^{k-1/k}\right] \qquad \text{A-3}$$

and the exit velocity by

$$V_{G_2} = \left[2g\,J\,(h_{G_1} - h_{G_2})\right]^{1/2} \qquad \text{A-4}$$

Mixing and Expansion

Case 1: Isentropic Flow With No Internal Temperature Difference

In this case the heat transfer between the liquid and gas is assumed to occur reversibly with no velocity lag between the liquid and gas and no wall friction. The flow is, therefore, frictionless, drag free, adiabatic, and reversible and, therefore, may be analyzed by means of the isentropic relationships. At the entrance to the nozzle, uniform mixture of the gas and liquid phases at temperature T_3 and velocity V_3 is assumed. The mixture velocity may be calculated by assuming that the momentum in the axial direction is conserved.

$$V_3 = \frac{M_{G_2} V_{G_2} + M_{L_2} V_{L_2}}{M_T} \qquad \text{A-5}$$

The mixture composition may be calculated from the energy balance

$$M_{G_1} h_{G_1} + M_{L_1} h_{L_1} = M_{G_3} h_{G_3} + M_{V_3} h_{V_3} + M_{L_3} h_{L_3} + \frac{M_T V_3^{\,2}}{2gJ} \qquad \text{A-6}$$

and the partial pressure of the components

$$\frac{M_{V_3}}{M_{G_3}} = \frac{W_V P_{V_3}}{W_G P_{G_3}} \qquad \text{A-7}$$

Eqs. A-6 and A-7 are solved by an iterative process. The temperature T_3 is assumed and employed for solving Eq. A-7 and then checked by substituting the results of the solution of Eq. A-7 to solve Eq. A-6.

The increase in entropy of the liquid and the gas during the mixing process (which is assumed isobaric) is calculated from the following relationships:

$$S_{L_3} - S_{L_2} = C_L \mathrm{in}\ T_3/T_{L_2} \qquad \text{(Liquid)} \qquad \text{A-8}$$

$$S_{G_3} - S_{G_2} = C_p \mathrm{in}\ \frac{T_3}{T_{G_2}} - \frac{R}{JW_G} \ln \frac{p_{G_3}}{P_2} \qquad \text{(Gas)} \qquad \text{A-9}$$

where P_2 is the total static pressure of the mixture.

Values of entropy for the vapor at the exit of the nozzle are looked up in a table of properties of the vapor.

During the expansion of the mixture in the nozzle there is no change in total entropy. Therefore

$$M_{G_3} S_{G_3} + M_{V_3} S_{V_3} + M_{L_3} S_{L_3} = M_{G_4} S_{G_4} + M_{V_4} S_{V_4} + M_{L_4} S_{L_4} \qquad \text{A-10}$$

If the nozzle exit temperature T_4 is known, and since the pressure at the exit is atmospheric, the ratio of the mass of vapor and the mass of the gas may be found by the solution of the following equations.

$$p_{G_4} = P_a - p_{V_4} \qquad \text{A-11}$$

$$\frac{M_{V_4}}{M_{G_4}} = \frac{W_V}{W_G} \frac{p_{V_4}}{p_{G_4}} \qquad \text{A-12}$$

$$S_{G_4} - S_{G_3} = C_p \ln \frac{T_4}{T_3} - \frac{R}{JW_G} \ln \frac{p_{G_4}}{p_{G_3}} \qquad \text{A-13}$$

In the case of the flow of helium gas and liquid nitrogen, Gibbs' phase rule indicates that because of the two components and two phases there are two degrees of freedom, and, consequently, P_4 does not uniquely determine T_4. In this case, since the total entropy has been assumed constant, a trial value of T_4 may be verified by finding S_{L_4}, S_{V_4} (property tables), M_{V_4}/M_{G_4} (Eq. A-12) and S_{G_4} (Eq. 13) and substituting these values into Eq. 10.

In the case of the flow of the nitrogen gas and liquid nitrogen, no iteration process is necessary, since Gibbs' phase rule indicates there is only one degree of freedom.

The enthalpies of the vapor and liquid may be found in the appropriate tables of the thermodynamic properties for the saturated fluids at temperature T_4. The enthalpy change for the gas during expansion may be written

$$h_{G_3} - h_{G_4} = C_p (T_3 - T_4) \qquad \text{A-14}$$

The velocity of the fluid mixture at the exit of the nozzle V_4 may be calculated from the energy equation; thus

$$M_{G_3} h_{G_3} + M_{V_3} h_{V_3} + M_{L_3} h_{L_3} + M_T \frac{V_3^2}{2gJ} =$$

$$M_{G_4} h_{G_4} + M_{V_4} h_{V_4} + M_{L_4} h_{L_4} + M_T \frac{(V_4)^2_{NTD}}{2gJ} \qquad \text{A-15}$$

The value of V_4 determined by this method is termed the "isentropic exit velocity for no internal temperature difference" and is designated by $(V_4)_{NTD}$

Case 2: Isentropic Flow With No Internal Heat Transfer

For Case 2, no internal heat transfer, it is assumed that there is no exchange of thermal energy between the phases and that after injection each phase experiences an isentropic expansion to a different exit velocity. Since the separate expansions are assumed isentropic, then

$$S_{G_3} = S_{G_4} \quad S_{L_3} = S_{L_4}$$

A model based on the presence of liquid and gas only (no vapor) was selected to represent Case 2. It is reasonable to assume that no appreciable vaporization occurs in the nozzle, since the stay time is less than 1 m sec. Moreover, it is difficult to reconcile the presence of vapor, which is a good carrier of thermal energy between the gas and liquid, with the assumption of no internal heat transfer. Thus, an imaginary insulator is assumed to exist at the liquid-gas interface rather than at some hypothetical vapor-gas interface.

The mixture velocity entering the nozzle is calculated assuming the total axial momentum is conserved (Eq. A-5). The enthalpy change in the gas is equal to the decrease in kinetic energy during the mixing process, since it was assumed that the temperature of the liquid did not change. Thus

$$M_G \left(h_{G_3} - h_{G_2}\right) = M_G \frac{V_{G_2}^2}{2gJ} + M_L \frac{V_{L_2}^2}{2gJ} - M_T \frac{V_3^2}{2gJ} \qquad \text{A-16}$$

The entropy of the gas at the nozzle inlet (the liquid entropy does not change) is given by

$$S_{G_3} = S_{G_1} + C_p \ln \frac{T_{G_3}}{T_{G_2}} \qquad \text{A-17}$$

Since it has been assumed that S_G and S_L do not change during the nozzle expansion

$$C_p \ln \frac{T_{G_4}}{T_{G_3}} - \frac{R}{JW_G} \ln \frac{P_{G_4}}{P_{G_3}} = 0 \qquad \text{A-18}$$

and

$$\ln \frac{T_{L_1}}{T_{L_4}} = \frac{v_{L_1} \frac{1}{v} \frac{(\partial v)}{(\partial T)_P} \left(P_{L_1} - P_{L_4}\right) \left[1 + \frac{\beta s}{2} \left(P_{L1} - P_{L4}\right)\right]}{J\, C_L \left[1 + \beta_T \left(P_{L_1} - P_{L_4}\right)\right]} \qquad \text{A-19}$$

from which T_{G_4} and T_{L_4} may be calculated.

The enthalpy change for the liquid is therefore

$$h_{L_1} - h_{L_4} = \frac{v_{L_{sat}}(P_{L_1} - P_4)}{1 + \rho_T(P_{L_1} - P_{sat})} \left[1 + \frac{\beta S}{2} (P_{L_1} - P_4) \right] \frac{1}{J} \qquad \text{A-20}$$

The equation for the energy balance across the nozzle may be written in the following form

$$(V_4)_{NHT} = \left\{ V_3^2 + \frac{2gJ}{M_T} \left[M_G (h_{G_3} - h_{G_4}) + M_L (h_{L_3} - h_{L_4}) \right] \right\}^{1/2} \qquad \text{A-21}$$

which permits the calculation of an "isentropic exit velocity for no internal heat transfer" and is designated by $(V_4)_{NHT}$.

NOMENCLATURE

c_L	specific heat of the liquid, B/lb$_m$-$^{\circ}$F
c_p	specific heat of the gas at constant pressure, B/lb$_m$-$^{\circ}$F
d_o	surface mean diameter of a liquid droplet at pressure P_3
D	diameter of the nozzle, ft
D_t	nozzle throat diameter, in.
F	thrust of the nozzle, lb$_f$
F_c	thrust contribution of liquid in the supply tank, lb$_f$
G	mass of gas, lb$_m$
h	heat transfer coefficient, b/hr-ft^2-$^{\circ}$F
h_G	specific enthalpy of the gas, B/lb$_m$
h_L	specific enthalpy of the liquid, B/lb$_m$
h_v	specific enthalpy of the vapor, B/lb$_m$
k_G	thermal conductivity of the gas evaluated at T_{av}, B/hr - ft - $^{\circ}$F
k_V	thermal conductivity of the vapor evaluated at T_{av}, B/hr-ft-$^{\circ}$

M_G	mass rate of flow of the gas, lb /sec
M_V	mass rate of flow of the vapor, lb_m/sec
M_L	mass rate of flow of the liquid, lb_m/sec
M_T	total mass rate of flow in the nozzle, lb_m/sec
Nu	Nusselt number, hd/k_G
p_G	partial pressure of the gas, psfa
p_V	partial pressure of the vapor, psfa
P	pressure in the nozzle, psfa
P_a	atmospheric pressure, psfa
P_G	gas pressure, psfa
P_L	liquid pressure, psfa
q	heat flux to a liquid droplet, B/ m sec
r	inlet mixture ratio, M_G/M_L, %
R	the universal gas constant, 1545 ft-lb_f/mole°R
Re	Reynolds number, dvp/μ
s_G	specific entropy of the gas, $B/lb_m{}^\circ F$
s_V	specific entropy of the vapor, $B/lb_m{}^\circ F$
S	entropy of the two-phase mixture, $B/lb_m{}^\circ F$
τ	time, sec
T_G	temperature of the gas, °R
T_L	temperature of the liquid, °R
v_G	specific volume of the gas, ft^3/lb_m
v_L	specific volume of the liquid, ft^3/lb_m
V	velocity of the two-phase mixture in the nozzle, fps

V_4	experimentally determined value of the effective exit velocity, fps
$(V_4)_{NHT}$	effective exit velocity calculated from the assumption of isentropic flow with no internal heat transfer, fps
$(V_4)_{NTD}$	effective exit velocity calculated from the assumption of isentropic flow with no internal temperature difference, fps
W_G	molecular weight of the gas, lb_m/mole
W_V	molecular weight of the vapor, lb_m/mole
α	thermal expansion factor, $\frac{1}{v} {\frac{v}{T}}_{P}$
β_S	adiabatic compressibility, $\frac{-1}{v} {\frac{v}{P}}_{S}$
β_T	isothermal compressibility , $\frac{-1}{v} {\frac{v}{P}}_{T}$
μ_L	dynamic viscosity of the liquid, lb/ft - sec
ρ_G	density of the gas, lb_m/ft^3
ρ_L	density of the liquid, lb_m/ft^3
ϕ_{NHT}	nozzle coefficient $(V_4)/(V_4)_{NHT}$, %
ϕ_{NTD}	nozzle coefficient, $(V_4)/(V_4)_{NTD}$, %

SUBSCRIPTS

1	inlet to nozzle injector
2	injector exit, before mixing
3	nozzle entrance after mixing
4	nozzle exit
G	gas
L	liquid

sat	saturated
t	nozzle throat
V	vapor

REFERENCES

1 Richard, Louis P., "The Effect of an Initially Large Internal Temperature Difference, and Condensibility of the Gas on the Exit Velocity for Two-Phase Flow of a Liquid and a Gas in a Nozzle," MSME Thesis, Purdue University, Lafayette, Indiana, August 1959.

2 Elliott, D. G., "Theoretical and Experimental Investigation of a Gas-Driven Jet Pump for Rocket Engines," PhD Thesis, Purdue University, Lafayette, Indiana, 1959 (Confidential).

3 Elliott, D. G., "Investigation of a Gas-Driven Jet Pump for Rocket Engines," Liquid Rockets and Propellants, Progress in Astronautics and Rocketry -- Vol. 2, Edited by L. E. Bollinger, M. Goldsmith and A. W. Lemmon, Jr., Academic Press, 1960, p.p. 497--541.

4 Ingebo, R. D., "Vaporization Rates and Heat Transfer Coefficients for Pure Liquid Drop," NACA TN 2368, Washington, D. C., July 1961.

5 Nukiyama, S. and Tanasawa, Y., "An Experiment on the Atomization of Liquid by Means of Air Stream," Trans. of the Society of Mechanical Engineers, Japan, Vol. 5, No. 18, February 1939.

6 Wilde, Kenneth A., "An Approximate Specific Impulse Equation for Condensible Gas Mixtures," Jet Propulsion, Vol. 27, 1957, p.p. 668-669.

7 Glasoner, A. and Winternitz, P. F., "A Theory of the Effect of Condensed Particles in the Exhaust of Rocket Motors," Reaction Motors Report RMI-293-TP2, December 23, 1950.

8 Altman, D. and Carter, J. M., "Expansion Processes," Chapter B, Vol. IX of Combustion Processes, High Speed Aerodynamics and Jet Propulsion Series, Princeton University Press, 1956. p.p. 26-63.

9 Maxwell, W. R., Dickerson, W., and Caldin, E. F., "Adiabatic Expension of a Gas Stream Containing Solid Particles," Aircraft Engineering, Vol. 18, 1946, p.p. 350-351.

10 Dempster, J. R. H. and Sodha, M. S,, "On Secondary Atomization of Droplets," Jet Propulsion, Vol. 27, 1957, p. 896.

11 Gilbert, M., Davis, L. and Altman, D., "Velocity Lag of Particles in Linearly Accelerated Combustion Gases," Jet Propulsion Vol. 25, 1955, p.p. 26-30.

12 Niesse, C. C. "Application of Droplet Ballistics Theory to Experiments of Ingebo," Jet Propulsion, Vol. 27, 1955, p. 36.

13 Ingebo, R. D., Vaporization Rates and Drag Coefficients for Iso-octane Sprays in Turbulent Air Streams, NACA TN 3265, October 1954.

14 Dillon, P. L. P. and Line, L. E., Jr., "Heat Transfer Between Solid Particles and Gas in a Rocket Nozzle." Jet Propulsion, Vol. 26, 1956, p.p. 1091-1097-1090.

15 Weiss, M. A. and Worsham, C. H., "Atomization in High Velocity Airstreams, ARS Journal, Vol. 29, 1959, p.p. 252-259.

16 Lype, E. F., One Dimensional Analysis of Non-Isentropic Two-Phase Flow, ARS Preprint 1605-61, February 1961, Salt Lake City, Utah.

17 Brown, B., "Particle Velocity Lag in Metalized Propellants," published elsewhere in this volume.

18 Crabtree, D. L., "Investigation of the Influence of the Design Parameters on the Flow Characteristics of the Drive Nozzle of a Gas Driven Jet Pump", MSME Thesis, Purdue University, Lafayette, Indiana, August 1961.

19 Williams, G. C., ScD Thesis in Chemical Engineering, Massachusetts Institute of Technology, 1942.

20 Chenoweth, J. M. and Martin, M. W., "Pressure Drop of Gas-Liquid Mixtures in Horizontal Pipes," Petroleum Engineering Vol. 28, No.4, April 1956, p.p. 42-45.

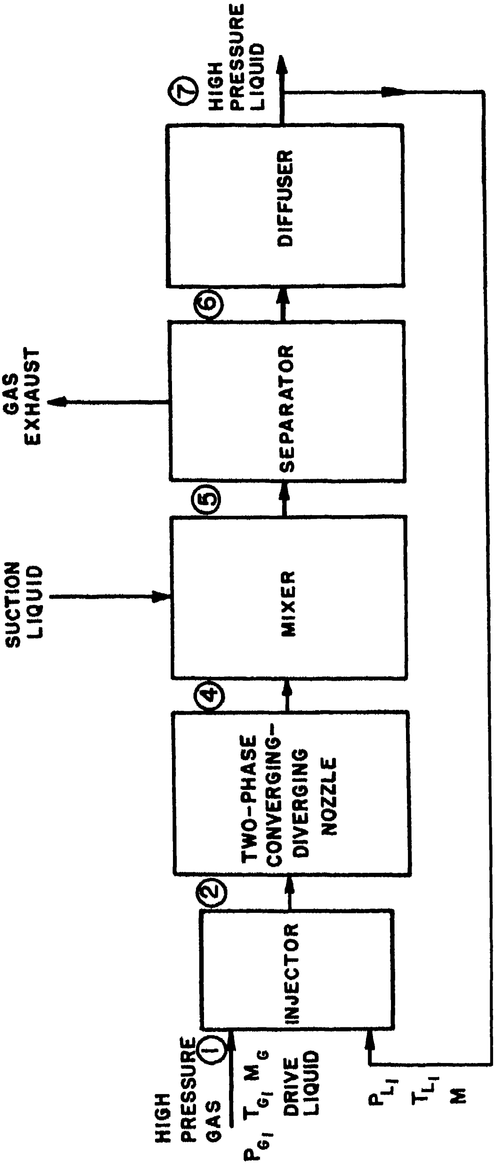

Fig. 1 Basic elements of the gas-drive jet pump

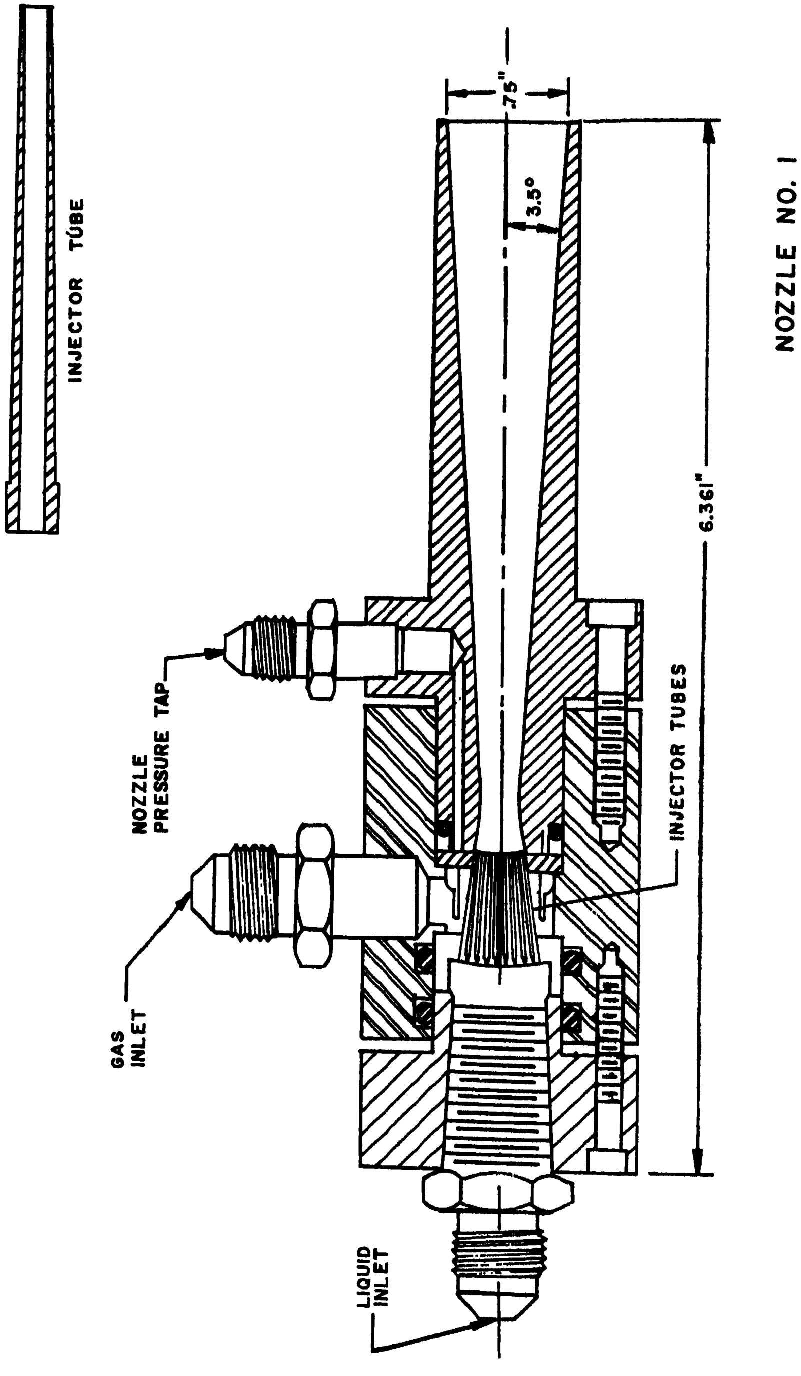

Fig. 2 Sectional view of nozzle assembly

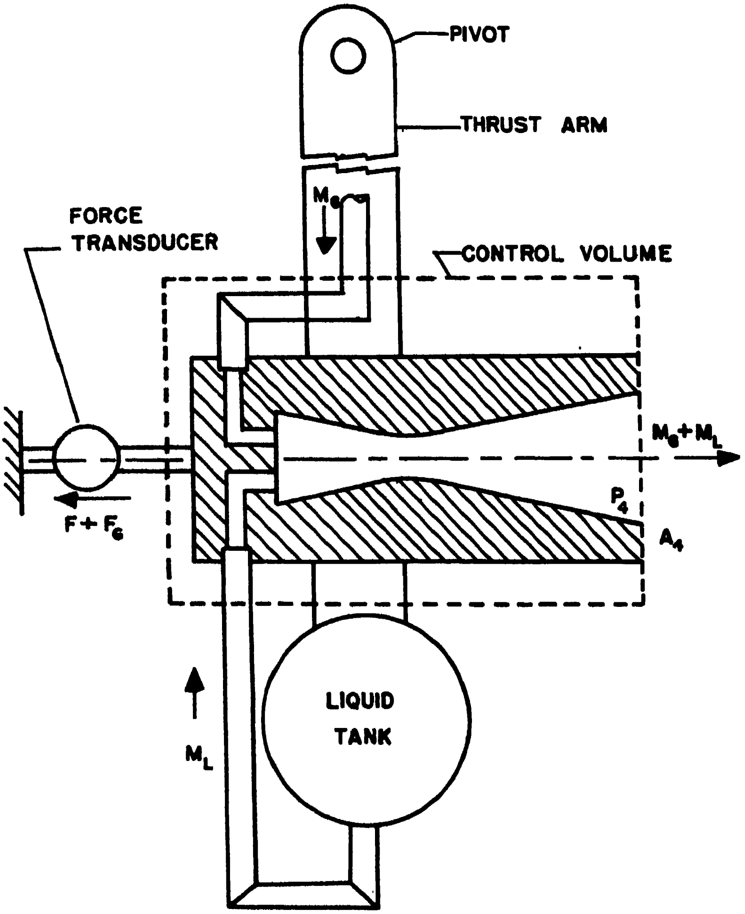

Fig. 3 Schematic diagram of experimental apparatus

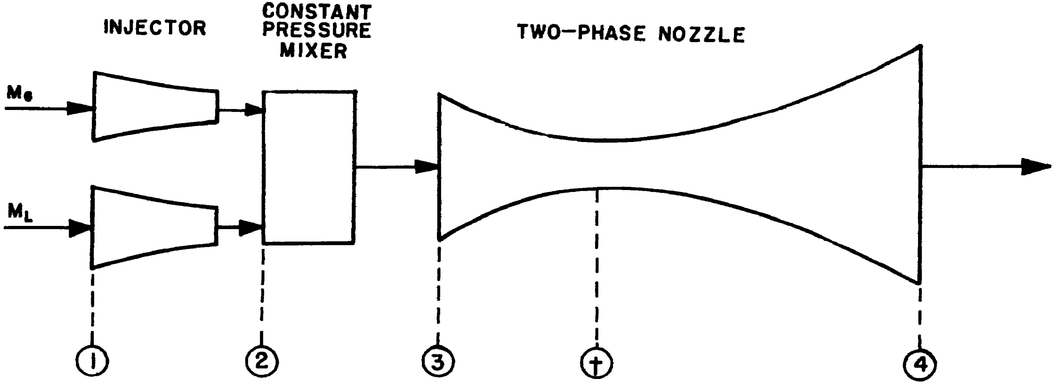

Fig. 4 Schematic flow diagram of two-phase nozzle

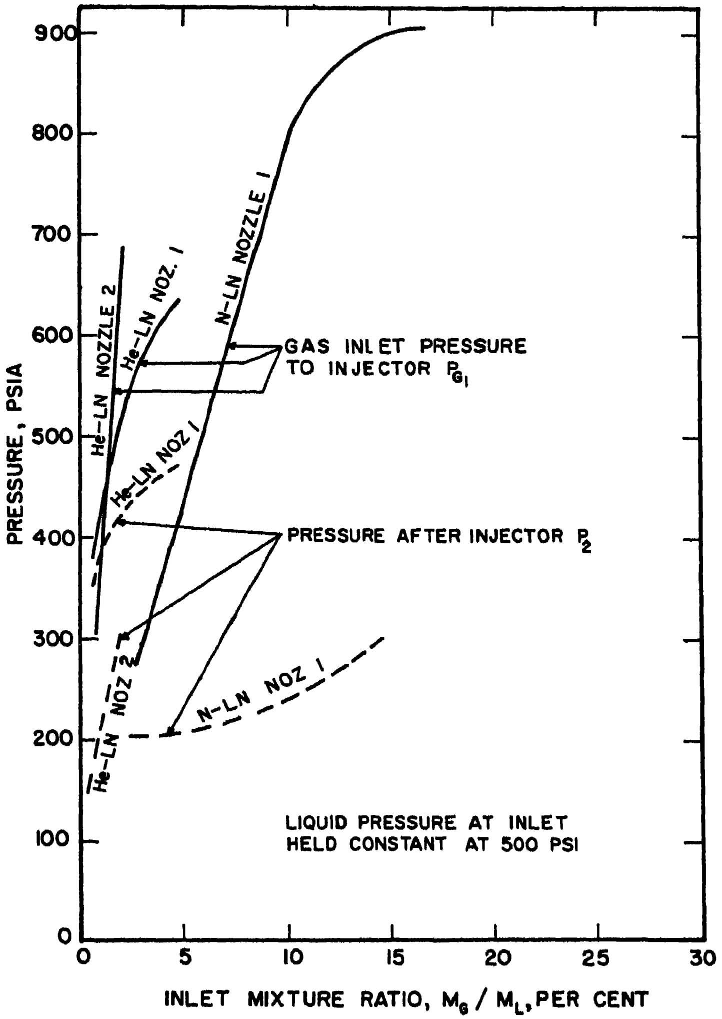

Fig. 5 Measured pressures for various experimental combinations

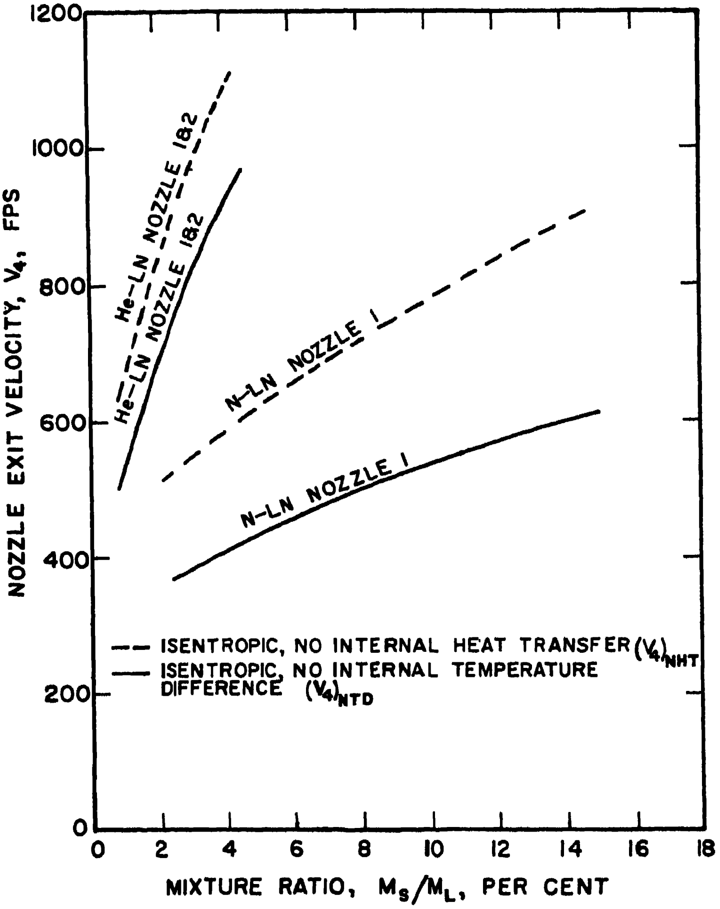

Fig. 6 Ideal exit velocity

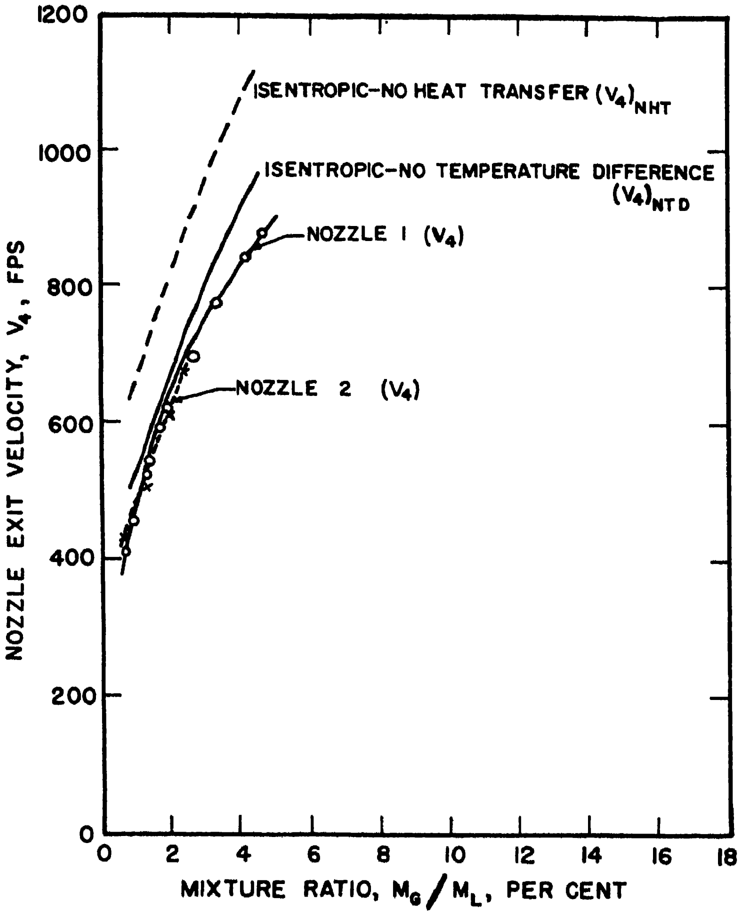

Fig. 7 Experimental nozzle exit velocity for helium-liquid nitrogen

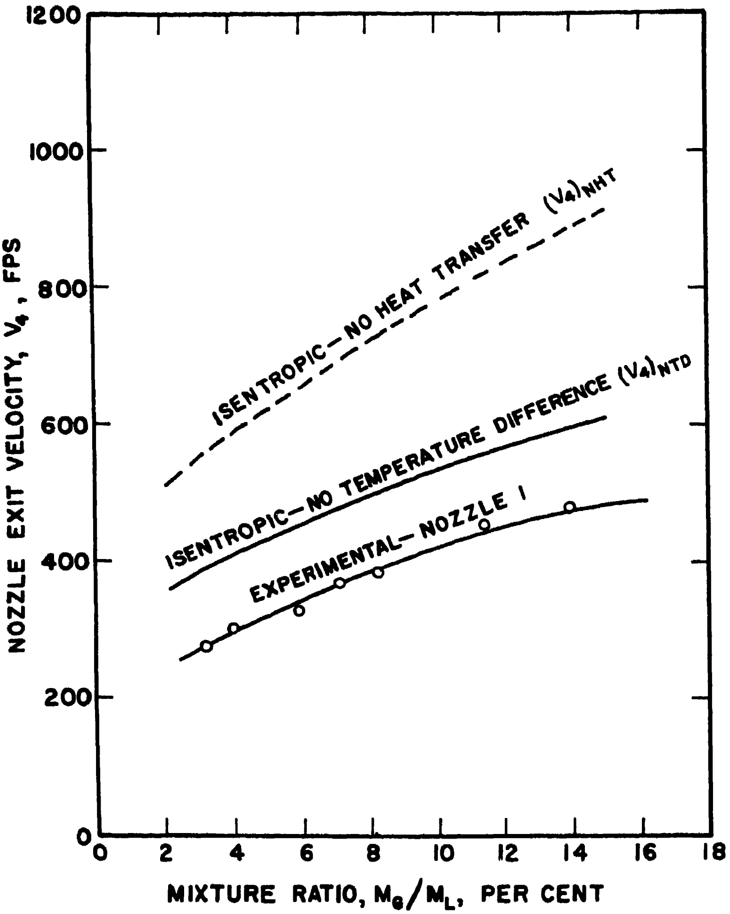

Fig. 8 Experimental nozzle exit velocity for nitrogen-liquid nitrogen

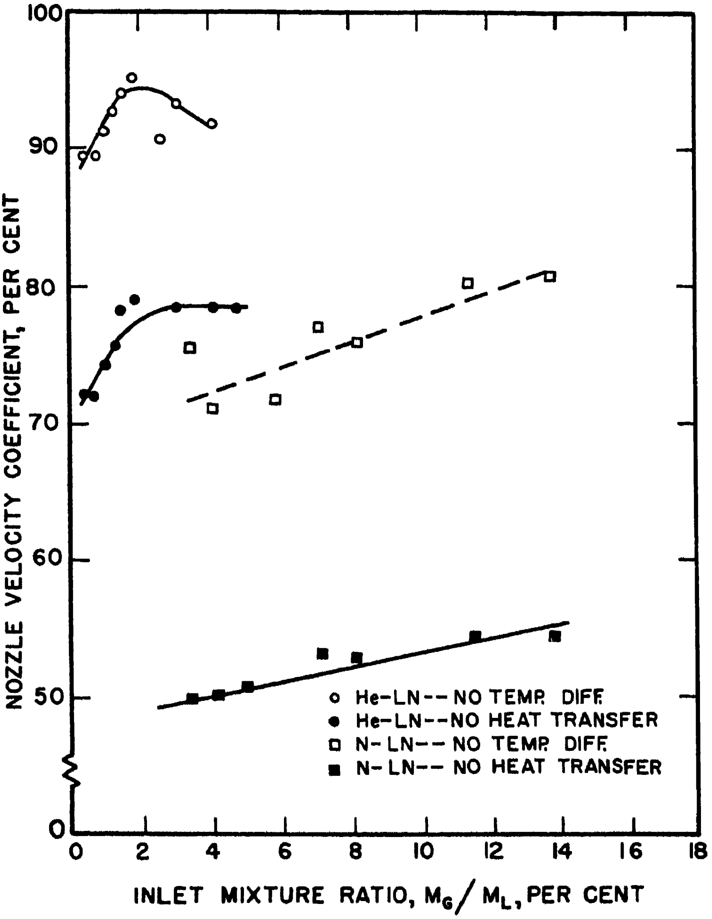

Fig. 9 Nozzle velocity coefficient for nozzle no. 1

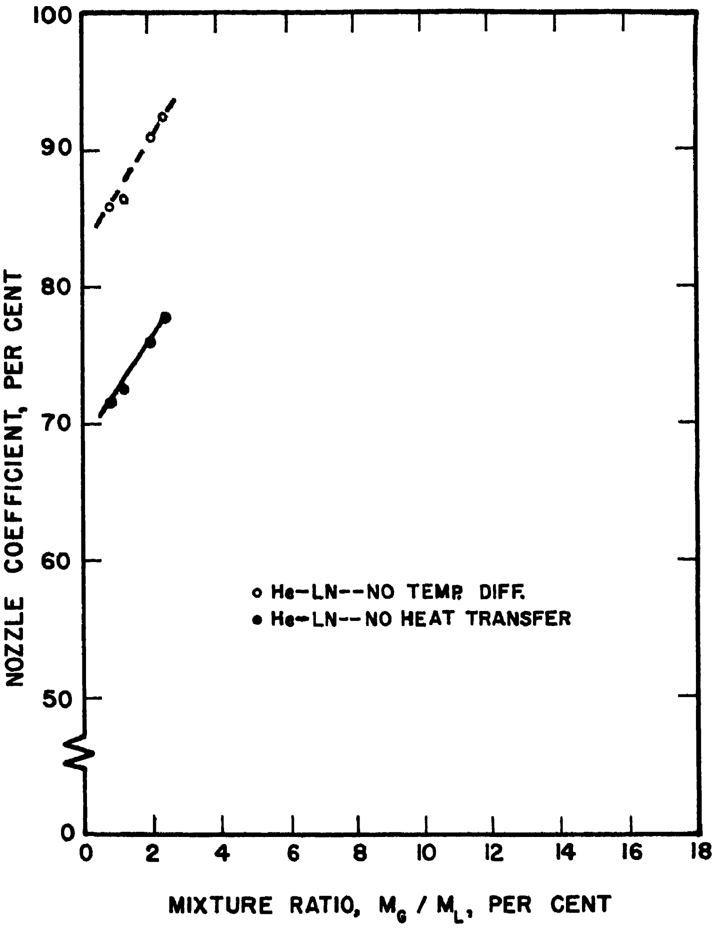

Fig. 10 Nozzle velocity coefficient for nozzle no. 2

PART 2

TWO-PHASE FLOW

B. Stable and Unstable Combustion Processes in Liquid Fuel Rocket Engines

SPRAY COMBUSTION MODEL WITH DROPLET BREAKUP: ANALYTICAL AND EXPERIMENTAL RESULTS

Samuel Z. Burstein, Sanford S. Hammer, and
Vito D. Agosta
Polytechnic Institute of Brooklyn, Brooklyn, N.Y.

ABSTRACT

A simplified model is proposed for the combustion of a bipropellant spray. The model considers two subsystems: one the spray, the other, combusted gases. These subsystems are coupled together by heat transfer, mass transfer, and momentum transfer. The solution of the problem relies on the integration of a system of seven nonlinear differential equations. The integration is performed using the IBM 704 digital computer. It appears that under the given boundary conditions a cooperative evaporation process occurs, in which increased velocity gradients cause increased evaporation that increases the velocity gradient. A series of tests has been made on a 2-in. variable length rocket motor, using JP-5A and liquid oxygen. A simple converging-diverging nozzle is employed to give high chamber exit Mach numbers (0.4 to 0.5). For a given set of injection parameters, under stable operating conditions, the results indicate that the steepest

---

S.Z. BURSTEIN is presently Associate Research Scientist, Courant Institute of Mathematical Sciences. This work is taken from the dissertation submitted to the Faculty of the Polytechnic Institute of Brooklyn in partial fulfillment of the requirements for the degree of Doctor of Philosophy, June 1962. S.S. HAMMER is Assistant Professor, Mechanical Engineering Dep. V.D. AGOSTA is Professor, Mechanical Engineering Dep. Paper presented at the ARS Propellants, Combustion, and Liquid Rockets Conference, Palm Beach, Fla., April 26-28, 1961. This work was sponsored by the Air Force Office of Scientific Research under Contract AF49(638)-165.

portion of the gradient, which corresponds to evaporation of the major portion of the fuel, is always found in a fixed region of the chamber, independent of the absolute length of the chamber. The experimental results appear to agree with the theory for the conditions investigated.

INTRODUCTION

The processes involved in the combustion phenomena in a liquid propellant rocket consist of spraying fuel and oxidizer into the chamber, mixing, evaporating the droplets, interdiffusion of the vapors, and then the chemical reaction. The chain of events stated here is still oversimplified. The overall process is so complex that simplified models having some of the most important features of the real physical phenomena must be studied first. In the evaporation and combustion of a spray, the models are simplified so that the ballistics, evaporation and combustion of individual droplets of fuel are discussed. If the interaction between single droplets is negligible, then evaporation rates of a distribution of droplets are additive. Thus, a distribution of droplets can be used to approximate the evaporation rates of certain spray configurations.

This paper depicts combustion in a rocket motor as controlled by the evaporation process of an arbitrary number of droplets of injected fuel. The evaporation rate of the droplet of fuel is most affected by its immediate environment, which in this case happens to be high velocity gases at temperatures in the range of 5800°R and a pressure of approximately 11 atm. The environment is determined, to a large extent, by the rate of evaporation of the droplet of fuel, that is, by the rate at which chemical energy is added to the system. Thus, there is a strongly coupled system consisting of the evaporation processes and the fluid dynamics of the environment. The results of the evaporation of the droplets of fuel are weighted to yield a mass rate of flow which is consistent with approximately a 500-lb thrust chamber.

DROPLET MODEL

The evaporation of a spray is treated as the summation of the evaporation of individual drops. The general reliability of droplet drag and vaporization rate correlations for single droplets, when applied to sprays, is suspect. This work is aimed at determining the consequences of the assumption of additivity of droplets.

Liquid

The liquid is completely mixed; it has a uniform temperature, and its composition, vapor pressure, surface tension, specific heat, and viscosity are that of JP-5; the vapor pressure, surface tension, specific heat, and viscosity are taken as functions of temperature.

Film

The film consists of two components: 1) with properties of JP-5A; and 2) with properties averaged between carbon dioxide and water vapor, including average critical pressure and temperature.

Outer Boundary of Film

The film boundary temperature is that of the bulk gas; where the temperature and pressure of bulk gas vary in a prescribed manner (from the hydrodynamic calculations), the partial pressure of the hydrocarbons equals zero and the partial pressure of the inert component equals the total pressure.

Bulk Gas

The bulk gas temperature, pressure, and velocity are determined by fluid dynamic calculations. Its composition is determined by assuming that all of the oxidizer is vaporized and that chemical equilibrium exists between the vaporized hydrocarbons and the oxidizer.

Inner Boundary of the Film

The inner boundary temperature is that of the liquid where the partial pressure of the hydrocarbon equals the vapor pressure, and the partial pressure of the combustion products equals the total pressure minus the partial pressure of the hydrocarbon.

Heat Transfer

The heat transfer process is assumed to be convection only where the correlation of Ranz and Marshall (1) [1] is used:

$$Nu_h = \frac{2hr}{K_m} = 2 + 0.6\, Pr^{1/3} Re^{1/2} \qquad [1]$$

---

[1] Numbers in parentheses indicate References at end of paper.

where r = droplet radius, ft
h = film coefficient Btu/ft^2-sec-°F
K_m = mean film conductivity, Btu/ft-sec-°F
Pr = Prandtl number, dimensionless = $\frac{C_p \mu}{K}$
Re = Reynolds number, dimensionless = $\frac{2r\,|u-v|\rho}{\mu}$

A correction is made for sensible heat carried by the evaporating fuel moving away from the drop (6)

$$q_v = hA_L(T_g - T_L)Z \qquad [2]$$

Here q_v is the heat in Btu per second absorbed by the droplet by convection, A_L is the area of the droplet in square feet, and T_g and T_L are the gas and droplet temperatures, respectively. Z is defined by

$$Z = \frac{\beta}{e^{\beta} - 1} \qquad \beta = \frac{\dot{w}c_p}{hA_L}$$

It is seen, then, that Z is that fraction of total heat transfer from the gas that arrives at the surface of the liquid drop. β is dimensionless, since W is the vapor from the evaporating drop in pounds per second, and C_p is the specific heat at constant pressure of the vapor in Btu/lb °F. The temperature change may then be computed, since λ, the latent heat of the drop (Btu/lb) is known. If θ is the time in seconds, then

$$\frac{dT_L}{d\theta} = \frac{q_L}{M_L C_L} \qquad [3]$$

where q_L, the net heat absorbed by the evaporating droplet, is given by

$$q_L = q_v - \dot{w}\lambda$$

C_L is the specific heat of the liquid (Btu/lb°F), and M_L is the weight of the liquid drop in pounds.

Mass transfer is assumed to be by film diffusion. Here thermal diffusion (the Dufour Effect) is neglected, and the correlation of Ranz and Marshall (1) is used:

$$Nu_{\dot{w}} = \frac{2 K_g r \bar{\bar{T}}}{D_v M_g / R} = 2 + 0.6\, Sc^{1/3}\, Re^{1/2} \qquad [4]$$

where N_u = Nusselt number, dimensionless
D_v = diffusivity, ft^2/sec
M_g = molecular weight of fuel vapor, lb/lb-mole
R = gas constant, ft-lb/lb-mole °R
Sc = Schmidt number, dimensionless = $\frac{\mu}{D_v \rho}$

The diffusivity is calculated by the equation given by Bird (2) for the molecular diffusion coefficient:

$$D_v = \frac{(P_{ca} P_{cb})^{1/3} (T_{ca} T_{cb})^{5/12}}{\left(\frac{2 M_a M_b}{M_a + M_b}\right)^{1/2}} \frac{a^*}{p} T_R^{\,b} \qquad [5]$$

Here

$$T_R = \frac{\bar{\bar{T}}}{(T_{ca} T_{cb})^{1/2}}$$

P_{ca} = pseudo-critical pressure of JP-5A, atm
P_{cb} = average critical pressure of CO_2 and H_2O, atm
$\bar{\bar{T}}$ = average temperature of liquid droplet and combustion products, °R
T_{ca} = pseudo-critical temperature of JP-5A, °R
T_{cb} = average critical temperature of CO_2 and H_2O, °R
a^* = correlation constant = 3.882×10^4
b = correlation constant = 1.8229
M_a = molecular weight of JP-5A, lb/lb-mole
M_b = average molecular weight of CO_2 and H_2O, lb/lb-mole

A correction is made for the effect of bulk motion of the fluid away from the evaporating interface (3). If p_L is the vapor pressure of the liquid fuel and p the total static pressure of the gases, then

$$\dot{W} = K_g A_L P_L \alpha \qquad [6]$$

where

$$\alpha = \frac{P}{P_L} \ln \frac{P}{P - P_L} \qquad [7]$$

α is a correction factor to account for the unidirectional diffusion process rather than just considering the equimolal diffusion transfer coefficient K_g that is computed from Eq. 4.

The change in radius of the fuel drop in time can be calculated if the liquid density ρ_L is known as a function of the drop temperature. The continuity equation for the liquid drop is

$$\frac{d}{d\theta}(\rho v)_L = -\dot{W}$$

where v = drop volume = $\frac{4}{3} \pi r^3$.

$$\frac{dr}{d\theta} = -\frac{\dot{W}}{A_L \rho_L} - \frac{r}{3\rho_L}\left(\frac{d\rho_L}{dT_L}\right)\frac{dT_L}{d\theta} \qquad [8]$$

Drag is calculated from Ingebo's correlation on liquid drops (4). The drop acceleration is known once the gas density ρ and velocity U are stated

$$\frac{dV}{d\theta} = -\frac{3}{8} C_D \frac{\rho}{\rho_L} \frac{(U-V)^2}{r} \qquad [9]$$

and is taken to have the same sign as (U - V). V is the drop velocity in fps, and C_D, the drag coefficient, is given by

$$C_D = \frac{27}{Re^{0.84}} \qquad [10]$$

Drop breakup was considered necessary since high pressures, above the critical temperature of the fluid, would be used. Liquid temperatures could not, physically, go to the critical without reduction of surface tension σ_L to the point where droplet stability is impaired. Therefore, provision was made for the droplet to be replaced by an arbitrary number of smaller drops of equal mass whenever an arbitrary Weber number was exceeded

$$We = \frac{2r(U-V)^2 \rho}{\sigma_L} \tag{11}$$

This number is a ratio of the distorting force to the restoring force. This is intended as a zero order approximation to qualitatively determine what effects may occur.

HYDRODYNAMIC MODEL

The thermodynamic properties of the combusted fuel and oxidizer were obtained from the second law restriction that the free energy must be a minimum at a given value of pressure and temperature for an equilibrium condition. The reaction equations used are

$$CO_2 - CO \rightarrow O$$

$$\tfrac{1}{2}CO_2 + \tfrac{1}{2}H_2O - \tfrac{1}{2}CO \rightarrow OH$$

$$2CO_2 - 2CO \rightarrow O_2$$

$$CO + H_2O - CO_2 \rightarrow H_2$$

$$\tfrac{1}{2}CO + \tfrac{1}{2}H_2O - \tfrac{1}{2}CO_2 \rightarrow H$$

These equations are written in the form of

$$\Delta G_j = \sum_i \mu_i \nu_{ij} \tag{12}$$

where

$$\mu_i = \left(\frac{\partial G}{\partial n_i}\right)_{T,P,n_j}$$

and ν_{ij} is the coefficient of the i^{th} component of the j^{th} reaction, n_i is the number of moles of species i. The changes in n_i are limited by the constraint.

$$dn_i = \sum_j \nu_{ij}\, d\xi_j \qquad [13]$$

Here ξ is the extent of the reaction. Also at a fixed T and p

$$dG = \sum_i \mu_i\, dn_i \qquad [14]$$

A parameter λ is introduced such that

$$d\xi_j = -\Delta G_j\, d\lambda$$

Then Eqs. 12, 13, and 14 yield

$$dG = -\left\{\sum_j (\Delta G_j)^2\right\} d\lambda \qquad [15]$$

If $d\lambda > 0$, then a thermodynamically possible change in G can occur; i.e, G decreases. From this form, the sum of the squares of ΔG may be computed and the computation terminated when $\sum_j (\Delta G_j)^2 \leq \delta$; δ is determined from the accuracy of the free energy data. A more detailed discussion is given in Ref. 7.

Once the minimum value of free energy is determined, then the n_i are known and, with a knowledge of the specific heat data, the enthalpy and molecular weight of the mixture may be determined. These two values are used in the energy equation, Eq. 22 and the equation of state, Eq. 16.

The relations for the steady state equations may be obtained from the nonsteady Eqs. 5. These equations relating the gas pressure P, density ρ, temperature T, and velocity U are the equation of state:

$$P = \rho\left(\frac{R_o}{M}\right)T \qquad [16]$$

where $\left(\frac{R_o}{M}\right)$ is the gas constant.

The continuity equation is

$$\frac{\partial \rho A}{\partial \theta} + \frac{\partial \rho U A}{\partial x} = \dot{W} \qquad [17]$$

where A = chamber cross-sectional area, ft^2

$\dot{W}$ = mass added per unit length per unit time

The momentum equation is

$$\frac{\partial U}{\partial \theta} + U\frac{\partial U}{\partial x} = -\frac{1}{\rho}\frac{\partial P}{\partial x} + f \qquad [18]$$

where f is the force between the liquid drops and gas, $\frac{\text{ft-lbf}}{\text{lbm}}$.

The energy equation following a gas particle is

$$\frac{\partial h}{\partial \theta} + U\frac{\partial h}{\partial x} = q + \frac{1}{\rho}\frac{\partial P}{\partial \theta} + \frac{U}{\rho}\frac{\partial P}{\partial x} \qquad [19]$$

This equation can be reduced to a relation between thermodynamic states once the relation between enthalpy h and temperature is known.

For the steady state, all time derivatives may be dropped in Eqs. 17 and 18 so that

$$d(\rho U A) = \dot{W} dx$$

$$U dU = -\frac{1}{\rho} dP + f dx$$

The integrated continuity equation becomes

$$(\rho U A)_x = \int_0^x \dot{W} dx = \Phi_x \qquad [20]$$

The integrated momentum equation becomes

$$P_{x+\Delta x} = P_x + \bar{\rho}\left[\int_x^{x+\Delta x} f dx + \left(U_x^2 - U_{x+\Delta x}^2\right)/2\right]$$

$$\bar{\rho} = (\rho_x + \rho_{x+\Delta x})/2 \qquad [21]$$

The energy equation for a control volume is

$$\Phi_x\left(c_p T_x + \frac{U_x^2}{2}\right) - \Phi_{x+\Delta x}\left(c_p T_{x+\Delta x} + \frac{U_{x+\Delta x}^2}{2}\right)$$
$$= (\Phi_{x+\Delta x} - \Phi_x)\left(h_f + \frac{V^2}{2}\right) + q_v \qquad [22]$$

Here q_V is obtained from Eq. 2, V is the drop velocity, and h_f the stagnation enthalpy. Eqs. 16, 20, 21, and 22 combined with Eqs. 3, 8, and 9, written in finite difference form, form the set of equations to be solved.

Strategy of Computation

The calculation was divided into two main parts. In the first part a single droplet is followed as it moves, evaporates, and breaks up, in a prescribed environment of gas pressure, temperature, and velocity.

Eqs. 3, 8, and 9 are simultaneous ordinary differential equations in the variables T_L, r, and V and can be solved if initial conditions plus values of T, p, and U as all points are known. This is repeated for each drop size present, and the results are weighted to give the total evaporation.

In the second part, the hydrodynamic equations are solved for a specified evaporation profile taken from the results of part one. Eqs. 16, 20, 21, and 22 are solved simultaneously, since $\Phi(x)$, $q_V(x)$, $f(x)$ are known from the evaporation calculation. The boundary conditions for the gas dynamic equations are given as

$$\text{at } x = x_0 = 0 \qquad P = P_0,\ T = T_f,\ U = 0$$
$$x = L \qquad U_L = \sqrt{\gamma R_0 T_L / M}$$

One hundred basic increments were subdivided into a number of sub-steps that were determined by the slope of the evaporation curve. With 10 substeps, satisfactory results were usually obtained. Normally, 1000 increments were used, unless the liquid temperature changed by more than 50°F in an increment. In this case, the increment size was reduced by a factor of 10 for that substep. If the liquid temperature change was still too large, then the substep was reduced by 10^2, etc. This insured slowly changing integrands and provided satisfactory convergence for all cases tried.

Physical properties, which were needed in computation of Eqs. 1-11, were provided by a series of subroutines, using a variety of equations, as well as tables with interpolations. Change of any basic equation would require altering the evaporation subroutine. Change in physical properties, other than input quantities, can be made by replacing the appropriate subroutine.

In the evaporation subroutine, droplet breakup takes place according to the Weber number criterion, Eq. 11.

After computing evaporation, the main program weights the results to compute total evaporation at each increment, which is part of the input information to the fluid dynamics subroutine.

Eqs. 16, 20, 21, and 22 form the heart of the fluid dynamic subroutine. The program uses information given to it by the evaporation subroutine to produce a matrix (3 x 100) of gas pressure, temperature, and velocity. That is, the combustion chamber and nozzle are divided into 100 sections (1, 2, 3,..., n, n + 1,..., 100). A separate calculation is carried out in each section, that is, going from (n) to (n + 1).

The area that is available to gas flow A_n, A_{n+1}, is calculated by a subroutine program, and the total mass that is present at any section Φ_n, Φ_{n+1} is obtained by a function program. The subroutine checks the ratio of the terms, i.e., Φ_{n+1}/Φ_n, and if a prescribed limit is exceeded, the step size

$$x_{n+1} - x_n = {}_n\Delta x_{n+1}$$

becomes

$$\Delta x' = \frac{{}_n\Delta x_{n+1}}{N}$$

where N may be any convenient number such that $\frac{\Phi'_{n+1}}{\Phi_n} \to 1$. Here the primes denote the new coordinate. The computational procedure is carried out N times, then the ratio Φ_{n+2}/Φ_{n+1} is checked, and so on. The method of solution consists of assuming a T_{n+1} and solving for U_{n+1} in Eq. 20. Then p_{n+1} may be solved for, knowing the U_{n+1} from Eq. 21 and p_n from Eq. 16. T_{n+1} may be solved for in Eq. 22 and if

$$|T'_{n+1} - T_{n+1}| < \epsilon \quad \epsilon > 0$$

then it may be said that the system of difference equations, Eqs. 16, 20, 21, and 22, are satisfied. By assuming $T_n + 2$ in the space calculations, the computations can be continued in a similar manner. The superscripts denote iteration number. Transfer after completion of 100 steps is to the main program, which controls the drop and gas calculation.

DESCRIPTION OF EXPERIMENTAL APPARATUS

The first series of tests was conducted with liquid oxygen and JP-5A in a 2-in. diam chamber, employing a showerhead type of injector and a simple converging-diverging nozzle (Fig.1). The only variable in this first series of tests was the chamber length; i.e., using the same injector-nozzle configuration, and the same propellant flow rates, the chamber length was to be varied from 8 to 24 in. Therefore, the chamber may be composed of one or more sections, depending on the total length desired. The three basic components (injector, chamber, and nozzle) are held together by a mechanical clamping arrangement. All components are uncooled and are fabricated from commercial brass, with the exception of the nozzle. This is composed of a graphite linear in a brass collar and is also uncooled. A complete description of the feed system, control system, and rocket motor can be found in Ref.8.

The design of the nozzle for the steady state program was influenced by the future objectives of the laboratory. Among these objectives was an investigation of the nonlinear aspects of combustion instability. In the theoretical analysis of combustion instability, the effect of the Mach number of the gases is highly significant, as indicated in Ref.9. Briefly stated, if $(1-M^2)$ is approximately unity, i.e., if $M \leq 0.2$, the mathematical analysis can be greatly simplified by means of linearizing assumptions. However, the actual problem is nonlinear, and in practice the Mach numbers at the nozzle entrance are well above the linear value of 0.2. Since the entire steady state program was being conducted as a preliminary step to a nonlinear analysis of combustion instability, the nozzle contraction ratio was designed for a nozzle entrance Mach number of 0.45, based on isentropic flow and constant isentropic exponent.

The verification of the nozzle entrance Mach number required a measurement of the total pressure at that point. This entails designing a probe that can withstand extremely high temperatures and an oxidizing atmosphere. A water-film cooled graphite probe was developed and employed successfully

(Fig.2). The cooling water is sprayed through the probe body into the gas stream at a pressure slightly in excess of the gas pressure. Thus, a film type of cooling is obtained. The mass flow of water into the chamber amounts to only 1 % of the propellant flow.

The instrumentation necessary for the measurement of static pressure gradients in a rocket motor was selected after a consideration of several factors: proximity of measurements, expected pressure gradient, accuracy, and cost. Fig. 3 shows the resulting scanner.

The scanner permits a single transducer to travel from pressure tap to pressure tap and consecutively record the pressure at eight different locations in the chamber. The pressure scanner consists of three piston and cylinder units. Units A and B each contain facilities for measuring the pressure at eight locations, whereas unit C is a hydraulic driver. The taps located in the rocket motor are extended to the bulkhead of either unit A or B and then to compartments formed by the inner cylinder or piston, O-rings, and the outer travelling cylinder, which houses a transducer. The reciprocating motion of the outer cylinders (which enables the transducer to consecutively measure the pressure at adjacent taps in the rocket motor) is governed by a double acting hydraulic piston and cylinder, unit C. Provisions have been made for varying the speed and length of stroke of the unit. In addition, a method of continuously recording the exact location of the transducer housing has been developed. This consists of measuring the voltage drop between a moving electrical contact mounted on the transducer housing and a flat copper bar mounted alongside the scanner cylinder. The copper bar is actually an eight stepped voltage divider. The length of each step is equal to the length of the compartments in the scanner cylinder. The distance between steps or sections is equal to the thickness of the O-rings separating the compartments. Each of the copper bar sections is at a different predetermined voltage. Therefore, by simultaneously recording the output of the transducer and the voltage drop to the moving electrical contact, it is possible to match the pressure magnitude with the location at which it was measured.

The output of the transducers is recorded on a recording oscillograph. In order to obtain maximum resolution, a suppressed zero is employed so that only the pressure difference about a fixed point is recorded. To determine the absolute pressure at each port from the records of the gradients requires a measurement of the absolute pressure at one point in the chamber.

Several objections may arise as to the accuracy and applicability of the previously described system for the measurement of pressure gradients in a rocket motor. It is obvious that the pressure at each chamber tap is not measured simultaneously, but rather there is a time lag between the measurement at successive ports. However, the speed of the scanner can be adjusted so that a complete traverse of the chamber can be made in one second. Since a normal test firing lasts six sec after steady state conditions have been reached, six complete traverses of the motor can be obtained in one run. Examination of the data indicates that one traverse is identical to the next, both as to gradient and absolute pressure at each port. Thus, it is concluded that once the maximum chamber pressure has been reached, the motor operation becomes steady unless an instability arises.

In spite of the previous remarks regarding the steadiness of operation and the reproducibility of gradients on a recording trace during a test run, the pressure at each chamber location is not invariant. Under the smoothest conditions there is still a good deal of combustion noise present. In addition, as pointed out in Refs. 9 and 10, there exists an instability regime for any particular oxidizer-fuel ratio of a given set of propellants. During the course of the tests, rough or unstable operation was encountered on several occasions, particularly with the shorter chambers, ranging in length from 8 to 12 in. Further discussion of the occurence of pressure oscillations in excess of combustion noise is presented in the discussion of experimental results. Despite the forementioned comments, it is still possible to determine the steady state pressure gradients, where steady state is defined as the average or d-c level of the transducer output.

EXPERIMENTAL RESULTS - COMPARISON WITH THEORY

Steady state pressure gradients were measured in a 2-in. diam variable length rocket motor. The first series of tests was conducted on a 17-in. chamber length (Fig. 4). Results indicate the presence of a steep pressure gradient between 4 and 10 in. from the injector face. The data indicates that a 29-psi gradient was measured between $1\frac{1}{4}$ in. and $14\frac{3}{8}$ in. from the injector face. This amounts to 17 % of the pressure measured at the $1\frac{1}{4}$-in. tap. In the region between 4 and 10 in. from the injector (35 % of the chamber length), a gradient of 21 psi was measured.

This is equal to 72 % of the measured total gradient, or a somewhat smaller percentage of the gradient obtained by extrapolating to the injector face and nozzle entrance.

The gradient in the remaining portion of the chamber (10 to 17 in.) is flat: 7 psi in 7 in. It is felt that this portion of the pressure drop is due to heat transfer and/or friction. The measured ratio of static to total pressure is 0.915 at the $14\frac{3}{8}$-in. tap. This corresponds to a Mach number of 0.41 for a gas whose isentropic exponent is 1.16. The value of 1.16 was determined by the thermochemical equations minimization of free energy. The oxidizer fuel ratio for this and all subsequent tests discussed in this report is 2.76 ± 5 %. The total propellant flow is 2.47 lbm/sec ± 5 %. The O/F equivalence ratio is 0.793. The percentage deviation stated in the foregoing does not account for the experimental error in a single test, but is due to a variation in measured flow from one test to another.

The theory predicted that the main evaporation and combustion of the drops occurred within a fractional section of the chamber length. Here the fluid dynamic flow field increased the evaporation rate, which in turn increased the velocity field and hence the pressure gradient.

Typical results of the integration of Eqs. 3, 8, 9, 16, 20, 21, and 22 are shown in Fig. 4. Curve A is the solution for p(x) when the boundary condition for temperature at the injector is equal to the flame temperature (5877°R). Curve B is the solution for p(x) when the gas temperature at the injector face is 5500°R. Curve B is intended to show the effect of incomplete combustion or heat transfer on the pressure drop. Curve B allows a greater mass flow through the nozzle due to lower chamber temperatures. $\Phi_{max} = 2.36$ is the experimentally measured flow rate.

In order to determine the effect of chamber length on the position of the steep portion of the gradient (and hence the combustion process), the chamber was reduced to $8\frac{3}{8}$ in. with subsequent tests to be run with chamber length increments of 2 to 3 in. The gradients obtained in an $8\frac{3}{8}$-in. chamber and a $10\frac{3}{8}$-in. chamber are presented in Fig. 5. Both curves indicate a continuously increasing gradient over a region that extends approximately 1 in. from the injector face to 1 in. from the nozzle entrance. It was stated previously that the gradient in the 17-in. chamber, Fig. 4, started to decrease 10 in. from the injector face. As a result of the increasing gradient at the nozzle entrance, it is concluded that evaporation and combustion of the fuel are not completed in the shorter chambers. The theoretical pressure calculation for the $8\frac{3}{8}$-in. chamber is also shown in Fig. 5. This computation indicated that some combustion in agreement with the experimental data was taking place in the nozzle, rather than the chamber.

The experimental results obtained with a $12\frac{1}{4}$, $15\frac{1}{2}$, and $19\frac{1}{4}$-in. chamber are reproduced in Fig. 7. All three tests indicate a decreasing gradient, or point of inflection, approximately 10 in. from the injector face. The gradient in the region of the injector face appears to be steeper in the case of the $12\frac{1}{4}$-in. chamber than in the longer length. This would indicate a rapid breakup of the injected jet, and hence evaporation and combustion closer to the injector face.

The above phenomenon (steep pressure gradients at the injector face) is also present, though to a somewhat lesser extent, in the $8\frac{3}{8}$ and $10\frac{3}{8}$-in. chambers. The steeper gradients, indicative of jet breakup and droplet evaporation, are attributed to rough or unstable operation. Due to the low frequency response of the recording oscillograph, it is not possible to quantitatively describe the pressure oscillations. However, based on the relative amplitude of the pressure oscillations and the frequency of chamber and nozzle burnout, the $12\frac{1}{4}$-in. chamber would be the most unstable configuration. The oscillations in the shorter chambers were of a lesser degree, whereas the longer lengths exhibited only normal combustion noise. It is felt that the increased pressure oscillations in the shorter chambers cause a more rapid breakup of the injected spray, resulting in a shift of the combustion zone towards the injector face. Previous work done at the Propulsion Research Laboratory (11) discusses, in detail, the effect of chamber length and pressure oscillations on liquid jet breakup. It might be mentioned at this time that the steady state analytical work did not include the jet breakup distance. It appears to be a critical factor for the initiation point of the evaporation computation. A fixed value of 2 in. was used in all computations for qualitative purposes. A more complete analysis would be to incorporate a mechanism for jet breakup and drop formation. It would appear from the results obtained under stable conditions that this 2 in. distance is of the right order of magnitude.

Fig. 8 shows the effect of initial drop radius on the position of the pressure gradient in the 15.5-in. chamber. The three drop model uses a Rosin-Rammler distribution (12) to describe the spray distribution. The small drops, which make up 28 °/o of the spray (represented by the 26 μ drop), evaporate and combust quickly. The pressure gradient is thus initially steep and results in accelerating the evaporation process of the larger drops. The 80μ drop is, thus, completely evaporated within the chamber. On the other hand, the 100μ model evaporates much more slowly due to the absence of this interaction, and so a 15.5-in. chamber is insufficient for proper combustion.

Fig. 9 shows the gas temperature and velocity as a function of position in the 15.5-in. chamber. Fig. 10 shows the results of the solution of the differential equations of the liquid subsystem for the 15.5-in. chamber. The liquid temperature rises rapidly but then remains practically constant throughout evaporation. r/r_0 initially increases due to expansion and then decreases due to evaporation. In this case $r_0 = .19 \times 10^{-3}$ft, $V_0 = 122$ fps, and $T_0 = 600$°R.

CONCLUSIONS

The picture is, then, one of slowly evaporating drops flowing down a field of gradually increasing velocity until a cooperative effect between the drops and flow field causes an acceleration of evaporation. In certain cases it has been found that if the velocity gradients are really severe, shattering of the droplets occurs. This happened in the nozzle of the 8-in. chamber.

When the Weber number is given a value of 100, droplet shattering (Fig. 8) occurs in the chamber (dashed curve) and drastically changes the picture of evaporation. Just as in the case of drops in a spray with continuous evaporation, a similar effect occurs with breakup. When the drops start breaking up evaporation increases very quickly, causing a pressure drop with a corresponding increase in the gas velocity. The resulting velocity gradient then increases the breakup, etc. The basic difference between continuous evaporation model and the breakup model is the thickness of the energy release zone [$W(x) = d\Phi/dx$].

For a given set of injection parameters under stable operating conditions, the results indicate that the steepest portion of the gradient, which corresponds to evaporation of the major portion of the fuel, is always found in a fixed region of the chamber, independent of the absolute length of the motor. For the tests discussed in this report, the steepest portion of the gradient was located between 4 and 10 in. from the injector face. Chambers shorter than 10 in. exhibited combustion in the nozzle. It was also found that rough or unstable operation shifted the gradient. Increasing pressure oscillations caused a shift of the steep portion of the gradient towards the injector face.

In conclusion, it appears that evaporation is a proper rate controlling mechanism for the cases investigated. By proper shaping of the combustion chamber, the evaporation schedule may be extended over the entire chamber length; i.e., a pear shape may distribute the energy release pattern Φ evenly over the entire chamber. An inverse effect may be created by introducing constrictions in the combustion chamber to localize combustion by shattering the droplets in a high velocity gradient field.

Finally, it must be observed that the intent of the experimental program was to determine steady state pressure gradients for verification of the theoretical analysis, and any conclusions based on the experimental program alone require further substantiation. The analytical work will be extended to a nonlinear nonsteady instability analysis using the results of the present investigation.

ACKNOWLEDGMENT

The authors wish to express their gratitude to Robert Corry for his valuable suggestions and to William Peschke and Imants Reba for their participation in the experimental program. Much appreciation is also given to Albert Burstein for the drawing of the figures.

REFERENCES

1 W.E. Ranz and W.R. Marshall Jr.: Evaporation from Drops, Part I. Chemical Engineering Progress, March 1952, vol. 48, pp. 141-146.

2 R.B. Bird: Theory of Diffusion. Advances in Chemical Engineering, pp. 190. Academic Press, New York, 1956.

3 M.M. El Wakil, O.A. Vyehara, and P.S. Myers: A Theoretical Investigation of the Heating-up Period of Injected Fuel droplets Vaporizing in Air. NASA T.N. 2368, May, 1954.

4 R.D. Ingebo: Vaporization Rates and Heat Transfer Coefficients for Pure Liquid Drops. NASA T.N. 2368, July, 1951.

5 T.P. Torda and S.Z. Burstein: Nonlinear Theory of Combustion Instability-Liquid Propellant Rocket Motors. Propulsion Research Laboratory PRL-TN-58-1 (ASTIA No.209-491, AFOSR Doc. No. TN 59-60) December, 1958.

6 R.J. Priem: Propellant Vaporization as a Criterion for Rocket Engine Design; Calculations of Chamber Lengths to Vaporize a Single n-Heptane Drop. NASA TN 3985, 1957.

7 L.M. Naphtali: Complex Chemical Equilibria by Minimizing Free Energy. AFOSR Doc. No. TN 60-228, Project No. 9751, January, 1960.

8 R. Corry and W. Peschke: The Propulsion Research Laboratory of the Polytechnic Institute of Brooklyn, A Symposium on Jet Propulsion. Polytechnic Institute of Brooklyn, February, 1961.

9 L. Crocco, J. Grey, and D. Harrje: Theory of Liquid Propellant Rocket Combustion Instability and its Experimental Verification. ARS Jour. February, 1960, vol. 30, p.159.

10 M.J. Zucrow and J.R. Osborn: An experimental Study of High-Frequency Combustion Pressure Oscillations, Jet Propulsion, October 1958, vol.28, p.654.

11 I. Reba and C. Brosilow: The Response of Liquid Jets to Large Amplitude Sonic Oscillations. WADC Tech. Rep. 59-720, Part III, September 1960.

12 S.Z. Burstein and L.M. Naphtali: A Spray Combustion Model with Droplet Breakup. Kinetics, Equilibria and Performance of High Temperature Systems, Proceedings of the First Conference, Butterworth and Co., London, 1960.

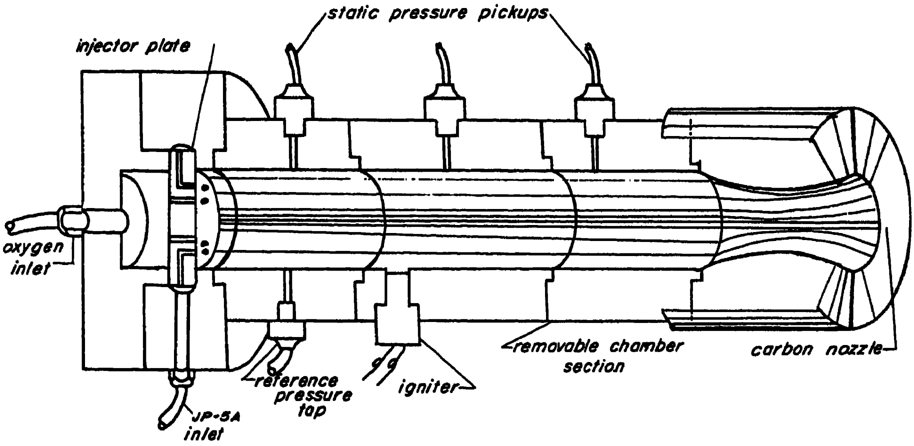

Fig. 1 Experimental rocket engine

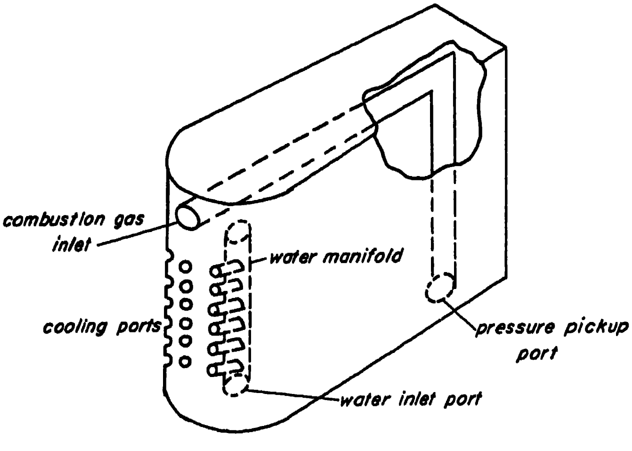

Fig. 2 Water cooled stagnation pressure probe

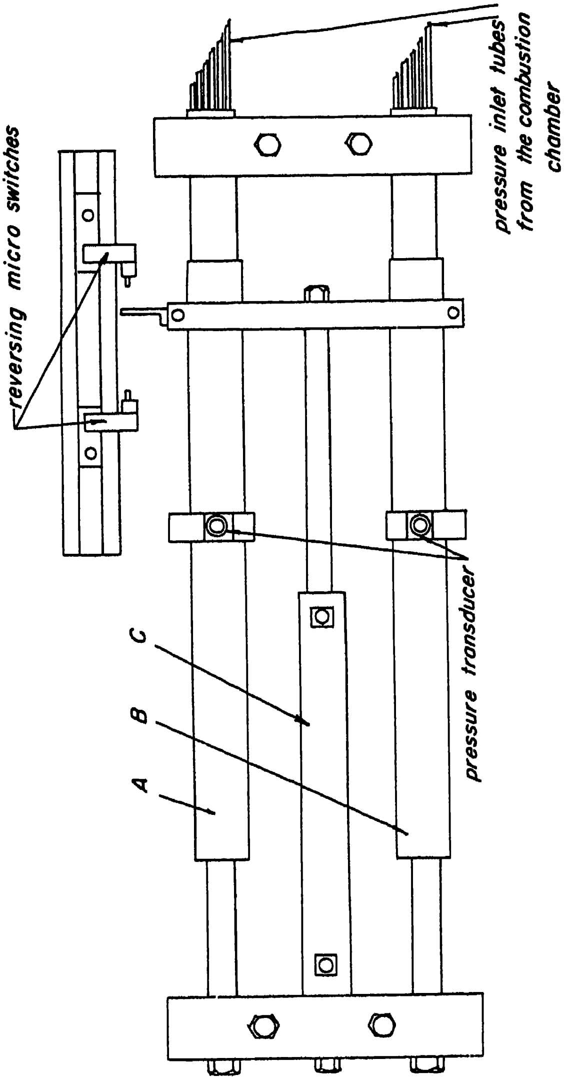

Fig. 3 Steady state pressure scanner

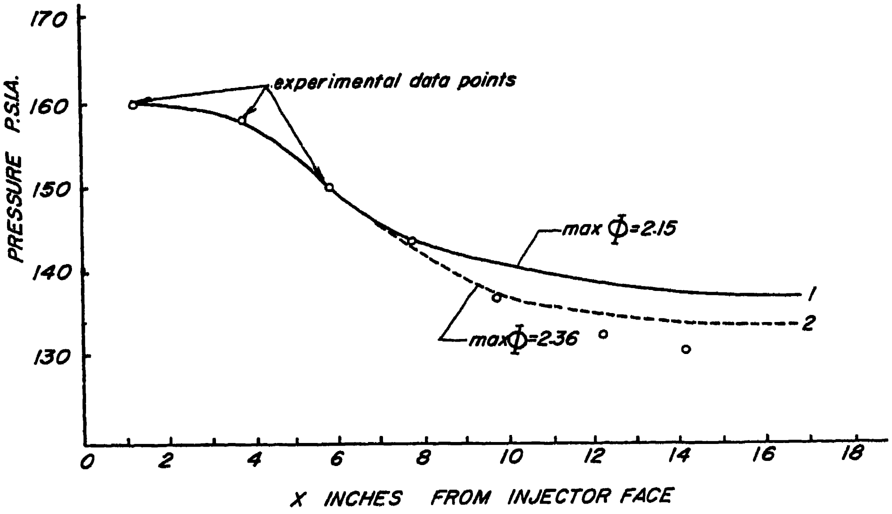

Fig. 4 Steady state pressure history for the 17.5 in. combustion chamber-experimental and theoretical results

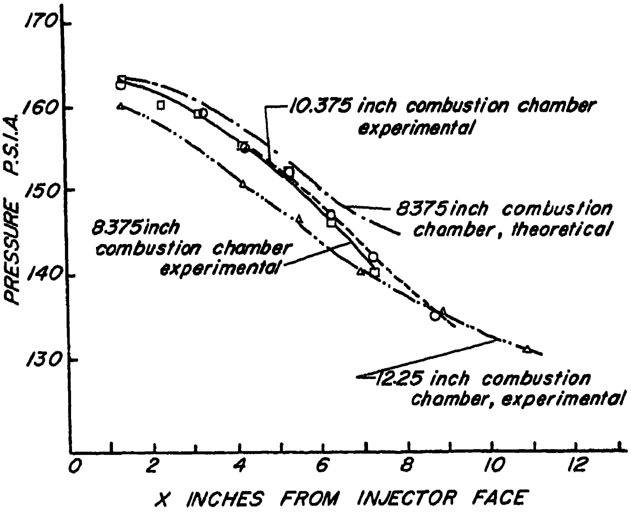

Fig. 5 Steady state pressure history for the 8.375 in., 10.375 in. and 12.25 in. combustion chambers-experimental and theoretical results

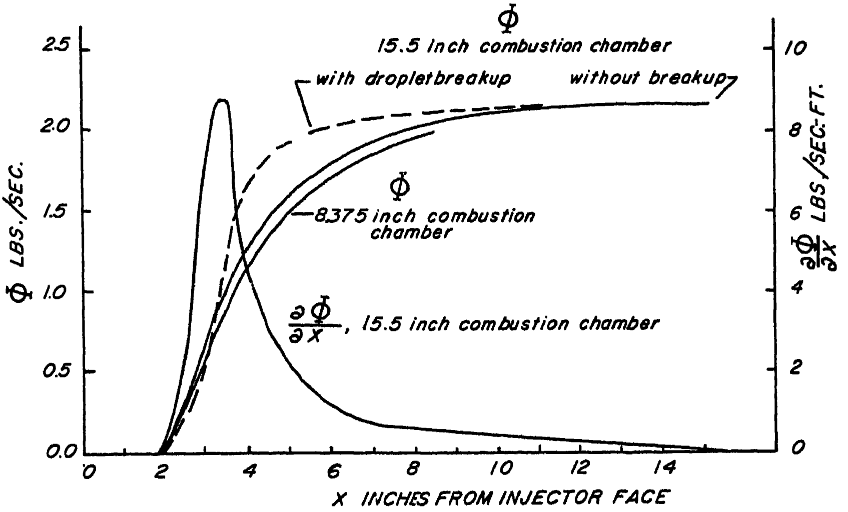

Fig. 6 Differential and integral mass flows for the 8.375 in. and 15.5 in. combustion chambers

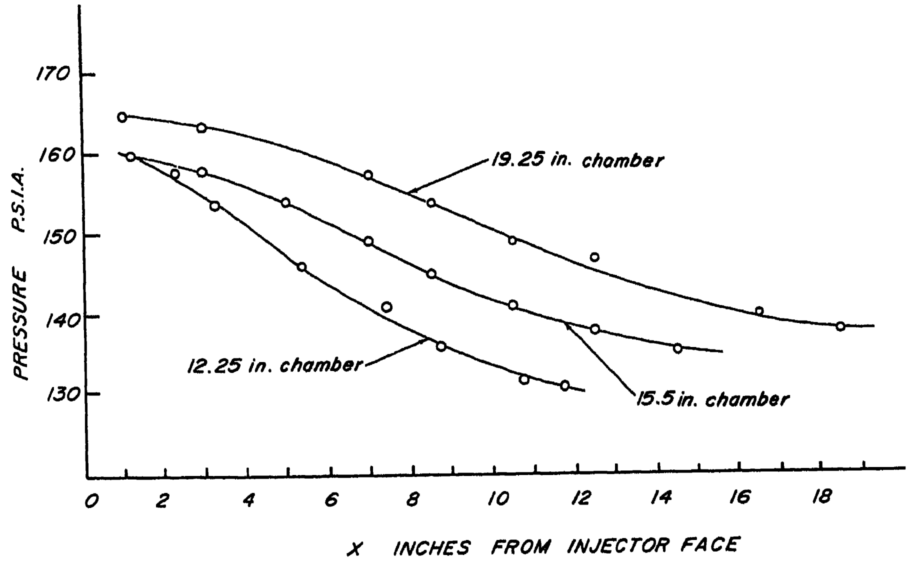

Fig. 7 Steady state pressure history for the 12.25 in., 15.5 in. and 19.25 in. combustion chambers-experimental results

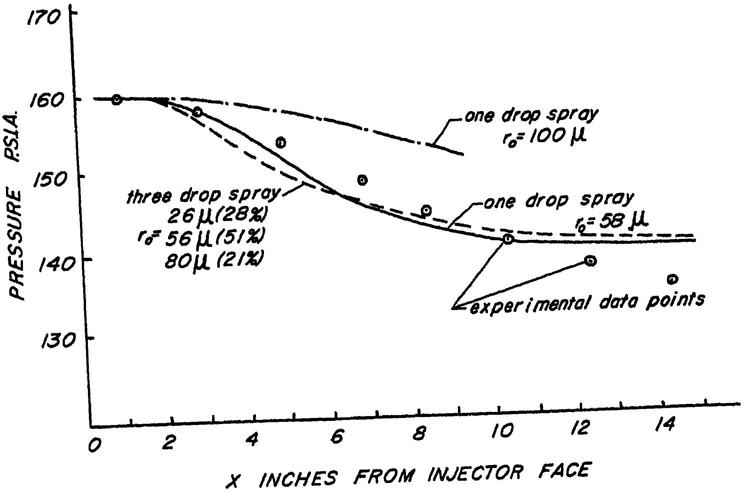

Fig. 8 Effect of drop size and distribution on the pressure history of the 15.5 in. combustion chamber

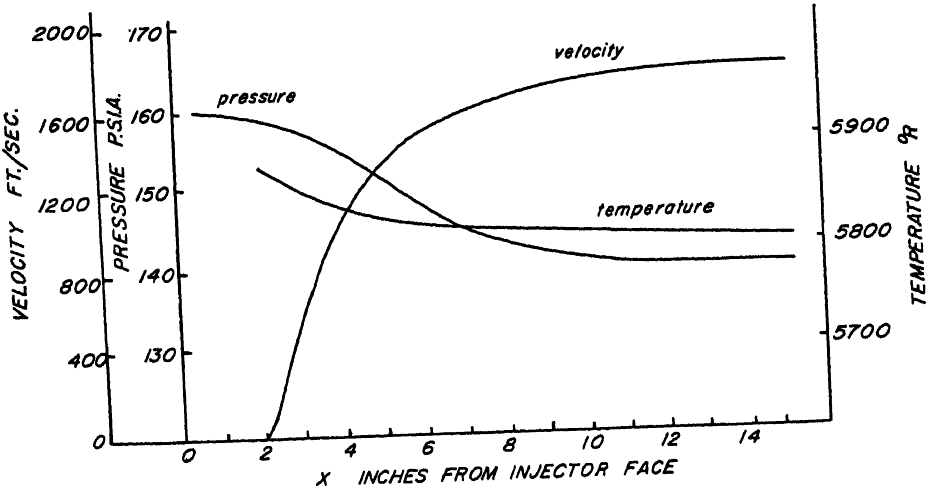

Fig. 9 Solution of the gas dynamic equations for the 15.5 in. combustion chamber

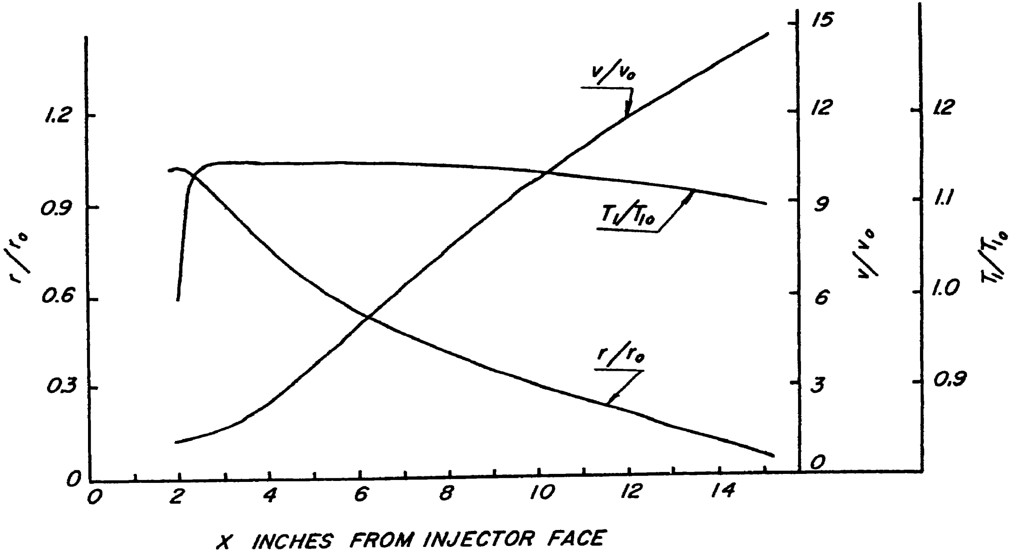

Fig.10 Solution of the droplet equations for the 15.5 in. combustion chamber

STEADY-STATE COMBUSTION MEASUREMENTS IN A LOX/RP-1 ROCKET CHAMBER AND RELATED SPRAY BURNING ANALYSIS

S. Lambiris and L. P. Combs

Rocketdyne, A Div. of North American Aviation, Inc.,
Canoga Park, Calif.

ABSTRACT

Streak photography was employed for measuring experimental axial flow velocities in a transparent two-dimensional rocket combustion chamber operated at 300-psig chamber pressure with LOX/RP-1 propellants. The highest of these measured velocities were found to correspond closely to combustion gas velocity along the chamber length. An analysis of fuel spray burning was used to show that the lowest measured velocities correspond to what might reasonably be that of the largest fuel droplets produced by the initial propellant atomization. Volume mean droplet diameters on the order of 80 to 100 μ, and maximum droplet sizes of 230 to 300 μ were indicated. Deviations between the experimental and calculated velocity profiles were found to be greatest near the nozzle end of the combustion chamber. Disintegration or shattering of the largest propellant droplets, not accounted for in the spray burning analysis, is believed to cause these deviations. The continued application and refinement of the experimental and analytical methods described offers a very effective combination for developing a quantitative description of liquid propellant rocket combustion details.

INTRODUCTION

The events and processes occurring in the combustion chamber of a liquid propellant rocket system during stable, steady-state mainstage operation are now fairly well known on a

---

S. Lambiris is Senior Research Engineer. His present address is Pratt and Whitney Aircraft, East Hartford, Conn. L. P. Combs is Principal Scientist, Combustion Dynamics Research. Paper presented at the National ARS-IAS Joint Meeting, Los Angeles, Calif., June 13-16, 1961. This work was conducted under USAF Contracts AF04(647)-318 and AF04(647)-672.

qualitative basis. Quantitative knowledge of the combustion details has long been sought, but the environmental conditions encountered in conventional rocket chambers present imposing difficulties to attainment of precise measurements. These conditions are relatively high temperatures (on the order of 6000° F for LOX/RP-1 propellants), high pressures (20 to 50 atm for current high thrust engines), and high flow velocities (up to Mach 0.5 at the nozzle entrance). The magnitude of the measurement difficulties may be appreciated more fully by considering that an element of liquid propellant, on injection into the combustion chamber, is atomized, heated, vaporized, mixed with combustion gases, converted to combustion products by chemical reaction, and exhausted from the chamber in times on the order of 2 to 5 millisec.

It is widely recognized that the combustion details need to be known quantitatively. Several investigators have attempted to develop analytical models to fill this need. Their models have shown various degrees of sophistication, but generally there has been little good experimental evidence available for guiding the selection of a best model or for tuning it up to give realistic analytical results.

In this paper, experimental results obtained by well-known, easily used streak photographic techniques are presented and compared with analytical results of a fuel spray combustion model.

DESCRIPTION OF TEST EQUIPMENT

Two-Dimensional Research Thrust Chamber

A transparent version of a two-dimensional research model thrust chamber, as shown in Fig. 1, was employed. The chamber is a 1-in. wide diametrical slice of a typical high thrust engine without the diverging part of the nozzle. The side walls of the chamber are made from Plexiglas 4 in. thick with a 0.25-in. pyrex liner protecting the Plexiglas from being burned by the hot combustion gases. A steel structural frame is designed to provide the required rigidity of the chamber, so that operation to 1000-psi chamber pressure can be achieved. The entire combustion process is observable except for the small areas obscured by the structural members.

During the tests discussed in this paper, the combustion chamber was operated at 300 psig with a 1.6 contraction ratio (A_c/A_t) nozzle configuration and a 2.3 mixture ratio r, using liquid oxygen as oxidizer for RP-1 (a narrow cut kerosene fuel).

Test duration was limited to about 1 sec of mainstage operation.

A self-impinging doublet injector, shown in Fig. 2, was used. Its design simulates a slice across the face of a particular high thrust engine's 18-ring injector. Counting from the outer end of the injector, the first, third, fifth, etc. inserts that simulate rings have fuel supplied to them. Each is drilled with two 0.089-in. diam holes at 70° angles from the face, so that two liquid streams impinge at 40° and 0.22-in. from the injector to form a more or less flat propellant spray parallel with the chamber walls. Oxidizer supplied to the second, fourth, sixth etc. simulated rings had identical impingement characteristics but from 0.113-in. diam holes. A triethyl-aluminum slug ahead of RP-1 flowing through a separate ignition system gave hypergolic ignition with a LOX-lead start. Thin baffles were welded on the injector body to insure combustion stability during the tests.

Instrumentation

Normal steady-state rocket engine test stand instrumentation was used to record chamber pressure, injection pressures, propellant flow rates, etc. In addition, several high frequency response Photocon pressure transducers were flush mounted at strategic locations in the chamber, including one in each propellant manifold. The Photocon outputs were recorded on FM magnetic tapes for use in cross correlation with photographic records used mainly in combustion instability studies not discussed in this paper.

The output of one Photocon transducer was also monitored electronically for detection of unstable combustion so that rapid test termination could prevent prolonged exposure of the hardware to damaging instability.

Equipment for Combustion Photography

Several Fastax cameras were used for obtaining photographic records of the combustion processes in the transparent chamber. High speed motion pictures were obtained by using techniques described in Ref. 1. The photographs of interest here, however, are not motion pictures but streak photographs.

Streak photographs were obtained by using a modified 16-mm Fastax camera in either of two ways. The framing prism was removed from the camera; its functions then were focusing combustion light on the film and transporting the film. One way of taking streak photographs is illustrated in Fig. 3. A 0.002-in. wide slit was positioned at the film plane, perpendicular to the film edges, so that only a 0.12-in. wide strip of the transparent chamber was viewed. In the other method, the 0.002-in. slit was left out of the camera, and the chamber walls were masked so that the only illumination was from a narrow slit in the chamber wall. Typical masking is seen in Fig. 1 for a slit parallel with the injector. In either case, the cameras were focused on the inside of the chamber wall.

EXPERIMENTAL RESULTS

The quantitative experimental results discussed in this paper were obtained from streak photographs of slits parallel with the axis of the chamber and aligned with the injection holes that form a fuel or oxidizer spray fan. Some typical enlarged streak photographs for slits aligned on an oxidizer and a fuel fan respectively are shown in Fig. 4. The geometrical details of the visible portions of the chamber associated with these photographs are shown in Fig. 3.

The streak photographs are continuous time records of the luminosity emitted from the narrow slits along the chamber length. Each luminous trace on the films is approximately parabolic and describes the trajectory of a combustion element whose emission gave the trace. The slope of such a trace represents the local axial velocity of the element as it moved along the length of the chamber.

A large number of luminous traces from the axial streak photographs obtained during steady-state combustion in the current studies were analyzed, using the following methods. For some streaks, selected at random, the axial location in the chamber was measured as a function of time with a Vanguard motion analyzer that offers a ten to one magnification (film to screen) and accuracy of about ±0.001 in. on the film. The data thus obtained were either plotted and the slopes reduced manually, or a second-degree equation was best fitted through the points by means of a digital computer program, and the velocities were calculated as a function of chamber length by differentiation of the equations. For several other traces another method of using the motion analyzer was employed. The slopes of many streaks were examined very cursorily at a specified distance from the injector until a few streaks with highest and lowest slopes were isolated. Detailed reduction of these streaks then give a good determination of the range of combustion element velocities throughout the combustion chamber. All methods gave consistent values for the range of measured streak velocities.

The results of this film data reduction are shown in Fig. 5. Films aligned with either a fuel or oxidizer fan gave the same maximum value for the axial velocities, whereas the minimum values for the traces obtained along a fuel fan were somewhat lower, over the first few inches, than those of corresponding traces along an oxidizer fan.

DISCUSSION OF EXPERIMENTS

Several other investigators (2-6)[1] have used similar streak photographic techniques to measure the slopes of luminous traces, and they have reported that these slopes correspond to the local axial velocities of the combustion gases in their experimental chambers. Assuming one-dimensional flow and uniform propellant distribution, the axial gas velocity in steady-state combustion has a single value at any prescribed chamber length. In the authors' experiments, however, measured velocities of luminous traces varied by as much as a factor of two at a constant chamber position. If a curve is drawn to enclose the experimental velocity points in Fig. 5 within an upper boundary, that curve does indeed appear to represent the local combustion gas velocity along the chamber length. This interpretation is strengthened by two facts: 1) examination of a few streaks at the throat location gave experimental throat velocities up to 3400 fps, which is close to the 3500 fps sound velocity estimated for throat conditions; and 2) the highest velocities measured near the beginning of convergence to the nozzle are close to that calculated to give, for the experimental contraction ratio, isentropic acceleration to sonic velocity at the throat.

Accepting that the highest observed streak velocities describe the combustion gas flow regime, the question immediately arises as to what produces the lower velocity streaks that are not only present but are quite dominant in the films. The obvious answer is that they must represent trajectories of burning propellant droplets. But then doubts arise, such as: Are they the tracks of very small carbon particles? Are they propellant droplets that have collided with and been slowed by the chamber wall? Are they simply pieces of molten pyrex flowing along the inside wall?

Some of these questions might be dismissed by observing that the velocity data points could be enclosed by a monotonically increasing lower boundary as well as by the upper bounding combustion gas velocity. To help determine the nature of those streaks whose velocities are lower than gas velocity, a digital computer program was formulated, as described in the following sections, to calculate trajectories of burning fuel sprays and their associated velocity distribution along the chamber.

---

[1] Numbers in parenthesis indicate References at end of paper.

DESCRIPTION OF STEADY-STATE ROCKET ENGINE COMBUSTION

A description of the current knowledge of the LOX/RP-1 combustion processes will make clear what assumptions may be made in formulating a simplified, yet realistic model of liquid bipropellant combustion.

As noted earlier, bipropellant injection with typical high thrust engine injectors produces discreet, separate sprays of each propellant species. Shear forces imposed on the sprays by the combustion gases that fill the chamber result in fairly rapid atomization into a dense array of individual propellant droplets. Near the injector, the propellants are not usually well mixed, so that strong concentration gradients exist across the injector face as alternate fuel-rich, oxidizer-rich, fuel-rich, etc. regions. This fact imposes an important restriction on a one-dimensional combustion model: a well-mixed, one-dimensional combustion mixture cannot be assumed near the injector. Motion pictures of the propellant sprays taken during the transparent two-dimensional chamber tests reported here indicate that this important gradient-rich region may be as short as 3 to 4 in. It must not, however, be ignored.

As the propellant spray elements are formed, they are immedately exposed to very hot combustion gases. Heat transfer from the gases to the spray particles (usually assumed to be spherical droplets) causes them to vaporize as they move along the chamber length. It has been shown (7) that the combustion gases, being in a dissociated state, are reactive with either fuel or oxidizer vapors. Furthermore, over a fairly broad range of local mixture ratios, the dissociation processes maintain the combustion gas temperature at a high value (on the order of 5000 to 6000°F for LOX/RP-1 propellants). Thus, a one-dimensional combustion model may realistically consider the combustion gases to have a constant temperature downstream of the short, gradient-rich injection region. Under these conditions of high, nearly constant gas temperature, the reaction rates are so fast that chemical kinetics need not be considered in the formulation of a combustion model (8). The rate of propellant burning is thus controlled by the physical processes of heat transfer to the propellant droplets, mass transfer from the droplets, and mixing of the propellant vapors with combustion gases. The spray combustion proceeds then, not with a flame front in the usual sense, but with a small flame front surrounding each individual spray element.

The vaporization rates of both propellant species must be considered in estimating the overall chamber combustion rate. It has been shown by Priem (8) that liquid oxygen vaporizes enough faster than hydrocarbon fuels that the fuel vaporization rate controls the combustion rate. In his model, however, he found it convenient to assume that the equations could be written for the fuel spray and that the oxidizer and fuel vaporization rates were proportional. This assumption was used in developing the combustion model in this paper as well.

As the combustion gases are generated along the chamber length, their velocity increases, as was shown experimentally in Fig. 5. The usual simplifying assumption of constant gas stagnation pressure (ignoring friction) requires that the static pressure and gas density decrease as the axial velocity increases. The value of the static pressure decrease in the constant area portion of the chamber is small if the contraction ratio is high enough. For conventional current liquid propellant rocket designs with contraction ratios of about 1.6, the static pressure decrease is on the order of 10% or less and is usually ignored in combustion models. A further assumption that the combustion gases have constant molecular weight gives an approximation that the combustion gas density is nearly constant throughout the chamber.

Combustion gas generation is a summation of the reaction products of all the individual propellant droplets and proceeds as far down the length of the chamber as the last remaining droplet maintains its identity in a dense (liquid) state. If the assumption of constant gas density is valid, the rate of gas generation is directly proportional to the summation of droplet vaporization rates; also, the magnitude of gas velocity at a given chamber length is directly proportional to the total fraction of propellant vaporized at that position.

COMBUSTION MODEL FORMULATION

The combustion model used for comparison with the experimental velocity profile was designed to take initial conditions at some arbitrary distance from the injector face from the experimental data. Calculations downstream of that point were then carried out to give analytical gas velocity and fuel spray droplet trajectories.

A multidisperse spray of spherical fuel droplets was assumed to be uniformly mixed with combustion gases and oxidizer droplets at 3 in. from the injector face (x = 3 in.). The volumetric rate of liquid spray passing through that chamber cross section is small compared with the volumetric flowrate of combustion gases through that section. For the two-dimensional chamber test conditions, the spray volume is less than 1% of the gas volume. It thus appeared reasonable to consider each spray droplet burning as an entity without regard for interactions with its neighbors.

The combustion model consists, therefore, of equations expressing the vaporization and acceleration of single fuel droplets, equations describing the number and size of droplets that make up the spray, and a continuity equation relating overall spray vaporization to combustion gas generation.

Equations for Single Droplet Combustion

For steady-state combustion of a single liquid fuel droplet in a stagnant oxidizing atmosphere, several investigators (9-11) have found that the droplet's size decreases according to

$$D^2 = D_o^2 - k't$$

Upon differentiation with respect to time

$$-\frac{dD}{dt} = \frac{k'}{2D} \qquad [1]$$

Here, k' is a coefficient frequently called the evaporation constant. Its value has been shown analytically (9, 12, 13) to be controlled by the heat transfer rate from the combustion gases (or flame-front surrounding the droplet) to the evaporating droplet surface and/or by the rate of diffusion of opposite propellant species molecules toward the flame front. An estimate of k' based on the heat transfer alone was found to be in good agreement with experimental results at low pressures (9) and is given by

$$k' = \frac{8\,k_g}{\rho_d c_p} \ln\left(\frac{L + c_p\,\Delta T}{L}\right) \qquad [2]$$

Under forced convective conditions, such as exist in a rocket engine, the heat and mass transfer processes, and therefore the droplet's combustion-rate processes, are speeded up. With combustion rate proportional to heat transfer rate, the following relations are derived.

The heat transfer rate Q to an object immersed in a hot flowing gas is given by

$$Q = hS\ \Delta T \tag{3}$$

The heat transfer coefficient h is related to Nusselt number for heat transfer by

$$Nu = \frac{hD}{k_g} \tag{4}$$

The combustion rate of a liquid fuel droplet in an oxidizing atmosphere is equal to the rate of mass decrease of the droplet, and since it has been assumed proportional to the rate of heat transfer to the droplet for constant droplet density

$$-\frac{dD^3}{dt} = \lambda Q$$

Substituting from Eqs. 3 and 4 and assuming that for rocket engine combustion k_g and ΔT are approximately constant

$$-\frac{dD}{dt} = \left(\frac{\lambda \pi k_g\ \Delta T}{3}\right)\frac{Nu}{D} = \lambda'\ \frac{Nu}{D} \tag{5}$$

where λ and λ' are constants. Eq. 5 resembles Eq. 1, which describes the free convection case. Since the value of the Nusselt number for a sphere in a stagnant infinite medium is equal to 2.0, it follows from Eqs. 1 and 5 that

$$\lambda' = \frac{k'}{4}$$

Hence a general relation

$$\frac{dD}{dt} = -\frac{k'\ Nu}{4D} \tag{6}$$

was arrived at, which describes the combustion of a fuel (or oxidizer) droplet in an oxidizing (or reducing) hot atmosphere under any flow conditions.

A commonly used analytical expression correlating Reynolds, Prandtl, and Nusselt numbers for a sphere in a convective flow field is (14)

$$Nu = \underline{2} + 0.6\ (Pr)^{1/3}\ (Re)^{1/2} \qquad [7]$$

whereas a slightly different correlating equation for the data with some additional estimation of the observed spread may be found in Ref 15. For rocket combustion gases with hydrocarbon-liquid oxygen propellants, the Prandtl number is taken as approximately equal to 0.7. Therefore, the relation between Nusselt number and Reynolds number is reduced to

$$Nu = 2 + 0.53\ (Re)^{1/2} \qquad [8]$$

It is noted here that if the mass transfer rate was chosen as controlling the rate of combustion for the liquid fuel droplet, an equivalent dependence of combustion rate on flow Reynold's number would result if the Schmidt number were equal to 0.7 for the combustion gas of the propellants in question.

The equation of motion of a droplet is determined from the aerodynamic drag-force equation

$$m_d\ \frac{dV_d}{dt} = \frac{C_D\ A_d\ \rho_g\ V_r\ |\ V_r\ |}{2} \qquad [9]$$

Substitution for m_d and A_d, assuming the droplet is spherical, gives

$$\frac{dV_d}{dt} = \frac{3\ C_D\ \rho_g\ V_r\ |\ V_r\ |}{4\ \rho_d\ D} \qquad [10]$$

For digital computer input, the appropriate equations were generalized for an n^{th} droplet size group at x inches from the injector and were written in difference-equation notation

$$\Delta D_{nx} = -\frac{k'}{4D_{nx}}\ Nu_{nx}\ \Delta t \qquad [11]$$

$$Nu_{nx} = 2 + 0.53\ Re_{nx}^{\ 1/2} \qquad [12]$$

$$Re_{nx} = \frac{\rho_{gx}\ D_{nx}\ |\ V_{r_{nx}}\ |}{\mu_g} \qquad [13]$$

$$\Delta V_{d_{nx}} = \frac{3}{4} C_{D_{nx}} \frac{\rho_{gx} V_{r_{nx}} \left| V_{r_{nx}} \right|}{\rho_d D_{nx}} \Delta t \qquad [14]$$

$$\Delta t = \frac{\Delta x}{V_{d_{nx}}} \qquad [15]$$

$$C_{D_{nx}} = f\ (Re_{nx}) \qquad [16]$$

Spray Description

The characterization of a spray depends strongly on the type of atomizer that produced it. Fortunately, spray atomization by the self-impinging doublet that forms the basic injection element of many high thrust liquid engine injectors has been carefully investigated by Ingebo at NASA (16) using liquid n-heptane. In his work, the Nukiyama-Tanasawa distribution function

$$\frac{dR}{dD} = \frac{b^6}{120} D^5 \exp \left[-bD \right] \qquad [17]$$

nearly described the nonburning spray from doublets. Ingebo found the spray constant b was related to the volume mean diameter of the spray by

$$b = \frac{3.915}{D_{30}} \qquad [18]$$

Substituting this relation in Eq. 17, writing the results in terms of the n^{th} size group of a spray composed of j total groups, and using difference-equation notation

$$\frac{\Delta R_n}{\Delta D_n} = \left(\frac{3.915}{D_{30}} \right)^6 \frac{D_n^5}{120} \exp \left[\frac{-3.915\ D_n}{D_{30}} \right] \qquad [19]$$

A few droplets of very large size will be found in a spray of this description. Ingebo observed maximum droplet sizes, however, which were (17) approximately limited to

$$D_{max} = 2.9\ D_{30} \qquad [20]$$

Eqs. 19 and 20 were used to develop fuel sprays for the combustion model calculations. A number j of droplet size groups was taken having equal diameter increments ΔD of ±10 μ about each D_n. The number of groups was determined by

$$j \, \Delta D = D_{max} \tag{21}$$

The volume fraction of spray mass ΔR_n in each size group was calculated with Eq. 19. All of that volume fraction, for computational convenience, was considered to produce droplets of the group's mean diameter D_n. The production rate of number of droplets $\dot{N}_n$ having diameter D_n was related to the total flowrate of the fuel spray passing through the chamber cross section at $x = 3$ inches by

$$\dot{N}_n = \frac{6(\dot{m}_f)_3 \, \Delta R_n}{\pi \rho_d \, D_n^3} \tag{22}$$

Because a maximum droplet size limitation was put on the spray, a small residual volume fraction $(\Delta R)_r$ of spray results

$$(\Delta R)_r = 1 - \sum_{n=1}^{n=j} \Delta R_n \tag{23}$$

and has a spray mass flowrate of

$$\dot{m}_r = (\dot{m}_f)_3 \, (\Delta R)_r \tag{24}$$

This residue was taken as additional volume fraction of the j^{th}, or largest, size group. Mass fraction distributions from Eq. 19 and residues for D_{max} are shown in Fig. 6. Eqs. 19-24 fully describe the fuel spray when values of $(\dot{m}_f)_3$ and D_{30} are either known or assumed.

Vaporization Rate Function

The droplet diameter D_n of the n^{th} size group has a decreasing value as the droplets burn. Since a one-dimensional model was assumed, D_n is a continuous function of distance from the injector x and is denoted by D_{nx}. The total mass rate of fuel spray vaporization between the injector and axial distance x is given by

$$\dot{F}_x = (\dot{m}_f)_i - \frac{\pi \rho_d}{6} \sum_{n=1}^{n=j} \dot{N}_n \, D_{nx}^3 \tag{25}$$

After differentiation, the local vaporization rate function is given in difference equation notation by

$$\Delta \dot{F}_x = -\frac{\pi}{2} \rho_d \sum_{n=1}^{n=j} \dot{N}_n D^2_{nx} \Delta D_{nx} \qquad [26]$$

since the injection rate is a constant during steady-state mainstage combustion.

Gas Velocity Equations

Conservation of mass requires that the vaporization rate function be related to combustion gas velocity. The assumption that fuel and oxidizer vaporization rates are proportional gives a linear relationship between gas velocity and the fuel vaporization rate function

$$V_{gx} A_x \rho_{g_x} = (r + 1) \dot{F}_x \qquad [27]$$

or

$$\Delta V_{gx} = \frac{3.3 \Delta \dot{F}_x}{A_x \rho_{g_x}} \qquad [28]$$

for an overall mixture ratio of 2.3 lb LOX/lb RP-1. The relative velocity between the combustion gases and n^{th} droplet group is

$$V_{r_{nx}} = V_{g_x} - V_{d_{nx}} \qquad [29]$$

Digital Computer Program

Eqs. 11-16, 26, 28, and 29 were programmed for solution with an IBM 7090 electronic data processing machine. Provisions were made for varying the input values concerning spray atomization (j, D_{n3}, N_{n3}), velocities of droplet size-groups (V_{dn3}), evaporation constant (k'), combustion gas viscosity(μ g), and dependence of the drag coefficient (C_D) on Reynolds number. Results printed out at 1/8-in. intervals between x = 3.00 and x = 13.00 (the beginning of nozzle convergence) were combustion gas velocity, droplet size-group velocities, and droplet size-group diameters cubed, as well as the Reynolds and Nusselt numbers of the odd numbered size-groups.

For all cases computed, the experimental mean fuel injection rate was maintained, and the combustion gas velocity at x = 3, V_{g3} was set equal to the experimentally determined gas velocity at that chamber length. From Eq. 27, the proportion of the fuel injection that was vaporized to give that gas velocity was estimated. The remainder, 72.5% for these calculations, was assumed to be fully atomized fuel spray flowing through the x = 3 section. This satisfied Eq. 25, which requires simply that

$$(\dot{m}_f)_3 = (\dot{m}_f)_i - \dot{F}_3$$

The atomization of the fuel spray $(\dot{m}_f)_3$ was prescribed by Eqs. 19-24 simply by assuming that $\Delta D = 20\,\mu$ and assuming a value for D_{30}. Five spray distributions were employed, as tabulated in Table 1. Also shown in Table 1 are the velocities assumed for the droplet size groups for most computed cases. These values of V_{n3} were obtained by setting V_{13} just below gas velocity V_{j3} at the lowest experimental streak velocity for x = 3 (which varied slightly as more and more streaks were reduced) and using linear interpolation for velocities of the intermediate size-groups. The effect of this arbitrarily assumed velocity distribution was examined by computing two cases with the extremes of V_{n3} = 200 and 400 fps for all size-groups.

Best estimates of important properties in the equations were made and used for all or nearly all the computed cases. Values used for droplet and combustion gas densities were 50.0 and 0.104 lb/ft^3, respectively. The value of the evaporation constant k' was estimated to be 0.027 cm^2/sec from data for diethylcyclohexane droplets burning at 20 to 30 atm in pure oxygen (18). Since the range of k' reported there was from 0.020 to 0.040 cm^2/sec, two cases were computed with values higher and lower than this best estimate. Combustion gas viscosity was estimated to be 1.65×10^{-3} poise with an equation in Ref. 8 for LOX/n-heptane combustion products. Other combustion models (e.g., Ref. 8) have used viscosity evaluated for a mixture of combustion gases and fuel vapor at some mean temperature between the droplet surface and combustion gas temperatures. Whereas this approach gives a mean viscosity about half that of the combustion gases, it is not as realistic as the straight forward use of product combustion gas viscosity for the model presented here. This is because the combustion parameters that depend on viscosity are here taken from experimental work correlated on the basis of free stream viscosity. Two cases were computed with assumed values of gas viscosity approximately 1/3 and 2/3 of that used for most cases. The droplet drag coefficient was obtained as a function of Reynolds number from Refs. 18 and 19. The correlation of Ref. 19 regarding accelerating spheres was used for low Reynolds numbers and that of Ref. 18 for Reynolds numbers high enough that droplet distortion becomes important

$$C_D = 27\ Re^{-0.84} \qquad Re < 80$$

$$= 0.271\ Re^{0.217} \qquad 80 < Re < 10{,}000 \qquad [30]$$

To determine whether this distinction between high and low Reynolds number is very important, one case was calculated with Ingebo's correlation (19) for all Reynolds numbers

$$C_D = 27\ Re^{-0.84} \qquad [31]$$

A summarization of all the cases calculated is given in Table 2.

ANALYTICAL RESULTS AND DISCUSSION

The velocity profiles calculated for sprays characterized by volume-mean droplet diameters of 65μ, 80μ, 100μ, and 120μ (cases 1 to 4, Table 2) are shown in Figs. 7a through 7d, respectively[2] Combustion gas velocity and velocities of selected droplet size-groups are shown as functions of chamber length. Comparison of these curves with the data of Fig. 5 makes it very clear that the observed streak trajectories must be traces from burning fuel droplets. One such comparison is shown in Fig. 8, where the calculated combustion gas velocity and 230μdroplet velocity from case 2 are shown to fit very closely the experimentally observed maximum and minimum velocities over most of the chamber length.

The possibility that the lowest velocity streaks could be those of solid carbon particles can be ruled out since such particles would be expected to be of the order of 1- to 5-μ diam and should move with velocities close to that of the combustion gas. The motion estimated for droplets larger than 300 μ was appreciably slower than that of any luminous streaks observed, and this fact should practically eliminate the possibility that molten pyrex could be responsible for any of the observed trajectories since such particles could be larger than 300-μ diam. Further, the 2 to 1 range of streak velocities was noted in the very early portion of mainstage operation, before pyrex melting could have occurred.

---

[2] The spray distribution and combustion of case 1 with D_{30} = 65 μ were computed without the $D_{max} = 2.9\ D_{30}$ limitation. In plotting Fig. 7a the velocities of droplets larger than 190μ were omitted.

The results of the spray combustion computations were fairly sensitive to the fuel spray size distribution. At x = 10 in., for example, approximately 100 fps higher velocities of both combustion gas and largest droplets resulted from taking a 20 μ smaller value of D_{30}. Comparison of calculated and experimental velocity results might then give a good quantitative description of the fuel sprays in operating rocket chambers. How well the spray distribution may be inferred depends, though, on how well known the other important combustion parameters are and how sensitive the computations are to their variation.

Results of computed cases having evaporation constant varied are indicated in Fig. 9, and cases having combustion gas viscosity varied are shown in Fig. 10. Cross comparison among Figs. 8, 9, and 10 indicates that the calculated spray combustion results are somewhat less sensitive to k' variation than to spray atomization changes and are even less sensitive to gas viscosity variation. From the cases computed, approximately equal effects on the velocity profiles may be expected to result from a 20% decrease in D_{30}, a 35% increase in k', or a 50% decrease in μ_g. The calculated responses to these changes were very nearly the same for both the combustion gas and largest droplets, unfortunately. Had the responses been significantly different, it would have been easier to select a best-fit combination of values.

One case was computed in which an assumed change did result in significantly different responses of the combustion gas and largest droplet size-group velocities. This occurred when the droplet aerodynamic drag coefficient was assumed to follow the functional relationship of Eq. 31 rather than Eq. 30. As noted before, the change in functional form at Re = 80 in Eq. 30 compensates for a tendency of the droplets to flatten and become disk-shaped as Reynolds numbers are increased. The calculated combustion gas and largest droplet velocities for cases 3 and 10 are compared in Fig. 11. It is readily apparent that the values of C_D expressed by Eq. 30 result in better approximations of both the spread and shape of the spray combustion velocity profiles seen experimentally. For that reason the functional relation Eq. 30 is recommended for all spray combustion model calculations.

Variation of the velocity distribution for the droplet size-groups at $x = 3$ was examined in two computation cases, with conditions as noted for cases 11 and 12, Table 2. Whereas the largest droplet's velocity was calculated to be appreciably higher than the experimental minimum for several inches in the twelfth case, the values of $V_{g_{13}}$ and $V_{d_{max}\,13}$ were only about 2% different than the comparable uniformly distributed velocity vs. size-group case (case 3, Table 2). Selected data are given in Table 3. It was concluded that the original assumption of uniformly distributed velocities is physically realistic and that the range of velocities calculated will be realistic even if the smallest droplet size-groups in the spray are actually traveling slower than assumed.

From the close correlation between particular calculated spray combustion cases and the experimental data up to about $x = 10.5$ in., it must be noted that the relatively simply spray combustion theory and the associated spray description, evaporation coefficient, and drag coefficient give a very realistic description of a major portion of liquid bipropellant combustion in present day rockets. The primary fuel atomization resulting from the particular self-impinging doublet injector and injection conditions used appears to be well represented by a volume-mean droplet diameter of 80 to 100 μ and maximum droplet diameters of 2.9 times that mean diameter. The evidence is strengthened by considering values of D_{30} predicted by the experimental correlation equation of Ref. 16. For the injection conditions used here, but depending on what value of gas velocity is assumed for the atomization region, values of D_{30} ranging from 70 to 200 μ were predicted.

The value of maximum droplet diameter is an important feature of the analytical modeling conditions. It may be questioned whether or not it is just fortuitous that using the ratio of D_{max}/D_{30} from experiments performed at one atmosphere with nonburning sprays (16) appears to adequately describe a burning spray at 20 atm. A criterion for droplet shattering, determined from experiments with burning and nonburning droplets at pressures to 30 atm (18), is that $We\ Re^{-1/2} \geq 1$ will result in droplet disintegration. This criterion was used to examine the maximum size data of Ref. 16 and found to be compatible (17). Because the relative velocities in the injection region of a rocket are variable and indeterminate for individual droplets, it is not practical to use this concept to predict an accurate maximum droplet diameter. If, however, the maximum diameters indicated to be physically realistic in this paper are tested by the breakup criterion, relative gas velocities on the order of 50 to 70 fps are indicated as being responsible for the spray atomization. From Fig. 5, it is seen that such relative velocities might easily be experienced by individual spray elements up to 2 in. from the injector.

The rather sizeable deviation between experimental and calculated gas velocity profiles beyond the 10-in. chamber length is believed to be caused by disintegration of droplets there. The breakup criterion, $We\ Re^{-1/2} \geq 1$, states the conditions that will cause breakup but does not indicate how long a droplet must be exposed to those conditions before disintegration is accomplished. A finite time is known to be required, but no quantitative correlation of direct experimental data is available. The good fit of the experimental data by a model that does not consider breakup (Fig. 8) implies that no appreciable breakup occurs between attainment of primary atomization in the injection region and approximately the 10-in. length. Comparison of the calculated and experimental rates of gas velocity increase, Fig. 12, accentuates the difference that apparently exists in that region.

To provide further elucidation for this case, Fig. 13 and 14 were prepared from the data of case 2, Table 2, from which Figs. 7b and 8 were derived. Plotted in Fig. 13 are the calculated percentages of both droplet size-group masses at 3 in. which are still liquid spray further downstream and the relative number of droplets remaining in the spray as the smallest size-groups burn out. In Fig. 14, the times required for selected combustion elements to pass through the constant area portion of the chamber or be completely burned are shown. The times required for passage from the injector face to x = 3 were estimated with linear means between injection velocity and V_{dn3} (Table 1) for droplets and between zero and V_{g3} for combustion gases.

Of the total number of fuel spray droplets at the x = 3 section, it is seen that only 20 to 25% remain at x = 10 (Fig. 13). All droplets smaller than 80 μ have been completely burned, and many of the remaining droplets are nearly consumed so that the combustion field at the 10-in. section consists of a few fairly large droplets burning rather slowly. This accounts for the tendency of the computed combustion gas velocity increase rate (Fig. 12) to approach zero asymptotically. As seen in Figs. 7b and 14, these large droplets are exposed to high relative velocities for longer times than the small droplets that are quickly consumed. Apparently, the exposure time of the large droplets becomes long enough that they gradually disintegrate into smaller droplets. This local increase in number of droplets and droplet surface area results in increased overall spray combustion rate. The effect is clearly shown by Fig. 12 where the rate of combustion gas increase may be considered as synonymous with spray combustion rate. The effect of droplet breakup apparently starts at 8-1/2 to 9 in. from the injector.

To obtain confirmation of this interpretation, desk computer calculations were performed to determine what size droplets would respond to the gas acceleration in the nozzle convergence (Fig. 5) in the same way that the minimum velocities observed experimentally did. These calculations indicated that droplets larger than 50 μ will move more slowly in the nozzle than any of the measured streaks and, therefore, probably do not exist there. These data are believed to confirm the conclusion that the large propellant droplets are shattered far down the combustion chamber.

The importance of this secondary atomization on combustion efficiency may be seen by comparing the gas velocity with and without it (Fig. 13). In the 3 in. of chamber length between 7 and 10 in. from the injector, the percent of final gas velocity increased from 80 to 85%, whereas in the 3 in. between 10 and 13 in., it increased from 85 to 100%, which is more than a twofold improvement attributed to droplet shattering.

CONCLUSIONS

1 Careful reduction of streak photographs, showing the luminosity emitted from narrow transparent slits through liquid propellant rocket combustion chamber walls during steady-state mainstage operation, reveals useful details of the propellant combustion processes. Velocity profiles of the combustion gases and largest spray droplets, as well as positions where droplet shattering becomes an important process, may be determined.

2 A one-dimensional spray combustion model, based on constant combustion gas temperature and density and fuel vaporization rate limited combustion, can come very close to realistically describing a major portion of the propellant combustion in a conventional rocket engine using LOX/RP-1 propellants. Appropriate values of gas physical properties, spray droplet sizes and distribution, droplet vaporization constant, and drag coefficient must be available.

3 For such a combustion model to be useful in estimating combustion efficiency as a function of chamber length, it should include a realistic description of droplet breakup.

Good quantitative data are not now available regarding the time dependence of droplet disintegration.

4 The combination of experimental streak photography with analytical spray combustion calculations provides a very good combustion research tool. Continued application and refinement of these techniques is expected to aid greatly in the development of a complete, quantitative description of the liquid propellant combustion processes.

NOMENCLATURE

A = cross sectional area, in^2
b = constant, in spray description, cm^{-1}
C_D = drag coefficient
c_p = specific heat, constant pressure, Btu/lb-°F
D = droplet diameter, in., cm, or μ
D_{30} = volume-mean diameter of a spray, in., cm, or μ
ΔD = droplet diameter change or increment, in., cm, or μ
D_{max} = largest droplet diameter in a spray, in., cm, or μ
D_{AB} = diffusion coefficient, ft^2/sec
e = base (2.718) of natural system of logarithms
$\exp[\ ]$ = e raised to the $[\ ]$ power
$\dot{F}_x$ = mass rate of spray vaporization between injection and section x, lb/sec
h = heat transfer coefficient, Btu/in^2-sec-°F
j = number of droplet size groups in spray
k' = evaporation coefficient, in^2/sec, cm^2/sec
k_g = thermal conductivity of combustion gas, Btu/in/in^2-sec-°F
L = latent heat of vaporization, Btu/lb
m = mass, lb
$\dot{m}$ = mass flowrate, lb/sec
$\dot{N}$ = rate of number of droplets
Nu = hD/k_g
= Nusselt number
Pr = $c_p \mu_g/k_g$
= Prandtl number
Q = heat transfer rate, Btu/sec

r = propellant flowrate ratio (mixture ratio). lb LOX/lb RP-1

R = volume fraction of spray having diameter > D

ΔR = volume fraction of spray in a size group $D_n - \frac{\Delta D}{2} < D \leq D_n + \frac{\Delta D}{2}$

Re = $\rho_g \, |V_r| \, D/\mu_g$

= Reynolds number

S = surface area, in^2

Sc = $\mu_g/\rho_g \, D_{AB}$

= Schmidt number

t = time, sec

T = temperature, °F

ΔT = $T_g - T_d$

= temperature difference for heat transfer to a droplet, °F

V = velocity, fps

V_r = $V_g - V_d$

= velocity difference, fps

We = $\rho_g \, D \, V_r^2/\sigma_d$

= Weber number

x = axial distance from injector, in

ρ = density, lb/ft^3 or lb/in^3

σ = surface tension, dyne/cm or lb/ft

μ_g = viscosity of combustion gases, lb/ft-sec

μ = unit of droplet diameter, micron, 10^{-4} cm

λ, λ' = constants

Subscripts

c = constant area portion of combustion chamber

d = droplet property or condition

f = fuel injection or fuel spray

g = combustion gases

i = injection conditions

n = n^{th} size group of a spray

o = initial value

r = residual portion of a spray (except V_r)

t = combustion chamber exhaust nozzle throat

x = particular position along chamber length

REFERENCES

1 R. B. Lawhead: Photographic Studies of Combustion Processes in Liquid Propellant Rockets. To be published in Eight Symposium (International) on Combustion, The Combustion Institute, Pittsburgh, Pa., 1961.

2 K. Berman and S. E. Logan: Combustion Studies with a Rocket Motor Having a Full Length Observation Window. Jour. ARS, March-April 1952, vol. 22, p. 78.

3 K. Berman and S. H. Cheney Jr.: Rocket Motor Instability Studies. Preprint 180-54, American Rocket Society, 1954.

4 M. F. Heidman and C. M. Auble: Rocket Performance Measurements with Streak Photographs. Preprint 239-55, American Rocket Society, 1955.

5 M. F. Heidman and C. M. Auble: Injection Principles from Combustion Studies in a 200-Pound-Thrust Rocket Engine Using Liquid Oxygen and Heptane. NACA RM E55C22, June 1955.

6 R. S. Pickford and R. G. Peoples: Inherent Stability of the Combustion Process. Preprint 1490-60, ARS 15th Annual Meeting, Washington, D.C., Dec. 5-8, 1961.

7 R. S. Levine: A Model of Liquid Rocket Engine Combustion. Rept. R-2077, Rocketdyne, a division of North American Aviation Inc., Canoga Park, Calif., December 1960.

8 R. J. Priem and M. F. Heidman: Propellant Vaporization as a Design Criterion for Rocket-Engine Combustion Chambers. NASA TR R-67, 1960.

9 G. A. E. Godsave: Studies of the Combustion of Drops in a Fuel Spray--The Burning of Single Drops of Fuel, p. 818. Fourth Symposium on Combustion, Williams and Wilkins, Baltimore, Md., 1953.

10 M. Goldsmith and S. S. Penner: On the Burning of Single Drops of Fuel in an Oxidizing Atmosphere. Jet Propulsion, July-August 1954, vol. 24, p. 245.

11 A. L. Smith and C. C. Graves: Drop Burning Rates of Hydrocarbon Fuels. NACA RM E57F11, 6 August 1957.

12 M. Goldsmith: Experiments on the Burning of Single Drops of Fuel, Jet Propulsion, March 1956, vol. 26, p. 172.

13 D. B. Spalding: Some Fundamentals of Combustion, p. 122 Butterworth's Scientific Publications, London, 1955.

14 W. E. Ranz and W. R. Marshall, Jr.: Evaporation from Drops. Chemical Engineering Progress, Part I, 1952, vol. 48, no. 3, p. 141; Part II, 1952, vol. 48, no. 4, p. 173.

15 W. H. McAdams: Heat Transmission, 3rd Ed., p. 265-266, McGraw-Hill Book Co. Inc., New York, 1954.

16 R. D. Ingebo: Drop-size Distributions for Impinging-Jet Break-up in Airstreams Simulating the Velocity Conditions in Rocket Combustors. NACA TN 4222, March 1958.

17 E. Rabin: Personal Communication. Rocketdyne, a division of North American Aviation Inc., February 1961.

18 E. Rabin, A. R. Schallenmuller, and R. B. Lawhead: Displacement and Shattering of Propellant Droplets. Final Summary Report, AFOSR TR 60-75, March 1960.

19 R. D. Ingebo: Drag Coefficients for Droplets and Solid Spheres in Clouds Accelerating in Air Streams. NACA TN 3762, September 1956.

Table 1 Spray Distribution Used in Computations

		Total Spray Mass: $(\dot{m}_f)_3 = 5.59$ lb/sec for all Sprays									
		$D_{30} = 65\mu$		$D_{30} = 80\mu$		$D_{30} = 100\mu$		$D_{30} = 120\mu$		$D_{30} = 140\mu$	
n Group Index Number	D_{n3} Group Diameter, μ	$\dot{N}_n$ x 10^{-8}	V_{dn3}, fps	$\dot{N}_n$ x 10^{-8}	V_{dn3}, fps	$\dot{N}_n$ x 10^{-8}	V_{dn3}, fps	$\dot{N}_n$ x 10^{-8}	V_{dn3}, fps	$\dot{N}_n$ x 10^{-8}	V_{dn3}, fps
1	10	25.8	434	8.48	430	2.46	434	0.877	435	0.365	438
2	30	69.8	418	28.71	410	10.07	418	4.11	420	1.87	426
3	50	58.5	402	29.96	390	12.77	402	5.95	405	2.98	414
4	70	34.6	386	22.07	370	11.48	386	7.25	390	3.34	402
5	90	17.2	370	13.69	350	8.70	370	5.22	375	3.15	390
6	110	7.74	354	7.69	330	5.88	354	4.06	360	2.69	378
7	130	3.26	338	4.03	310	3.77	338	2.96	345	2.15	366
8	150	1.30	322	2.02	290	2.30	322	2.05	330	1.63	354
9	170	0.505	306	0.975	270	1.34	306	1.369	315	1.20	342
10	190	0.19	290	0.458	250	0.77	290	0.893	300	0.857	330
11	210	0.07	274	0.210	230	0.43	274	0.567	285	0.598	318
12	230	0.025	258	0.213	210	0.24	258	0.354	270	0.410	306
13	250	0.009	242	--	--	0.13	242	0.218	255	0.277	294
14	270	0.0031	226	--	--	0.07	226	0.1324	240	0.185	282
15	290	0.0026	210	--	--	0.10	210	0.0794	225	0.122	270
16	310	--	--	--	--	--	--	0.0474	210	0.0795	258
17	330	--	--	--	--	--	--	0.0263	195	0.0485	246
18	350	--	--	--	--	--	--	0.0420	180	0.0331	234
19	370	--	--	--	--	--	--	--	--	0.0212	222
20	390	--	--	--	--	--	--	--	--	0.0134	210
21	410	--	--	--	--	--	--	--	--	0.0311	198

Table 2 Summary of Spray Combustion Gases Calculated

Case	D_{30}, μ	k', cm^2/sec	μ_g, poise	C_D	V_{n3}, fps
1	65	0.027	1.65×10^{-3}	Eq. 21	Table 1
2	80	0.027	1.65×10^{-3}	Eq. 21	Table 1
3	100	0.027	1.65×10^{-3}	Eq. 21	Table 1
4	120	0.027	1.65×10^{-3}	Eq. 21	Table 1
5	140	0.027	1.65×10^{-3}	Eq. 21	Table 1
6	100	0.020	1.65×10^{-3}	Eq. 21	Table 1
7	100	0.035	1.65×10^{-3}	Eq. 21	Table 1
8	100	0.027	1.00×10^{-3}	Eq. 21	Table 1
9	100	0.027	0.50×10^{-3}	Eq. 21	Table 1
10	100	0.027	1.65×10^{-3}	Eq. 22	Table 1
11	100	0.027	1.65×10^{-3}	Eq. 21	200
12	100	0.027	1.65×10^{-3}	Eq. 21	400

Table 3 Calculated Velocities of Gases and Selected Size Groups for Various Initial Velocity Assumptions

Chamber Position	V_{dn3} = 400 fps for all n				V_{dn3} = 200 fps for all n				V_{dn3} distributed as in Table 1			
x, in.	Gas	90μ	190μ	290μ	Gas	90μ	190μ	290μ	Gas	90μ	190μ	290μ
3	450	400	400	400	450	200	200	200	450	370	290	210
4	623	423	407	405	820	379	320	295	679	408	326	267
5	801	487	442	431	1005	566	469	425	882	508	417	366
6	948	584	508	484	1117	724	589	535	1027	622	524	471
7	1058	700	588	550	1195	877	685	625	1128	754	623	565
8	1142	825	666	619	1253	1022	765	700	1203	887	709	647
9	1207	950	737	683	1300	1153	832	764	1261	1016	782	718
10	1259	1073	801	742	1334	1268	890	819	1306	1138	846	779
11	1301	1187	858	795	1368	1362	940	868	1343	1249	902	833
12	1336	1289	908	842	1394	—	985	911	1374	1344	951	880
13	1366	--	953	885	1416	—	1024	950	1400	--	994	923

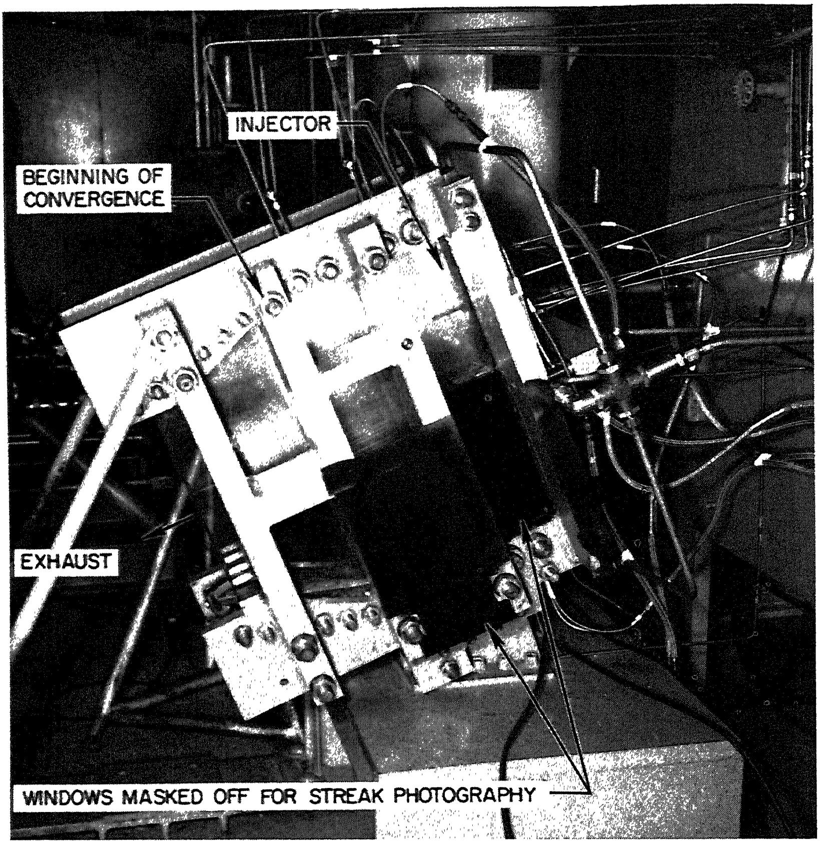

Fig. 1 Transparent walled two-dimensional research combustion chamber

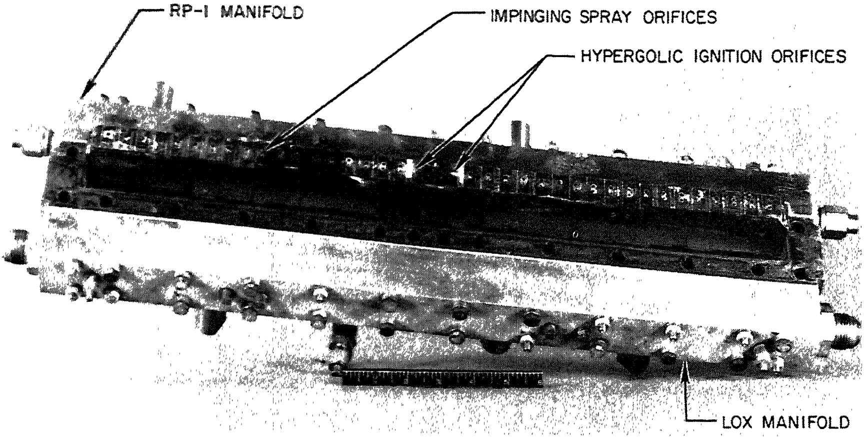

Fig. 2 Injector for two-dimensional research combustion chamber

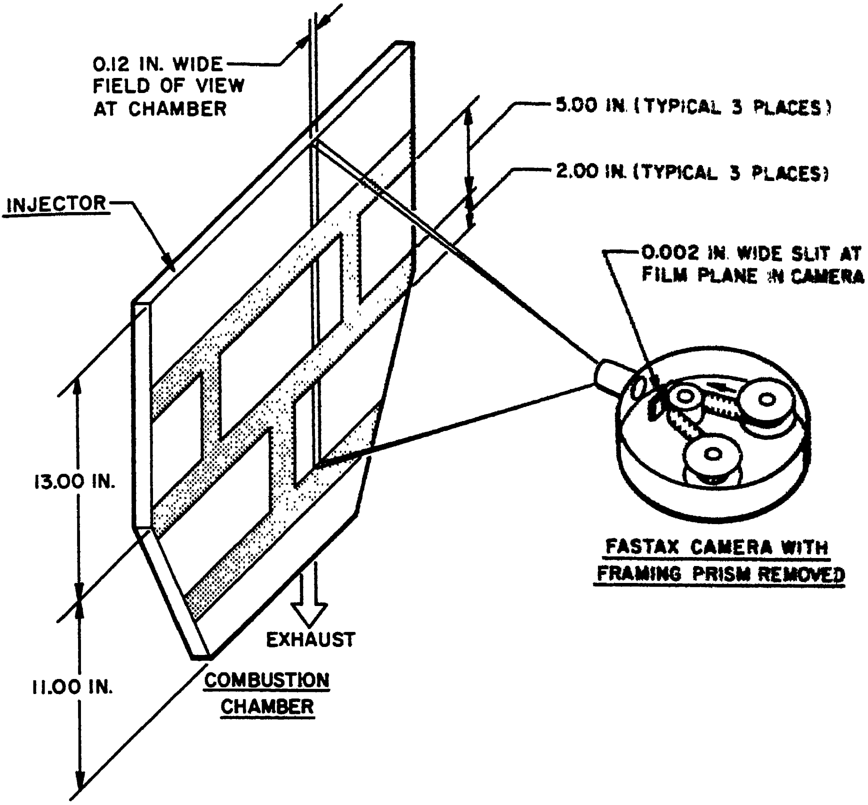

Fig. 3 Streak camera arrangement

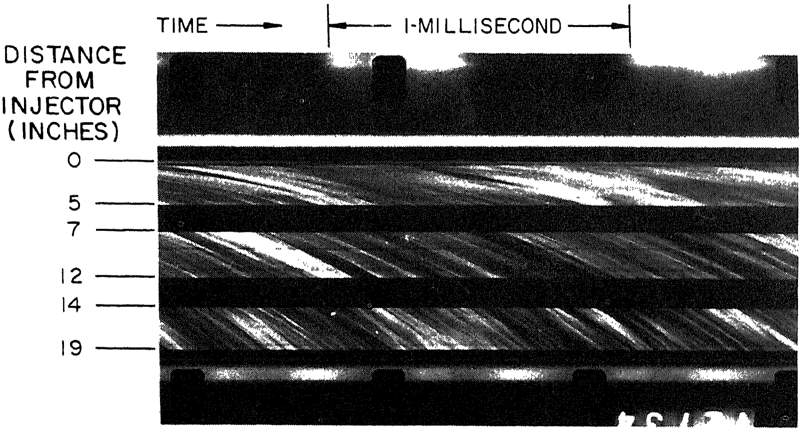

(a) LONGITUDINAL SLIT ALIGNED WITH OXIDIZER SPRAY

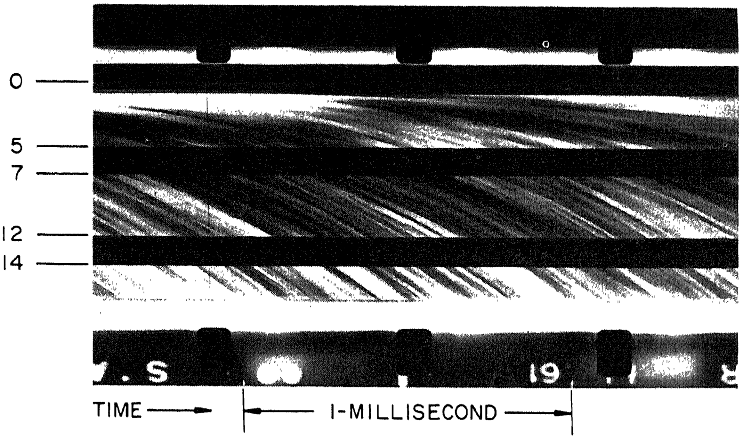

(b) LONGITUDINAL SLIT ALIGNED WITH FUEL SPRAY

Fig. 4 Typical enlargements of streak photograph

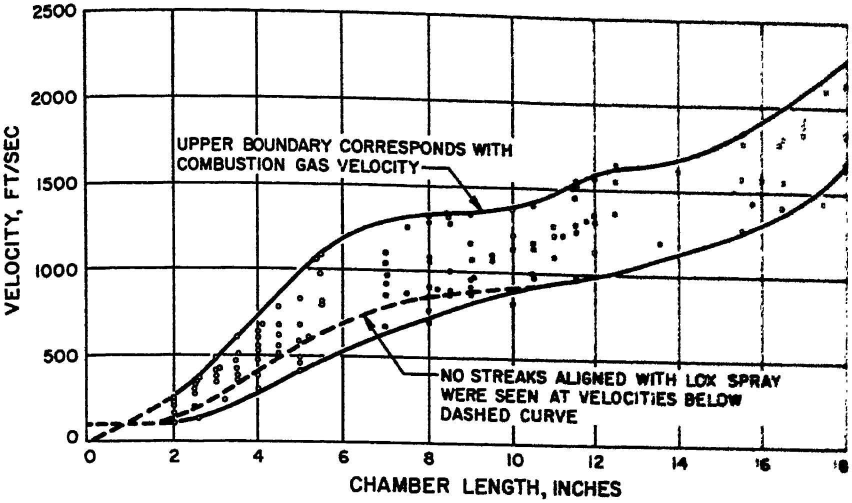

Fig. 5 Velocities derived from streak photographs vs. chamber length

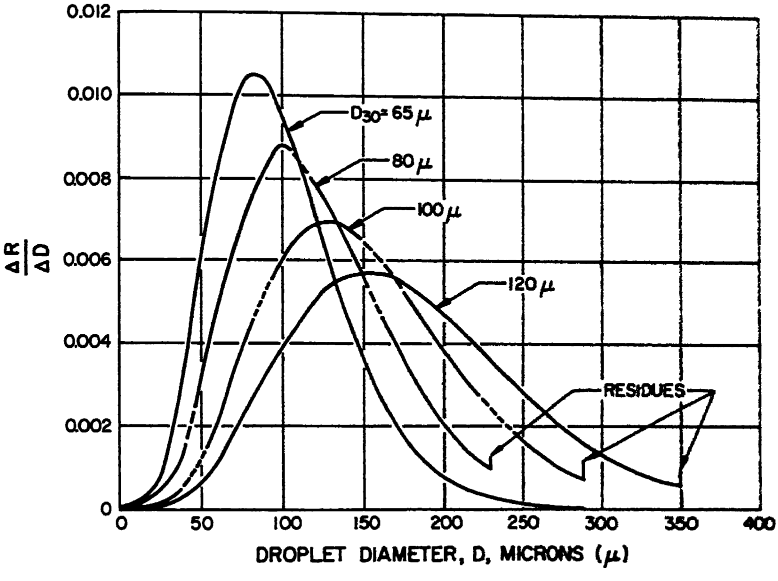

Fig. 6 Droplet size distribution used in calculations

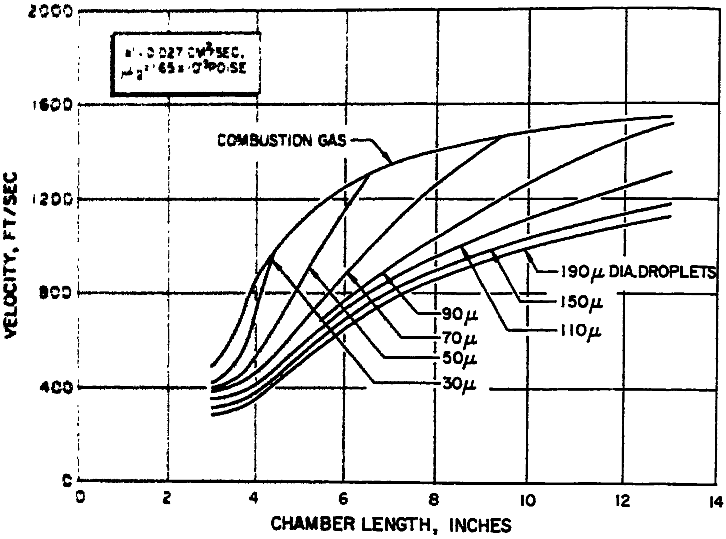

Fig. 7a Calculated results for various sprays: $D_{30} = 65\mu$, $D_{max} = 190\mu$

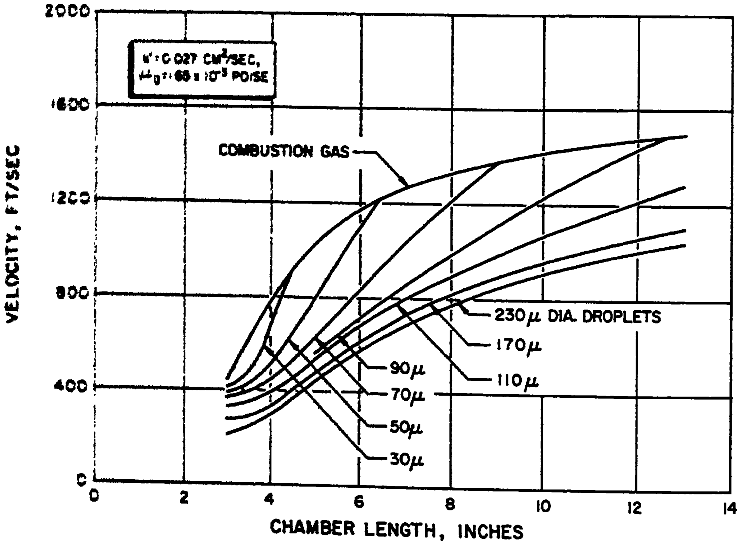

Fig. 7b Calculated results for various sprays: $D_{30} = 80\mu$, $D_{max} = 230\mu$

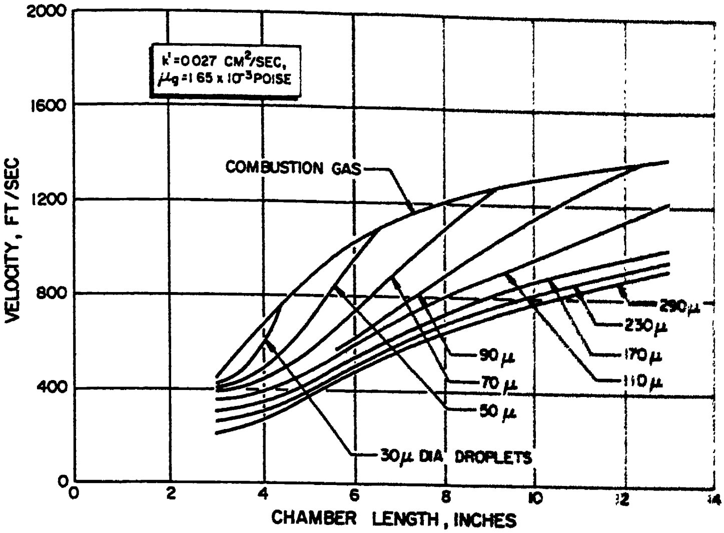

Fig. 7c Calculated results for various sprays: $D_{30} = 100\mu$, $D_{max} = 290\mu$

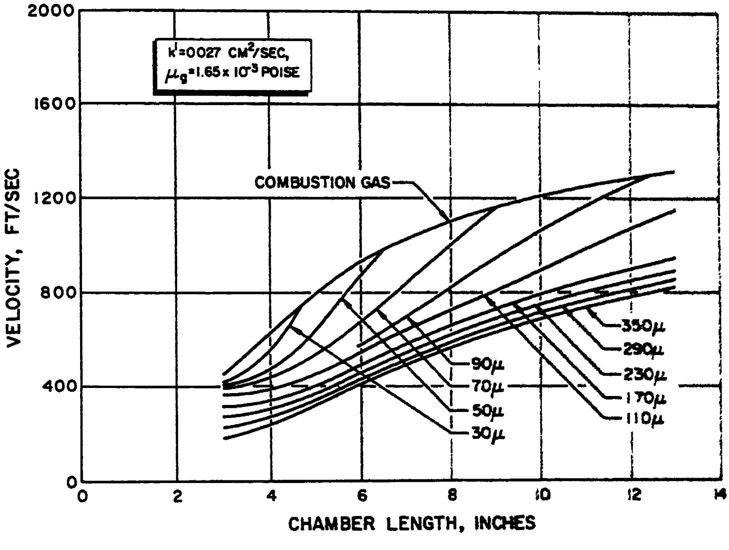

Fig. 7d Calculated results for various sprays: $D_{30} = 120\mu$, $D_{max} = 350\mu$

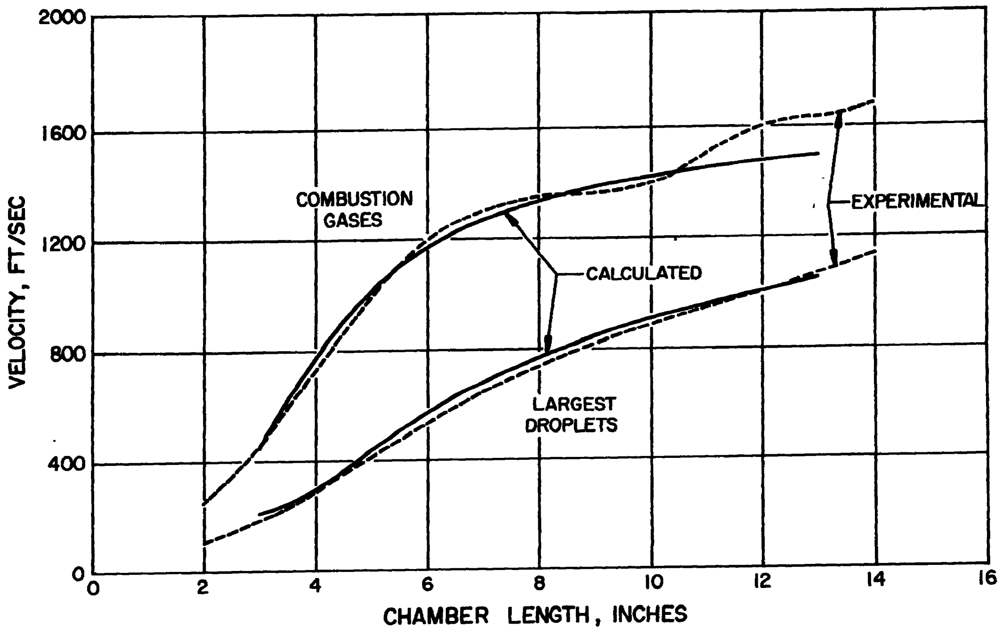

Fig. 8 Comparison between experimental results and calculated results: $D_{30} = 80\,\mu$, $k' = 0.027$ cm^2/sec, $\mu_g = 1.65 \times 10^{-3}$ poise

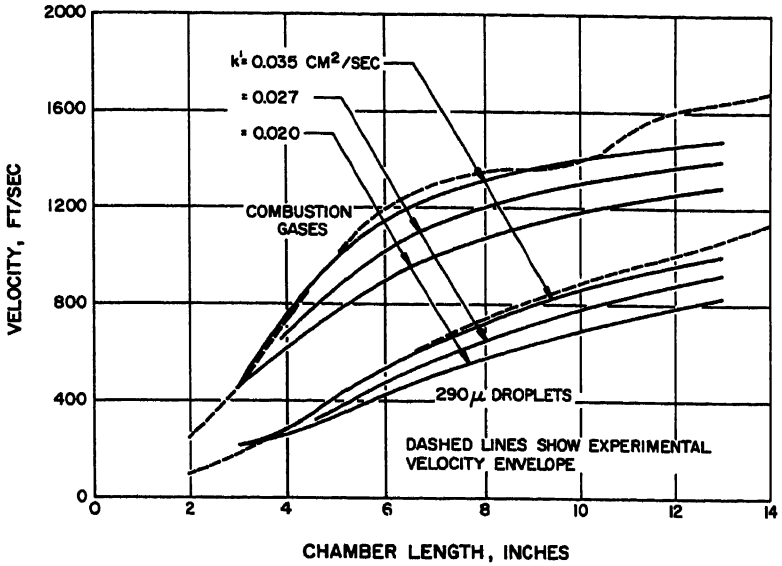

Fig. 9 Calculated results for various values of k' with $D_{30} = 100\ \mu$, $\mu_g = 1.65 \times 10^{-3}$ poise

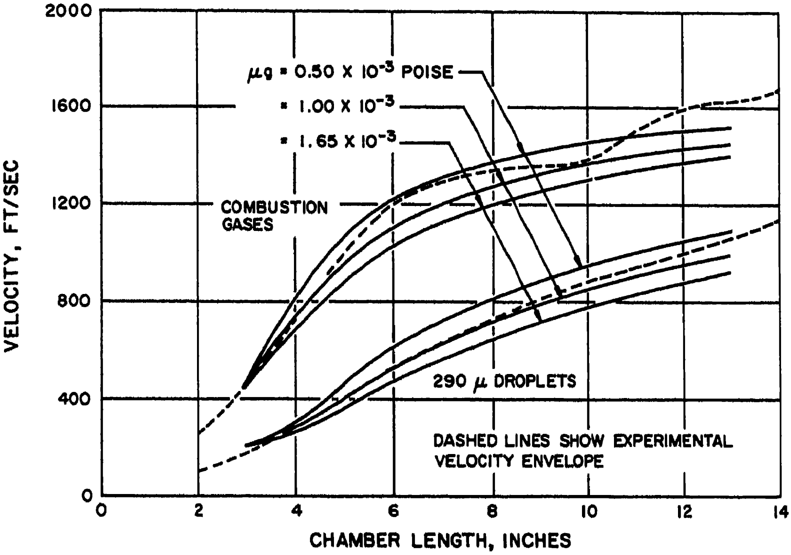

Fig. 10 Calculated results for various values of μ_g with $D_{30} = 100\mu$ and $k' = 0.027\ \text{cm}^2/\text{sec}$

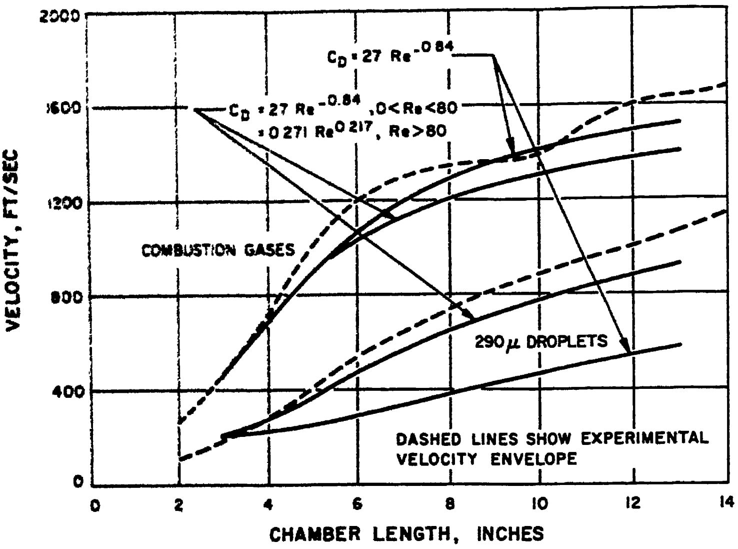

Fig. 11 Calculated results for two different functional relationships between C_D and Re number:
$D_{30} = 100\mu$, $k' = 0.027\ cm^2/sec$, $\mu_g = 1.65 \times 10^{-3}$ poise

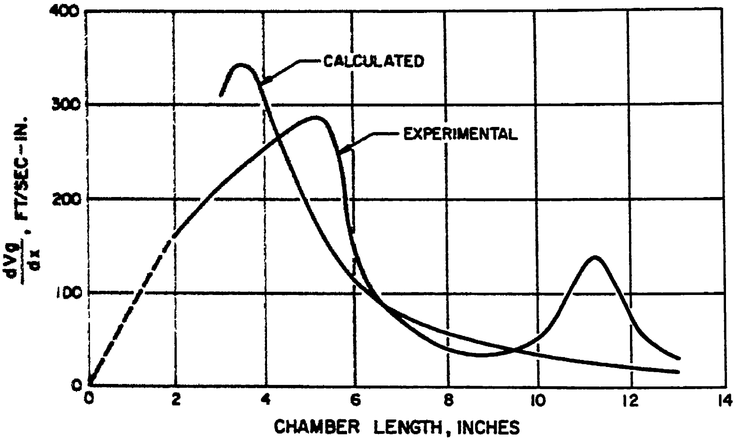

Fig. 12 Rate of combustion gas velocity increase, experimental and calculated:
$D_{30} = 80\mu$, $k' = 0.027\ cm^2/sec$, $\mu_g = 1.65 \times 10^{-3}$ poise

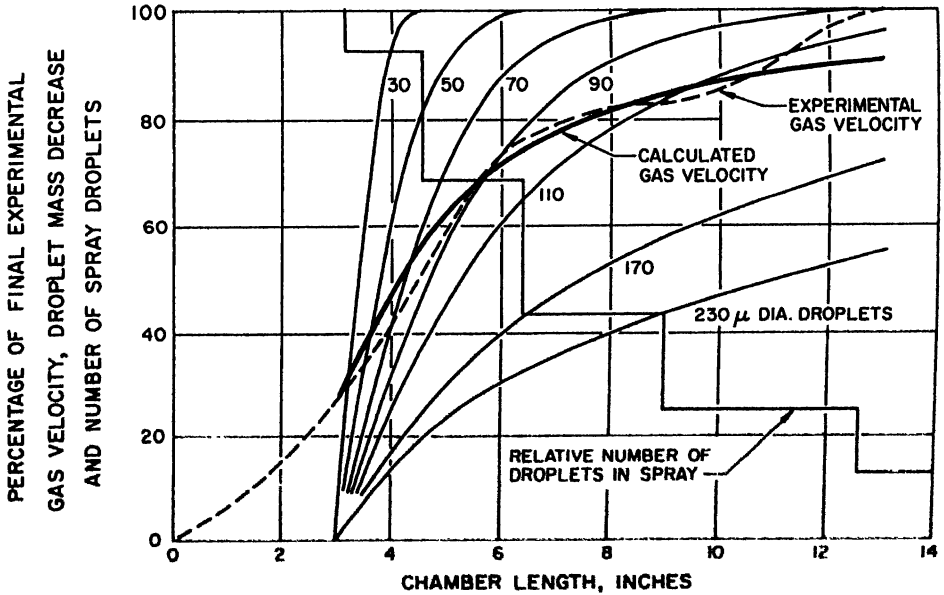

Fig. 13 Combustion gas velocities and calculated droplet consumption for conditions of best correlation: $D_{30} = 80\mu$, $k' = 0.027\ cm^2/sec$, $\mu_g = 1.65 \times 10^{-3}$ poise

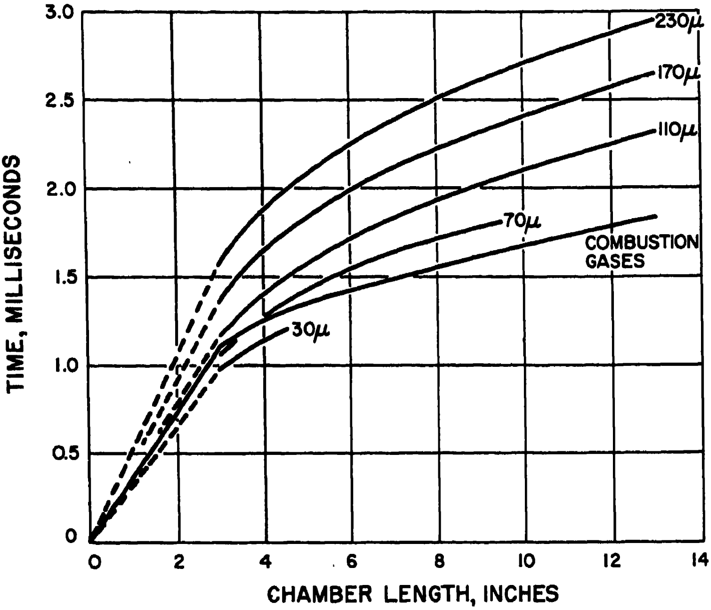

Fig. 14 Time for combustion elements to flow through chamber: $D_{30} = 80\mu$, $k' = 0.027$ cm^2/sec, $\mu_g = 1.65 \times 10^{-3}$ poise

APPLICATION OF SIMILARITY PARAMETERS FOR CORRELATING HIGH FREQUENCY INSTABILITY BEHAVIOR OF LIQUID PROPELLANT COMBUSTORS

Richard J. Priem and Gerald Morrell

NASA Lewis Research Center, Cleveland, Ohio

ABSTRACT

A transformation of the continuity, motion, and energy equations indicated two parameters, one a measure of viscous dissipation and the other a measure of combustion rate, which could be used as similarity criteria. Values of these parameters were calculated for a series of hydrocarbon-liquid oxygen combustors by using two different expressions for the burning rate, one based on a steady-state vaporization model and the other on a process of drop or jet breakup by a shock wave. With both rate expressions, group separation of stable and unstable combustors was obtained, and it was concluded that the parameters can be used for first-order prediction of stability.

INTRODUCTION

Recent investigations of combustion instability in liquid propellant rocket engines have been concerned with many phenomena that could occur in the presence of pressure and velocity oscillations. Refs. 1 and 2 discuss similarity parameters for rocket engines and show that it is not possible to maintain similarity with respect to stability while retaining similarity with respect to flow and reaction rate, for example. Stability of premixed gaseous combustion systems is treated in Refs. 3 and 4, and in Ref. 5 the vaporization rate of a single drop in an acoustic field is considered; possible conditions for amplification of an initially linear wave are presented. In Ref. 6 the combustor is treated as a control loop with a pressure dependent time lag that must be determined from stability limit experiments.

R.J. PRIEM is Head, Rocket Combustion Section. G. MORRELL is Chief, Chemical Rocket Fundamentals Branch. Paper presented at the ARS Propellants, Combustion, and Liquid Rockets Conference, Palm Beach, Fla., April 26-28, 1961.

In this study two similarity parameters were derived by a transformation of the general nonlinear equations of continuity, motion, and energy with mass addition. One parameter, a measure of viscous dissipation, is a Reynolds number based on average acoustic velocity in the combustor; the second parameter is a measure of the heat release rate. Since no linearizing assumptions were included in the transformation, there should be no arbitrary limitations on the validity of these parameters as stability criteria.

Values of the parameters were calculated for a series of hydrocarbon-liquid oxygen rocket combustors. Two different expressions for the heat release rate were used for these calculations: one was based on a steady-state spray vaporization model, and the other was based on a model of drop or jet shattering by a shock wave. With both rate expressions, group separation of stable and unstable combustors was obtained, and it was concluded that the parameters are suitable for first-order prediction of combustion stability.

THEORY

The rocket combustor is considered here to be a system in which propellants are introduced uniformly at the injector boundary. The propellants are assumed to burn at a rate that depends on the position within the combustor. As the propellants burn, random disturbances occur within the combustor, and if a disturbance is large enough it may develop into a steady-state wave traveling within the combustor. The object of this study is to determine a set of parameters that will correctly group combustors having the same response to a normal distribution of disturbance amplitudes.

The flow of burned gas in the combustor is described by the continuity, motion, and energy equations with mass addition. It is assumed that the liquid propellant is at rest with respect to the burned gas. In the notation of Ref. 7, the equations are

Continuity

$$\frac{\partial \rho}{\partial t} = -\vec{\nabla} \cdot (\rho \vec{v}) + w \qquad [1]$$

This equation states that within a volume element fixed in space, the mass of gas changes because of: 1) transport of mass by virtue of the bulk flow; and 2) addition of mass by burning.

Motion

$$\frac{\partial}{\partial t}(\rho\vec{v}) = -\vec{\nabla}\cdot(\rho\vec{v}\cdot\vec{v}) - g\vec{\nabla}P - \vec{\nabla}\cdot\tau + w\vec{v} \qquad [2]$$

Here the momentum of unburned material is assumed to be negligible compared with that of burned gas. The equation states that the momentum in a volume element fixed in space changes because of: 1) transport of momentum by bulk flow; 2) pressure difference; 3) shear stresses; and 4) momentum of gas added by burning.

Energy

$$\frac{\partial}{\partial t}(\rho c\ T) = -\vec{\nabla}\cdot(\rho c_v T\vec{v}) - \vec{\nabla}\cdot(-K\vec{\nabla}T) - \frac{P}{J}\vec{\nabla}\cdot\vec{v}$$

$$-\frac{1}{gJ}(\tau:\vec{\nabla}\vec{v}) + w\lambda - wc_pT - \frac{wv^2}{2gJ}$$

Here a constant specific heat and ideal gas behavior have been assumed, and the energy of unburned material has been assumed to be negligible as compared with that of burned gas. The equation states that in a volume element fixed in space the energy changes because of: 1) energy carried by the bulk flow; 2) heat conduction; 3) compression work; 4) viscous dissipation by bulk flow; 5) chemical energy released in burning; 6) sensible heat of gas added by burning; and 7) kinetic energy of gas added by burning.

In this analysis only transverse wave motion in a cylindrical reactor is considered, and the combustor radius R is used as a suitable characteristic length. To nondimensionalize Eqs. 1, 2, and 3 the following transforms are used:

$$t^* = tV_o/R \quad \rho^* = \rho/\rho_o \quad T^* = T/T_o \quad \nabla^* = R\nabla$$

$$P^* = P/P_o \quad v^* = v/V_o \quad w^* = w/w_o \quad \tau^* = \frac{\tau R}{\mu_o V_o}$$

$$z^* = z/R \quad r^* = r/R \quad \theta^* = \theta/2\pi$$

and the following expressions:

$$gT_o\mathcal{R}\gamma = V_o^2 \qquad c_p/c_v \equiv \gamma \qquad \lambda \cong c_pT_o$$

$$P = \rho\mathcal{R}T \qquad c_p - c_v = \mathcal{R}/J \qquad \frac{c_p\mu}{K} \cong 1$$

and

$$c_v = \frac{R}{J}\,\frac{1}{\gamma - 1}$$

With the further assumption that the physical properties of the burned gas are constant, the transformed equations are

Continuity

$$\frac{\partial}{\partial t^*}\left(\frac{P^*}{T^*}\right) = -\frac{P^*}{T^*}\vec{\nabla}^*\cdot\vec{v}^* + \left[\!\!\left[\frac{Rw_o}{\rho_o V_o}\right]\!\!\right] w^* \qquad [4]$$

Motion

$$\frac{\partial}{\partial t^*}\left(\frac{P^*}{T^*}\vec{v}^*\right) = -\vec{\nabla}^*\cdot\left(\frac{P^*}{T^*}\vec{v}^*\cdot\vec{v}^*\right) - \left[\!\!\left[\frac{1}{\gamma}\right]\!\!\right]\vec{\nabla}^* P^*$$

$$- \left[\!\!\left[\frac{\mu_o}{R\rho_o V_o}\right]\!\!\right]\vec{\nabla}^*\cdot\tau^* + \left[\!\!\left[\frac{Rw_o}{\rho_o V_o}\right]\!\!\right] w^*\vec{v}^* \qquad [5]$$

Energy

$$\frac{\partial P^*}{\partial t^*} = -\vec{\nabla}^*\cdot(P^*\vec{v}^*) - \left[\!\!\left[\frac{\mu_o}{R\rho_o V_o}\right]\!\!\right][\![\gamma]\!]\vec{\nabla}^*\cdot(-\vec{\nabla}^* T^*)$$

$$- [\![\gamma - 1]\!] P^*\vec{\nabla}^*\cdot\vec{v}^* - \left[\!\!\left[\frac{\mu_o}{R\rho_o V_o}\right]\!\!\right][\![\gamma(\gamma - 1)]\!](\tau^* : \vec{\nabla}^*\vec{v}^*)$$

$$+ \left[\!\!\left[\frac{Rw_o}{\rho_o V_o}\right]\!\!\right] w^*\gamma\left[(1 - T^*) - \frac{\gamma - 1}{2} v^{*2}\right] \qquad [6]$$

In the cylindrical coordinate system these equations involve the eight variables P^*, v^*, T^*, w^*, t^*, z^*, r^*, and θ^*. An additional equation of the type $w^* = f(v^*, T^*, P^*)$ would permit each of the variables P^*, v^*, T^*, and w^* to be expressed as functions of the time and space coordinates t^*, z^*, r^*, and θ^*.

For the additional equation, the Arrhenius expression for the chemical reaction rate is chosen:

$$w_o = ka_o^n \rho_o^n \exp(-\beta/T_o) \qquad [7]$$

where it has been assumed that the concentration of each reactant is proportional to a_o. If it is also assumed that the local reaction follows the same law

$$w = ka^n \rho^n \exp(-\beta/T) \qquad [8]$$

then

$$w^* = a^{*n} \rho^{*n} \exp\left[\frac{\beta}{T_o}\left(1 - \frac{1}{T^*}\right)\right] \qquad [9]$$

If the rate of production of reactant is assumed to be constant and equal to w_o, the concentration may be written as

$$a = \int_0^z \left(\frac{w_o}{\rho_o} - \frac{w}{\rho}\right) \frac{dz}{v} \qquad [10]$$

and

$$a^* = \frac{Rw_o}{\rho_o V_o} \int_0^{z^*} \left(\frac{T^*}{P^*}\right) (1 - w^*) \frac{dz^*}{v^*} \qquad [11]$$

Substitution in Eq. 9 yields

$$w^* = \left[\!\left[\frac{P^*}{T^*} \right]\!\right]^n \exp \frac{\beta}{T_o}\left(1 - \frac{1}{T^*}\right) \left\{ \left[\!\left[\frac{Rw_o}{\rho_o V_o} \right]\!\right] \int_0^{z^*} \frac{T^*}{P^*} (1 - w^*) \frac{dz^*}{v^*} \right\}^n$$

[12]

With Eqs. 4-6 and 12, the variables P^*, T^*, v^*, and w^* can be expressed in the following form:

$$P^* = f_1\left(t^*, z^*, r^*, \theta^*, \left[\!\left[\frac{Rw_o}{\rho_o V_o} \right]\!\right], \left[\!\left[\frac{\mu_o}{R\rho_o V_o} \right]\!\right], \gamma, n, \beta\right)$$

[13]

$$T^* = f_2(t^*, \ldots, \beta) \qquad [14]$$

$$v^* = f_3(t^*, \ldots, \beta) \qquad [15]$$

$$w^* = f_4(t^*, \ldots, \beta) \qquad [16]$$

These equations imply that all combustors having the same value of $\left[Rw_o/\rho_oV_o \right]$, $\left[\mu_o/R\rho_oV_o \right]$, γ, n, and β/N_D and subjected to the same initial conditions at $t^* = 0$ are similar; that is, they will exhibit the same time and space histories of P^*, T^*, v^*, and w^*. The first bracketed term is similar to Damköhler's first similarity group except that it is based on the sound velocity rather than gas velocity. The second term in brackets is a Reynolds number based on the sound velocity rather than gas velocity. Furthermore, since γ, n, and β^* are usually functions of the propellant alone, the two terms $\left[Rw_o/\rho_oV_o \right]$ and $\left[\mu_o/R\rho_oV_o \right]$ are sufficient for comparing combustors operating with the same propellant system. For example, if a combustor having certain values of these terms and subjected to a normal distribution of disturbance amplitudes at $t^* = 0$ is unstable, any other combustor operating on the same propellants and subjected to the same initial condition should also be unstable if it has the same values for the two terms given in the foregoing.

For calculations based on the usual rocket combustor variables, it is convenient to transform the forementioned terms by applying the following expressions:

$$c^* = \frac{P_cA_tg}{\dot{w}} = \frac{\sqrt{g\gamma \mathcal{R} T_o}}{\gamma\sqrt{\left(\frac{2}{\gamma - 1}\right)^{\frac{\gamma+1}{\gamma-1}}}} \qquad w_o = m\,\frac{\dot{w}}{A_c}$$

$$P_o = \rho_o \mathcal{R} T_o \qquad \mathcal{A} = A_c/A_t \qquad V_o^2 = g\mathcal{R}\gamma T_o$$

which results in

$$\frac{Rw_o}{\rho_oV_o} = \frac{Rm}{\mathcal{A}}\sqrt{\left(\frac{2}{\gamma - 1}\right)^{\frac{\gamma+1}{\gamma-1}}} \qquad [17]$$

and

$$\frac{\mu_o}{\rho_o R V_o} = \frac{\mu_o c^*}{R P_o g} \sqrt{\left(\frac{2}{\gamma - 1}\right)^{\frac{\gamma+1}{\gamma-1}}} \qquad [18]$$

For given propellants, only the terms $\mathscr{L}$ and $\mathscr{J}$ need be considered

$$\mathscr{L} \equiv \frac{Rm}{\mathscr{A}} \qquad [19]$$

$$\mathscr{J} \equiv \frac{\mu_o c^*}{R P_o g} \qquad [20]$$

In the following, $\mathscr{L}$ is referred to as the burning rate parameter, and $\mathscr{J}$ is referred to as the viscous dissipation parameter. By examining its influence in Eqs. 4-6, $\mathscr{L}$ can be thought of as a measure of the energy that could be added to a wave, and, similarly, $\mathscr{J}$ can be considered a measure of the energy that could be removed from a wave. It might be expected, therefore, that stability will be increased by an increase in $\mathscr{J}$ and a decrease in $\mathscr{L}$.

CORRELATION OF COMBUSTOR STABILITY

To test the similarity hypothesis outlined above, the values of $\mathscr{L}$ and $\mathscr{J}$ were calculated for a series of hydrocarbon-liquid oxygen rocket combustors.[1] In performing such calculations, the values of R, $\mathscr{A}$, and P_o are either known or specified, the value of μ_o can be estimated for known operating conditions, and the value of c^* is either measured or can be calculated by assuming chemical equilibrium in the combustor. Only the calculation of m is not straightforward and requires the specification of a model for the rate process that is subjected to an initial disturbance. In this study two models were considered: a steady-state vaporization model and one based on jet or drop shattering by a shock wave. Of course, other processes might have been tried, e.g., turbulent mixing, chemical reaction, or liquid mixing, but previous research indicated that the ones chosen had a higher probability of success.

---

[1] The data for these values were supplied by the Rocketdyne Division of North American Aviation Inc. Additional data on these combustors were supplied by the NASA George C. Marshall Space Flight Center.

Steady-State Vaporization

Previous theoretical and experimental studies (8-12)[2] have indicated that during steady-state operation, propellant vaporization is the rate controlling process in a rocket combustor. By making the assumption that the atomization process is unaffected by the random disturbances prior to unstable combustion, the results of Ref. 8 can be used to determine the burning rate near the injector where a wave is most likely to be driven. For this purpose, the average rate corresponding to 50% vaporization appears to be appropriate, and a correlation of the calculated drop histories of Ref. 8 yields the following expression:

$$m_i \equiv \frac{0.5}{L_{50}} \frac{\mathcal{K}(P_0/300)^{0.5}}{\mathcal{A}^{0.3}(1 - T_r)^{0.2}\left(\frac{\lambda_m}{0.003}\right)^{1.5}\left(\frac{V_j}{1200}\right)^{0.8}} \qquad [21]$$

where $\mathcal{K}$, a correlation constant, is 0.276 for hydrocarbons, 0.257 for ammonia, 0.180 for hydrogen, 0.65 for oxygen, and 0.58 for fluorine, and m_i is the vaporization rate of oxidizer $(i = O)$ or fuel $(i = F)$, where the vaporization rate has been assumed equal to the burning rate. The total burning rate is determined by assuming that combustion takes place at the stoichiometric mixture ratio $(\dot{w}_O/\dot{w}_F)_{st}$ so that

$$m = \left[\frac{1 + \left(\frac{\dot{w}_O}{\dot{w}_F}\right)_{st}}{1 + \left(\frac{\dot{w}_O}{\dot{w}_F}\right)}\right] m_F \qquad [22]$$

based on fuel vaporization rate, and

$$m = \left[\frac{1 + \left(\frac{\dot{w}_F}{\dot{w}_O}\right)_{st}}{1 + \left(\frac{\dot{w}_F}{\dot{w}_O}\right)}\right] m_O \qquad [23]$$

based on oxidant vaporization rate.

---

[2] Numbers in parentheses indicate References at end of paper.

With Eqs. 21 and 22 or 23 the burning rate, $\mathcal{L}$, and $\mathcal{J}$ were calculated from the hydrocarbon-oxygen combustor data mentioned previously. The resultant $\mathcal{J}$-$\mathcal{L}$ plot is shown in Fig. 1. The value of μ_o was calculated by the viscosity equation for heptane-oxygen combustion products given in Ref. 8, p. 52. The average combustion temperature and characteristic velocity were assumed to have their theoretical values of 6400° R and 5900 fps, respectively, for a mixture ratio of 2.4. The value of r_m was obtained from injector jet diameter by using Fig. 32 of Ref. 8. Where the injector design involved more than one jet size or impingement pattern, an average r_m was computed based on the fraction of total injection area for each jet size or impingement pattern.

The $\mathcal{J}$-$\mathcal{L}$ plot of Fig. 1 shows a clear group separation of stable and unstable combustors. A 45° straight line was arbitrarily drawn for the boundary between the groups, as it seemed logical that the viscous damping parameter required to maintain stability should increase directly with the burning rate parameter.

Qualitatively, the distance of a point from the line of separation appears to be a measure of the stability of the corresponding combustor. The occurrence of instability appears to be a statistical phenomenon, however, probably related to the random nature of the initiating disturbances, since all the stable combustors exhibited a small percentage of unstable runs and all the combustors in the unstable group exhibited varying percentages of stable runs. Because of this statistical behavior and the limited number of tests of the two stable combustors in the unstable region of Fig. 1, it is not possible to state whether these represent the same degree of instability as the other members of the group.

Jet or Drop Shattering by a Shock Wave

Recent research (e.g., Refs. 13-15) has laid the foundation for quantitative prediction of the breakup times of drops and jets subjected to shock waves and of the threshold value of disturbance required to initiate shattering. The evidence indicates that burning drops behave in the same way as nonburning drops (14) so that it appears reasonable to investigate the influence of liquid disintegration on combustor stability.

The model chosen assumes that a disturbance, approximated by a shock wave, initiates a breakup process of the jets or drops and that the fine spray produced burns instantaneously as compared with the burning rate of the original liquid mass. The burning rate of either fuel or oxidant may then be expressed as

$$m_i = 1/t_b v_j \qquad [24]$$

where t_b is the time for complete disintegration behind the shock wave, and v_j is jet velocity or drop velocity, assumed equal in this analysis. For simplicity, only the fuel breakup was considered, and by the same analysis as was used in the previous section it can be shown that

$$m = \left[\frac{1 + \left(\frac{\dot{w}_O}{\dot{w}_F}\right)_{st}}{1 + \left(\frac{\dot{w}_O}{\dot{w}_F}\right)}\right] m_F = \left[\frac{1 + \left(\frac{\dot{w}_O}{\dot{w}_F}\right)_{st}}{1 + \left(\frac{\dot{w}_O}{\dot{w}_F}\right)}\right]\left[\frac{1}{t_b v_j}\right] \qquad [25]$$

Consequently, the burning rate parameter becomes

$$\mathscr{L} \equiv \left[\frac{1 + \left(\frac{\dot{w}_O}{\dot{w}_F}\right)_{st}}{1 + \left(\frac{\dot{w}_O}{\dot{w}_F}\right)}\right]\left[\frac{1}{t_b v_j}\right]\left[\frac{R}{\mathscr{A}}\right] \qquad [26]$$

For given combustor design and operating conditions, therefore, evaluation of $\mathscr{L}$ reduced to an evaluation of jet or drop breakup time.

A theoretical relation among breakup time t_b, wave action time t_a, and Weber number for the breakup of a jet behind a shock wave is presented in Ref. 15 and is shown to agree reasonably with experimental values of t_b. In the absence of knowledge about the magnitude of the initial disturbance, the threshold value was assumed, in which case a unique relation between t_b and t_a is obtained, as shown in Fig. 2. The value of t_a should be some fraction of the period of the particular mode of oscillation being considered. In this analysis it was chosen to be equal to the calculated period of the transverse mode of oscillation. Fig. 2 may also be used for drop breakup, since the expression derived in Ref. 16 for the breakup time of drops is quite similar to that of Ref. 15. The fundamental natural periods of drops and jets are given in Ref. 17 as

$$\mathcal{T} = 2\pi \sqrt{\frac{\rho_l r^3}{6\sigma}} \qquad [27]$$

for a jet, and

$$\mathcal{T} = 2\pi \sqrt{\frac{\rho_l r^3}{8\sigma}} \qquad [28]$$

for a drop, where ρ_l is liquid density, r is radius, and σ is liquid surface tension.

With breakup times obtained from Fig. 2 for the same combustors as were considered in the previous section, $\mathcal{J}$ - $\mathcal{L}$ plots were prepared on the basis of jet and drop breakup and are shown in Figs. 3 and 4, respectively. For Fig. 4 the mass median drop size r_m, obtained as described previously, was chosen to represent the spray.

Both plots show clear group separations between stable and unstable combustors, quite similar to that shown in Fig. 1. The lines of separation are again arbitrarily drawn 45° lines.

It is not possible from Figs. 3 and 4 alone to decide whether drop or jet shattering is the appropriate initiating mechanism for instability. It might be expected, however, that if shattering did occur, the $\mathcal{L}$ values should be much larger than those corresponding to steady-state vaporization (Fig. 1), and on this basis Fig. 4 appears preferable to Fig. 3 as a stability correlation.

CONCLUSIONS

On theoretical grounds, since both proposed mechanisms give equally good group correlations, it is not possible to decide which is a better description of the actual process leading to growth of a disturbance in a liquid propellant rocket combustor. The qualitative success of a mechanistic approach to describing combustion stability indicates the types of research that should be pursued. The rate processes considered here, as well as others, e.g., chemical reactions, turbulent mixing, spray formation, and liquid mixing, deserve intensive study to establish quantitative steady-state and transient rate laws. Numerical solutions of the nonlinear mass, momentum, and energy equations should be pursued with assumed mechanisms to provide a sound basis for experimental work.

For the designer, the correlations represent a first step toward a priori criteria for combustion stability. When established by application to physically similar systems, the correlations provide a guide to the effect of proposed design changes on the stability of the resultant system.

NOMENCLATURE

a = mass fraction of reactant, dimensionless
A_c = cross-sectional area of combustor, $in.^2$
A_t = cross-sectional area of nozzle throat, $in.^2$
$\mathscr{A}$ = contraction ratio A_c/A_t, dimensionless
c_p = specific heat of gases at constant pressure, Btu/lb-°R
c_v = specific heat of gases at constant volume, Btu/lb-°R
c^* = characteristic exhaust velocity, ips
$f()$ = function of parameters within (), dimensionless
g = acceleration due to gravity, 386.09 $in./sec^2$
J = mechanical equivalent of heat, 9339.1 in.-lb/Btu
$\mathscr{J}$ = viscous dissipation parameter $\mu_0 c^*/RP_0 g$, dimensionless
K = thermal conductivity of gases, Btu/in.-sec-°R
$\mathscr{K}$ = proportionality constant, dimensionless
k = pre-exponential constant in Arrhenius equation, sec^{-n}
L_{50} = length required to vaporize 50% of the propellant, in.
$\mathscr{L}$ = burning rate parameter $Rm/\mathscr{A}$, dimensionless
m = fractional burning rate of propellants per unit length, $in.^{-1}$
n = exponent in Arrhenius equation, dimensionless
P = pressure, $lb/in.^2$
R = combustor radius, in.
r = radial distance from axis of combustor, in.
$\mathscr{R}$ = specific gas constant, in./°R
$\mathscr{r}$ = radius of liquid drop or jet, in.
$\mathscr{r}_m$ = mass-median drop size from Fig. 32 of Ref. 8, in.
T = temperature, °R
T_c = critical temperature, °R
T_{lo} = initial propellant temperature, °R
T_r = reduced propellant temperature T_{lo}/T_c, dimensionless
t = time, sec
t_a = wave action time for drop or jet breakup, sec
t_b = breakup time, sec
$\mathscr{T}$ = natural period of oscillation for jets or drops, sec
V = speed of sound in gases, ips
v = gas velocity, ips
v_j = velocity of drops or jets, ips
w = burning rate, $lb/sec\text{-}in.^3$
$\dot{w}$ = propellant flow rate, lb/sec
z = axial distance from injector, in.
β = activation energy function in Arrhenius equation, °R
γ = specific heat ratio c_p/c_v, dimensionless

θ = angular position, radians
λ = heat of combustion of propellants, Btu/lb
μ = gas viscosity, lb/in.-sec
ρ = gas density, lb/in.^{3}
ρ_l = liquid density, lb/in.^{3}
σ = liquid surface tension, lb/sec^2
τ = stress tensor (p. 89, Ref. 7), lb/in.-sec^2

Subscripts

F = fuel
o = average value
O = oxidant
st = stoichiometric

Superscripts

$*$ = nondimensional transformed variable
$\rightarrow$ = vector quantity

REFERENCES

1 C.C. Ross: Scaling of Liquid Fuel Rocket Combustion Chambers. AGARD Selected Combustion Problems, vol. 2, pp. 444-456. Butterworths Scientific Publications, London, 1956.

2 S.S. Penner: Rational Scaling Procedures for Liquid-Fuel Rocket Engines. Jet Propulsion, February 1957, vol. 27, pp. 156-161.

3 G. Rosen: Nonlinear Pressure Oscillations in a Combustion Field. ARS Jour., April 1960, vol. 30, pp. 422-423.

4 M.J. Zucrow and J.R. Osborn: An Experimental Study of High-Frequency Combustion Pressure Oscillations. Jet Propulsion, October 1958, vol. 28, pp. 654-658.

5 P.R. Wieber and W.R. Mickelsen: Effect of Transverse Acoustic Oscillations on the Vaporization of a Liquid-Fuel Droplet. NASA TN D-287, May 1960.

6 L. Crocco, J. Grey, and D.T. Harrje: Theory of Liquid Propellant Rocket Combustion Instability and Its Experimental Verification. ARS Jour., February 1960, vol. 30, pp. 159-168.

7 R.B. Bird, W.E. Stewart, and E.N. Lightfoot: Transport Phenomena, pp. 89, 318-324. John Wiley and Sons Inc., New York, 1960.

8 R.J. Priem and M.F. Heidmann: Propellant Vaporization as a Design Criterion for Rocket-Engine Combustion Chambers. NASA TR-67, 1960.

9 B.J. Clark, M. Hersch, and R.J. Priem: Propellant Vaporization as a Criterion for Rocket-Engine Design; Experimental Performance, Vaporization, and Heat-Transfer Rates with Various Propellant Combinations. NASA Memo 12-29-58E, January 1959.

10 M.F. Heidmann: Experimental Effects of Chamber Diameter on Performance. NASA TN D-65, September 1959.

11 R.J. Priem and M. Hersch: Effect of Fuel Orifice Diameter on Performance. NACA RM E57F26, February 1958.

12 B.J. Clark: Propellant Vaporization as a Criterion for Rocket-Engine Design; Experimental Effect of Combustor Length, Throat Diameter, Injection Velocity, and Pressure on Rocket Combustor Efficiency. NASA TN D-258, April 1960.

13 G. Morrell: Critical Conditions for Drop and Jet Shattering. NASA TN D-677, February 1961.

14 E. Rabin and R. Lawhead: Motion and Shattering of Burning and Nonburning Propellant Droplets. AFOSR TN-59-129, March 1959.

15 G. Morrell: Breakup of Jets by Transverse Shocks. Presented at 8th International Symposium on Combustion, Pasadena California, August 1960.

16 J.O. Hinze: *Applied Scientific Research*, vol. A1, p. 273. Martinus Nijhoff, The Hague, 1949.

17 H. Lamb: *Hydrodynamics*, 6th ed., p. 472. Dover Publications, New York, 1945.

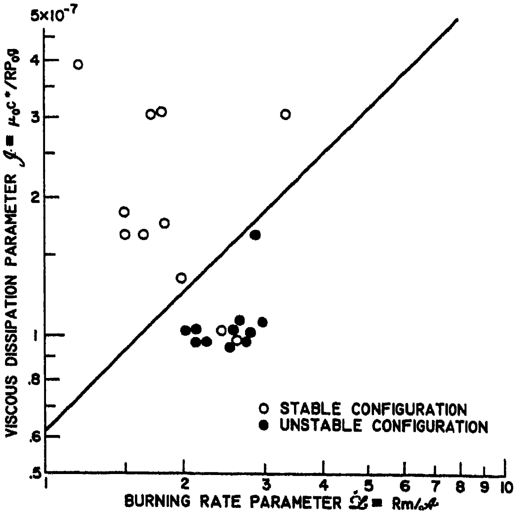

Fig. 1 Stability plot based on steady-state propellant vaporization

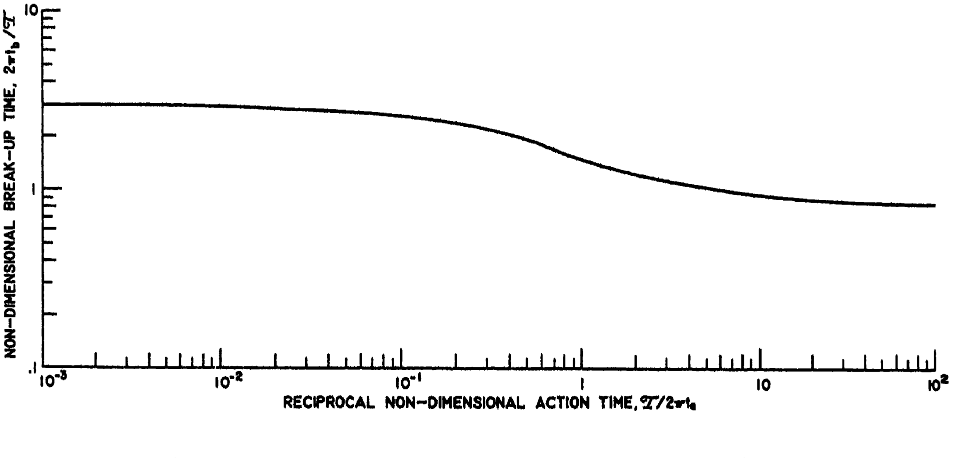

Fig. 2 Plot of maximum breakup time as a function of wave action time

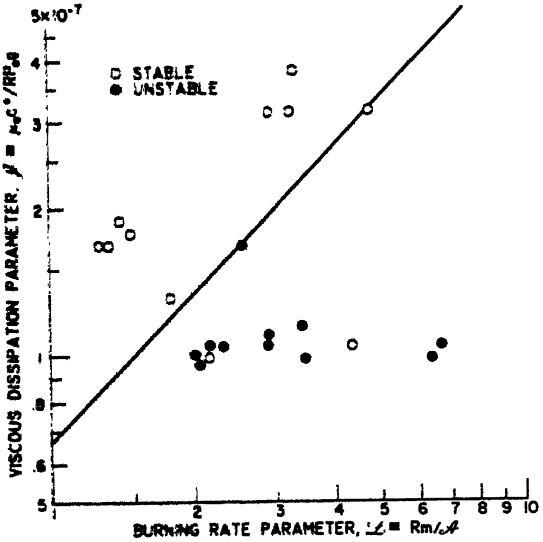

Fig. 3 Stability plot based on fuel jet breakup by a shock wave

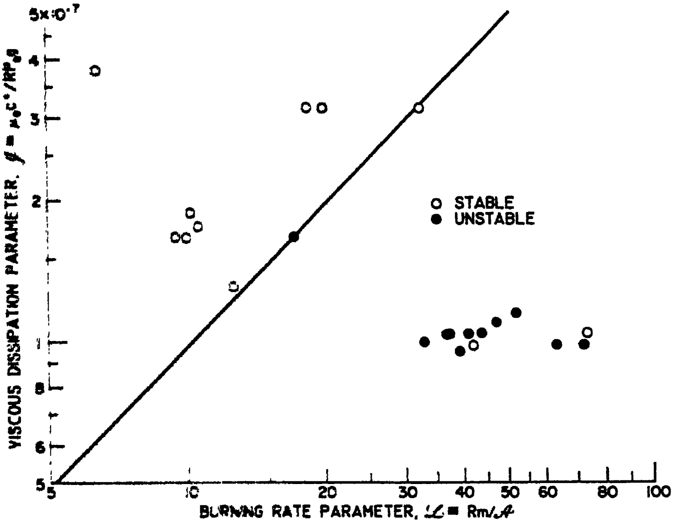

Fig. 4 Stability plot based on mass median fuel drop breakup by shock wave

VIBRATION AND COMBUSTION INVESTIGATION OF THE LR99 ENGINE

Mario J. Luperi and Sanford J. Tick

Thiokol Chemical Corp., Reaction Motors Division,
Denville, N. J.

ABSTRACT

The inherent combustion stability aspects of the LR99 engine injector thrust chamber configuration are presented. The LR99 engine spherical-type combustion section geometry, which is a radical departure from conventional engine design, is shown to provide good attenuation of acoustic pressure oscillations and a high degree of damping of induced combustion disturbances. The random occurrences of amplified vibrations experienced with the LR99 engine are shown to be a direct result of resonance with the airframe thrust mount at a known acoustic mode of the thrust chamber. By means of experimentally induced combustion oscillations, evidence was obtained demonstrating that combustion oscillations can be isolated from the airframe thrust mount structure.

INTRODUCTION

The LR99 engine is a man-rated, throttling rocket engine of 50,000 lb sea level thrust operating on liquid oxygen and anhydrous liquid ammonia (Fig. 1). It is used to power the X-15 aircraft. The engine is described in detail in the literature (1,2).[1]

The LR99 is the only operational rocket engine of its size in the country which fully meets the stringent requirements for manned aircraft safety as outlined in military specification MIL-E-5149. In addition to the man-rated requirements, the

---

M.J. LUPERI and J.S. TICK are Senior Engineers in the Thrust Chamber Section of the Engineering Services Department, Thiokol Chemical Corporation, Reaction Motors Division, Denville, N.J. Paper presented at the ARS Propellants, Combustion, and Liquid Rockets Conference, Palm Beach, Fla., April 26-28, 1961.

[1] Numbers in parentheses indicate References at end of paper.

LR99 engine has successfully demonstrated such significant capabilities as throttleability, multiple restart, operation over a broad environmental temperature range, imposed accelerations up to 9.5 g, operation in any attitude, and a service life of one hour comprising 100 firing cycles.

The man-rated requirement was one of the major concerns in the development of the LR99 engine, since this necessitated an engine system designed to prevent hazardous failure of the engine in the event of any single malfunction condition. Since almost all other large rocket engines have been plagued by destructive combustion instability, it was evident that particular attention would have to be paid to the design and development of a stable combustion chamber in order to achieve the required safety for this application to a manned vehicle.

A majority of the large rocket engines in operation or under development have a typical combustion chamber configuration that closely resembles a closed cylinder, that is, a cylindrical combustion zone, a flat injector surface and a chamber contraction ratio on the order of two. It has been recognized in recent years that unstable combustion pressure oscillations are acoustic in nature and that a cylindrical type of combustion chamber geometry increases the probability of these oscillations. Costly and time consuming programs have been conducted in efforts to solve the combustion instability problems that have occurred in many of the large rocket engines using cylindrical type combustion chambers.

Since the man-rated philosophy of the LR99 engine was strongly dependent on combustion safety criteria, careful consideration was given to: 1) the design of an injector-combustion section geometry that would provide good attenuation of acoustic type combustion pressure oscillations; and 2) optimization of the distribution and staging of the injected propellants to achieve reliable and stable ignition. To implement these two considerations, the RMD approach in the design of the LR99 injector-combustion section geometry was to minimize cylindrical surfaces and to use a hemispherical headed injector surface (Fig. 2) in conjunction with a centrally located igniter that fires throughout the run.

The hemispherical head injector directs the injected propellants into the igniter flame, thereby achieving reliable main stage ignition and stabilization of the flame front. It also provides a degree of distribution of injection along the length of the chamber. The curved injector surface serves to scatter, and thereby prevent amplification of, reflected acoustic pressure waves that may occur as a result of any induced combustion disturbance. A large radius at the throat entrance section also provides a reflective surface that scatters acoustic pressure waves. A moderately large contraction ratio (ratio of chamber area to throat area) of 4 is used to attain the desired L* with essentially no cylindrical section. Nevertheless, it was recognized at the outset of the engine program that the engine would probably provide significant vibrational outputs at thrust chamber acoustic modes. The calculated frequencies were set forth in the engine model specification. These values were 132 cps, 1630 cps, 1680 cps, 2790 cps, 3500 cps, and 3840 cps.

This paper summarizes the development experience of the LR99 engine injector thrust chamber configuration in regard to combustion stability and presents the results of an experimental program that confirmed the inherent combustion stability of the LR99 flight type of injector thrust chamber configuration.

SUMMARY OF LR99 INJECTOR TEST EXPERIENCE

Flat Plate Multispud Injector

The initial design of the hemispherical injector was of the "spaghetti" type. Fabrication difficulties encountered with units of this type, however, led to its abandonment in favor of a multispud arrangement. Design and procurement of flight type of injectors of this configuration were initiated. To reduce lead time so that engine testing could proceed, however, a workhorse flat plate multispud injector was used. This unit incorporated the same number, 18, of propellant injector spuds as the hemispherical injector designed for flight engines, but they were arranged in a plane normal to the axis of symmetry of the chamber. A short cylindrical section in the flat plate injector was used to obtain the same combustion volume as with the hemispherical design.

Testing experience with the flat plate injector revealed a marked tendency towards combustion instability. Test runs often resulted in severe erosion of both the injector and chamber. The pattern of the erosion was indicative of a transverse type of combustion oscillation. The cases of destructive instability experienced with the flat plate injector substantiated the basic RMD philosophy that flat injection surfaces are undesirable in large rocket engines. Because of the destructive effects produced by unstable operation of this injector, it was decided to use only hemispherical head injectors for further testing.

Hemispherical Flight Type of Injector

During the initial testing of the hemispherical head multi-spud injector, random occurrences (2 to 4% of total engine runs) of severe vibration, resulting in structural damage to the injector, were encountered. Accelerations recorded when the vibration phenomenon appeared during the start transient were as high as 500 g. The nature of the damage to the injector, and the circumstances that accompanied it, led to the preliminary conclusion that the vibration was initiated by unstable combustion, which, in turn, was initiated by an injector failure. It was noted, however, that there was neither erosion of the injector or thrust chamber nor other evidence of extremely high rates of heat transfer. In this important respect, experience with the hemispherical injector differed from that with the flat faced unit as well as from that reported by most other agencies in connection with combustion instability.

VIBRATION INVESTIGATION

Establishment of Hypothesis

In order to permit the continuation of testing while minimizing the danger of excessive loss of hardware, a device for automatically shutting down the engine on the initiation of vibration was installed on all units. By this means, it was learned that severe vibration could take place without damage to the injector. At this point, structural failure was eliminated as a contributory cause and recognized to be a result. An investigation to determine the actual source of the difficulty was started.

If it is assumed that a chamber pressure oscillation occurs with an amplitude of zero to 100% of the mean chamber pressure at the maximum thrust level, the resulting maximum acceleration of the engine mass ($\sim$900 lb) will be 55 g. Thus, the extremely high accelerations (up to 500 g) measured during vibration indicated either that the corresponding thrust oscillations were several times full scale or that amplification through mechanical resonance was present. Since the latter appeared to be more likely, it was hypothesized that the phenomenon was comprised of two components, namely a triggering mechanism and an amplifying device. The program was, therefore, directed at identifying these two components.

Search for the Triggering Mechanism

It was readily recognized that the triggering mechanism was associated with the combustion process, since this was the only source of high energy. Acoustic pressure oscillation modes are inherent in all rocket engine combustion processes. These acoustic oscillations, when sustained and amplified by some feedback mechanism, usually produce combustion pressure oscillations, severe vibration, and destructive erosion of hardware. A means of deliberately initiating combustion oscillations was first sought.

Pulsing Techniques

It was decided to attempt to induce combustion instability by using pulsing techniques. This approach is not new. It has, in fact, been used with considerable success by several other agencies (3,4,5).

The following methods were used in the LR99 program:

1 Pyrotechnic squibs (7 to 124 grains) fired both radially and tangentially through ports located at the chamber periphery (Fig. 3).

2 Nitrogen gas at 1500 psig injected across the face of an injection spud through a tube installed through a port in the chamber wall (Fig. 4).

3 Cartridge cases (0.38 caliber) loaded with 10 and 13 grains of high explosive powder and fired across an injection spud (Fig. 5).

Experience with the engine had shown that damage resulting from vibration could be avoided if shutdown were initiated when accelerations of 70 g or greater persisted for 50 millisec. These limits were established as defining a rough operation for the purposes of the vibration investigation.

The attempts to initiate combustion instability by means of pulsing met with very little success. In 18 runs with the pyrotechnic squib, for example, not only were there no rough operations, but also no measurable disturbance rate occurred. When nitrogen gas was used in 46 runs, a measurable disturbance rate (Fig. 6) was experienced in 12 runs (36%), but there were only three rough operations (7%). It was only when pulses were used in combination with a main propellant fuel valve lead (an abnormal condition for the engine) that a measurable disturbance was noted in a significant percentage of the runs. Thus, in 37 runs made under these conditions (26 using nitrogen gas plus fuel valve lead and 11 using cartridge plus fuel valve lead), there was a measurable disturbance rate in 23 cases (62%). In spite of this, however, there were only five rough operations (14%).

In addition to the low incidence of rough operations experienced during this program, it should be noted that the external pulse energy required to initiate a combustion disturbance was 25 times as great as reported by other agencies using similar techniques. In view of these results, it can only be concluded that the configuration of the LR99 combustion chamber is inherently very stable. Furthermore, since other agencies have reported much higher rates of combustion disturbances produced by external pulses of relatively low energy, it must be assumed that the combustion chamber configurations tested were inherently unstable.

Search for the Amplifying Device

When the hypothesis was advanced that a mechanical resonance in the system was serving as the amplifying device that caused the extremely high vibrational accelerations measured on the engine, a program to determine the source of the resonance was started. Several factors directed specific attention to the thrust mount, which is supplied by the air frame manufacturer. This unit is obviously in a very critical position with regard to mechanical vibration. It is a truss-like structure consisting of long, slender tubes that would tend to have well defined natural frequencies of relatively small magnitude. It was used in all tests that resulted in severe vibration.

During rough operation, the predominant vibration and combustion frequency was 1600 to 1650 cps. The calculated first transverse acoustic combustion mode of the chamber is 1630 cps. Calculations also showed that several tubular members of the air frame thrust mount had natural frequencies very close to 1600 cps. A complete engine, with the thrust mount, was subjected to a series of vibration tests. These showed conclusively that the mount was in resonance at 1600 cps and that, as a result, accelerations on the engine were amplified by a factor of ten as compared to the input accelerations to the mount.

Having identified the amplifying device in the system, it was now necessary to eliminate it and evaluate the effect by firing tests. Two approaches were considered, namely, installing vibration isolators between the engine and the air frame thrust mount and changing the natural frequency of the mount members. The former course offered the advantages of fewer changes and shorter time required. A set of isolators, not suitable for flight use because of space requirements, was procured and installed on a test engine (Fig. 7). Vibration tests revealed that the transmissibility (output acceleration/input acceleration) was approximately 20% in the range of frequencies from 1500 to 1700 cps. This compares with the amplification factor of 10 at 1600 cps without isolators.

Firing tests, with the isolators installed on the engine, were now made. The first portion of this program consisted of 200 runs with the normal starting sequence of the engine. Not a single vibration shutdown (i.e., rough operation) occurred.

Additional tests were then conducted. Deliberate attempts to induce vibration were made. Main propellant fuel valve lead was used for this purpose, since it had been learned that this condition was more conducive to rough operation. Although the results of this part of the program were somewhat inconclusive, they did demonstrate the desirability of incorporating vibration isolators in the design of the air frame thrust mount. In 25 runs without isolators and with a six degree fuel valve lead, vibration accelerations as high as 430 g occurred in 10 cases. With the isolators installed, and still retaining the fuel lead, accelerations were considerably lower. Four runs were made under these conditions. The maximum acceleration was 150 g in one case. In all other cases, it was lower but still not eliminated. This is understandable since the transmissibility of the isolators used was still 20% as noted above.

Further efforts to eliminate the mechanical resonance that can lead to destructive vibration are required. The airframe manufacturer has designed a flight type of vibration isolator. This will be evaluated in the near future. An attempt to detune the thrust mount has also been initiated by the airframe manufacturer.

ANALYSIS OF CHAMBER PRESSURE AND VIBRATION DATA

High frequency response ($\sim$10,000 cps) chamber pressure measurements were taken during this program to substantiate the fact that an acoustic pressure oscillation was exciting the resonant frequency of the thrust mount structure.

Fig. 8 shows a typical chamber pressure trace for a rough operation. Fig. 9 shows the wave form and phase relationship of the chamber pressure oscillations for a rough operation.

During rough operation, the predominant combustion and vibration frequency was 1600 to 1650 cps, with an attendant harmonic frequency of 3200 to 3300 cps with an amplitude of ± 10% of the mean chamber pressure. The maximum vibration levels recorded during rough operation were on the order of 70 to 500 g. During rough operation the amplitude of chamber pressure oscillations were on the order of ± 50% of the average chamber pressure and the oscillations persisted during the programmed duration of the run.

It is significant to note that the amplitude of the chamber pressure oscillations never were greater than ± 50% during rough operation. This nondiverging characteristic of the pressure oscillation confirms the attenuating aspects of the LR99 injector thrust chamber configuration.

In every rough operation, the thrust mount vibration frequency corresponded to the combustion frequency. The thrust mount vibration levels were on the order of 2 to 3 times higher than the engine vibration levels. However, when isolators were installed between the engine and the thrust mount, the absolute value of the engine vibration level was reduced by 60% over vibration levels observed without isolators. These data indicate the coupling of thrust mount resonance with an acoustic combustion mode and confirm the amplifying feedback characteristic from the thrust mount to the engine.

Examination of the chamber pressure data reveals that the rough operations exhibit a transverse type of pressure oscillation as evidenced by the symmetrical type of combustion pressure waves and the wave phase relationship (Fig. 9). The identification of the transverse wave form has been made by many investigators (3 to 11). The longitudinal mode is probably very difficult to excite because of the scattering of pressure wave reflections from the curved surfaces of the nozzle and injector.

As noted earlier, during development testing with flat face injectors in which rough operations were experienced, severe injector burnout occurred (face erosion and chamber barrel erosion). The pattern of erosion was believed to be indicative of a transverse type of combustion oscillation. There is no evidence of any erosion with the present hemispherical headed injector as a result of combustion oscillations during any rough operations. This can probably be attributed to the curved injection and nozzle entrance surfaces which would afford much greater attenuation of transverse oscillations than the flat face injector.

SUMMARY AND CONCLUDING REMARKS

The unique design concept of the LR99 injector thrust chamber configuration represents a major breakthrough towards the solution of unstable combustion aspects of large rocket engines. The development program has shown that the LR99 combustion chamber configuration, using a hemispherical, multispud injector, is inherently stable as originally hypothesized when the design was conceived.

It was determined that the random occurrences of severe vibration were the direct result of vibration amplification caused by resonance of the airframe thrust mount at a known acoustic mode of combustion oscillation. Successful decoupling of the combustion oscillations and the mount resonance characteristics was demonstrated. It is concluded that the severe vibrations can be eliminated by an effective isolator system or by redesign of the thrust mount to change its natural frequency so that it does not coincide with the fundamental acoustic frequencies of the thrust chamber.

Attempts to obtain a reproducible combustion and vibration disturbance were unsuccessful except when operating under an intentional fuel lead condition (off design engine condition). The inability to obtain a reproducible combustion disturbance is attributed to the inherent stability of the combustion process in the LR99 engine. It is considered that the LR99 engine spherical type of combustion section geometry, which is a radical departure from conventional designs, provides excellent acoustic gas damping characteristics. The rough operation experienced with the LR99 engine is unique in that an amplification of engine vibration levels results from resonance of the thrust mount and that the combustion oscillations do not produce any erosion or overheating of hardware. Also, the authors conclude that the high values of chamber pressure oscillation, that is, those in the range of 10 to 50%, are the result of mechanical vibration of the thrust chamber and injection system.

REFERENCES

1 R.W. Seaman and D.S. Smith: Flight Rating Test Demonstration of the XLR99-RM-1 Rocket Engine. Preprint 1409-60, ARS 15th Annual Meeting, Washington, D.C., Dec. 5-8, 1960.

2 P.S. Gwozdz and V. Sjoberg: Design Concepts and Simulated Altitude Testing of the X-15 Aircraft Rocket Engine. Symposium on Simulated Altitude Testing of Rocket and Missile

Components, AEDC TR 60-6, December 1959.

3 L. Crocco and J. Grey: Combustion Instability. Proc., Gas Dynamics Symposium, pp. 55-70, Northwestern University, August 1955.

4 A.O. Tischler and T. Male: Oscillatory Combustion in Rocket Propellant Engines. Proc., Gas Dynamics Symposium, pp. 71-83, Northwestern University, August 1955.

5 R.B. Lawhead, R.S. Levine and W.T. Webber: Liquid Propellant Rocket Instability Studies. Rocketdyne Rept. No. P-122, January 1959.

6 J.R. Osborn and R.M. Schiewe: An Experimental Investigation of High Frequency Combustion Pressure Oscillations in a Gaseous Bipropellant Rocket Motor. Purdue Univ. Rept. No. I 58-1, June 1958.

7 J.R. Osborn and J.M. Bonvell: On The Importance of Combustion Chamber Geometry in High Frequency Oscillations in Rocket Motors. Preprint 1108-60, ARS Semi-Annual Meeting, Los Angeles, Calif., May 9-12, 1960.

8 L. Crocco and S. Cheng: Theory of Combustion Instability in Liquid Propellant Rocket Motors. Butterworths Scientific Publications, London, 1956.

9 J.R. Osborn and A.C. Pinchak: Investigation of Aerothermo Dynamic Interaction Phenomena in Combustion Pressure Oscillations. Purdue Univ. Rept. No. I 59-2, June 1959.

10 L. Crocco, J. Grey, and D.T. Harrje: Theory of Liquid Propellant Rocket Combustion Instability and Its Experimental Verification. ARS Jour., February 1960, Vol. 30, pp. 159-168.

11 F.K. Moore and S.H. Maslen: Transverse Oscillations in a Cylindrical Combustion Chamber. NACA TN 3152, October 1954.

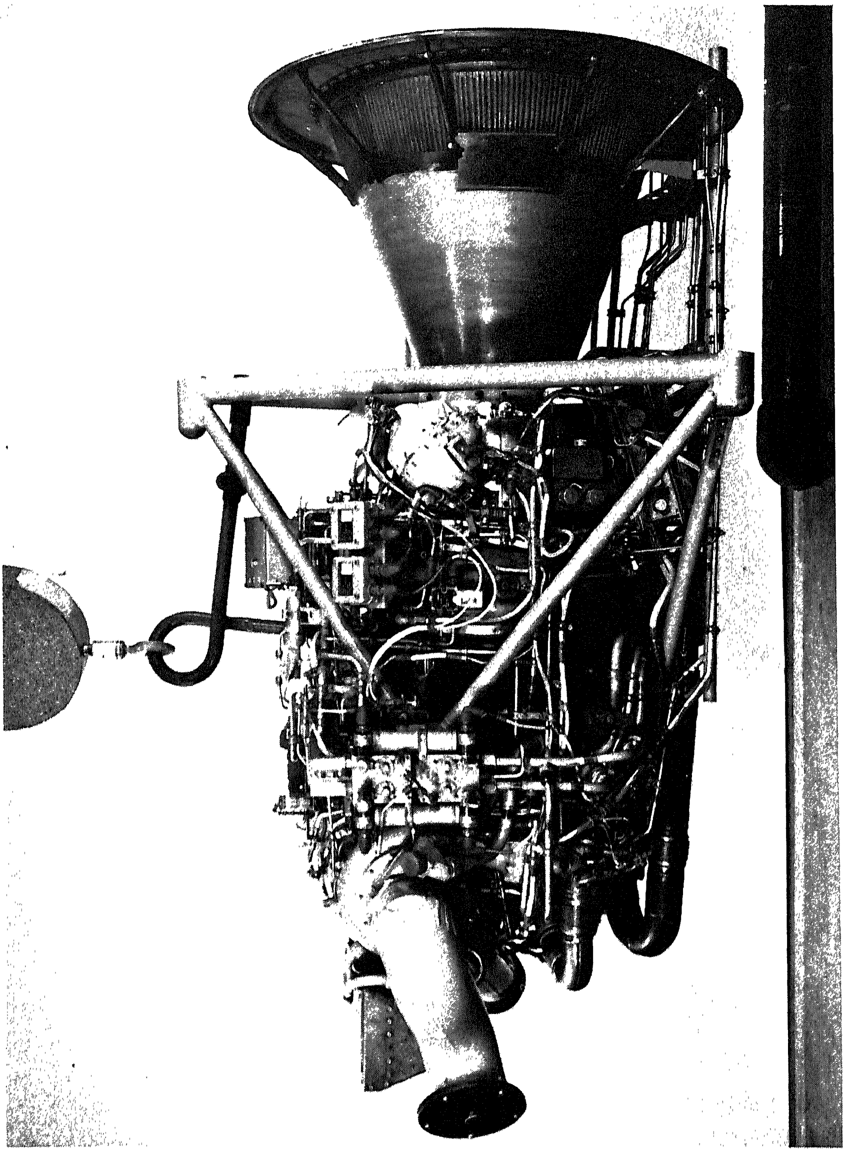

Fig. 1 Side view of LR99 engine

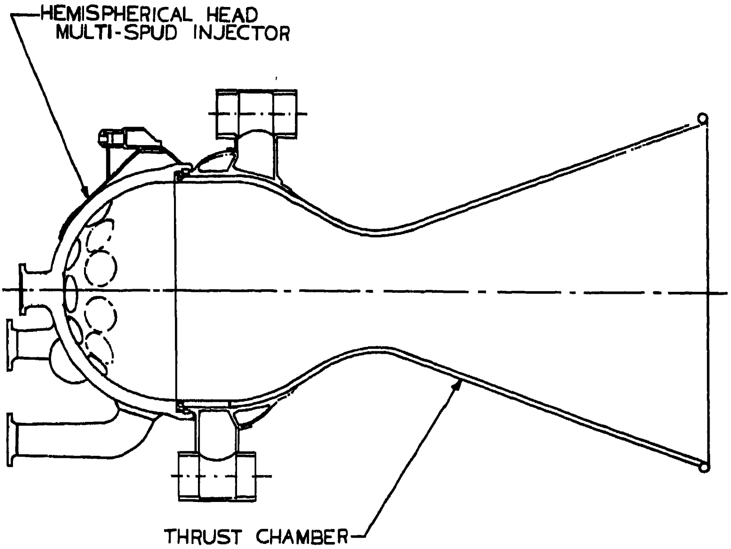

Fig. 2 IR99 Injector thrust chamber configuration

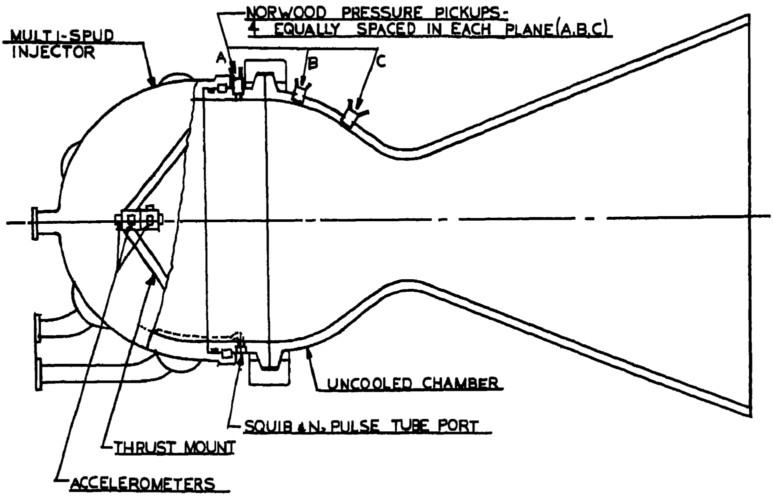
NORWOOD PRESSURE PICKUPS-
4 EQUALLY SPACED IN EACH PLANE (A,B,C)
MULTI-SPUD
INJECTOR
A
B
C
UNCOOLED CHAMBER
SQUIB & N_2 PULSE TUBE PORT
THRUST MOUNT
ACCELEROMETERS

Fig. 3 Uncooled thrust chamber assembly

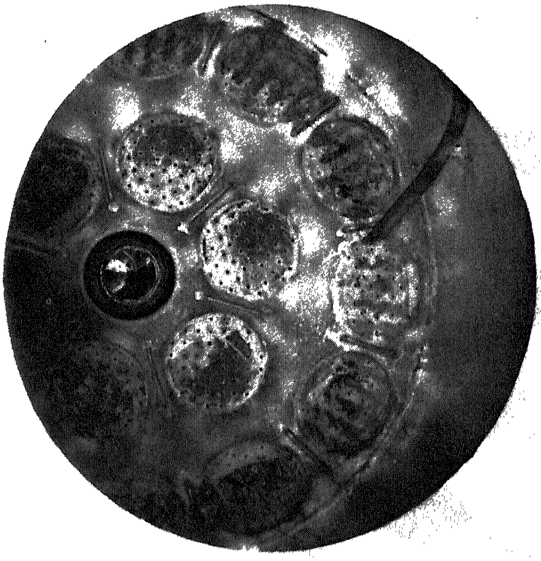

Fig. 4 Nitrogen gas pulse tube

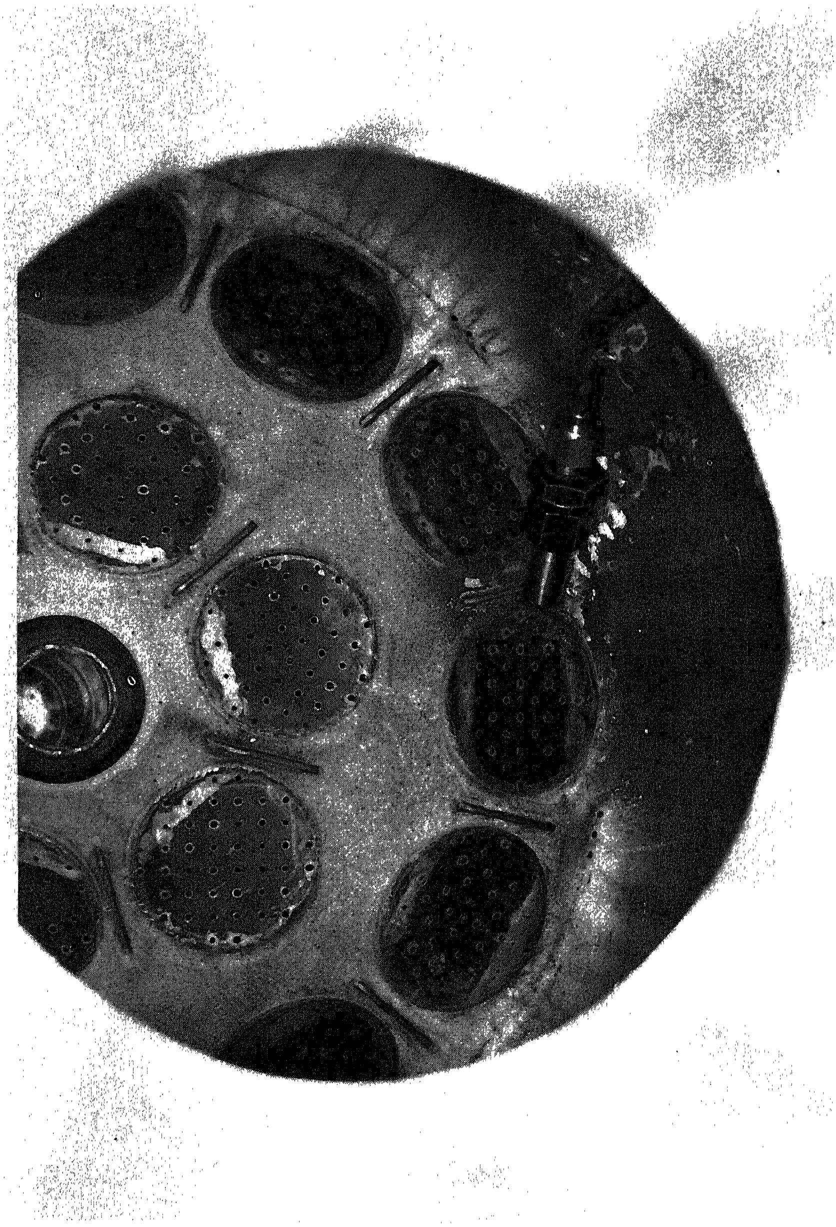

Fig. 5 Cartridge pulse tube

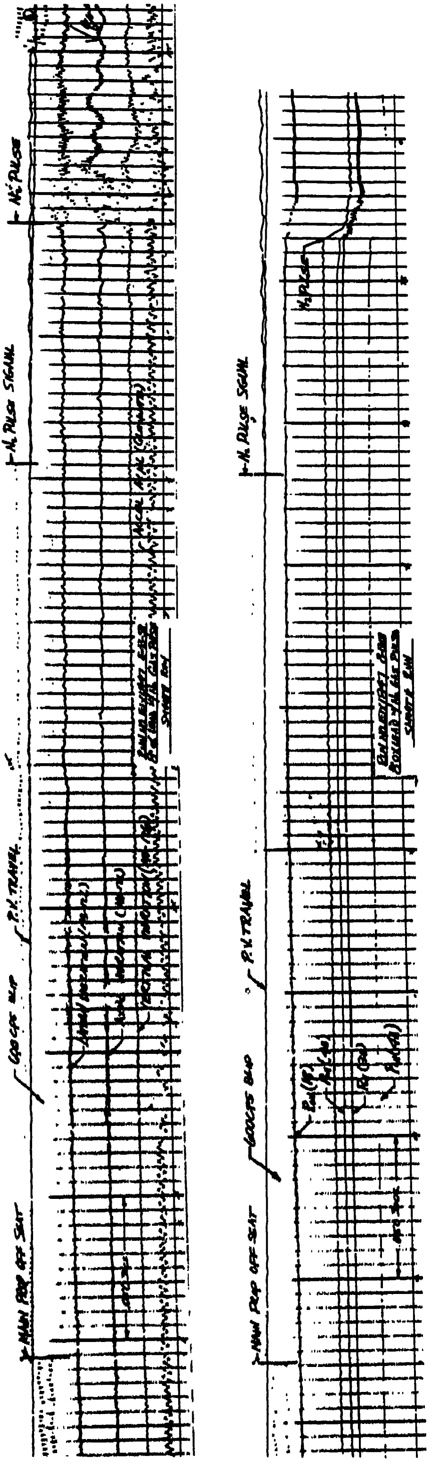

Fig. 6 Oscillograph record of smooth run

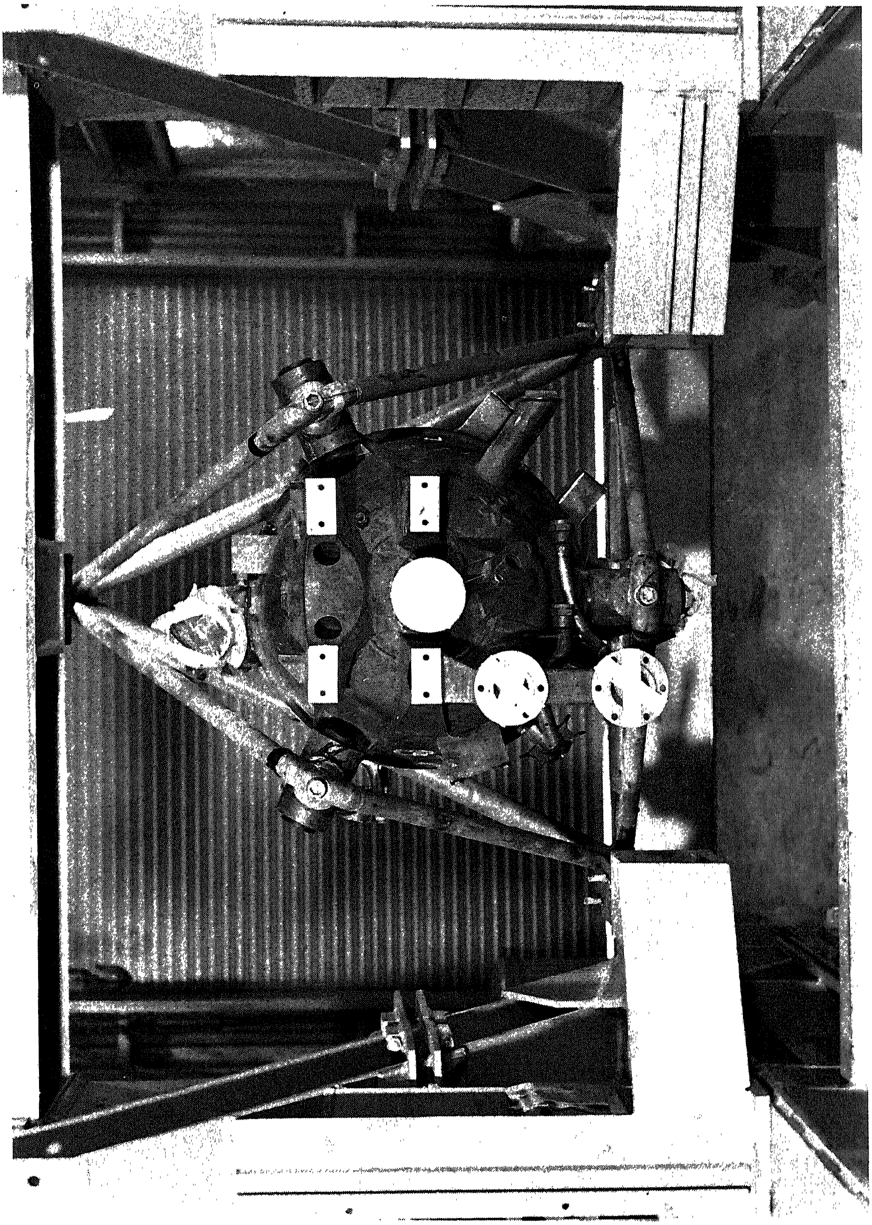

Fig. 7 Breadboard engine front view with thrust mount isolators

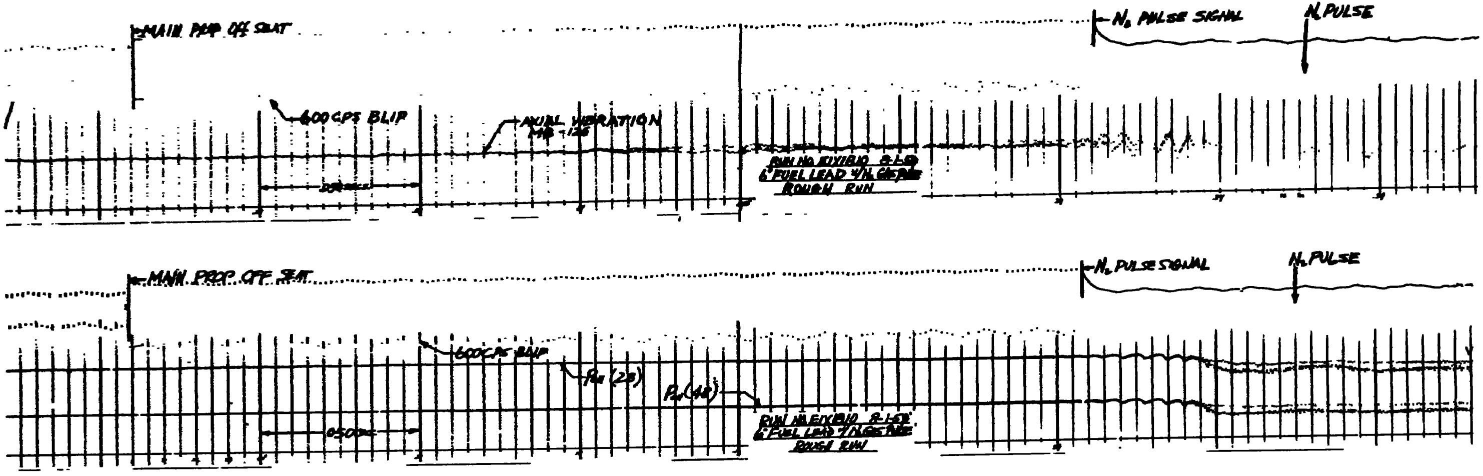

Fig. 8 Oscillograph record of rough run

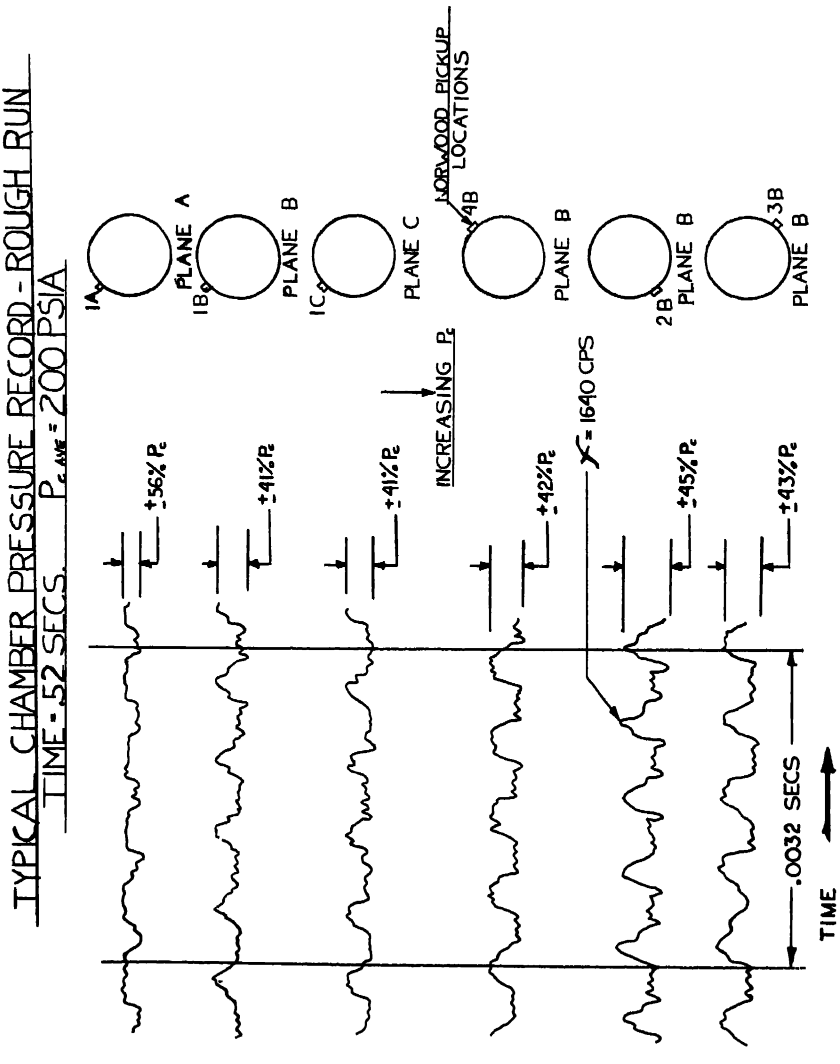

Fig. 9 Rough run combustion oscillation

TANGENTIAL MODE OF COMBUSTION INSTABILITY

H. C. Krieg Jr.

Aerojet-General Corp., Azusa, California

ABSTRACT

The results of pulse motor investigations into the tangential mode of combustion instability are discussed. Particular emphasis is placed on: The axial and radial distribution of the instability front within the experimental chamber; correlation of luminosity, instantaneous pressure with the front motion; and estimation of the chamber-gas movement during unstable combustion. A combustion model for tangential instability is presented, and its application to combustion systems is discussed. The inherent stability of combustion processes is shown to be dependent on the relationship between cyclic pressure modes and the mechanism for replenishment of pressure sensitive energy. It is shown that the pressure modes are controlled by chamber geometry, whereas the replenishment of energy is a function of the chemical and physical processes.

INTRODUCTION

The ability to control combustion instability in liquid propellant rocket combustion chambers is of prime concern. Unstable combustion is caused by varied and unrelated phenomena and occurs in many forms. Often the cure for one type of instability is the cause of another type, but regardless of the cause or type of instability, its presence in a development program spells delays and increased costs. In the earliest days of liquid-propellant rocket-engine development, chugging and screaming modes were usually encountered. Chugging (low frequency combustion instability) was associated

---

H.C. KRIEG Jr. is Assistant Senior Engineer. Paper presented at the ARS Propellants, Combustion and Liquid Rockets Conference, Palm Beach, Florida, April 26-28, 1961. Part of this research was developed under programs sponsored by AFOSR, Air Force Flight Test Center, Edwards Air Force Base, and Wright Air Development Center.

with feed-line impedance, and screaming instability was an acoustic axial mode related to the combustion-chamber length. Investigations of these phenomena (1-4)[1] were made and methods of achieving stable combustion were soon established. As thrust chambers became larger, the tangential and radial acoustic modes became more prevalent.

During the past seven years, the Aerojet-General Corp., under contract to various government agencies, has been conducting intensive research into the nature and mechanism of the tangential mode of combustion instability. The initial studies[2] described the physical processes occurring in the combustion chamber during unstable combustion. This work established the basic mechanism of sustained unstable combustion and described a model diagram for the various tangential-front systems. The basic tangential front, shape, and pressure profiles at the chamber walls were established during unstable combustion (5). Later investigations[3] developed an experimental rating technique for determining the inherent stability levels of various injection systems. This contribution permitted evaluation of rocket performance parameters with respect to stability and operating conditions of the full scale engine prior to actual engine construction. The technique, called the pulse motor technique and described in the section following, eliminated the tedious and expensive statistical approach previously used in trial and error development techniques. The stability rating method not only identified those systems which possessed poor stability, it also permitted comparisons to be made of the degree of inherent stability between two "stable" configurations. Current work in combustion research is concerned with investigating the relationship of rocket performance parameters, particularly that of injector design to the inherent stability of existing engines.

The objective of this paper is to relate the results of Aerojet's investigations into the physical nature of the unstable tangential mode mechanism, and to describe several of the applications.

---

[1] Numbers in parentheses indicate references at end of paper.

[2] Conducted under contract to the Air Force Office of Scientific Research.

[3] Conducted under contract to the Air Force Ballistic Missile Division and the Air Research Development Command, in addition to the Office of Scientific Research.

TEST HARDWARE

In order to conduct an experimental investigation of the tangential combustion instability mode, it was necessary to develop a suitable laboratory tool. The investigation, if conducted in a full scale thrust chamber, would be expensive and time consuming, since full scale injectors are expensive to fabricate and are usually damaged during any prolonged instability. Moreover, testing in a high thrust range (over 100 k-lb) would require an extensive test facility and the propellant cost would be prohibitive on a research level. It was urgent to speed development of a low cost, laboratory-type tool operating within low thrust ranges yet capable of giving results comparable to those of the full scale thrust chamber. Some of the tools developed by Aerojet are described in Ref. 6 and are repeated here for continuity.

The Pulse Motor

One of the laboratory tools developed was the pulse motor. A typical pulse motor is shown schematically in Fig. 1. The thrust chamber is designed to favor the tangential mode by confining the propellant injection to an annulus extending radially inward from the circumference of the chamber. The injector is divided into replaceable elements, resulting in a discontinuous injection around the chamber circumference. To facilitate rapid changes in injection patterns, the injection elements are removable. One type of element consists of a series of interchangeable strips into which the injection patterns are drilled.

The outermost portion of the full scale injector pattern is reproduced in the small orifices which have approximately 10% of a full scale pattern orifice area. The combustion conditions immediately downstream of the injector elements, therefore, are similar to those experienced in the full scale thrust chamber; however, the flow rates and thrust levels are about 10% of the corresponding parameters in the full scale chamber. The stability of an injector pattern may be evaluated over a range of test conditions by adjustment in the propellant flow rate, mixture ratio, and chamber pressure. Various pulse motors which have different internal geometries are available to determine the effect of chamber diameter, length, and contour on stability.

Combustion instability is induced in the pulse motor by firing gaseous pulses tangentially into the chamber, across the injector face. These pulses, simulating fully developed, tangential, high frequency instability fronts, are fired into the chamber by means of pulse generators, one of which is shown in Fig. 1. When a measure of the instability resistance between two injection patterns (or two rocket parameters) is required, a series of calibrated gas pulses, each of successively increasing intensity, are fired into the chamber until instability is developed. By noting the energy of the pulse required to initiate such instability, a rating of that parameter's effect on the stability index is thereby obtained.

In terms of physical parameters, the stability index is a measure of the relative magnitude of the induced pulse perturbation as compared with the chamber pressure into which it is fired. It is defined as

$$i = (\Delta P)/(P_c)$$

where i = stability index

P_c = steady-state chamber pressure, psia

ΔP = increase over P_c due to pulse, psi

In general, the relative stability obtained with any given injection pattern or any propellant combination at a given chamber pressure and mixture ratio is defined by the two test values: The value of i corresponding to the largest pulse not causing instability; and the value corresponding to the smallest charge causing instability.

The stability index associated with each standard pulse charge is determined experimentally by measurement of that pressure perturbation when fired into a shock tube.

The occurrence of instability in the pulse motor is detected by two methods: A combustion luminosity record; and high response pressure instrumentation.

Combustion luminosity records are obtained through a slit window placed in the chamber section of the motor. They are recorded, via a strip film technique, on cameras which are capable of film velocities of over 100 fps. Timing dots are placed on films and pressure records simultaneously, at 1-millisec intervals. The pressure records are provided by a high response pressure transducer recorded through a high fidelity instrumentation system on an oscillograph. The pressure sensing diaphragm of the gage is mounted flush with the chamber wall in all cases. Thus, a relatively thorough means is provided to prove the existence of any tangential mode instability, and to acquire knowledge of the number, type, velocity, and severity of shock fronts which may be present.

Reproductions of a typical film record are shown in Fig. 2. Shown in sequence are: 1) stable steady-state combustion before firing of pulse; 2) firing of the pulse; 3) a shock front developing 20 millisec after the pulse; and 4) a fully developed instability front 60 millisec after firing of pulse.

PHYSICAL PROPERTIES OF THE TANGENTIAL FRONT

The following information summarizes the physical characteristics of the tangential mode as presented in Ref. 5.

Motion of the Tangential Front in a Chamber

Test data obtained for numerous pulse motor tests indicate that the tangential front is concentrated in an annular zone. The outer boundary of this zone is formed by the chamber wall, and the front rotates about the thrust chamber axis, parallel to this boundary. The location of the front within an axial segment of the chamber was obtained through photographic records obtained by cameras located approximately 90° to each other, as illustrated in Fig. 3. The instability occurring in this figure is a continuous single-front instability. The points A, B, and C which are marked on the film are related to corresponding points in the schematic diagram shown at the bottom of the page. Point A appears at the bottom of the camera record No. 1, and at the same time it appears on the far side of the chamber in camera record No. 2. When the front arrives at point B, midway between points A and C, it is approaching nearest to camera No. 1 and will soon pass around to the far side of the chamber. As viewed from camera No. 2, the front at point B has just passed this closest point and has just appeared on the near side of the chamber. As the front revolves on to position C, it appears on the far side of the chamber to camera No. 1, and it appears at the second peak excursion point to camera No. 2. Thus, the motion of the front is seen to propagate circumferentially around the chamber.

Correlation of Pressure and Luminosity Fronts

The relationship between the pressure perturbations sensed by the pressure recording system and the luminosity record during unstable operation may be illustrated in Fig. 4. The two records are correlated by means of the timing marks placed on the photographic film and pressure records. It may be seen that the peak pressure perturbation corresponds to the arrival of the intense luminosity at the location of the pressure gage. The location of the front, therefore, is defined as the zone of intense luminosity. A discontinuous double front was used for this particular figure and, although there is often more than one front present in a chamber, the correlation between pressure peaks and luminosity zones is easily seen. No true "step-function" pressure rises were detected with the passage of the front by the pressure sensing equipment. However, tangential front propagational rates at velocities up to Mach 3 with respect to the chamber wall were found in many instances, and the behavior simulates a detonation front in many aspects. It is believed that the shape of the pressure profile, if true, is a result of the internal chamber geometry and the heterogeneous mixture of the combustion gases. It is interesting to note that at a pressure ratio of 4.49 a Mach number of 2.05 is calculated for a normal one-dimensional shockwave in a perfect gas where the ratio specific heat γ equals 1.2 (10). During the fully developed instability portion of the test shown in Fig. 4, the front velocity was 6900 fps or approximately Mach 2.0. The length of the pressure discontinuity is found to be 1.2 in., as measured by the pressure gage at the chamber wall. This interface thickness is large when compared with the narrow thickness associated with true shock or detonation waves.

Distribution of Front in the Combustion Chamber

The shape of the tangential front was determined with the aid of split window photography, taken in all three dimensions of the chamber. The axial distribution of the front is illustrated in Fig. 5 for a continuous, single-front instability. Only a small portion of the front is parallel to the axis of the chamber, and the luminosity level is higher in this area than over the rest of the chamber length. Therefore, the major portion of the energy released during instability takes place during this zone which, for this test condition, extends approximately 3 to 4 in. from the injector face. This verifies some earlier reports that higher performance could be achieved by operating chambers normally unstable. The phenomena permits a more effective use of chamber length L^*, thus producing an increase in combustion efficiency. To verify this, an experimental program was conducted in which the chamber length was varied from approximately 0.5 to 14 in. long, while maintaining a constant throat area. Combustion efficiency, as measured by the characteristic velocity C^* showed a marked reduction in the smaller length during the stable combustion, but no significant change was noted during fully developed steady-state combustion instability.

Recent work performed by Pickford and Peoples (7), in which the gas-evolution rate was measured as a function of chamber length, indicated that the gas-evolution rate (and therefore energy release) maximizes within three inches of the injector face and then sharply decreases. This also tends to support the conclusion that the major portion of energy released occurs within this brighter parallel portion of the film.

Downstream of the high energy zone, the front is not parallel to the axis of the chamber and the nozzle end of the front lags behind the injector end. A reflection similar to a bow wave extends from the entrance of the nozzle back toward the injector. All motions of the front, however, do maintain the same cyclic relationships; this indicates a cyclic propagation in the zone viewed by the camera.

Considering the axial window record by itself, the question may arise: Is the luminosity record that of a tangential front or that of an axial mode which is moving between the injector face and the nozzle entrance cone? If such were the case, the axial velocity from this wave (as computed from the slope of the tail) would be approximately 8700 fps. The usual velocity for an axial front existing in this type of a combustion system seldom exceeds a 4500-fps level. In any event, the existence of axial and circumferential window photographs precludes the existence of this instability mode. Assuming that the velocity of the front is dependent on the energy available for consumption in the front, the front velocities downstream of the high energy zone should be less than that within the zone; if so, the following model may be constructed:

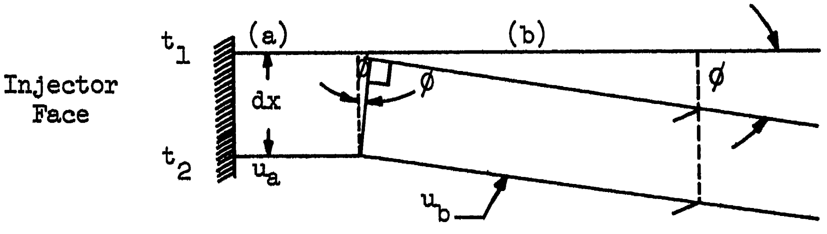

a = high energy zone   b = low energy zone where $u_a = dx/dt$, front velocity in high energy zone

$u_b = dx/dt \cos \phi$, front velocity in low energy zone

$u_b = u_a \cos \phi$

The high energy portion of the front has a velocity of 6900 fps, whereas the low energy zone is computed to be 6883 fps. The differences in front propagational velocities are only a few feet per second.

A radial window record taken during fully developed combustion instability is shown in Fig. 6. As may be seen, the front appears alternately on one side of the chamber and then on the other. The luminosity reaches its maximum extent at the time the front arrives, even though this area emits relatively little light during stable combustion or between front arrivals. These records support the belief that the front is concentrated near the outer zone of the thrust chamber.

A typical circumferential window view of a tangential instability is shown in Fig. 1. The luminosity streaks between the front arrivals are easily seen, and are interpreted as gas motion induced by the pressure disturbance. A detailed discussion of this type of record is included in Ref. 8.

Gas Motion and Pressure Distributions

The chamber gas motion and pressure distribution may be obtained through a three-dimensional pictorial integration of the axial, radial, and circumferential film records. Fig. 7 indicates what is believed to take place during a continuous single-front tangential instability. During the integration, four assumptions had to be made.

1) The luminosity streaks, most probably burning droplets of fuel, which appeared between the front arrivals and through the fronts themselves, represent the velocity of the gas particles.[1]

---

[1] Actually the droplet velocities will tend to lag behind the local gas velocity, at the time of this calculation this velocity difference was not considered and therefore Figs. 7, 8, and 9 should be considered qualitatively rather than quantitatively. The velocity curve and particle path presented in Figs. 8 and 9 will change slightly; however, their characteristic shape should be retained.

2) The front velocity and the cycle period are constant.

3) Axial movement of the chamber gases during one cycle is negligible.

4) Circumferential motion and velocity of the gas particles are the same along any radius of the chamber with respect to the tangential front.

With these basic assumptions and film record data, the chamber gas velocities and instantaneous vectors may be constructed for any given instant of time. The segment of the chamber considered was within the high energy release zone and parallel to the injector face. The radial and circumferential velocities from the film records discussed previously were resolved into velocity vectors for each part of the cycle. A plot of these vectors and vector angles is given in Fig. 8. Fig. 7 shows these vectors as drawn on a cross section of the chamber segment. Polar plots of gas velocity magnitude and pressure profiles as measured at the chamber wall are shown with respect to location of the tangential front. An abrupt motion of chamber gases radially outward is noted just prior to the arrival of the front. The chamber gas velocities across the chamber face reached a maximum of 2450 fps at this point. The atomization and heat transfer input to the liquid propellant streams, with such high velocity gaseous motion, becomes very effective and accounts for the exceedingly short time required for the preparation of the instability supporting media. These velocities can also partially account for the high rates of heat transfer to the injector face and chamber walls during this type of combustion instability. The instability front considered in this typical test attained a front velocity of 6860 fps, and is considered to be of medium strength.

Gas Particle Path

The path of a gas particle during one cycle of combustion instability was calculated in Ref. 5 and is shown in Fig. 9. The location of gas particles chosen for the foregoing calculations was one inch from the chamber wall, with the particle and the front initially at the same angular position in the chamber.

At position 1, the front and particle under consideration have the same angular position. The particle is suddenly accelerated as the front passes and travels in the same direction as the front movement. The sudden release of combustion gases directly behind the front causes the particle to be deflected toward the center of the chamber. The particle is seen to be traveling in a direction opposite its original path. It begins to move radially outward and toward its initial angular position at the time the front revolves to the 180° position. During this period, the particle velocity is at its lowest. The particle starts accelerating just prior to the arrival of the front, which passes the particle for the second time at position 5.

THE MECHANISM OF THE TANGENTIAL FRONT

Analysis of over 700 pulse motor tests and full scale test data has developed a mechanism for the tangential mode which is based on the amount and distribution of pressure sensitive energy in the path of a pressure perturbation, and on the reinforcement of that disturbance by the release of this energy. Pressure sensitive energy is defined as that energy available for unburned, mixed, and reactive vapors which can be instantaneously combusted when subjected to a positive pressure discontinuity. The following conditions are necessary for establishing high frequency instability:

1) The proper distribution of pressure sensitive media

2) High chemical reactivity in this pressure sensitive media

3) Relatively low energy drag losses from the instability front as it circumvents the chamber

4) A rapid replenishment of the pressure sensitive energy after front passage

5) The occurrence of an initiation mechanism.

This means that for instability to propagate it is necessary that the cycle period of the perturbation be equal to, or greater than, the energy recovery time (time required to replenish energy to its initial level). It is also required that the pressure sensitive energy released to the path be equal to, or more than, the energy dissipated from the front. The front propagation (or the motion of the pressure discontinuities) tends to exhibit superacoustical velocities, while the front strengths are similar to those expected for detonation wave systems. The general motion of the front is in the circumferential direction.

APPLICATIONS TO FULL SCALE THRUST CHAMBER DESIGN

Pulse motors, during the six years that they have been used at Aerojet-General, have been developed in various sizes ranging from 15 to 72 in. in diameter, with capabilities of simulating full scale thrust chambers with nominal thrust ranges from 50,000 to 3,000,000 lb thrust (9). The value of the pulse motor has been demonstrated by an extensive series of correlations between stability results as determined by the pulse motors and those actually encountered in the full scale thrust chambers. In each case in which a pattern tested in the pulse motor was also tested in the full scale chamber, the prediction of the pulse motor had been verified by the full scale tests. These results show that the pulse motor is a useful tool in the control of tangential, high frequency, combustion instability. Its use and the combustion theories derived from its use at Aerojet have minimized the development problems usually encountered in this field.

The effect of various system operating parameters on stability may be determined by the use of this technique. The results of some of these investigations are presented in the following section.

CHAMBER GEOMETRY

The chamber geometry can be a significant factor in determining whether combustion instability will occur, and, if it does occur, its degree and severity. Considerations must be made of the internal contour of the thrust chamber, of whether injector face baffles should be used on the injector, and the effect of diameter on combustion process.

Chamber Diameter

Fig. 10 illustrates three streak film records which were obtained during a study of chamber diameter. The tests were conducted in three different pulse motor sizes (15-, 22-, and 30-in. diam), each using the IRFNA/JP-4 propellant combination. Test conditions of injection velocity, mixture ratio, chamber pressure, and injector pattern were all maintained constant. The study yielded the following information:

1) When combustion instability was initiated in the 15-in. diam pulse motor, a continuous single front resulted. This mode of tangential instability, although of intermediate strength, is severe enough to cause thrust chamber destruction.

2) When tested in the 22-1/2-in. diam pulse motor, a single continuous front also developed. The front velocity and the steady-state chamber pressure fluctuation were found to be higher than those of the 15-in. diam motor; thus, the front ~~was~~ considered to be stronger. The occurrence of this instability would be of even more serious consequence than that obtained in the 15-in. diam motor.

3) When the chamber diameter was increased to 30 in., a continuous system was not obtained. Instead, a relatively weak discontinuous system developed and the instability appeared less severe than that occurring in either the 15- or 22-in. diam pulse motors.

In each chamber, the local front velocities were the same even though there were relatively large differences in the chamber diameters. Hence, the cycle period of the front increased with diameter. Similar tests with the LO_2/RP-1 propellant combination and a like-on-like injection pattern showed that at a given chamber pressure stability varied markedly between the 15- and 22-1/2-in. diam pulse motors tested. At a chamber pressure of about 500 psi, stability was poor in the 15-in. diam chamber and good in the 22-1/2-in. diam chamber. Later tests with the LO_2/RP-1 propellant combination with a different pattern in a 48-in. diam pulse motor resulted in poor stability. Thus, it appears that there may be an "optimum" chamber diameter for a given propellant and injection system or, conversely, that an optimum injection technique can be developed for a given propellant combination and chamber diameter.

THE EFFECT OF PATTERN ORIENTATION

The orientation of an injection pattern in an injector face can have a major effect on combustion stability. For example, tests have shown that the angular position of a showerhead matrix relative to the thrust chamber wall has a substantial effect on combustion instability (as measured by the size of a pulse charge required to initiate this instability and the severity of the instability thus excited). An example of this, showing the result of angular rotation of a showerhead matrix on stability using WFNA and JP-4 in the 15-in. diam pulse motor appears in Fig. 11. As may be seen, the stability is at its lowest when the oxidizer and fuel are introduced along a radius. An explanation for this phenomenon may be seen by considering the chamber gas motion directly behind a front, as shown in Fig. 9. It can be seen that at angles where one liquid stream may be driven into the opposite propellant (by the gas motion), severe instability problems exist. As the pattern is rotated to angles where the fuel and oxidizer streams do not converge, the stability problem is less severe.

EFFECT OF PROPELLANT CHARACTERISTICS

Bipropellant Characteristics

Propellant characteristics were known to exercise significant effects on combustion instability. Test results such as those in Fig. 12 showed the "tuning" effects caused by the addition of water to the propellant. A low water content produced a double-front cycle. As water was added, a very strong, destructive, single-front cycle appeared. At still higher water contents, the single front weakened the available energy recovery functions, also shown on the figure. The data indicate that a dry propellant requires a relatively short physical preparation time, resulting in a double-front system. By the addition of water, the required preparation time was increased and two fronts could no longer be supported. As a result, a single-front cycle with a relatively long preparation time resulted.[1] When still more water was added, increasingly more time was required for the same degree of preparation; consequently, a weaker front developed.

Monopropellant Characteristics

Test results indicate that the monopropellant decomposition of a propellant is a significant factor. Tests with the N_2O_4/hydrazine propellant combination indicate that the stability of patterns using this propellant combination is sensitive to changes in mixture ratio to a very significant degree, as shown in Fig. 13. This may be understood when one considers the parameter, preparation time, and what it consists of. First, there must exist in any combustion process a significant time for the two molecules of oxidizer and fuel to collide and react. This time can be broken up into two portions; a transport time (relatively long) and a chemical reaction time (relatively short). With a monopropellant, the transport time is eliminated, permitting extremely short preparation times. As the concentration of the monopropellant increases for a given injector system, more and more energy is available at a faster rate.

---

[1] Preparation time is defined as that time required to restore the quantity of pressure sensitive energy consumed by the passage of the instability front. For a detailed discussion of this parameter, the reader is referred to Refs. 7 and 8.

CONCLUSIONS

Investigations into the nature of the tangential mode of high frequency combustion instability have revealed many characteristics of this phenomenon. A brief summary of the major conclusions and the results from the investigations includes the following:

1) The radial and axial distribution of the tangential front in a rocket chamber has been defined.

2) The motion of the chamber gas during a single-front tangential instability has been outlined.

3) The estimated particle path and radial motion of the gas particle during the presence of a front has been defined.

4) A procedure for rating stability has been developed and applied to the development of full scale thrust chambers.

5) The function of various rocket performance parameters and their effect on combustion instability has been investigated.

REFERENCES

1 Y. C. Lee, M. R. Gore, and C. C. Ross: Stability and Control of Liquid Propellant Rocket Systems, Jour. American Rocket Society, March-April 1953, pp. 75-81.

2 Sin-I Cheng: Low Frequency Combustion Stability of Liquid Propellant Rocket Motors with Different Nozzles, Jet Propulsion, vol. 25, 1955, p. 163.

3 A. O. Tischler and D. R. Bellman: Combustion Instability in an Acid-Heptane Rocket with a Pressurized-Gas Propellant Pumping System, NACA Note 2936, 1953.

4 Luigi Crocco and Sin-I Cheng: Theory of Combustion Instability in Liquid Propellant Rocket Motion, Butterworths Scientific Publication, London, 1956.

5 R. S. Pickford, H. C. Krieg Jr., and H. B. Ellis: Basic Research on Combustion in Liquid Rocket Thrust Chambers, Aerojet-General Rept. no. 1193, Jan. 1957.

6 J. A. Bottorff: Research Tools for Experimental Evaluation of New Storables, Semi-Annual Meeting, July 1960, Preprint 1270-60.

7 R. S. Pickford and R. G. Peoples: Inherent Stability of the Combustion Process, ARS Paper No. 1490-60, December 1960.

8 H. B. Ellis and R. S. Pickford: High Frequency Combustion Instability, Aerojet-General Rept. TN 17, Sept. 1956.

9 H. C. Krieg Jr. and G. A. Coultas: Analytical and Stability Scaling Techniques, Presented to the Combustion Institute, April 1960, Preprint 61-12.

10 J. H. Keenan and F. G. Keyes, Gas Tables, 4th ed., John Wiley and Sons, Inc., New York, 1954, p. 171, table 51.

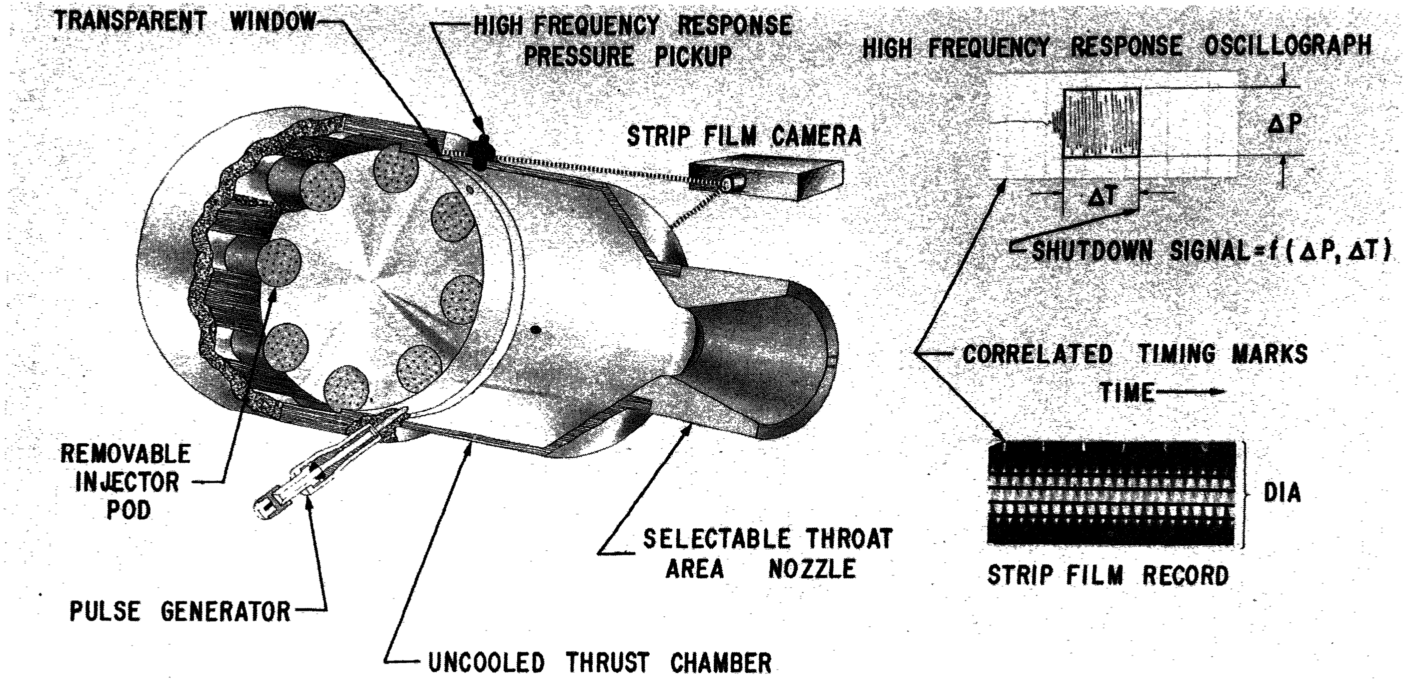

Fig. 1 Elements of the pulse motor

STEADY COMBUSTION

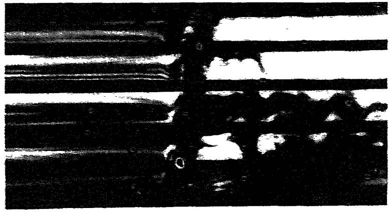

EXCITING PULSE

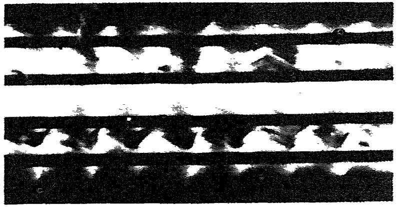

0.020 SECONDS AFTER PULSE

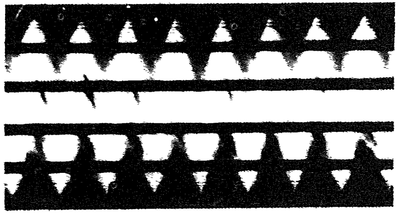

0.060 SECONDS AFTER PULSE
FULLY DEVELOPED CONTINUING FRONT

Fig. 2 Combustion sequence

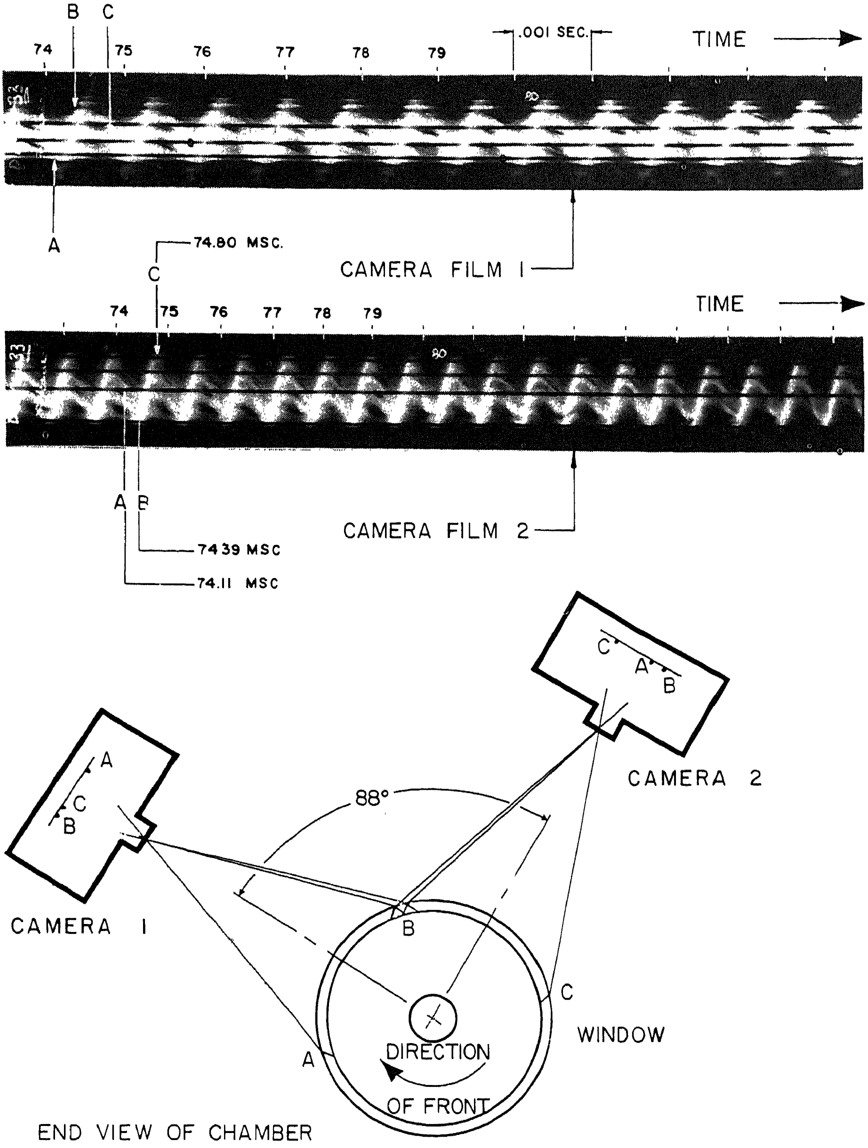

Fig. 3 Circumferential propagation of tangential front

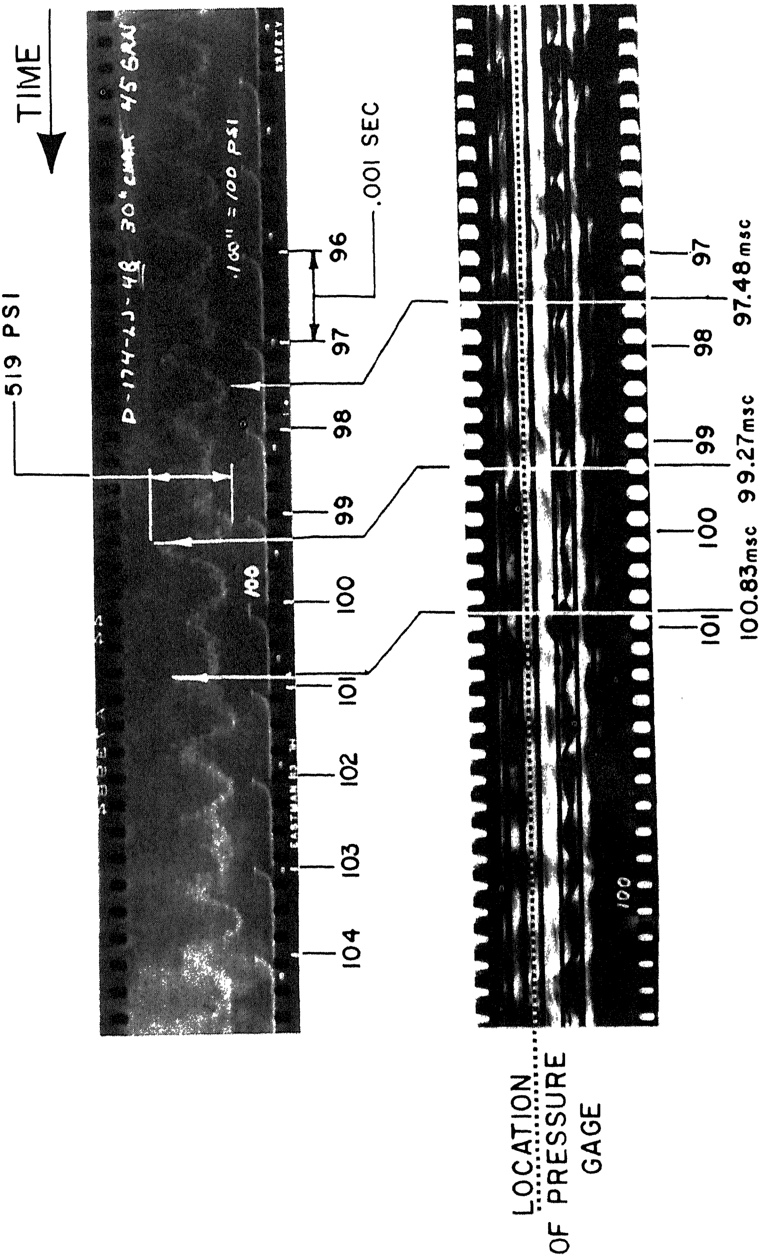

Fig. 4 Correlation of chamber pressure and slit-window luminosity; discontinuous double front

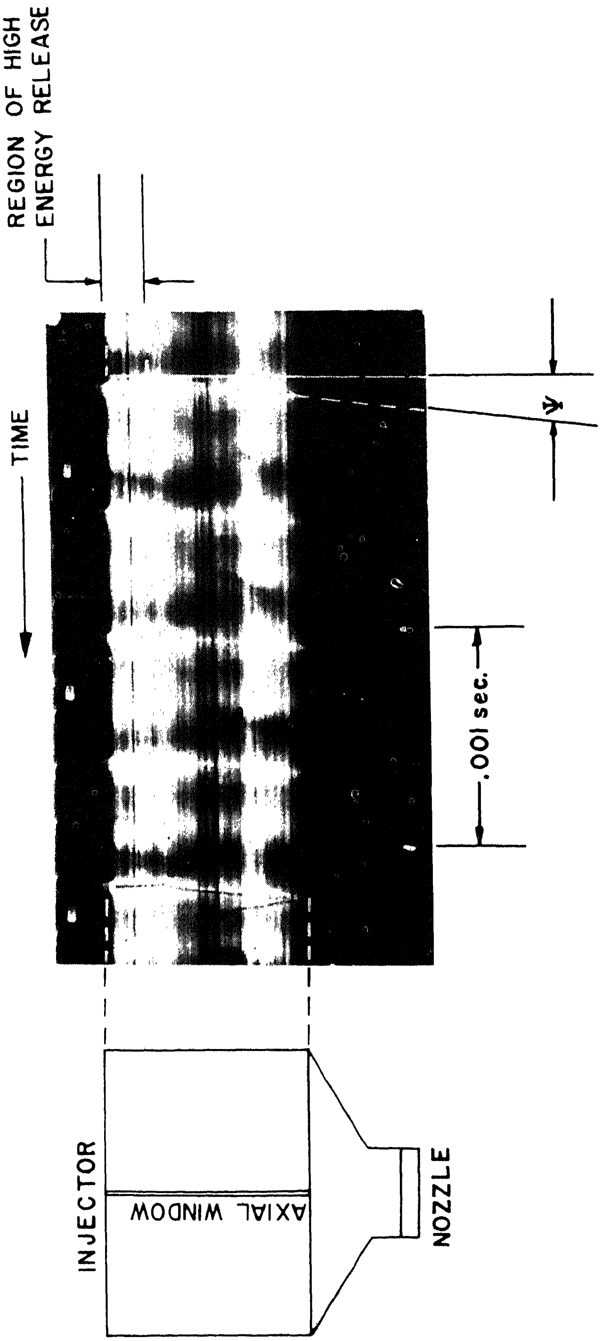

Fig. 5 Axial distribution of tangential front

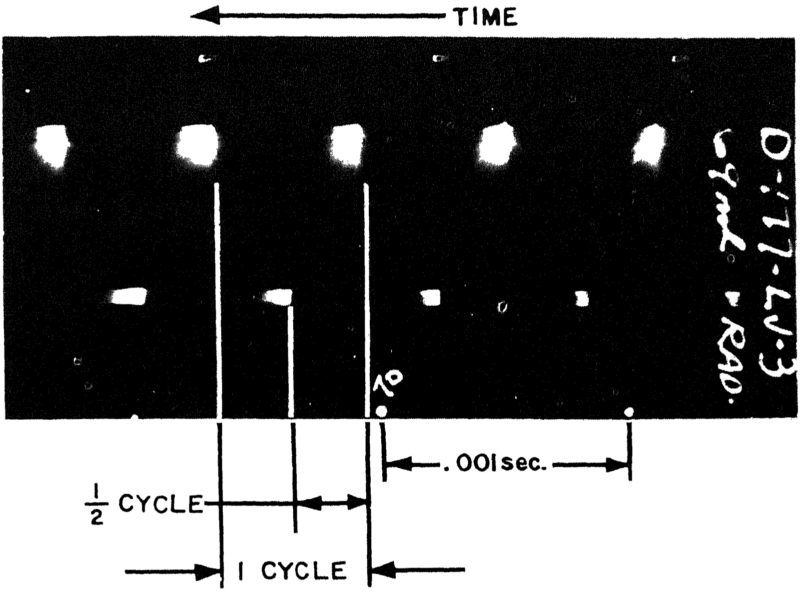

Fig. 6 Radial distribution showing single-front tangential instability

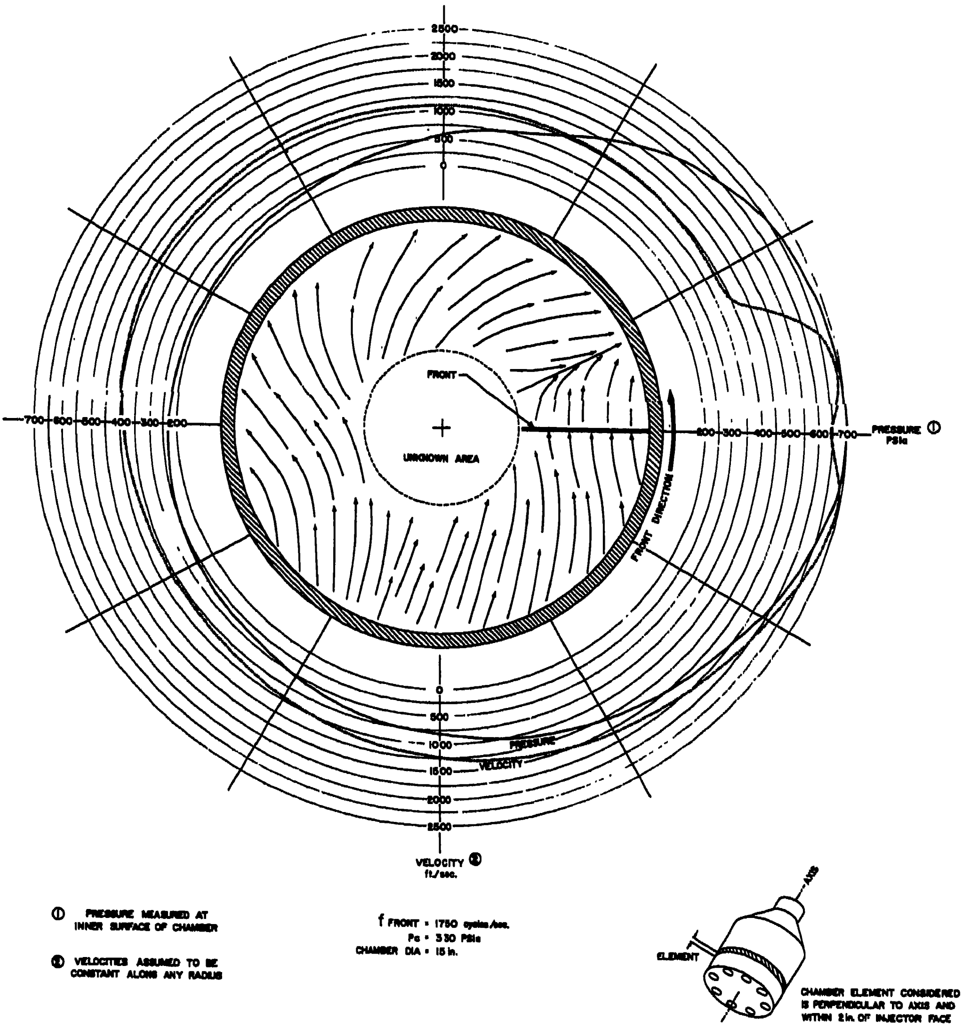
2500
2000
1500
1000
500
0
FRONT
UNKNOWN AREA
FRONT DIRECTION
700 600 500 400 300 200
200 300 400 500 600 700
PRESSURE ①
PSIa
PRESSURE
VELOCITY
VELOCITY ②
ft./sec.
① PRESSURE MEASURED AT INNER SURFACE OF CHAMBER
② VELOCITIES ASSUMED TO BE CONSTANT ALONG ANY RADIUS
f FRONT = 1750 cycles/sec.
Pc = 330 PSIa
CHAMBER DIA = 15 in.
AXIS
ELEMENT
CHAMBER ELEMENT CONSIDERED IS PERPENDICULAR TO AXIS AND WITHIN 2 in. OF INJECTOR FACE

Fig. 7 Instantaneous pressures in a cross-sectional element of chamber

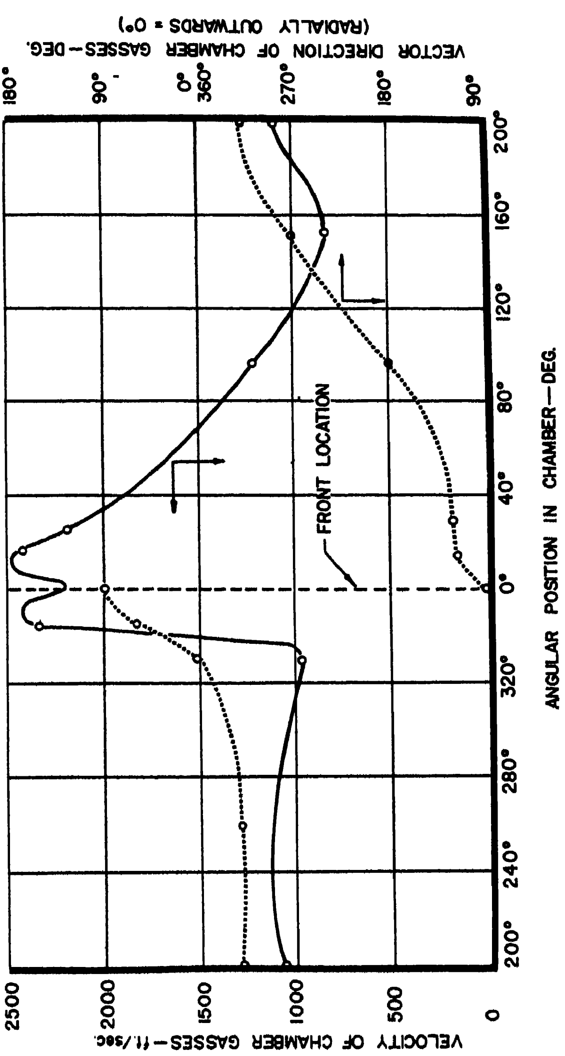

Fig. 8 Instantaneous velocity and vector diagram

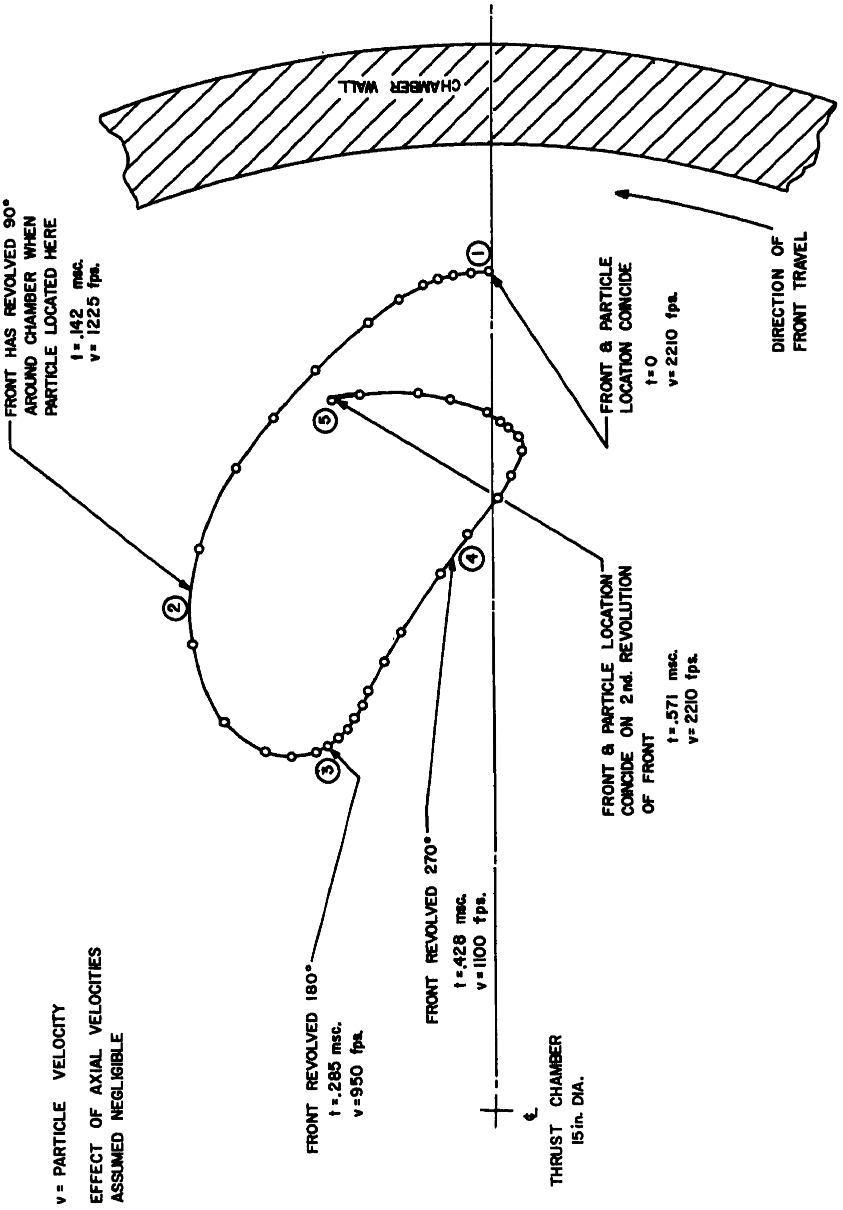
CHAMBER WALL
DIRECTION OF FRONT TRAVEL
①
FRONT & PARTICLE LOCATION COINCIDE
t = 0
v = 2210 fps.
②
FRONT HAS REVOLVED 90° AROUND CHAMBER WHEN PARTICLE LOCATED HERE
t = .142 msc.
v = 1225 fps.
③
FRONT REVOLVED 180°
t = .285 msc.
v = 950 fps.
④
FRONT REVOLVED 270°
t = .428 msc.
v = 1100 fps.
⑤
FRONT & PARTICLE LOCATION COINCIDE ON 2nd. REVOLUTION OF FRONT
t = .571 msc.
v = 2210 fps.
℄
THRUST CHAMBER
15in. DIA.
v = PARTICLE VELOCITY
EFFECT OF AXIAL VELOCITIES ASSUMED NEGLIGIBLE

Fig. 9 Estimated particle path

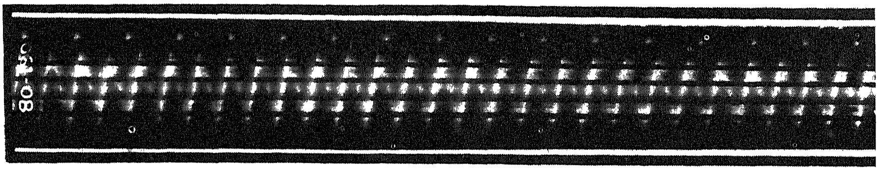

Pc = 210 psia. MR = 3.76 W_t = 22.03 lbs./sec.

CONTINUOUS SINGLE FRONT — VELOCITY = 6740 ft./sec.

15 in. DIA. CHAMBER

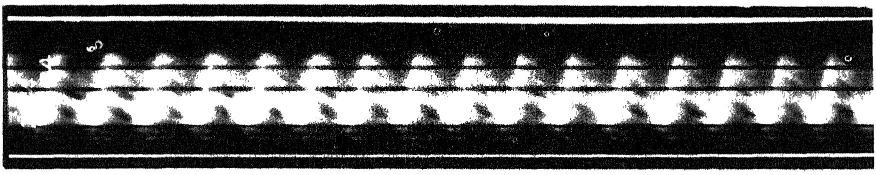

Pc = 242 psia. MR = 3.65 W_t = 36.68 lbs./sec.

CONTINUOUS SINGLE FRONT — VELOCITY = 6900 ft./sec.

22.5 in. DIA. CHAMBER

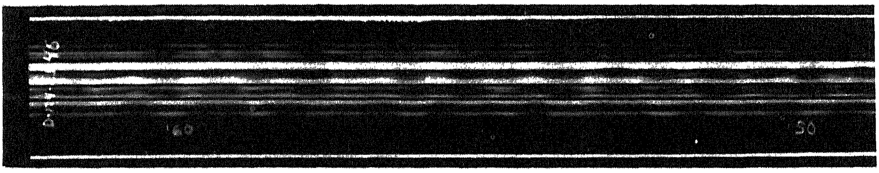

Pc = 238 psia. MR = 3.54 W_t = 48.1 lbs./sec.

DISCONTINUOUS MULTI - FRONT SYSTEM — TYPICAL VELOCITY = 6860 ft./sec.

30 in. DIA. CHAMBER

SHOWERHEAD INJECTOR # 0—007098A
PROPELLANTS: IRFNA -JP4

Fig. 10 Effect of chamber diameter on tangential mode

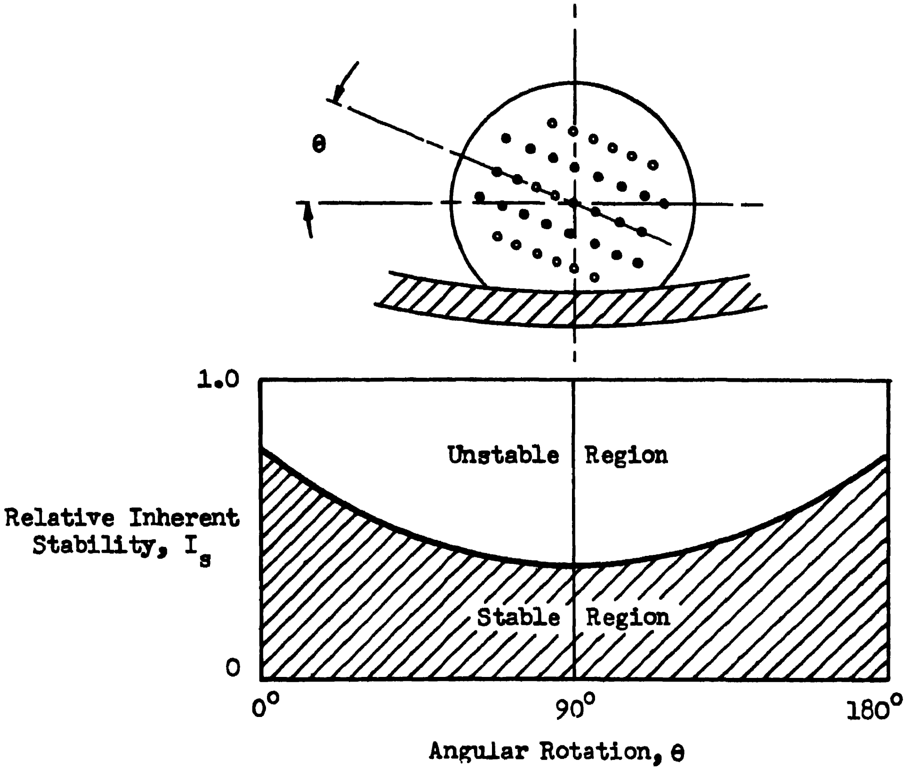

Fig. 11 Effect of injector orientation on relative inherent stability

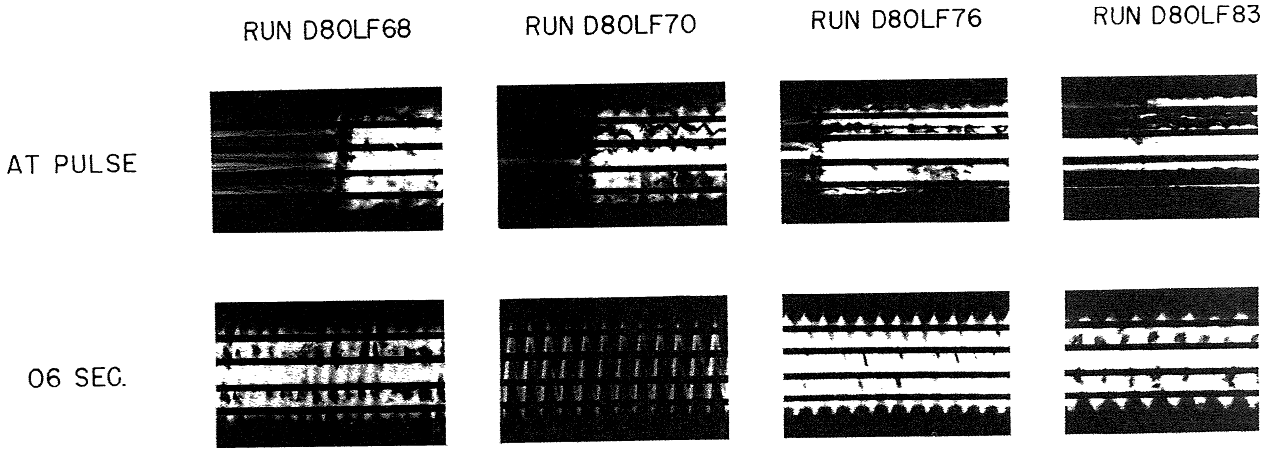

WATER CONTENT
(% BY WEIGHT)

	RUN D80LF68	RUN D80LF70	RUN D80LF76	RUN D80LF83
TOTAL	2.20%	2.51%	4.04%	4.81%
WFNA	2.25	2.11	2.51	2.50
30AN-70FA	2.00	4.00	9.80	13.50

MIXTURE RATIO=3.75 15 GRAIN CHARGE INJECTOR O-011147 PATTER

Fig. 12 Effect of total water content on inherent instability

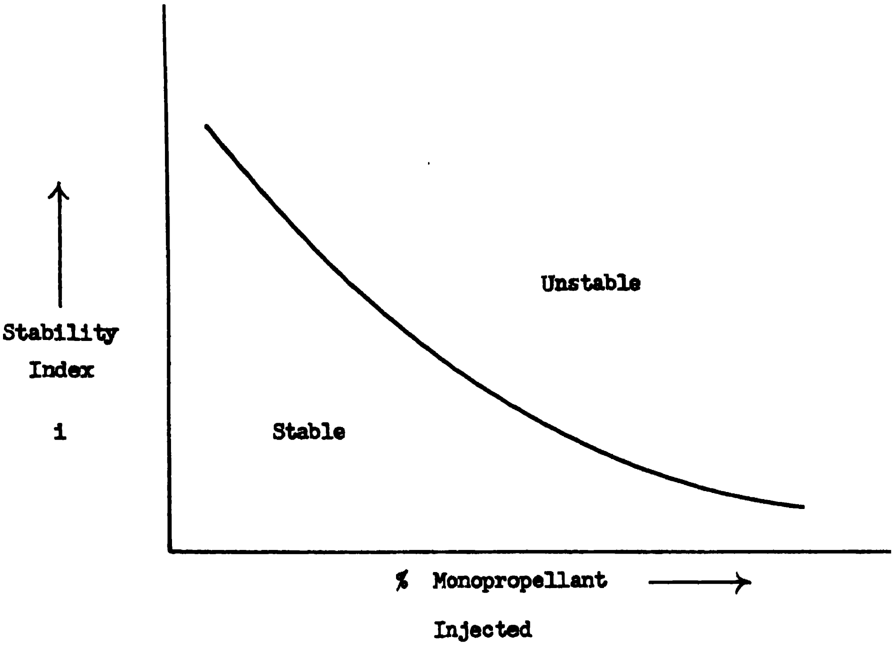

Fig. 13 Effect of monopropellant reactivity

CONTRIBUTORS TO VOLUME 6

Agosta, Vito D., Mechanical Engineering Department, Polytechnic Institute of Brooklyn, Brooklyn, New York... p. 243.

Boyer, M. H., Chemistry Department, Aeronutronic Division of Ford Motor Company, Newport Beach, California... p. 75.

Brown, B., Basic Research Division, Hercules Powder Company, Salt Lake City, Utah... p. 195.

Burstein, Samuel Z., Polytechnic Institute of Brooklyn, Brooklyn, New York[1]... p. 243.

Combs, L. P., Combustion Dynamic Research Group, Rocketdyne, A Division of North American Aviation, Inc., Canoga Park, California... p. 269.

Fay, James A., Department of Mechanical Engineering, Massachusetts Institute of Technology, Cambridge, Massachusetts... p. 3.

Foreman, K. M., Plasma Propulsion Laboratory, Republic Aviation Corporation, Farmingdale, New York... p. 47.

Grandey, Ray, Radiation Physics Department, Aeronutronic Division of Ford Motor Company, Newport Beach, California... p. 75.

Hammer, Sanford S., Mechanical Engineering Department, Polytechnic Institute of Brooklyn, Brooklyn, New York... p. 243.

Kliegel, James R., Space Technology Laboratories Inc., Los Angeles, California... p. 173.

Krieg, H. C., Jr., Aerojet-General Corporation, Azusa, California... p. 339.

Lambiris, S., Rocketdyne, A Division of North American Aviation, Inc., Canoga Park, California[2]... p. 269.

Luperi, Mario J., Reaction Motors Division, Thiokol Chemical Corporation, Denville, New Jersey... p. 321.

---

[1] Presently at Courant Institute of Mathematical Sciences, New York, New York

[2] Presently at Pratt & Whitney Aircraft Division, United Aircraft Corporation, East Hartford, Connecticut

MacMillan, R., Plasma Propulsion Laboratory, Republic Aviation Corporation, Farmingdale, New York... p. 47.

Miller, Riley O., Chemistry and Energy Conversion Division, NASA Lewis Research Center, Cleveland, Ohio... p. 65.

Morgenthaler, John H., Kinetics and Combustion Division, Atlantic Research Corporation, Alexandria, Virginia... p. 145.

Morrell, Gerald, Chemical Rocket Fundamentals Branch, NASA Lewis Research Center, Cleveland, Ohio... p. 305

Nickerson, Gary R., Space Technolgy Laboratories Inc., Los Angeles, California... p. 173.

Pevney, H., Plasma Propulsion Laboratory, Republic Aviation Corporation, Farmingdale, New York... p. 47.

Priem, Richard J., Rocket Combustion Section, NASA Lewis Research Center, Cleveland, Ohio... p. 305

Rannie, W. D., Daniel and Florence Guggenheim Jet Propulsion Center, California Institute of Technology, Pasadena, California... p. 117.

Reese, Bruce A., Jet Propulsion Center, Purdue University, Lafayette, Indiana[3]... p. 209.

Richard, Louis P., Jet Propulsion Center, Purdue University, Lafayette, Indiana[4]... p. 209

Richmond, J. Kenneth, Flight Sciences Laboratory, Boeing Scientific Research Laboratories, Seattle, Washington... p. 17.

Tick, Sanford J., Reaction Motors Division, Thiokol Chemical Corporation, Denville, New Jersey... p. 321

Williams, F. A., Division of Engineering and Applied Physics, Howard University, Cambridge, Massachusetts... p. 99.

---

[3] Presently (on leave) at U.S. Army Ordnance Missile Command, Huntsville, Alabama

[4] Presently at The Martin Company, Denver, Colorado